Université de Montréal

On Turbulence and the Formation of Riffle-Pools in Gravel-Bed Rivers

(La turbulence et la formation des seuils-mouilles dans les rivières à lit de gravier)

par

Bruce J. MacVicar

Département de géographie

Faculté des arts et des sciences

Thèse présentée à la Faculté des études supérieures

en vue de l'obtention du grade de

Philosophiae Doctor (Ph.D.) en géographie

May, 2006

Univesité de Montréal

Faculté des études supérieures

Cette thése intitulée:

Turbulence and the Formation of Riffle-Pools in Gravel-Bed Rivers

(La turbulence et la formation des seuils-mouilles dans les rivières à lit de gravier)

présentée par:

Bruce J. MacVicar

a été évaluée par un jury composé des personnes suivantes:

Lael Parrott - présisent-rapporteur

André Roy - directeur de recherche

François Courchesne - membre du jury

Michel Lapointe - membre du jury

Douglas Thompson - examinateur externe

Alain Vincent - représentent du doyen de la FES

RÉSUMÉ

Cette thèse doctorale porte sur l'organisation des rivières à lit de graviers. La formation du lit en séquences à grande échelle - les séquences seuil-mouille - est une caractéristique de ces rivières qui contrôle la stabilité et la productivité écologique. Malgré son importance, le mécanisme qui génère les seuil-mouilles reste obscur. Ce problème est lié à trois facteurs: les données de terrain qui existent ne sont pas suffisantes pour accepter ou rejeter les hypothèses qui existent; la complexité des interactions entre l'écoulement, le transport des sédiments, et les formes du lit; et le rôle de la turbulence qui n'est pas considéré de façon adéquate. L'approche de cette thèse est d'aborder ces facteurs simultanément avec des méthodes innovatrices pour mesurer les paramètres importants sur le terrain et de modéliser des processus non linéaires dans une rivière. Les objectifs sont: (a) de développer un modèle qui est capable de simuler le transport des sédiments et les interactions avec l'écoulement turbulent, (b) en utilisant le modèle, de montrer le rôle des mécanismes de rétroaction dans le développement des formes du lit, (c) de tester les vélocimètres dans des écoulements à fortes vitesses et fortes intensités turbulente, (d) de mesurer et caractériser les dynamiques de l'écoulement dans un seuil-mouille forcé, (e) de mesurer et caractériser les dynamiques de la sédimentologie et la morphologie dans un seuil-mouille forcé, et (f) en utilisant le modèle et l'analyse des données de terrain, d'identifier les mécanismes qui contribuent à la formation des seuils-mouilles.

En considérant une rivière comme un système complexe, nous avons créé un modèle qui simule le transport des sédiments individuellement, c'est-à-dire un modèle 'discret'. Les particules répondent aux paramètres locaux de l'écoulement et des boucles de rétroaction sont possibles. Les processus physiques sont simplifiés afin de permettre la considération des mécanismes qui génèrent les formes du lit. Nous montrons que les formes du lit à grande échelle émergent quand la turbulence varie en fonction de l'accélération et de la décélération de l'écoulement.

Nous avons suivi les dynamiques d'un seuil-mouille forcé pendant 18 mois. Cette période était très active en terme de changements géomorphologiqies à cause d'une série de crues de haut niveau. La plus grande était une crue d'une période de 15 ans. Nous avons échantillonné des séries de vitesses instantanées à 90 - 270 positions au site pendant des

crues de bas niveau jusqu'a plein bord. Les instruments ont été testés dans les environnements comparables afin d'assurer leurs capacités de fonctionner comme prévu. Les données hydrauliques nous ont montré quelques résultats importants. La décélération et l'accélération définissent respectivement l'écoulement dans le début et la fin de la mouille. Ceci a un effet important sur la forme des profils de vitesse moyenne, où des vitesses relativement basses sont présentes proche du lit dans la zone de décélération et des vitesses relativement hautes sont présentes proche du lit dans la zone d'accélération. Cet effet explique les observations d'un renversement de vitesses. Cependant, le renversement de vitesses est présent seulement dans la zone vers la fin de la mouille où la pente du lit est positive. Pour expliquer le transport des sédiments dans le début de la mouille, un effet secondaire est requis. Dans cet environnement, l'intensité de la turbulence est haute. Nous avons observé la séparation intermittente de l'écoulement dans cette région de l'écoulement et il apparaît que cette zone génère la turbulence observée.

Afin de suivre les mouvements des particules et de caractériser les patrons spatiaux du transport des sédiments, nous avons utilisé une technique relativement nouvelle basé sur les 'Passive Integrated Transponder (PIT) tags'. Nous avons marqué 300 roches de différentes tailles. Nous avons aussi cartographié le lit de la rivière plusieurs fois pendant cette même période afin de suivre les changements morphologiques. Un événement majeur s'est passé au début de la période d'étude. Cet événement a déplacé l'arbre qui détermine le lieu de la mouille, ce qui a provoqué une nouvelle période de développement morphologique que nous avons caractérisée. En général, la morphologie et le transport de sédiment reflètent la variabilité de l'écoulement. En aval de l'arbre, toutes les tailles de particules marquées ont été enlevées de la mouille et l'érosion de la mouille à été progressive. En contraste, en amont de l'arbre nous avons observé que le transport de sédiment est très sensible aux tailles des particules et que deux cycles d'aggradation et de dégradation se sont produits. Les particules plus larges que le D_{84} n'ont pas été déplacées du début de la mouille pendant la période d'études, malgré au moins un événement avec une fréquence de retour de 15 ans.

La conclusion centrale de la modélisation et de l'étude de terrain est que la turbulence est nécessaire pour expliquer la formation des seuil-mouilles. Le modèle est très important pour la généralisation des résultats parce qu'il démontre que des formes du lit

avec une taille, un triage de particule par taille, et une stabilité similaire à ce que nous observons dans les seuil-mouilles naturels peuvent être générées sans qu'un élément comme l'arbre soit présent pour le provoquer. Pour cela, il faut que le modèle inclue une règle qui lie la turbulence à l'accélération, une autre règle qui imite l'effet de la séparation de l'écoulement, et les sédiments de tailles hétérogènes. La convergence de ces facteurs avec les observations de terrain encourage l'hypothèse que tous les seuil-mouilles sont générés par un mécanisme similaire. Il apparaît que les éléments qui forcent les seuil-mouilles fonctionnent comme des catalyseurs qui activent les processus associés à l'écoulement non uniforme, mais que ces processus peuvent aussi émerger du système complexe qui constitue une rivière à lit graveleux. Ces résultats sont uniques dans la littérature et portent une nouvelle vision sur les dynamiques fluviales, la complexité, et l'organisation d'une rivière.

Mot-clés: rivières à lit graveleux; seuil-mouille; turbulence; système complexe; transport de sédiment; pistage de sédiment; formes du lit; cohérence; mesure de vitesse; écoulement non uniforme; accélération; décélération; séparation intermittente; émergence; auto-organisation.

SUMMARY

This thesis is a study of organization in rivers. Riffle-pool sequences determine the macro-scale structure in a broad range of gravel-bed rivers. They are defined by a scaling relation with stream width, sorting of sediment by size, and the formation of lateral bars. These features are of interest because they exert a significant control on stream stability and ecology. In spite of considerable effort, there is no consensus on the mechanism(s) by which the forms develop and are maintained. This problem is related to three factors: field data that is inadequate to accept or reject proposed hypotheses, the complexity of the possible interactions between the flow, sediment transport and bed form development, and inadequate consideration of the effects of turbulence. The approach of this thesis is to address these factors simultaneously through new modelling strategies and improved field methods and measurements. The specific objectives are: (a) to develop a model to simulate flow and sediment dynamics in order to examine the dynamics of bed form development in gravel-bed rivers and to demonstrate the role of feedback mechanisms in bed form development including the effect of turbulence; (b) to test available instrumentation for measuring turbulent flow properties in gravel-bed rivers during floods; (c) to measure and characterize the mean and turbulent flow dynamics of a forced riffle-pool and the sediment and morphologic dynamics in a forced riffle-pool; and (d) to use both the numerical simulations and analysis of the field data, to identify the mechanisms that lead to the formation and maintenance of riffle-pools in gravel-bed rivers.

Based on the assumption that a gravel-bed river may be described as a complex system, we developed a discrete particle model that simulates the transport of individual particles based on local rules to determine particle entrainment and the feedbacks between flow and bed form development. Physical processes were simplified to allow us to consider the mechanisms by which bed forms occur and are maintained. The model is capable of generating a wide range of bed forms at different scales. By varying turbulence intensity in response to flow acceleration and deceleration, we demonstrated the emergence of macro-scale bed forms.

To measure and characterize the flow and sediment dynamics of riffle-pools, we monitored a forced riffle-pool intensely for an 18 month period. The site is located in

Moras Creek, a 6 m wide gravel bed stream near Victoriaville (Quebec). The location of the riffle-pool is forced by a large tree with an intact root wad that slid in to the stream. The study period was geomorphically active. At the beginning of the study period, a large flood event rotateded the tree and reinitiated pool scour. A series of subsequent events, the largest of which had a return period of approximately 15 years, changed pool geometry. We sampled series of instantaneous velocity at up to 270 points through the study site during floods as high as the bankfull level. To measure velocity, we used Electromagnetic Current Meters (ECMs). These instruments were tested in comparable highly turbulent environments to ensure accuracy. The hydraulic data from the forced riffle-pool yielded a number of important and original results. Flow deceleration and accceleration were found to dominate the pool-head and pool-tail, respectively. This has a strong effect on the shape of mean velocity profiles, such that relatively low velocities occur near the bed in decelerating flows while relatively high velocities occur near the bed in accelerating flows. This effect explains the occurrence of a near-bed velocity reversal between the riffle and the pool-tail. However, mean velocity is not adequate to explain sediment transport in the pool-head. Instead, we observed high turbulence intensities, and it appears that intermittent flow separation near the bed generates high amplitude and short duration turbulent fluctuations that may be sufficient to initiate sediment transport.

To tag and track the movements of sediment particles, we utilized a relatively new technique based on Passive Integrated Transponder (PIT) tags. We followed morphological changes during the study period by repeatedly surveying the bed topography. Morphology and sediment transport reflect the observed variability of flow hydraulics. Downstream of the tree, all sizes of tagged particles were evacuated from the pool center and tail on at least two occasions and progressive erosion takes place so that the pool increased in length through the study period. In contrast, the region upstream of the tree was characterized by alternate cycles of scour and fill and highly size-selective sediment entrainment. Tagged particles larger than the D_{84} were not transported out of the pool-head during the study period in spite of events as large as the 15 year flood.

The key conclusion from both the numerical modelling and the field study is that turbulence is a critical factor in the formation of riffle-pools. Sediment transport by high turbulence in zones of low mean velocity appears to initiate pool scour and selectively

transport the finer sediments out of the pool-head. The numerical model is critical in the generalization of results because it demonstrates that bed forms with similar size, sorting, and stability to riffle-pools can emerge in the absence of forcing elements if three elements are included: 1) a rule that links acceleration to turbulence intensity, 2) flow separation downstream of steep lee slopes, and 3) heterogeneous sediments. The convergence of modeling results with field observations encourages the conclusion that acceleration and deceleration combined with turbulence generation are at the core of a general model of riffle-pool formation. Forcing elements appear to act as a catalyst to activate processes associated with non-uniform flow that can also emerge from the complex system of a gravel-bed river. These results are unique in the literature and offer a new insight into the flow and sediment dynamics, complexity, and organization of a gravel-bed river system.

key words: gravel-bed river; riffle-pool; turbulence; complex systems; sediment transport; bed forms; coherence; velocity measurement; sediment tracking; non-uniform flow; acceleration; deceleration; intermittent separation; emergence; self-organization.

TABLE OF CONTENTS

RÉSUMÉ ..... **III**

SUMMARY ..... **VI**

TABLE OF CONTENTS ..... **IX**

LIST OF TABLES ..... **XIII**

LIST OF FIGURES ..... **XIV**

NOMENCLATURE ..... **XXIV**

ACKNOWLEDGEMENTS ..... **XXVIII**

1 INTRODUCTION **1**

2 BACKGROUND **5**

2.1 CONTEXT: THE GRAVEL-BED RIVER 5

2.1.1 Turbulent flow over a gravel bed *5*

2.1.2 Sediment transport in gravel-bed rivers *13*

2.1.3 Bed form development *15*

2.2 RIFFLE-POOL MORPHOLOGY 18

2.3 SEDIMENT TRANSPORT IN RIFFLE-POOLS 25

2.4 FLOW DYNAMICS OF RIFFLE-POOLS 28

2.5 FORMATION OF RIFFLE-POOLS: THEORY AND FIELD EVIDENCE 37

2.6 MODELLING 42

2.7 PROBLEM IDENTIFICATION 48

2.8 OBJECTIVES 48

2.9 METHODOLOGY 49

2.10 THESIS STATEMENT 52

3 A 2-D DISCRETE PARTICLE MODEL OF GRAVEL-BED RIVER SYSTEMS **55**

3.1 INTRODUCTION 55

3.2 GRAVEL BED FORMS 57

3.3 MODEL DESCRIPTION 58

3.3.1 Conceptual Approach *58*

3.3.2 Initial Conditions *60*

3.3.2.1 Simulation Matrix 60

3.3.2.2 Flow Stage 61

3.3.3 Model Algorithms *62*

3.3.3.1 Particle Entrainment and Movement 62

3.3.3.2 Particle Hiding 63
3.3.3.3 Particle Imbrication 64
3.3.3.4 Local Instantaneous Velocity 65
3.3.3.5 Turbulence 65
3.3.3.6 Flow Acceleration 66
3.3.4 Summary of Model Execution *67*
3.4 Model Simulations 68
3.5 Results 69
3.5.1 Space-Time Plots *69*
3.5.2 Profile plots *76*
3.5.3 Roughness *78*
3.5.4 Pool dimensions *79*
3.5.5 Sensitivity *82*
3.6 Emergent Bed forms 83
3.7 Discussion 85
3.8 Conclusions 90

4 MEASURING WATER VELOCITY IN HIGHLY TURBULENT FLOWS: FIELD TESTS OF AN ELECTROMAGNETIC CURRENT METER (ECM) AND AN ACOUSTIC DOPPLER VELOCIMETER (ADV) 92

4.1 Introduction 92
4.2 Methodology 94
4.2.1 Field Site and Experimental Design *94*
4.2.2 Signal Processing *97*
4.2.3 Data Quality Analysis *98*
4.2.4 Comparison of Turbulence Statistics *103*
4.3 Results 104
4.3.1 Internal ADV Parameters *104*
4.3.2 Spectral Analysis *105*
4.3.3 Error Analysis *109*
4.4 Comparison of Turbulent Flow Parameters and Discussion 111
4.5 Conclusion 117

5 FLOW DYNAMICS OF A FORCED POOL IN A GRAVEL-BED RIVER PART A: MEAN VELOCITY AND TURBULENCE INTENSITY 120

5.1 Introduction 120
5.2 Methodology 122
5.2.1 Field Site *122*
5.2.2 Flow Measurements *124*

5.2.3 Data Quality and Post-Processing *129*
5.2.4 Turbulence intensity and shear stress in non-uniform flow *130*
5.3 RESULTS AND ANALYSIS 133
5.3.1 Spatial and Flow Stage Variability *133*
5.3.2 Mean velocity profiles at bankfull flow *139*
5.3.3 Effect of flood stage on inner flow region *140*
5.3.4 Turbulence intensity and shear stress *142*
5.4 DISCUSSION 145
5.4.1 Streamwise velocity profiles *146*
5.4.2 Laterally converging flow and secondary circulation *148*
5.4.3 Turbulence generation and energy dissipation *149*
5.4.4 Shear Stress in Non-Uniform Flow *150*
5.5 CONCLUSIONS 152

6 FLOW DYNAMICS OF A FORCED POOL IN A GRAVEL-BED RIVER PART B: THE STRUCTURE AND SCALE OF TURBULENT EVENTS 154

6.1 INTRODUCTION 154
6.2 METHODOLOGY 157
6.2.1 Field Site and Data Collection *157*
6.2.2 Model of mean velocity and turbulence intensity *158*
6.2.3 Data Analysis *159*
6.2.3.1 Flow Separation 159
6.2.3.2 Spectral analysis 160
6.2.3.3 Space-time correlation and auto-correlation 160
6.2.3.4 Event Analysis 161
6.3 RESULTS 163
6.3.1 Flow Separation *163*
6.3.2 Spectral analysis *165*
6.3.3 Space-time correlation and auto-correlation *168*
6.3.4 Event analysis *173*
6.3.5 Effect of discharge *184*
6.4 DISCUSSION 186
6.5 CONCLUSION 189

7 SEDIMENT DYNAMICS OF A FORCED POOL IN A GRAVEL-BED RIVER 192

7.1 INTRODUCTION 192
7.2 METHODOLOGY 194
7.3 RESULTS 204
7.3.1 Topographical changes *204*

7.3.2 Path lengths of sediment transport *208*

7.3.3 Spatial distribution of entrainment and deposition of tagged particles *210*

7.4 DISCUSSION 216

7.5 CONCLUSIONS 222

8 GENERAL DISCUSSION AND CONCLUSIONS 223

8.1 INTRODUCTION 223

8.2 SUMMARY OF KEY FINDINGS 223

8.3 ORIGINALITY OF THE THESIS 226

8.4 CONCEPTUAL MODEL 228

8.5 FUTURE RESEARCH 229

BIBLIOGRAPHY 233

APPENDIX A – ACCORD DES COAUTEURS ET PERMISSION DE L'ÉDITEUR 250

APPENDIX B – AUTORISATION DE RÉDIGER LA THÈSE EN ANGLAIS 255

APPENDIX C – AUTORISATION DE RÉDIGER LA THÈSE SOUS FORME D'ARTICLES 256

LIST OF TABLES

TABLE 2.1 - EMPIRICAL STUDIES OF POOL-RIFFLE MORPHOLOGY 19

TABLE 2.2 - MORPHOLOGY AND EXPERIMENTAL DESIGN OF FIELD-BASED STUDIES 30

TABLE 2.3 - MODELLING STUDIES RELEVANT TO RIFFLE-POOL MECHANICS 45

TABLE 3.1 - DISCRETE PARTICLE MODELS IN FLUVIAL ENVIRONMENTS 54

TABLE 3.2 - GRAVEL BED FORMS 56

TABLE 3.3 – ROQ-B INITIAL PARAMETERS 59

TABLE 3.4 – ROQ-B CONTROL PARAMETERS 62

TABLE 4.1 - PAST STUDIES COMPARING THE PERFORMANCE OF ADVS AND ECMS 92

TABLE 4.2 - PARAMETERS FOR ESTIMATION OF ADV MEASUREMENT ERRORS 99

TABLE 4.3 - VARIANCE BETWEEEN ECM AND ADV DATA 112

TABLE 4.4 - SUMMARY OF CONTRIBUTIONS BY QUADRANT 114

TABLE 5.1 - SUMMARY OF FLOW SAMPLING DATES 125

TABLE 5.2 - PARAMETERS OF FLOW PROFILES 126

TABLE 7.1 - SUMMARY OF FLOOD SEQUENCES BETWEEN SURVEYS 196

TABLE 7.2 - SAMPLES OF TAGGED PARTICLES BY SIZE CLASS 197

TABLE 7.3 - SUMMARY OF FLOOD SEQUENCES BETWEEN PIT TAG SURVEYS 199

LIST OF FIGURES

FIGURE 2.1 - CONCEPTUAL MODEL OF INTERACTIONS BETWEEN FLOW, REPRESENTED BY A MEASURED TIME SERIES OF INSTANTANEOUS VELOCITIES; PARTICLE MOVEMENT, REPRESENTED BY INDIVIDUAL PARTICLES, AND BED FORM DEVELOPMENT, REPRESENTED BY A RIFFLE-POOL UNIT (FROM *LEEDER*, 1983). 5

FIGURE 2.2 - CONCEPTUAL DIAGRAM OF REGIONS IN THE FLOW FIELD AND COORDINATE SYSTEM. 7

FIGURE 2.3 -VELOCITY PROFILES FOR UNIFORM AND NON-UNIFORM FLOWS [*KIRONOTO AND GRAF*, 1995] 7

FIGURE 2.4 - NORMALIZED REYNOLDS SHEAR STRESS IN UNIFORM FLOW VERSUS DEPTH [*NEZU AND NAKAGAWA*, 1993] 8

FIGURE 2.5 - DISTRIBUTION OF TURBULENCE INTENSITIES IN UNIFORM FLOW OVER SMOOTH AND ROUGH BEDS [*NEZU AND NAKAGAWA*, 1993] 9

FIGURE 2.6 - TURBULENCE INTENSITIES AND NORMALIZED REYNOLDS SHEAR STRESS DISTRIBUTIONS IN NON-UNIFORM FLOW [*KIRONOTO AND GRAF*, 1995] 10

FIGURE 2.7 - SUCCESSIVE LAYERS OF THE FLOW NEAR A FLAT PLATE [*KLINE ET AL.*, 1967] 11

FIGURE 2.8 - TURBULENT BOUNDARY LAYER ON A WALL [*FALCO*, 1977] 12

FIGURE 2.9 - A FLOW MODEL IN SEPARATING FLOWS [*SIMPSON ET AL.*, 1981]. ID DENOTES INCIPIENT DETACHMENT, ITD DENOTES INTERMITTENT TRANSITORY DETACHMENT; AND D DENOTES DETACHMENT. 12

FIGURE 2.10 - DOWNSTREAM VARIATION OF THE VIRTUAL VELOCITY FOR TAGGED SEDIMENT BY SIZE CLASS [FERGUSON AND HOEY, 2002] 13

FIGURE 2.11 - BEDLOAD TRANSPORT AS A FUNCTION OF STREAM POWER FOR DATA SETS USED IN *GOMEZ AND CHURCH* [1989] 15

FIGURE 2.12 - A UNIFIED BED FORM PHASE DIAGRAM ACROSS A RANGE OF SAND AND GRAVEL SIZES [BEST, 1996] 16

FIGURE 2.13 - MEASURED DISTRIBUTIONS OF STREAMWISE VELOCITY, REYNOLDS SHEAR STRESS, AND NORMAL STRESS (u'^2) OVER FIXED DUNE FORMS [*NELSON ET AL.*, 1993] 17

FIGURE 2.14 - SCHEMATIC DIAGRAM OF THE PRINCIPAL REGIONS OF FLOW OVER ASYMMETRICAL DUNES [*BEST*, 2005] 18

FIGURE 2.15 - FLOW REGIONS ASSOCIATED WITH THE PRESENCE OF A PEBBLE CLUSTER [*BUFFIN-BÉLANGER AND ROY*, 1998] 18

FIGURE 2.16 – VISUALIZATION OF TRACERS IN LOWER LEE AND TROUGH OF LOW-ANGLED DUNE SHOWING INTERMITTENT FLOW SEPARATION [*BEST AND KOSTASCHUK*, 2002] 18

FIGURE 2.17 - SCHEMATIC DIAGRAM TO DEFINE THE RIFFLE-POOL SEQUENCE [*CHURCH AND JONES*, 1982] 21

FIGURE 2.18 - A DESCRIPTIVE MODEL OF SEDIMENT TRANSPORT PROCESSES IN A RIFFLE-POOL [*SEAR*, 1996]....21

FIGURE 2.19 - STAGES IN FORMATION OF A BAR SHOWING THE DEPOSITION OF A COARSE BAR HEAD AT H [*LISLE ET AL.*, 1991] 23

FIGURE 2.20 - SCHEMATIC DIAGRAM OF THE CHANNEL MORPHOLOGY [*PYRCE AND ASHMORE*, 2005] 24

FIGURE 2.21 - A FIVE-STAGE MODEL OF DEVELOPMENT THAT SHOWS A PROGRESSION FROM ALTERNATE BARS TO MEANDERING [*KELLER*, 1972] 25

FIGURE 2.22 - CHANGES IN STORAGE OF BED SEDIMENT IN RESPONSE TO CHANGES IN WATER DISCHARGE ON THREE MAJOR RIFFLES (LEFT) AND THREE MAJOR STORAGE AREAS (RIGHT) IN THE EAST FORK RIVER [*MEADE*, 1985] 27

FIGURE 2.23 - COMPARISON OF DISCHARGE VERSUS SEDIMENT TRANSPORT RELATIONS FROM (A) *RYAN ET AL.* [2002] AND (B) *JACKSON AND BESCHTA* [1982]. 27

FIGURE 2.24 - BED SHEAR STRESS NEEDED TO INITIATE AND TO FULLY MOBILIZE SEDIMENTS IN A POOL VERSUS GRAIN SIZE [*HASSAN AND WOODSMITH*, 2004]. ALSO SHOWN ARE RESULTS FROM FLUME EXPERIMENTS [*WILCOCK AND MCARDELL*, 1993], AND HARRIS CREEK [*CHURCH AND HASSAN*, 2002]. 28

FIGURE 2.25 - WIDTH VERSUS SLOPE FOR HYDRAULIC STUDIES OF RIFFLE-POOLS AS LISTED IN TABLE 2.2. PARTICLE SIZE (D_{50}) AND POOL TYPE ARE SHOWN FOR EACH SITE. RELATIONS A AND B FOLLOWING $S \propto Z^{-1}$ WERE FIT BY EYE TO THE DATA. MORAS CREEK, THE STUDY SITE IN THIS THESIS, IS ALSO SHOWN. 32

FIGURE 2.26 - VELOCITY PROFILES AT POOL AND RIFFLE CROSS-SECTIONS [*BHOMICK AND DEMISSIE*, 1982] 33

FIGURE 2.27 - SPATIALLY AVERAGED VELOCITY PROFILE FOR POOLS AND RIFFLES DURING HIGH FLOW CONDITIONS ($Q = 2/3\ Q_{BF}$) [*ROBERT*, 1997] 34

FIGURE 2.28 - NEAR-BED VELOCITIES MEASURED AT (A) LOW FLOW (B) MODERATE FLOW (C) HIGH FLOW THROUGH A STRAIGHT RIFFLE-POOL AT RM - RIFFLE MIDPOINT, RC - RIFFLE CREST, PT - POOL-TAIL, AND PM - POOL MIDPOINT [*CLIFFORD AND RICHARDS*, 1992]. FLOW IS FROM RIGHT TO LEFT AND THE HEIGHT OF THE BAR REPRESENTS THE VELOCITY. 34

FIGURE 2.29 - VARIATION IN ABSOLUTE TURBULENCE INTENSITY (RMS IN M/S) THROUGH TWO RIFFLE-POOLS DURING MODERATE DISCHARGE [*CLIFFORD*, 1996]. FLOW DIRECTION IS FROM RIGHT TO LEFT. CLOSED SYMBOLS REFER TO STREAMWISE VELOCITY COMPONENTS AND OPEN SYMBOLS REFER TO VERTICAL VELOCITY COMPONENTS. 36

FIGURE 2.30 - PLAN-VIEW MAPS OF 10 CM, 40 CM, AND 70 CM LONG POOLS SHOWING VELOCITY VECTORS FOR THE STREAMWISE AND LATERAL COMPONENTS OF NEAR-BED (BLACK ARROWS) AND $0.4Y$ (WHITE ARROWS) VELOCITIES. THE ARROWS ARE SUPERIMPOSED ON TURBULENT KINETIC ENERGY (E_k) AT $0.4Y$ [*THOMPSON*, 2004] 36

FIGURE 2.31- THE EFFECT OF AN INCREASE OF TIME ON PATH LENGTH DISTRIBUTIONS [*EINSTEIN*, 1937]. TIME INCREASES FROM A-F. [*PYRCE AND ASHMORE*, 2003] 38

FIGURE 2.32 - CHANNEL WIDTH VERSUS MODES OF TRANSPORT DISTANCE FROM STUDIES COMPILED BY *PYRCE AND ASHMORE* [2003] 39

FIGURE 2.33 - VELOCITY REVERSAL HYPOTHESIS FOR A RIFFLE-POOL IN DRY CREEK [*KELLER*, 1982]. THE DATA IN *KELLER* [1971] DO NOT EXTEND PAST THE THRESHOLD POINT AND THE DASHED LINES HAVE NOT BEEN VERIFIED. 40

FIGURE 2.34 - NEAR-BED VELOCITY AT CHANNEL CENTERLINE IN RIVER QUARME AT RM - RIFFLE MIDPOINT, RC - RIFFLE CREST, PT - POOL-TAIL, AND PM - POOL MIDPOINT [*CLIFFORD AND RICHARDS*, 1992]. ONLY THE POOL-TAIL ALWAYS INCREASES WITH DISCHARGE. 41

FIGURE 2.35 - MODELLED CROSS-SECTIONAL AREA, VELOCITY, AVERAGE NEAR-BED VELOCITY, AND SHEAR STRESS AT MID-RIFFLE (R) AND MID-POOL (P) CROSS-SECTIONS [*BOOKER ET AL.*, 2001] 43

FIGURE 2.36 - A PERPECTIVE VIEW OF BED TOPOGRAPHY OF ALTERNATE BARS PREDICTED BY THE STABILITY MODEL OF *COLUMBINI ET AL.* [1987] 44

FIGURE 2.37 - AN EXAMPLE OF THE BED TOPOGRAPHY GENERATED BY THE DISCRETE MODEL OF *NADEN* [1987]. 45

FIGURE 2.38 - IMAGE OF MIXED SEDIMENT-SIZE BED DURING MODELLED TRANSPORT [*SCHMEECKLE AND NELSON*, 2003] 46

FIGURE 2.39 - DUNE DEVELOPMENT IN A DICRETE PARTICLE MODEL IN WHICH SIMPLE RULES ARE USED TO REPRESENT AEOLIAN TRANSPORT [*ANDERSON AND BUNAS*, 1993] 46

FIGURE 3.1 - RELATION OF VELOCITY PROBABILITY DISTRIBUTIONS TO MOVEMENT MODE THRESHOLDS AT THREE FLOW STAGES FOR THREE PARTICLE SIZES. THIS FIGURE REPRESENTS EQUATIONS 1 AND 2 WHEN FEEDBACK RULES ARE INACTIVE. SALTATION PATHS ARE SHOWN IN FIGURE 3.5 MEDIUM AND LARGE PARTICLES HAVE A 'HANDLE' ON THE UPPER RIGHT CORNER, AND THIS HANDLE IS DARKENED SLIGHTLY TO AID THE DISTINCTION OF INDIVIDUAL PARTICLES. 60

FIGURE 3.2 - SCHEMATIC DIAGRAM OF MODELED FLOW AND PARTICLE FEEDBACK MECHANISMS. 60

FIGURE 3.3 - INITIAL SIMULATION MATRIX SHOWING DEFAULT MATRIX DIMENSIONS, PARTICLE SIZE DISTRIBUTION (PERCENTAGES OF EACH SIZE CLASS INDICATED BY $\acute{I}$), AND BED SLOPE (S). FLOW IS FROM LEFT TO RIGHT. 61

FIGURE 3.4 - DEFAULT HYDROGRAPH SHOWING SIX PYRAMID-SHAPE FLOODS. 62

FIGURE 3.5 SALTATION PATHS FOR $\nearrow^1$ - $\nearrow^4$. THE PATHS ARE THOSE FOLLOWED, FROM LEFT TO RIGHT, BY THE PARTICLE HANDLE (THE UPPER RIGHT CORNER OF MEDIUM AND LARGE PARTICLES). THE OCCUPATION OF A GRID SQUARE IN THE PATH OF ANY PART OF THE PARTICLE WILL TERMINATE SALTATION AND INDUCE DEPOSITION. 63

FIGURE 3.6 - FIVE EXAMPLES, TWO FOR SMALL PARTICLES (1X1) AND THREE FOR LARGE PARTICLES (3X3), SHOWING THE CALCULATION OF BURIAL DEPTH (Y_B) FOR DETERMINATION OF HIDING FACTOR. PARTICLES ARE SHADED AS FOR FIGURE 3.1 64

FIGURE 3.7 - CALCULATION OF IMBRICATION. FOR PARTICLE INDICATED BY *, PARTICLES IN CHAIN UPSTREAM (M) = 1 AND PARTICLES DOWNSTREAM IN CHAIN (N) = 3. USING EQUATION 3.4 AND $K_I = 0.5$: I = 3(0.5 + 0.5 + 0.52 + 0.53) = 4.125 65

FIGURE 3.8 - EXAMPLE TO DEMONSTRATE FLOW FEEDBACK RULE CALCULATIONS. (A) DASHED LINE - WATER SURFACE; SOLID LINE - BED SURFACE; (B) TURBULENCE RULE WITH CONTROL PARAMETER (K_T) = 3.0 (BLACK LINE - MEAN VELOCITY V; WHITE LINE - DEPTH AVERAGED VELOCITY V_{DA}; GREY BARS - STANDARD DEVIATION Σ); (C) ACCELERATION RULE WITH CONTROL PARAMETER (K_A) = 0.003, AND K_T = 3.0; AND (D) INSTANTANEOUS VELOCITY SAMPLES; (+ TURBULENCE RULE; * ACCELERATION RULE). 67

FIGURE 3.9 - FLOW CHART OF MODEL EXECUTION. 68

FIGURE 3.10 - SPACE-TIME PLOTS OF BED SURFACE ELEVATIONS FOR BASIC MODEL SIMULATIONS. BED SURFACE ELEVATIONS HAVE BEEN NORMALIZED BY REMOVING THE MEAN SLOPE AND DIVIDING BY THE LARGEST STANDARD DEVIATION OF THE FINAL BED SURFACES IN THE SERIES (Y_s/S_s*). ACCUMULATIONS OF PARTICLES ABOVE THE MEAN SLOPE APPEAR WHITE, WHILE POOLS ARE DARK. FINAL SURFACE PROFILES ARE INCLUDED FOR EACH SIMULATION RUN TO AID INTERPRETATION OF THE GRAPHICS. FLOW DIRECTION IS FROM LEFT TO RIGHT. 71

FIGURE 3.11 - SPACE-TIME PLOTS OF Y_s/S_s* FOR HIDING RULE SIMULATIONS. SEE CAPTION OF FIGURE 3.10 FOR MORE DETAILED EXPLANATION. 72

FIGURE 3.12 - SPACE-TIME PLOTS OF Y_s/S_s* FOR IMBRICATION RULE SIMULATIONS. SEE CAPTION OF FIGURE 3.10 FOR MORE DETAILED EXPLANATION. 73

FIGURE 3.13 - SPACE-TIME PLOTS OF Y_s/S_s* FOR TURBULENCE RULE SIMULATIONS. SEE CAPTION OF FIGURE 3.10 FOR MORE DETAILED EXPLANATION. 74

FIGURE 3.14 - SPACE-TIME PLOTS OF Y_s/S_s* FOR ACCELERATION RULE SIMULATIONS. SEE CAPTION OF FIGURE 3.10 FOR MORE DETAILED EXPLANATION. 75

FIGURE 3.15 - PROFILE PLOTS AT TWO DIFFERENT SCALES. SMALL, MEDIUM, AND LARGE PARTICLES ARE COLORED GREY, YELLOW, AND RED, RESPECTIVELY. (A) BASIC MODEL (K_I = 1, T = 2000, X = 7000 - 7800); (B) HIDING RULE (K_H = 3, T = 3000, X = 5000 - 5800); (C) IMBRICATION RULE (K_I = 0.60, T = 2500, X = 4500 - 5300); (D) TURBULENCE RULE (K_T = 3 ; T = 3000 ; X = 1500 - 2300); (E) TURBULENCE RULE (K_T = 5, T = 2750, X = 4850 - 5650); AND (F) ACCELERATION RULE (K_A = 0.0004, K_T = 5, T = 3000, X = 7000 - 7800)...77

FIGURE 3.16 - SPATIAL ROUGHNESS AS CALCULATED USING EQUATION 3.11 AND A WINDOW SIZE OF 20 GRID SQUARES. SELECTED CASES ARE AS IN TABLE 3.4. 79

FIGURE 3.17 - BOX PLOTS OF SPATIALLY DISTRIBUTED ROUGHNESS VALUES. THE HORIZONTAL LINES THROUGH THE BOXES REPRESENT THE MEDIANS AND THE LIMITS OF THE BOX ARE SET AT THE INTER-QUARTILE RANGES. THE WHISKERS ARE TWICE THE QUARTILE RANGES AND + MARKERS INDICATE VALUES BEYOND THESE LIMITS. 79

FIGURE 3.18 - POOL DIMENSIONS (LP' AND YP') VERSUS TIME FOR THE FIVE SIMULATIONS AS SELECTED IN TABLE 3.4. 81

FIGURE 3.19 - POOL DIMENSIONS PLOT SHOWING WEIGHTED MEAN LENGTHS (LP') AND DEPTHS (YP') OF RESIDUAL POOLS ON THE FINAL BED SURFACE (T = 3000) OF BASIC MODEL AND FEEDBACK SIMULATIONS. THE CONTROL PARAMETER VALUE INCREASES FROM A - D (VALUES ARE LISTED IN TABLE 3.4). NOTE THAT THE Y-AXIS IS REVERSED SO THAT LONGER AND DEEPER POOLS PLOT TOWARDS THE BOTTOM RIGHT-HAND CORNER. ERROR BARS ARE SHOWN IN BLACK FOR CASES SELECTED FOR REPEAT SIMULATIONS. ERROR BARS WERE SET AT 1.64 TIMES THE STANDARD DEVIATION OF THE WEIGHTED MEAN POOL DIMENSION TO ENCOMPASS 95% OF THE VARIABILITY. 82

FIGURE 3.20 - SENSITIVITY TO INITIAL PARAMETERS: (A) K_I = 1, (B) K_H = 3, (C) K_I = 0.60, (D) K_T = 3, AND (E) K_A = 0.0004. AXES REPRESENT THE DIFFERENCE BETWEEN MEAN POOL DIMENSIONS (LP' AND YP') CALCULATED FROM THE FINAL BEDS OF THE SENSITIVITY SIMULATIONS AND THE AVERAGE DIMENSIONS

CALCULATED FROM THE REPEATABILITY SIMULATIONS. THE DIFFERENCES ARE NORMALIZED BY THE STANDARD DEVIATIONS OF THE DIMENSIONS AS CALCULATED FROM THE REPEATABILITY SIMULATIONS (S_{L_i}'). SIMULATIONS WERE CONSIDERED SENSITIVE TO THE INDICATED PARAMETER WHERE THE DIFFERENCE WAS GREATER THAN THE ERROR BARS (A = 0.05). INITIAL PARAMETER VALUES USED IN THESE SIMULATIONS ARE LISTED IN TABLE 3.4.....83

FIGURE 3.21 - HIGH SALTATION OF LARGE PARTICLES VERSUS THE IMBRICATION RULE CONTROL PARAMETER (K_I). K_I = 2 FOR ALL SIMULATIONS IN THIS FIGURE. HIGH SALTATIONS OF LARGE PARTICLES ARE DEFINED AS THOSE WHICH ARE SUFFICIENT FOR A LARGE PARTICLE TO SALTATE OVER ANOTHER LARGE PARTICLE ($\geq \lambda^2$).....84

FIGURE 3.22 - SPACE-TIME AND PROFILE PLOTS OF TWO SIMULATIONS TO DEMONSTRATE THE VELOCITY PROFILE/FLOW SEPARATION RULE. THE TRIMODAL SEDIMENT IS THAT USED IN THE OTHER SIMULATIONS. THE BIMODAL SEDIMENT CONSISTS OF 40% SMALL AND 60% MEDIUM SIZED PARTICLES. ALL OTHER PARAMETERS ARE HELD CONSTANT IN THE TWO SIMULATIONS. PARTICLES ARE COLORED BY SIZE ON THE PROFILE PLOTS (SMALL - LIGHT GRAY; MEDIUM - DARK GRAY; AND LARGE - BLACK).....89

FIGURE 4.1 - EATON-NORD RIVER FIELD SITE LOOKING UPSTREAM.....95

FIGURE 4.2 - NICOLET RIVER FIELD SITE LOOKING DOWNSTREAM AND SAMPLING SECTION BATHYMETRY. NOTE JET OF WATER AS A RESULT OF CONSTRICTION OF FLOW BETWEEN TWO LARGE BOULDERS. SAMPLING LOCATIONS ARE SHOWN. 96

FIGURE 4.3 - WADING ROD WITH ADV AND THREE ECMS. ONLY THE TOP ECM (AT 25 CM) WAS USED FOR THIS STUDY.....96

FIGURE 4.4 - EFFECT OF QUALITY ASSURANCE PROCEDURE ON TYPICAL SIGNAL. DASHED LINES FACILITATE COMPARISON WITH KOLMORGOROV'S -5/3 LAW AND F_1, THE FREQUENCY AT WHICH THE LARGER SAMPLING VOLUME OF THE ECM SHOULD REDUCE S_F BY 10%. A) ECM SIGNAL OUTPUT; (B) ECM SIGNAL AFTER REMOVAL OF INTERNAL FILTERING (NOTE SMALL INCREASE OF S_E NEAR F_1) AND THE RAW ADV SIGNAL; (C) ECM AND ADV SIGNALS AFTER DE-SPIKING PROCEDURE; (D) ECM AND ADV SIGNALS AFTER FILTERING WITH THIRD ORDER BUTTERWORTH FILTER.....99

FIGURE 4.5 - ESTIMATION OF TOTAL VARIANCE DUE TO NOISE (Σ_T^2) USING THE NOISE FLOOR TECHNIQUE. F_K IS THE FREQUENCY RANGE OVER WHICH THE KOLMOGOROV -5/3 SCALING LAW IS APPLICABLE AND S_N IS THE SPECTRAL NOISE CALCULATED FROM THE DIFFERENCE BETWEEN THE ACTUAL SPECTRAL DENSITY AND THE PROJECTED VALUE. Σ_T^2 IS CALCULATED BY INTEGRATING S_N OVER THE TOTAL FREQUENCY RANGE.....101

FIGURE 4.6 - SPATIAL PLOT OF REPRESENTATIVE STATISTICS IN THE NICOLET RIVER. THE SAMPLED TRANSECT HAS BEEN HAS BEEN SEPARATED INTO FOUR SECTIONS BASED ON OBSERVED MORPHOLOGICAL CONTROL ON FLOW DYNAMICS.....105

FIGURE 4.7 - SELECTED SPECTRAL PLOTS OF SIGNALS FROM THE EATON-NORD RIVER. SPECTRA HAVE BEEN SMOOTHED USING THE WELCH TECHNIQUE TO FACILITATE COMPARISON BETWEEN THE SIGNALS [*WELCH*, 1967]. SIGNAL (A) AND (B) ARE REPRESENTATIVE OF TWELVE OF THE SIXTEEN MEASURED TIME SERIES.

CONTAMINATION IS EVIDENT IN (C) AND (D). THIS OCCURRED AT FOUR LOCATIONS. LOWER SPECTRAL ENERGY IS NOTED IN PLOT (D), WHICH WAS MEASURED IN A SLACK WATER AREA IN THE RIVER. 106

FIGURE 4.8 - SPECTRAL PLOTS OF SIGNALS FROM THE NICOLET RIVER. SPECTRA HAVE BEEN AVERAGED BY SUBDIVIDING THE TIME SERIES USING THE WELCH TECHNIQUE TO FACILITATE COMPARISON BETWEEN THE SIGNALS..... 107

FIGURE 4.9 - VARIANCE IN THE ADV SIGNAL DUE TO NOISE AS ESTIMATED USING THE *VOULGARIS AND TROWBRIDGE* [1998] (VT98) AND *MCLELLAND AND NICHOLAS* [2000] (MN00) TECHNIQUES: (A) SUBCOMPONENTS CONTRIBUTING TO DOPPLER NOISE, AND (B) COMPONENTS CONTRIBUTING TO TOTAL NOISE..... 110

FIGURE 4.10 - VARIANCE DUE TO NOISE IN THE STREAMWISE NORMAL SHEAR STRESS (Σ_T^2) NORMALIZED BY THE TOTAL VARIANCE IN STREAMWISE NORMAL SHEAR STRESS $\left(\overline{u_i^2}\right)$ AND PLOTTED AGAINST MEAN DOWNSTREAM VELOCITY. ERROR ESTIMATES USING THE VT98, MN00, THE NOISE FLOOR, AND THE CORRELATION METHODS ARE SHOWN..... 111

FIGURE 4.11 - COMPARISON OF MEAN VELOCITIES (U, V), STANDARD DEVIATIONS (U', V'), TURBULENT KINETIC ENERGY (E_K), AND REYNOLDS SHEAR STRESS (T_R) OF VELOCITY TIME SIGNALS MEASURED USING AN ADV AND AN ECM. 113

FIGURE 4.12 - HOLE SIZE ANALYSIS OF REYNOLDS SHEAR STRESS CONTRIBUTIONS BY QUADRANT FOR MEASURED TIME SERIES IN THE NICOLET RIVER FOR BOTH THE ADV AND THE ECM MEASUREMENTS. THE REYNOLDS SHEAR STRESS OF EACH QUADRANT HAS BEEN NORMALIZED BY THE TOTAL REYNOLDS SHEAR STRESS IN QUADRANTS 2 AND 4 $\left(\overline{u_i v_{iq}} / \overline{u_i v_{i24}}\right)$..... 117

FIGURE 5.1 - TOPOGRAPHY OF AREA SURROUNDING MORAS CREEK FIELD SITE. 122

FIGURE 5.2 - MORAS CREEK THALWEG PROFILE AND RESIDUAL POOLS. 123

FIGURE 5.3 -BED TOPOGRAPHY OF STUDY SITE ON AUGUST 6, 2004 AND PHOTO FROM SPRING OF 2004 DURING LOW FLOW. MEASUREMENT LOCATIONS ARE BLACK CIRCLES, AND YELLOW CIRCLES DISTINGUISH THE THALWEG. CROSS-SECTION NUMBERS (XS) ARE ALSO SHOWN FOR REFERENCE. THE BLUE STARS INDICATE THE LOCATION OF THE TREE. 125

FIGURE 5.4 - SETUP PHOTOS SHOWING (A) THE SYSTEM OF BRIDGES AS INSTALLED LOOKING UPSTREAM (THE TREE IS ON THE NEAR BANK, (B) A TYPICAL BRIDGE BASE INSTALLED ON THE FLOODPLAIN, (C) THE WADING ROD WITH A 20 CM SPLIT AND THE ARRAY OF FOUR ECMS, (D) SAMPLING CONDITIONS AT XS 2 AND Z = 3 M DURING THE BANKFULL FLOOD..... 127

FIGURE 5.5 - FILTERING AND DESPIKING OPERATIONS ILLUSTRATED WITH A 30 S SEGMENT AND POWER SPECTRA FROM A TIME SIGNAL AT MODERATE VELOCITY (U = 0.74 M/S) AND MODERATE TURBULENCE (U' = 0.39 M/S). (A) THE MEASURED ECM OUTPUT, (B) THE DE-FILTERED SIGNAL, (C) THE DE-SPIKED SIGNAL, (D) THE RE-FILTERED SIGNAL AND OUTPUT FROM THE QUALITY ASSURANCE PROCEDURE. REFERENCE LINES ARE INCLUDED ON THE SPECTRAL PLOTS FOR IDENTIFICATION OF INTERMEDIATE AND INERTIAL SUBRANGES, AND THE FREQUENCY ABOVE WHICH SAMPLING VOLUME EFFECTS ARE SIGNIFICANT. 130

FIGURE 5.6 - MEAN STREAMWISE VELOCITY (U) CONTOURS DURING THREE EVENTS INCLUDING BANKFULL. FLOW DIRECTION IS FROM TOP TO BOTTOM. THE TREE THAT FORCES THE POOL IS LOCATED BETWEEN SECTIONS 5 AND 6 ON THE LEFT BANK OUT TO A DISTANCE OF APPROXIMATELY 5 M. 135

FIGURE 5.7 - MEAN VERTICAL VELOCITY (V) CONTOURS. FLOW DIRECTION IS FROM TOP TO BOTTOM. THE TREE THAT FORCES THE POOL IS LOCATED BETWEEN SECTIONS 5 AND 6 ON THE LEFT BANK OUT TO A DISTANCE OF APPROXIMATELY 5 M. 136

FIGURE 5.8 - STANDARD DEVIATION OF STREAMWISE VELOCITY (u') CONTOURS. FLOW DIRECTION IS FROM TOP TO BOTTOM. THE TREE THAT FORCES THE POOL IS LOCATED BETWEEN SECTIONS 5 AND 6 ON THE LEFT BANK OUT TO A DISTANCE OF APPROXIMATELY 5 M. 137

FIGURE 5.9 - STANDARD DEVIATION OF VERTICAL VELOCITY (v') CONTOURS. FLOW DIRECTION IS FROM TOP TO BOTTOM. THE TREE THAT FORCES THE POOL IS LOCATED BETWEEN SECTIONS 5 AND 6 ON THE LEFT BANK OUT TO A DISTANCE OF APPROXIMATELY 5 M. 138

FIGURE 5.10 - PROFILES OF U DURING THE BANKFULL FLOW EVENT 140

FIGURE 5.11 -EFFECT OF DISCHARGE (Q) ON NEAR BED MEAN VELOCITY (U) AND STANDARD DEVIATION (u'). PLOTTED VALUES REPRESENT THE MEAN OF ALL PROBES IN THE INNER ZONE ($y/Y < 0.20$). 141

FIGURE 5.12 - NORMALIZED TURBULENCE INTENSITY PROFILES DURING THE BANKFULL FLOW EVENT. THIN BLACK LINES INDICATE UNIFORM FLOW RELATIONS FROM *KIRONOTO AND GRAF* [1995]. IN THEIR LABORATORY STUDIES, ACCELERATING FLOW PLOTTED TO THE LEFT OF THIS LINE AND DECELERATING FLOWS PLOTTED TO THE RIGHT. 142

FIGURE 5.13 - LOCAL ESTIMATES OF SHEAR STRESS DURING THE BANKFULL FLOW EVENT USING FOUR METHODS: NEAR-BED VELOCITY (τ_U); NEAR-BED VELOCITY GRADIENT ($\tau_{\Delta U}$); REYNOLDS STRESS (τ_R); AND TURBULENT KINETIC ENERGY (τ_K). THE REACH-AVERAGED SHEAR STRESS τ_o = 67 PA. 144

FIGURE 5.14 - CONCEPTUAL MODEL OF FLOW DYNAMICS IN (A) A FORCED RIFFLE-POOL SUCH AS THE MORAS CREEK STUDY SITE AND (B) A STRAIGHT POOL WITHOUT A CONSTRICTION. SURFACES REPRESENT STREAMWISE VELOCITY VECTORS IN UNIFORM, DECELERATING, AND ACCELERATING FLOWS, RESPECTIVELY. THESE SURFACES ARE SHADED AS A FUNCTION GRADIENT AND DEMONSTRATE THE FORMATION OF A HIGH VELOCITY CORE IN DECELERATING FLOWS AND THE OCCURRENCE OF HIGH MEAN VELOCITIES CLOSE TO THE BOUNDARY IN ACCELERATING FLOWS. 145

FIGURE 6.1 -BED TOPOGRAPHY OF STUDY SITE ON AUGUST 6, 2004 AND PHOTO FROM SPRING OF 2004 DURING LOW FLOW. MEASUREMENT LOCATIONS ARE BLACK CIRCLES, AND YELLOW CIRCLES DISTINGUISH THE THALWEG. THE BLUE STARS INDICATE THE LOCATION OF THE TREE. 157

FIGURE 6.2 - CONTOURS OF THE INTERMITTENCY OF THE STREAMWISE VELOCITY (Γ_U) AT THREE DISCHARGES. FLOW DIRECTION IS FROM TOP TO BOTTOM. THE TREE THAT FORCES THE POOL IS LOCATED BETWEEN SECTIONS 5 AND 6 ON THE LEFT BANK OUT TO A DISTANCE OF APPROXIMATELY 5M. 164

FIGURE 6.3 - SPECTRAL DENSITY PLOTS OF PROBES AT y = 15 CM IN THALWEG AT FIVE DISCHARGES. 167

FIGURE 6.4 – SPACE-TIME CORRELATIONS BETWEEN PROBE-PAIRS AT 5 AND 15 CM FROM THE BED AND 15 AND 25 CM FROM THE BED. THE MAXIMUM CORRELATION COEFFICIENT (R_{MAX}) AND THE TIME LAG AT R_{MAX} (L_{MAX}) ARE REPRESENTED AS SHOWN IN THE LEGEND. 169

FIGURE 6.5 - CONTOURS OF INTEGRAL TIME SCALE (*ITS*) FOR STREAMWISE COMPONENT OF VELOCITY (U) AT THREE DISCHARGES. FLOW DIRECTION IS FROM TOP TO BOTTOM. THE TREE THAT FORCES THE POOL IS LOCATED BETWEEN SECTIONS 5 AND 6 ON THE LEFT BANK OUT TO A DISTANCE OF APPROXIMATELY 5M. 171

FIGURE 6.6 - CONTOURS OF INTEGRAL TIME SCALE (*ITS*) FOR VERTICAL COMPONENT OF VELOCITY (V) AT THREE DISCHARGES. FLOW DIRECTION IS FROM TOP TO BOTTOM. THE TREE THAT FORCES THE POOL IS LOCATED BETWEEN SECTIONS 5 AND 6 ON THE LEFT BANK OUT TO A DISTANCE OF APPROXIMATELY 5M. 172

FIGURE 6.7 – INTEGRAL TIME SCALE OF THE STREAMWISE VELOCITY (ITS_U) VERSUS MEAN STREAMWISE VELOCITY (U). TWO RELATIONS WERE FIT BY EYE TO ENCOMPASS THE DENSE REGION OF DATA POINTS. 173

FIGURE 6.8 - SPACE-TIME VELOCITY MATRICES OF SIX POSITIONS AT THREE DISCHARGES. THREE TO FOUR PROBES ALONG A VERTICAL PROFILE AT EACH LOCATION ARE SHOWN. LOCATIONS CONSIST OF FOUR POSITIONS IN THE THALWEG (A-D), ONE POSITION IN THE RECIRCULATION ZONE TO THE RIGHT OF THE CHANNEL (E), AND ONE POSITION IMMEDIATELY DOWNSTREAM OF THE TREE THAT WAS CHARACTERIZED BY RECIRCULATION AT LOW FLOW AND BOILS AT HIGH FLOW. TIME IS REVERSED ON THE HORIZONTAL AXES SO THAT VELOCITY STRUCTURE APPEARS AS IT WOULD IF, ASSUMING 'FROZEN' TURBULENCE, A PHOTO WAS TAKEN FROM A SIDE VIEW OF THE RIVER. 175

FIGURE 6.9 - DURATION-FREQUENCY PLOTS OF HIGH-SPEED EVENTS ($U' > U$) AT $Y = 15$ CM IN THE THALWEG AT BANKFULL DISCHARGE. THE LINEAR REGRESSION MODEL IS SHOWN AND THE FREQUENCY-DURATION SLOPE (S_U) IS INCLUDED. EVENT ANALYSIS OF 100 PERMUTATIONS OF NORMALLY DISTRIBUTED RANDOM SIGNALS WAS USED TO GENERATE THE RANDOM EVENT ENVELOPES DEFINED BY THE SHADED AREA. ... 176

FIGURE 6.10 - CONTOUR PLOT OF THE FREQUENCY-DURATION SLOPE OF HIGH-SPEED EVENTS (S_U) AT THREE DISCHARGES. FLOW DIRECTION IS FROM TOP TO BOTTOM. THE TREE THAT FORCES THE POOL IS LOCATED BETWEEN SECTIONS 5 AND 6 ON THE LEFT BANK OUT TO A DISTANCE OF APPROXIMATELY 5M. 178

FIGURE 6.11 -SLOPE OF THE FREQUENCY-DURATION RELATION OF HIGH-SPEED EVENTS (S_U) VERSUS MEAN STREAMWISE VELOCITY (U). 179

FIGURE 6.12 - HOLE SIZE ANALYSIS OF SIX POSITIONS AT BANKFULL DISCHARGE. POSITIONS ARE THE SAME AS THOSE SHOWN IN FIGURE 6.8. 181

FIGURE 6.13 - CONTOURS OF THE NORMALIZED CONTRIBUTIONS OF *Q4* TO THE REYNOLDS SHEAR STRESS (χ_4) AT THREE DISCHARGES. FLOW DIRECTION IS FROM TOP TO BOTTOM. THE TREE THAT FORCES THE POOL IS LOCATED BETWEEN SECTIONS 5 AND 6 ON THE LEFT BANK OUT TO A DISTANCE OF APPROXIMATELY 5M. 182

FIGURE 6.14 - CONTOURS OF THE NORMALIZED CONTRIBUTIONS OF THE NEGATIVE QUADRANTS (*Q1* AND *Q3*) TO THE REYNOLDS SHEAR STRESS (χ_{13}) AT THREE DISCHARGES. FLOW DIRECTION IS FROM TOP TO BOTTOM. THE TREE THAT FORCES THE POOL IS LOCATED BETWEEN SECTIONS 5 AND 6 ON THE LEFT BANK OUT TO A DISTANCE OF APPROXIMATELY 5M. 183

FIGURE 6.15 – EFFECT OF THE DISCHARGE (Q) ON INTERMITTENCY (Γ_U) THE INTEGRAL TIME SCALE (ITS_U) AND FREQUENCY-DURATION SLOPE (S_U) OF THE STREAMWISE VELOCITY AND ON THE CONTRIBUTION OF QUADRANTS $Q1$ AND $Q3$ TO THE REYNOLDS SHEAR STRESS (χ_{13}). POINTS REPRESENT AN AVERAGE OF THE NEAR-BED PROBES (Y/Y < 0.2). 185

FIGURE 7.1 - TOPOGRAPHY OF AREA SURROUNDING MORAS CREEK FIELD SITE. 195

FIGURE 7.2 - MORAS CREEK THALWEG PROFILE AND RESIDUAL POOLS. 196

FIGURE 7.3 - PRECIPITATION AND TEMPERATURE DATA FROM ON SITE METEOROLOGICAL STATION AND WATER STAGE DATA FROM PRESSURE TRANSDUCER INSTALLED APPROXIMATELY 100 M DOWNSTREAM OF THE RIVER REACH SHOWN IN FIGURE 7.1. DATES ON WHICH TOPOGRAPHICAL SURVEYS (TOPO) TAGGED PARTICLE SURVEYS (PIT) AND FLOW MEASUREMENTS (FLOW) WERE MADE ARE ALSO SHOWN. SCALED DATA FROM A NEARBY GOVERNMENT GAUGING STATION WAS USED TO FILL IN THE PERIOD WHERE THE PRESSURE TRANSDUCER WAS REMOVED FOR WINTER. 197

FIGURE 7.4 - PARTICLE SIZE DISTRIBUTIONS OF THE STREAM SEDIMENT, AS MEASURED BY A WOLMAN PEBBLE COUNT (N = 800), AND THE TAGGED PARTICLES (N = 299). 200

FIGURE 7.5 - STACKED BAR CHARTS OF TAGGED PARTICLE SURVEYS. 201

FIGURE 7.6 - INITIAL (DATE IS VARIABLE) AND END (OCT 06/04) POSITIONS OF TAGGED PARTICLES. LAST KNOWN POSITION GIVES THE LAST COORDINATES OF PARTICLES WHOSE LOCATIONS WERE NOT FOUND IN THE FINAL SURVEY. 202

FIGURE 7.7 – BED TOPOGRAPHY DURING THE STUDY PERIOD. THE EXTENT OF THE THIRD SURVEY WAS LIMITED BY ICY CONDITIONS. 206

FIGURE 7.8 - EROSION/DEPOSITION MAPS OVER THE STUDY PERIOD. THE EXTENT OF ANY MAP IS THE MINIMUM OF THE TWO MORPHOLOGY MAPS THAT WERE USED TO CALCULATE IT. 207

FIGURE 7.9 - CUMULATIVE TRANSPORT DISTANCE FOR ALL TAGGED PARTICLES AT THE END OF THE STUDY PERIOD. PARTICLES THAT WERE NEVER FOUND AFTER THEIR INITIAL PLACEMENT ARE ALSO SHOWN.... 208

FIGURE 7.10 - PATH LENGTHS OF TAGGED PARTICLES FOR EACH MEASUREMENT DATE SEPARATED BY INSERTION DATE. 209

FIGURE 7.11 - PATH LENGTHS FOR SEDIMENT TRANSPORT IN THE FINAL SURVEY PERIOD OF THE TAGGED PARTICLES. SEDIMENT HAS BEEN DIVIDED INTO 'REWORKED' AND 'INSERTED' CLASSES TO DISTINGUISH PARTICLES THAT HAD BEEN IN THE RIVER FOR PREVIOUS FLOODS FROM THOSE THAT HAD BEEN PLACED ON THE BED AT THE BEGINNING OF THE PERIOD. 211

FIGURE 7.12 - SPATIAL PLOT OF SEDIMENT MOVEMENT FOR INITIAL SEEDING OF PARTICLES BETWEEN MAY 28/03 AND SEPTEMBER 26/03. PARTICLES ARE DISTINGUISHED BY SEDIMENT CLASS. PARTICLE MOVEMENTS ARE OVERLAIN ON ZONES OF EXCESS SHEAR STRESS DURING THE BANKFULL EVENT FOR SHEAR STRESS AS A RESULT OF BOTH MEAN VELOCITY (T_t) AND TURBULENT VELOCITY FLUCTUATIONS (T_k). 214

FIGURE 7.13 - SPATIAL PLOT OF SEDIMENT MOVEMENT BETWEEN SEPTEMBER 26/03 AND NOVEMBER 28/03. IT WAS NOT POSSIBLE TO SURVEY DOWNSTREAM OF THE TREE DUE TO ICE. SEE FIGURE 7.12 FOR MORE COMPLETE EXPLANATION. 214

FIGURE 7.14 - SPATIAL PLOT OF SEDIMENT MOVEMENT BETWEEN NOVEMBER 28/03 AND APRIL 28/04. SOME MOVEMENTS DOWNSTREAM OF THE TREE MAY HAVE TAKEN PLACE DURING THE PREVIOUS PERIOD. . SEE FIGURE 7.12 FOR MORE COMPLETE EXPLANATION.....215

FIGURE 7.15 - SPATIAL PLOT OF SEDIMENT MOVEMENT BETWEEN APRIL 28/04 AND JULY 2/04. SEE FIGURE 7.12 FOR MORE COMPLETE EXPLANATION. 215

FIGURE 7.16 - SPATIAL PLOT OF SEDIMENT MOVEMENT BETWEEN JULY 2/04 AND OCTOBER 6/04. THE LAST KNOWN POSITIONS OF PARTICLES THAT WERE NOT FOUND ON THE FINAL SURVEY ARE ALSO SHOWN. SEE FIGURE 7.12 FOR MORE COMPLETE EXPLANATION.....216

FIGURE 7.17 - SUMMARY DIAGRAM OF MORPHOLOGY CHANGES IN RESPONSE TO TWO CYCLES OF FLOOD EVENTS OF VARIOUS MAGNITUDES. THE MOVEMENT OF THE TREE IS SHOWN IN (A) FOR A FLOOD EVENT GREATER THAN THE BANKFULL DISCHARGE ($Q>>Q_{BF}$). SEDIMENT FLUX IS INDICATE BY BLACK ARROWS, AND TRANSPORTED SIZE FRACTIONS ARE INDICATED. NOTE ALTERNATING CYCLES OF SCOUR AND FILL THAT LEAD TO DEVELOPMENT OF DISTINCT SEDIMENTOLOGY IN RIFFLE/POOL-HEAD IN ZONE OF FLOW DECELERATION AND TURBULENCE GENERATION, AND ENLARGEMENT OF THE POOL DOWNSTREAM OF THE TREE IN ZONE OF FLOW ACCELERATION.....218

FIGURE 8.1 - CONCEPTUAL MODEL OF FLOW AND SEDIMENT IN DYNAMICS IN GRAVEL-BED RIVERS. SEE TEXT FOR EXPLANATION.....229

FIGURE 8.2 - INTEGRAL TIME SCALE OF THE STREAMWISE VELOCITY (ITSU) VERSUS THE STREAMWISE VELOCITY (U) AT FIVE DISCHARGES IN THE DITTON RIVER. DASHED LINES REPRESENT THE ENVELOPE OF DATA FROM MORAS CREEK (SEE FIGURE 6.7) 232

NOMENCLATURE

A	acceleration factor
B	total bandwidth broadening due to Doppler noise
B_r, B_t, B_d	residence time, turbulence decorrelation, and beam divergence Doppler noise sub factors
c	speed of sound (m/s)
d	particle diameter (grid squares)/length scale
d_v	length of sampling volume (m)
d_x, d_y, d_z	streamwise, vertical and lateral size of sampling volume (m)
D_p	particle diameter of percentile p (mm)
E	entrainment threshold (non-dimensional)
E_k	turbulent kinetic energy (m^2/s^2)
f	frequency (s^{-1})
f_{adv}	ADV operating frequency (s^{-1})
f_N	Nyquist frequency (s^{-1})
f_s	sampling frequency (s^{-1})
f_v	frequency above which sampling volume is expected to reduce measured variance
g	constant of acceleration (9.81 m/s^2)
H	hole size in turbulence quadrant analysis
H	hiding factor (non-dimensional) in ROQB model
I	imbrication factor (non-dimensional)
ILS	integral length scale (m)
ITS	integral time scale (s)
k_A	acceleration rule control parameter
k_H	hiding rule control parameter
k_I	imbrication rule control parameter

k_T turbulence rule control parameter

k_v mean velocity control parameter

k_s roughness length (m)

K_l proportionality constant for τ_k calculation (0.19)

l time lag (s)

l_p pool length (grid squares)

L_p' weighted mean pool length (grid squares)

n number of upstream imbricate particles

m number of downstream imbricate particles

M transport mode in ROQB model

M number of pulse pairs measured in a sampling period

N_s Strouhal number

p^2 agreement between flow statistics measured with ECM and ADV

q quadrant

q_c quadrant color in space-time velocity matrix

q flow stage in ROQB model

r roughness (grid squares) in ROQB model

r correlation coefficient

R^2 ADV correlation coefficient

R hydraulic radius (m)

s_s standard deviation of bed surface elevation (grid squares)

S channel slope

S_e energy slope

S_f spectral density (cm^2/s)

SNR ADV signal to noise ratio

t time (intervals) in ROQB model

t	time (s)
t_a, t_b, t_c	ADV pulse durations (s)
t_D, t_M, t_O	ADV time constants - dwell time, measurement time and calculation time (s)
T	turbulence factor (non-dimensional) in ROQB model
T	total length of time (s)
u, v, w	instantaneous velocity in streamwise, vertical, and lateral directions (m/s)
u_i, v_i, w_i	instantaneous velocity fluctuation in streamwise, vertical, and lateral directions (m/s)
U, V, W	mean velocity in streamwise, vertical, and lateral directions (m/s)
$\overline{U}$	depth integrated streamwise velocity (m/s)
u', v', w'	standard deviation of velocity in streamwise, vertical, and lateral directions (m/s)
u^*	shear velocity (m/s)
u_{beam}	ADV user-set velocity range (cm/s)
V	mean velocity (non-dimensional)
V_{DA}	depth averaged velocity (non-dimensional)
v	instantaneous velocity (non-dimensional)
v_p	unit pool volume (grid squares^3)
w	window size used in roughness calculation (grid squares)
x, y, z	local coordinate system in streamwise, vertical and lateral directions (m)
x	longitudinal position in matrix (grid squares) in ROQB model
x_t	transport length (grid squares)
y	elevation (grid squares) in ROQB model
y_b	burial depth (grid squares)
y_d	flow depth (grid squares)
y_n	normal depth (grid squares)
y_p	pool depth (grid squares)
Y, Y_{bf}	water depth (m), bankfull water depth (m)
Y_p'	weighted mean pool depth (grid squares)

y_s	bed surface elevation (grid squares)
y_t	transport height (grid squares)
Z	channel width (grid squares) in ROQB model
Z, Z_{bf}	stream width (m), bankfull width (m)
β	acceleration parameter
χ	normalized contribution by quadrant to Reynolds shear stress
η	placeholder for χ calculation
γ	intermittency (%)
σ	standard deviation of velocity distribution (non-dimensional)
σ_{vr}	standard deviation of radial velocity (m/s)
σ_t^2	total variance due to noise (m^2/s^2)
σ_s^2, σ_d^2, σ_u^2	variance due to phase shift, Doppler noise, and velocity shear (m^2/s^2)
σ_φ^2	phase uncertainty
κ	Von-Karman coefficient (0.40)
θ	ADV bistatic angle (30°)
ρ	fluid density (1000 kg/m^3)
ρ_s	sediment density (2650 kg/m^3)
τ	shear stress (N/m^2)
τ_c	critical shear stress (N/m^2)
τ_k	turbulent kinetic energy shear stress (N/m^2)
τ_o	reach-average shear stress (N/m^2)
τ_u	velocity-roughness shear stress (N/m^2)
$\tau_{\Delta u}$	velocity gradient shear stress (N/m^2)
τ_t	Reynolds shear stress (N/m^2)

ACKNOWLEDGEMENTS

I'd like to first of all thank my advisor André Roy pour m'avoir accueillie dans son laboratoire et de m'avoir donnée l'opportunité de faire ce doctorat à l'Université de Montréal. Ton support était constant et la sagesse avec lequel tu gères les projets et les étudiants est une merveille.

I'd also like to thank Lael Parrott for her help and support during the modelling and extended revision process. You were also the person who introduced me to Matlab and the ideas around complex systems, both of which shaped this thesis.

Je remercie aussi les étudiants du département de Géographie. Merci d'avoir accueillie chalereusement ce pauvre gars de Toronto est si je sors avec un petit accent québecois - quand je parle anglais - ou avec un meilleur slapshot, c'est grâce à vous.

Dans le laboratoire j'aimerais remercier Hélène Lamarre (merci), Antoine Richer (merci/thanks), Eva Enders (danke), and Jay Lacey (hmm, actually forget it) en particulier. Excellent collaborators and friends throughout the whole process.

Je ne peux pas passer à coté de tout le monde qui m'a aidé au terrain. Autres que les personnes en haut, Claudine Boyer, Genvieve Marquis, Jöelle Quirion-Sicard, Valerie Champagne, Eric Beaulieu, Sylvie Manna, Geneviève Paiement-Paradis, Bruno Vallée, Sophie Roberge, Julie Thieren, Mathieu Roy, et Vitalie Bondue on tous contribué a l'effort. Souvent c'était le samedi, souvent sous la pluie, la neige, la grail, le soleil brulante ou attaquer par les bébites et les arbres qui tombent dans le vent, mais je me souviens même pas des plaintes … bon peut-être quelques petites. Cette thèse à seulement été possible avec un effort supplémentaire de vos parts.

Thank-you as well to my family and friends, who should be thanked all the time and not just when finishing a thesis, for being there and for caring.

I am also grateful to the Natural Sciences and Engineering Research Council of Canada, the Fonds de recherche sur la nature et les technologies, the Canadian Foundation for Innovation, et la Faculté des études supérieures de l'Université de Montréal for their financial support. This research is conducted as part of the program of the Canada Research Chair in fluvial dynamics.

1 INTRODUCTION

Rivers are self-organizing systems. Given sediment and water inputs and allowed to develop over time, patterns will emerge from the interactions amongst individual elements or parts within the system. These patterns occur on a wide range of scales from the formation of ripples on a sand bed [*Simons et al.*, 1965] to the organisation of river networks at the watershed scale [*Horton*, 1945; *Strahler*, 1952]. Understanding how these patterns develop and their effect on the properties and behaviour of the system is fundamental to the field of fluvial geomorphology. It is also necessary to inform discussions on biological activity within rivers and of anthropogenic influence on the landscapes. This thesis focuses on one pattern that plays an important role in gravel-bed river dynamics: the riffle-pool sequence. Riffle-pools define the macro-scale structure in a broad range of gravel-bed rivers [*Grant et al.*, 1990; *Montgomery and Buffington*, 1997; *Chartrand and Whiting*, 2000]. This bed form helps to stabilize the stream bed [*Madej*, 1999; *Eaton and Lapointe*, 2001] and dissipate energy [*Thompson*, 2002; *Walker et al.*, 2004]. Stream ecology is adapted to the structure it provides, and many studies have documented the use of riffle-pools by invertebrates and fish [*Stuart*, 1953; *Edo and Suzuki*, 2003; *Moir et al.*, 2004]. Riffle-pools provide a range of hydraulic habitats including refugia during extreme low and high flows [*Newbury and Gaboury*, 1993]. These properties make it a frequent target for stream restoration projects [*Harper et al.*, 1998; *Emery et al.*, 2003]. In spite of the interest in this bed form, there is still considerable disagreement regarding the central mechanisms that leads to the formation and maintenance of riffle-pools in gravel-bed rivers [*Milan et al.*, 2001; *Wilkinson et al.*, 2004].

Disagreement over formative mechanisms may be related to any number of factors, but we have identified two major shortcomings in the existing literature. First, available field data is insufficient to accept or reject competing theories. Previous studies have not anticipated the degree of spatial variability in flow properties [*Clifford and Richards*, 1992], have had difficulty measuring flow and sediment transport during flood conditions when sediment transport is active [*Thompson et al.*, 1998; *Carling*, 1991], and have rarely considered the role of turbulence [*Clifford*, 1996]. Increased sampling density, intense monitoring of temporal changes and innovative field techniques are required to address the

data gap. The second major factor that may be preventing a convincing theory of pool formation is more fundamental in nature. 'Riffle-pool' is the name given to a collective form that develops through the movement of individual sediment particles during many cycles of scour and fill in a complex hydraulic environment. Consensus of the most rigorous field studies only extends to the fact that the key processes continue to resist our attempts to reduce dynamics to a single variable [*Clifford and Richards*, 1992; *Thompson et al.*, 1998; *Hassan and Woodsmith*, 2004]. A new approach is needed that acknowledges the inherent complexity of the form.

This thesis explores the formation of riffle-pools in gravel-bed rivers using the complementary approaches of numerical modelling and field-based research. For the field data component, the decision was made to focus on one example of the pattern, a single forced riffle-pool in a small creek located in Southern Quebec. We monitored the site from May 2003 to November 2004 by continuously measuring flow stage, air temperature, and precipitation, periodically surveying topography and sediment tracers, and characterizing flow dynamics over a range of flow discharges up to and including the bankfull discharge. A series of floods and a period of active pool formation produced a wealth of information that is unique in the literature. Results are significant because they allow us to test theories of riffle-pool formation and suggest resolutions to apparent contradictions in previous studies. Despite these advances, a single field site is not an adequate support for a general theory of pool formation. It is necessary to demonstrate that the observed mechanics are sufficient and necessary for the formation of pools and riffles. The second approach was to develop a model of stream processes that allows the incorporation of the key variables such as sediment mobility, sediment size, flow velocity, and turbulence. Fully mechanistic models are not suitable because of limitations in our ability to quantify the non-linear relation between sediment transport and the surrounding flow field [*McEwan et al.*, 2000; *Schmeeckle and Nelson*, 2003]. An alternative approach, borrowed from the cross-disciplinary field of complex systems research, is hierarchical modelling [*Werner*, 1999; *Murray*, 2003]. This approach is based on the abstraction of 'fast' processes such as sediment transport in order to investigate 'slow' processes such as bed form development. Results show that macro-scale patterns with properties similar to dunes and riffle-pools can be generated by considering the effect of acceleration and deceleration on turbulence generation and mean velocity profiles. Implications of the model go beyond the formation

of a single pattern because, by varying parameter values in a set of simple rules, it shows how very different patterns can be generated in a range of river systems.

The thesis is composed of eight chapters. The background to the problem is developed in the second chapter. A literature review will help to refine the objectives of the thesis and to justify the methodology upon which this work is based. A brief overview of gravel-bed river dynamics is presented to establish the context of the problem. The morphology of the riffle-pool sequence is defined, the various mechanisms that have been theorized to account for its formation are presented, supporting evidence is reviewed, and the various models that discuss riffle-pools are summarized. From this discussion, a set of remaining research questions and the methodology to tackle them emerges. The body of results from this thesis is contained within five articles that have been prepared for submission to international research journals (Chapters 3-7). There is necessarily some repetition between chapters to allow each article to be submitted independently. The link between each chapter is assured through a liason paragraph.

Chapter 3 presents the two-dimensional simulation model that we developed to explore bed form dynamics. The model is placed before the field results because it was conceived and developed before the field campaign was undertaken. Preliminary results determined the field methodology to some extent because it focused attention on the need to clarify the role of the turbulent character of the flow. This article has been accepted for publication in the *Journal of Geophysical Research - Earth Surface*. Chapter 4 describes a test of two instruments that measure instantaneous flow velocity at frequencies sufficient for our field experiments. This test was necessary because their reliability in highly turbulent flows is uncertain. We have submitted the article to *Earth Surface Processes and Landforms* as a technical communication on measurement error and instrument selection. The characterization of the flow environment in a riffle-pool is presented in two articles that will be submitted as companion papers to *Water Resources Research* (Chapters 5 and 6). These articles offer the most detailed hydraulic analysis of a natural riffle-pool yet available. Time-independent statistics of mean velocity and turbulence intensity for a range of discharges up to and including the bankfull discharge are presented in the first of the companion articles. The time-dependant structure and scale of coherent turbulent events are explored in the second paper. A conceptual model on the effect of deceleration and

acceleration on flow properties in the pool is presented. In the final article, sediment transport data are presented along with detailed morphological changes during the study period (Chapter 7). Sediment transport was measured with the relatively new technique of Passive Integrated Transponder (PIT) tags. This technique provided information on the spatial distribution of sediment entrainment in a riffle-pool. In addition, because of the hydraulic information available, we were able to associate the spatial variability of entrainment with the patterns of mean and fluctuating shear stress values on the stream bed.

General conclusions and future directions are presented in Chapter 8. The main contribution of the thesis is to provide new insight into the flow and sediment dynamics of riffle-pools in gravel-bed rivers. We show that the formation of riffle-pools can be explained by considering the effects of acceleration on turbulence intensity and by considering the effects of short duration turbulent fluctuations on the transport of heterogeneous sediments. This contribution results from the combination of intense measurements of the active physical processes in a riffle-pool with a modelling approach that demonstrates the effectiveness of the identified processes in the formation of riffle-pools in gravel-bed rivers.

2 BACKGROUND

2.1 Context: the gravel-bed river

The dynamics of gravel-bed rivers are defined by open channel flow over a mobile boundary. This section introduces key concepts that describe this environment. The trinity diagram proposed by *Leeder* [1983] presents a general model of the interactions between the turbulent flow, sediment transport, and bed topography from which the bedforms we observe emerge (Figure 2.1). Landmark studies from each of the three areas are briefly reviewed to present a more general introduction to the formation of riffle-pools.

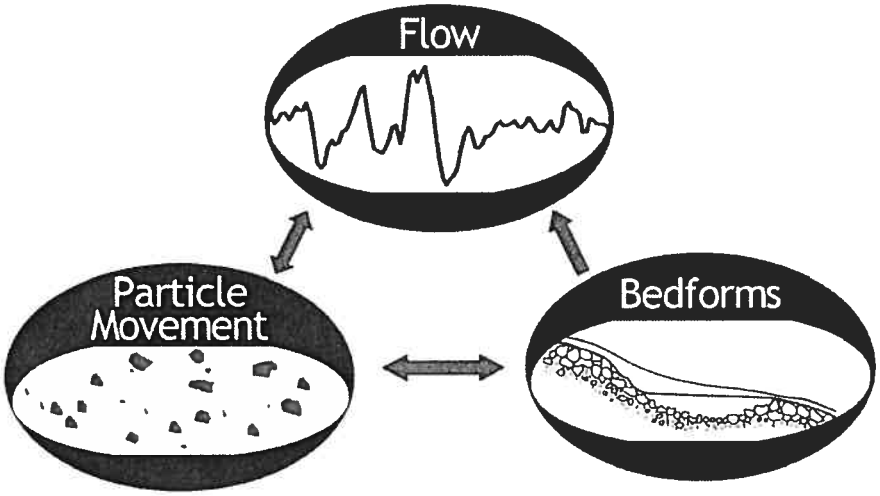

Figure 2.1 - Conceptual model of interactions between flow, represented by a measured time series of instantaneous velocities; particle movement, represented by individual particles, and bed form development, represented by a riffle-pool unit (from *Leeder*, 1983).

2.1.1 Turbulent flow over a gravel bed

There are two main approaches for describing the flow field: time-independent statistics and time-dependent definitions of coherent events. The following paragraphs define and review standard distributions of common turbulent flow statistics such as mean velocity, shear stress, and turbulence intensity. For two-dimensional flows, the streamwise velocity profile is calculated within the boundary layer using the law of the wall [*Prandtl*, 1925]:

$$\frac{U}{u^*}=\frac{1}{\kappa}\ln\frac{y}{k_s}+C \qquad (2.1)$$

where U is the mean downstream velocity, u^* is the shear velocity, κ is the Von-Karman constant (≈ 0.40), y is the elevation above the bed, k_s is the roughness height, and C is a constant. u^* is calculated from the shear stress (τ):

$$u^* = \sqrt{\frac{\tau}{\rho}} \tag{2.2}$$

where ρ is the fluid density. The boundary layer is defined as the region close to a solid surface wherein the surface exerts a drag force on the moving fluid [*Henderson*, 1966]. A conceptual diagram of the boundary layer is shown in Figure 2.2. The boundary layer can be divided into the inner or wall region, and the intermediate and the near surface regions, collectively referred to as the outer region. Equation 2.1 only applies in the wall region. In the outer region, a wake defect parameter can be applied [*Coles*, 1956] such that

$$\frac{U_{max} - U}{u^*} = \frac{1}{\kappa} \ln \frac{y}{k_s} + \frac{2\Pi}{\kappa} \cos^2\left(\frac{\pi y}{2k_s}\right) \tag{2.3}$$

where U_{max} is the maximum time-averaged velocity in the water column and Π is Coles' wake parameter.

A critical question for this study is the effect of a non-uniform boundary on turbulent flow properties. In a series of flume experiments to examine topographically induced deceleration and acceleration over rough surfaces, *Kironoto and Graf* [1995] found that Π varies as a function of the parameter β, which represents the rate of flow expansion/constriction:

$$\Pi = 0.08\beta \qquad \text{for } Z/Y \sim 2 \tag{2.4a}$$

$$\Pi = 0.08\beta + 0.23 \qquad \text{for } Z/Y > 5 \tag{2.4b}$$

$\beta = -1$ in uniform flow, $\beta < -1$ in accelerating flow and $\beta > -1$ in decelerating flow. The effect of β on flow profiles is shown in Figure 2.3. The profile is fuller in accelerating flows so that the highest velocity occurs closer to the bed, whereas decelerating flows are characterized by a positive gradient between velocity and depth throughout the flow depth. This change has implications for shear stress and the generation of turbulence.

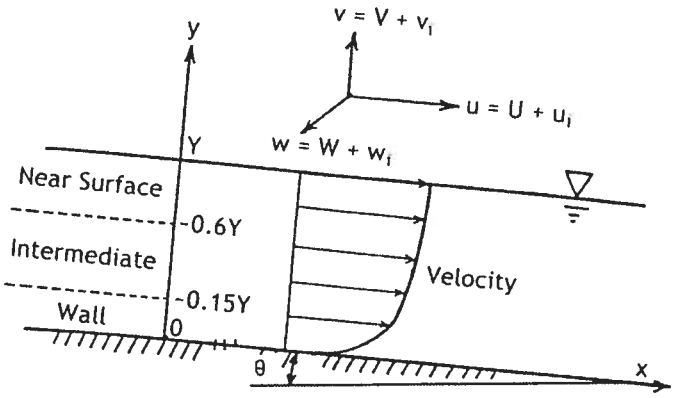

Figure 2.2 - Conceptual diagram of regions in the flow field and coordinate system.

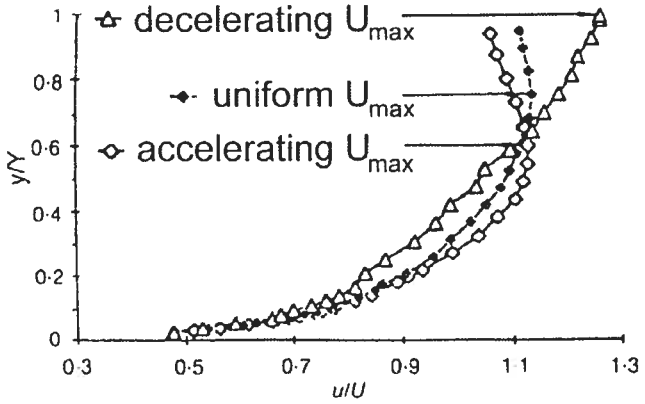

Figure 2.3 -Velocity profiles for uniform and non-uniform flows [*Kironoto and Graf*, 1995]

Reynolds shear stresses represent the momentum flux due to the exchange of fluid between layers of fluid travelling at different velocities. In two-dimensional uniform flows, this stress can be represented as

$$\tau_r = -\rho \overline{u_i v_i} \qquad (2.5)$$

where u_i and v_i are the instantaneous velocity fluctuations about the mean and the overbar indicates the mean over the length of the velocity series. The behaviour of the Reynolds shear stress through the boundary in uniform flow is shown for smooth and rough channel boundaries in Figure 2.4. When normalized by the product of the streamwise and vertical velocity standard deviations to obtain the correlation coefficient (r), the distribution is independant of the properties of mean flow and of roughness [*Nezu and Nakagawa*, 1993]. The correlation coefficient reaches a maximum between 4 and 5 in the intermediate zone and is nearly constant throughout this zone.

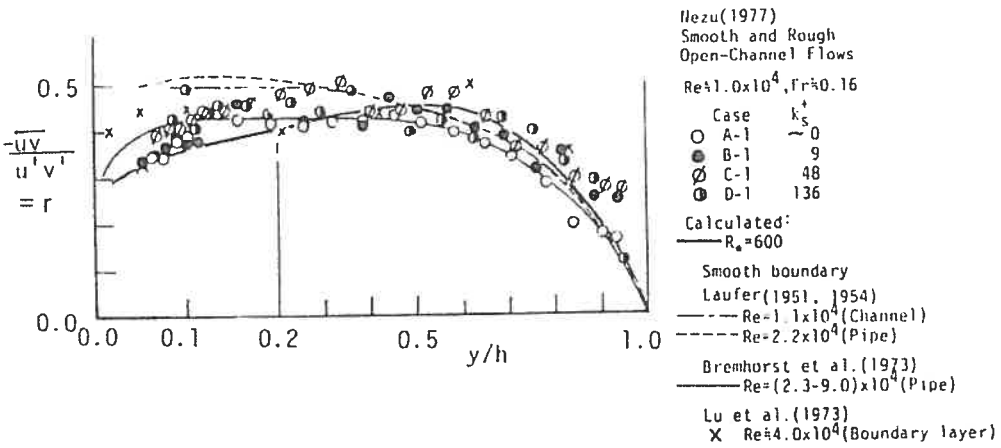

Figure 2.4 – Correlation coefficient of the Reynolds shear stress in uniform flow [*Nezu and Nakagawa*, 1993]

Turbulence is generated as a result of the torque resultant from opposite shear stresses applied between layers of fluid moving at different speeds. In uniform and 2D flows the rate of turbulence generation (G) can be obtained from the velocity gradient [*Nezu and Nakagawa*, 1993]:

$$G=-\overline{u_i v_i}\left(\frac{\partial U}{\partial y}\right) \qquad (2.6)$$

Measured turbulence intensities are shown for smooth and rough bed channels in Figure 2.5. The relations are independent of roughness except near to the wall, where the normalized turbulence intensity is larger over smooth boundaries. Peak turbulence intensities occur closer to the wall than maximum correlation values.

The results of *Kironoto and Graf* [1995] demonstrate the effects of the changes to mean velocity profiles in non-uniform flow on turbulence intensities and Reynolds shear stress (Figure 2.6). In decelerating flows, the velocity gradient is greater in the outer region compared with uniform flows. This increases momentum exchange and turbulence generation in the outer region, which translates into higher turbulence intensities. In accelerating flows, velocity gradients are much less in the outer layer, which reduces shear stress and turbulence, especially when compared to the tremendous shear stresses in the inner layer, where a large velocity gradient exists. These results have been confirmed by subsequent studies to clarify specific aspects of the changes to the boundary layer in non-

uniform flows, but this research area remains active [*Song and Graf*, 1994; *Afzalimehr and Anctil*, 1999; *Song and Chiew*, 2001].

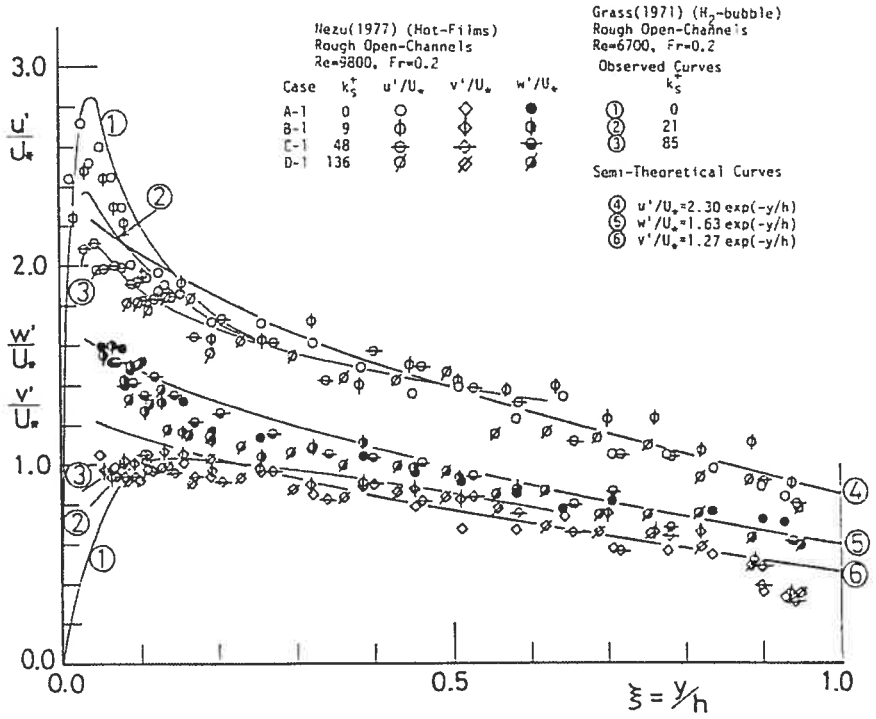

Figure 2.5 - Distribution of turbulence intensities in uniform flow over smooth and rough beds [*Nezu and Nakagawa*, 1993]

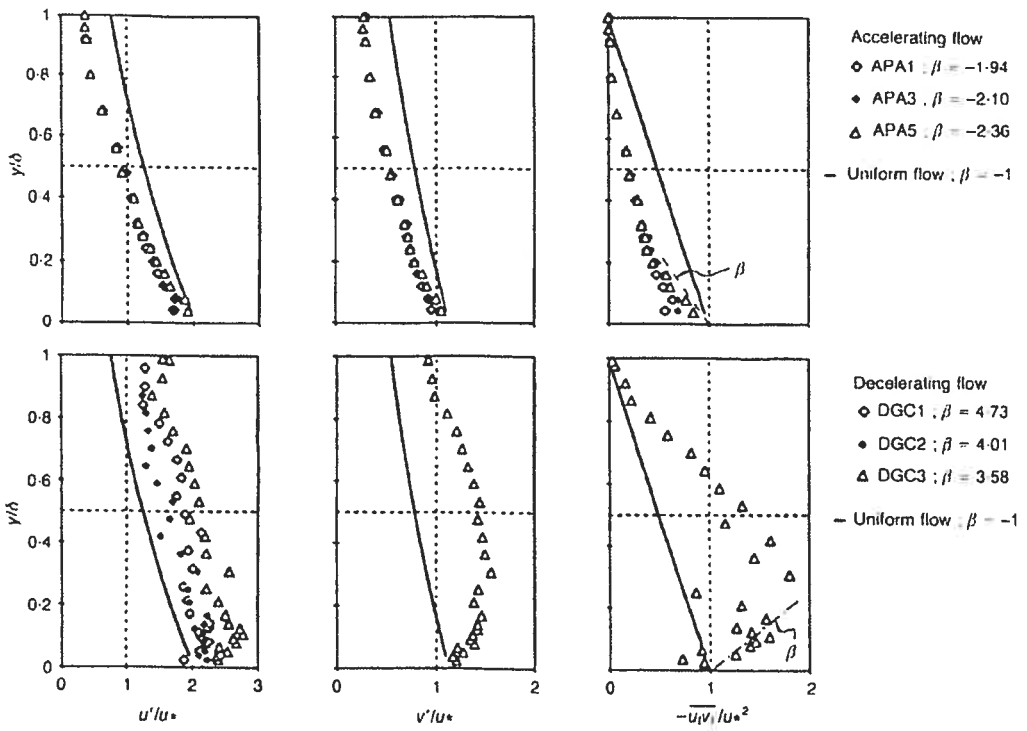

Figure 2.6 - Turbulence intensities and normalized Reynolds shear stress distributions in non-uniform flow [*Kironoto and Graf*, 1995]

Although preliminary observations of turbulent structure in rivers [*Matthes*, 1947] and conceptual model of wall turbulence [*Theodosen*, 1952] indicated otherwise, turbulence was long thought to be a fundamentally stochastic or time-independent phenomenon [*Henderson*, 1966]. Ground-breaking work in the 1960's permanently changed this view. *Kline et al.* [1967] were the first to demonstrate the occurrence of coherent events in the form of streaks and intermittent bursts above a smooth boundary (Figure 2.7). *Corino and Brodkey* [1969] subsequently identified a sweep-ejection sequence and confirmed that these events were responsible for the significant part of the momentum exchange between the inner and outer flow regions. Coherent structures are not restricted to smooth wall boundaries. *Grass* [1971] and *Grass and Mansour-Tehrani* [1996] found that the sweep-ejection model could be applied to flow over rough boundaries in spite of the disruption to the boundary layer. *Kirkbride* [1993] demonstrated that the ejections may derive from the separation zones behind sediment clasts in gravel bed. Coherent structures also occur in the outer region. *Falco* [1977] used the controlled injection of a fog of oil droplets to identify coherent structures occurring at two scales (Figure 2.8) At low Reynolds numbers the structure was dominated by three-dimensional vortices he called 'typical eddies'. As the

Reynolds number was increased, the typical eddies diminished in scale and began to ride on large bulges in the boundary layer delineated by fog-free regions extending to the wall he called large scale motions. *Kirkbride and Ferguson* [1995] and *Buffin-Bélanger et al.* [2000] have confirmed the presence of large-scale coherent structures in turbulent flows over rough beds. These researchers used the term 'flow wedge' to define a structure that is generally inclined downstream and occupies the full depth of flow. Well developed high-speed wedges were associated with peaks in shear stress at the bed and are thought to control the bursting processes at the wall.

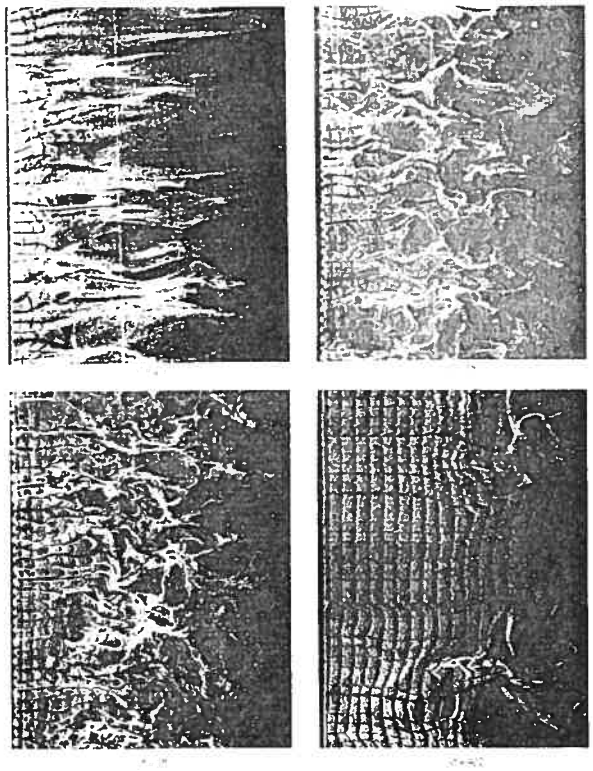

Figure 2.7 - Successive layers of the flow near a flat plate [*Kline et al.*, 1967]

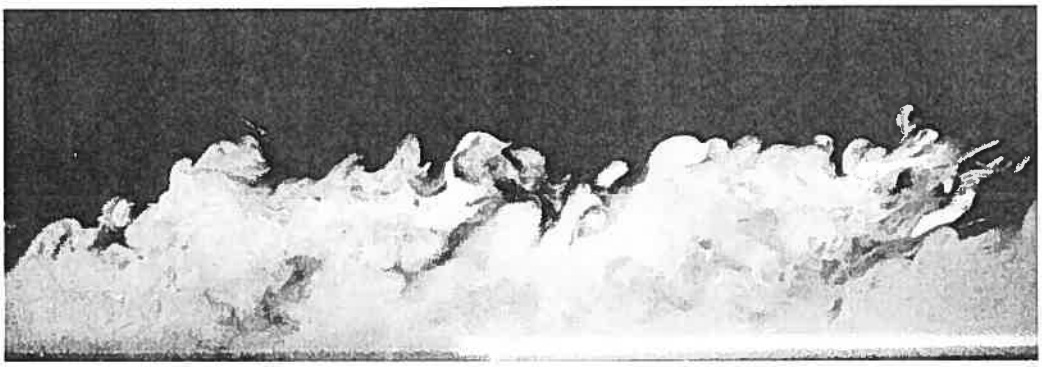

Figure 2.8 - Turbulent boundary layer on a wall [*Falco*, 1977]

Non-uniform flow strongly affects the development of coherent turbulent structure as a result of flow separation. Figure 2.9 shows a model of flow separation from *Simpson et al.* [1981]. Although this model represents separation over a flat surface such as an airplane wing, similar processes occur in areas of flow expansion. Under this model, turbulence in a zone of flow separation is controlled by the outer region. The backflow is fed by large eddies that move towards the bed from the zone of interaction, represented by a dashed line, between the separated zone and the outer region. Importantly for this thesis, a condition of incipient detachment is identified wherein instantaneous rather than mean flow separation occurs. *Azad* [1996] observed this state in conical diffusers at expansion angle sufficiently mild to prevent full flow separation. This demonstrates that there is a continuum between uniform flow and flow separation in terms of the changes to the boundary layer. The peak in turbulence production shifts from the inner to the outer flow region [*Simpson et al.*, 1981] and the relative strength of large eddies increases [*Azad and Kassab*, 1989].

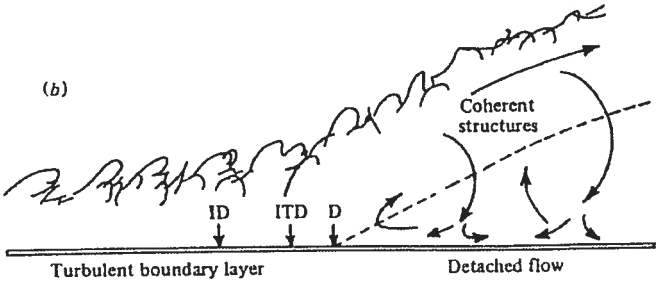

Figure 2.9 - A flow model in separating flows [*Simpson et al.*, 1981]. ID denotes incipient detachment, ITD denotes intermittent transitory detachment; and D denotes detachment.

2.1.2 Sediment transport in gravel-bed rivers

Sediment transport in gravel-bed rivers is a notoriously difficult problem [*Henderson*, 1966]. Solid material can be transported by rolling or sliding on the bed, by short hops called 'saltations', or by suspension in the flow [*Bagnold*, 1966]. In natural streams, bed material is typically composed of a range of sizes and shapes, all of which are entrained at different thresholds that are altered by the thresholds of the neighbouring particles [*Komar*, 1996]. Experience has found gravelly streams to armour their bed, i.e. that the bed surface is typically coarser than the sub surface material, and to transport their sediment in a size selective manner, i.e. large sizes are under-represented in the bed load when compared to their occurrence in the substrate [*Andrews*, 1994; *Wilcock and McArdell*, 1997; *Church and Hassan*, 2002]. As discharge increases, the armour begins to break up and larger size material is transported more frequently [*Wilcock and McArdell*, 1993; 1997]. In the long term, the greater mobility of the smaller sediments is compensated by their being hidden from the flow by the armour layer and the total sediment output has a similar size distribution to the substrate - a condition defined as equal mobility [*Parker et al.*, 1982]. However, equal mobility may not characterize the transport regime in all cases. *Lisle* [1995] undertook a review of available sediment transport data sets and identified a systematic deviation from equal mobility associated with lower order streams whose substrate consisted of a wide range of sizes. Decreasing bed material size in the direction of flow, a condition referred to as downstream fining, has been found to occur in many of these systems [*Paola et al.*, 1992; *Hoey and Ferguson*, 1997; *Ferguson and Wathen*, 1998; *Rice and Church*, 1998; *Ferguson and Hoey*, 2002] (Figure 2.10).

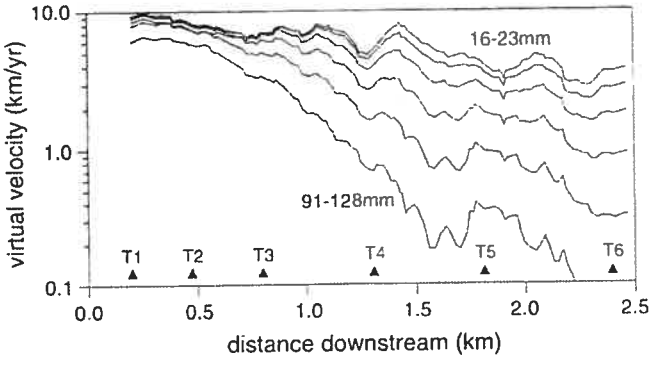

Figure 2.10 - Downstream variation of the virtual velocity for tagged sediment by size class [Ferguson and Hoey, 2002]

There have been many attempts to develop a predictive relation for gravel transport. A review of entrainment criteria by *Montgomery and Buffington* [1997] found a range of values as a result of heterogeneous sediments, particle shape, and the development of bed forms in rivers. Beyond the entrainment threshold, the relation between sediment transport and flow is steep (Figure 2.11). In a review of available relations, *Gomez and Church* [1989] found that all formulae needed calibration for application to any given river. This limitation was primarily related to their construction as one-dimensional equilibrium formulae. River channels are heterogeneous environments and the complexities of the entrainment thresholds combined with the steep nature of the relation between sediment transport and discharge means that spatial averaging produces large errors. Additionally, the work of *Nelson et al.* [1995] and *Sumer et al.* [2003] has highlighted the response of sediment transport to turbulent fluctuations. In the light of the experiments of *Kironoto and Graf* [1995] in non-uniform flow, this indicates that any empirical relation between shear stress and sediment transport based on experiments in plane-bed channels cannot be applied where bed forms are significant. An alternate approach to empirical relations is to analyse the forces that govern the entrainment and transport of individual grains [*Laronne and Carson*, 1976; *Abbott and Francis*, 1977; *Hassan and Church*, 1992; *Sekine and Kikkawa*, 1992; *.Habersack*, 2001; *Schmeeckle and Nelson*, 2003]. This research has the advantage of working on the process scale where local mechanisms such as the pocket geometry, hiding from flow forces, and the influence of bed surface structure can be explicitly modelled. The problem is exceedingly complex, however, and there is continued uncertainty in the calculation of lift forces, the resolution of collisions between moving grains, the feedback effects of developing bed forms, and a method with which to include turbulence [*McEwan et al.*, 2000]. The difficulty of accurately characterising sediment transport remains a significant impediment to the study of bed form development, especially at channel forming discharges.

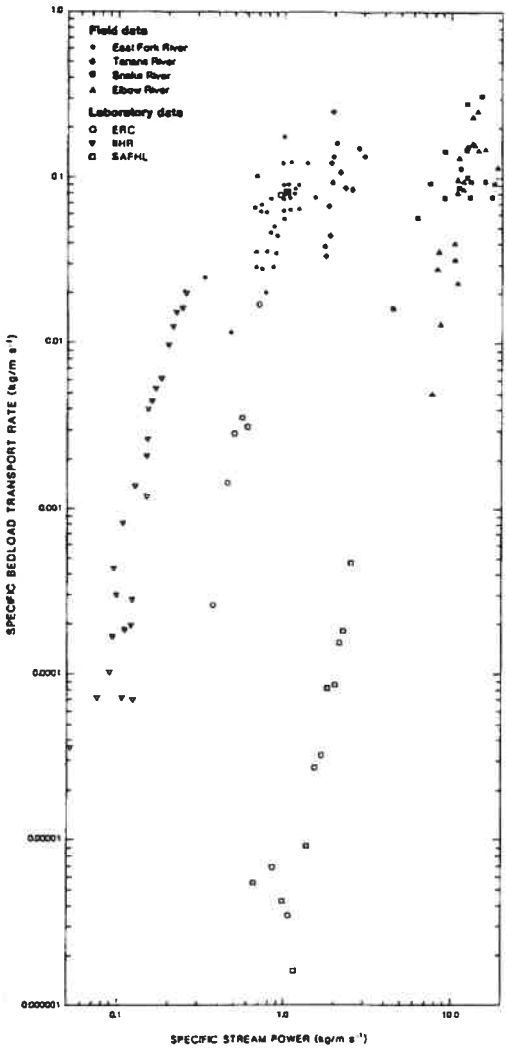

Figure 2.11 - Bedload transport as a function of stream power for data sets used in *Gomez and Church* [1989]

2.1.3 Bed form development

The seminal studies of *Matthes* [1948] and *Jackson* [1976] observed the interaction of sediment transport, turbulent flow, and bed forms and anticipated the interactive model of *Leeder* [1983] (Figure 2.1). Bed forms occur in nearly all systems where sediment is in motion (Figure 2.12). A range of patterns are commonly observed, the occurrence of which depends on the applied shear stress imparted from the flow and a representative grain diameter. Significantly, riffle-pools do not appear on the phase-space diagram, and their relation to other bedforms is not clear. Turbulence is thought to play a central role in the mechanics of bed form development. In the absence of bed forms, *Grass* [1982] was the

first to convincingly demonstrate that turbulence could lead to their development by inducing the development of sand streaks on a glass plate. The sweep-transport model of *Drake et al.* [1988] provided a second bed form initiation mechanism, and *Best* [1992] demonstrated how this mechanism could lead to the formation of bed forms on the scale of ripples. These mechanisms, however, operate in the near-wall region and cannot account for larger structures such as dunes, pebble clusters, gravel sheets, and riffle-pools.

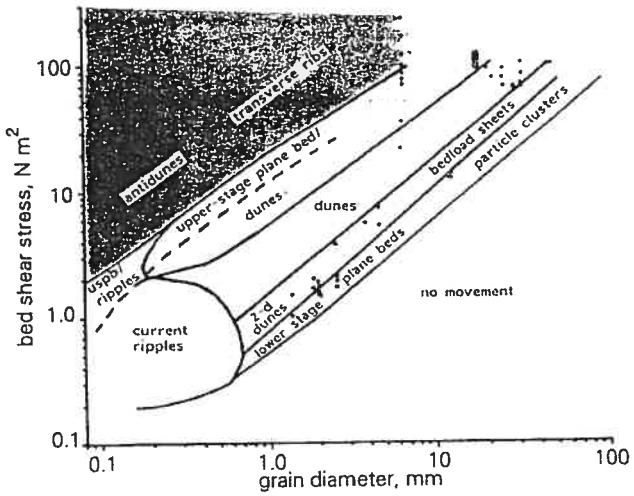

Figure 2.12 - A unified bed form phase diagram across a range of sand and gravel sizes [Best, 1996]

The flow mechanics of sand dunes have been the subject of detailed analyses in the laboratory and in natural rivers. *Raudkivi* [1963] calculated mean statistical properties over a fixed ripple form in a flume and noted systematic deviations of mean velocity, turbulence intensity and Reynolds shear stress from the uniform boundary values. This result has been confirmed by *Nelson et al.* [1993] (Figure 2.13) and other dune studies [*Kostaschuk and Church*, 1993; *Bennett and Best*, 1995; *Venditti and Bennett*, 2000]. It is also consistent with controlled laboratory tests of non-uniform flow [*Kironoto and Graf*, 1995; *Song and Chiew*, 2001]. Flow separation appears to drive the key mechanics of the form. A schematic diagram from *Best* [2005] is shown in Figure 2.14. The shedding of eddies from the separation zone leads to large coherent flow structures that are transported away from the bed where they appear as 'boils' at the water surface. High shear stresses at the reattachment point scour material that is transported up the stoss slope of the bed form in the developing boundary layer and avalanches down the lee slope in the subsequent separation area. In many ways, pebble clusters create a similar flow environment to those

surrounding sharp-angled dunes. *Buffin-Bélanger and Roy* [1998] present a conceptual model from detailed measurements around a natural cluster in a gravel-bed river (Figure 2.15). Their model shows the same zones of flow acceleration over the crest, separation downstream, a shear zone that produces shedding eddies that are transported towards the surface, and a reattachment zone. These results have been confirmed by subsequent studies [*Lawless and Robert*, 2001; *Strom et al.*, 2004]. A link between the flow mechanics and the occurrence of pebble clusters has not been observed, although *de Jong and Ergenzinger* [1995] have hypothesized that this mechanism may lead to a preferred cluster spacing. In low-angled dunes, many studies have noted a lack of flow separation in the lee of the dune [*Kostaschuk and Villard*, 1996; *Carling et al.*, 2000]. *Best and Kostaschuk* [2002] confirmed the occurrence of a small zone of intermittent separation on the lee side of the dunes (Figure 2.16). They noted a more intense mixing in this area, a characteristic that is similar to what occurs downstream of asymmetrical dunes. They proposed the hypothesis that this zone may produce macro-scale coherent structures. Similar to pebble clusters, the link between flow mechanics and bed form development is not yet clear.

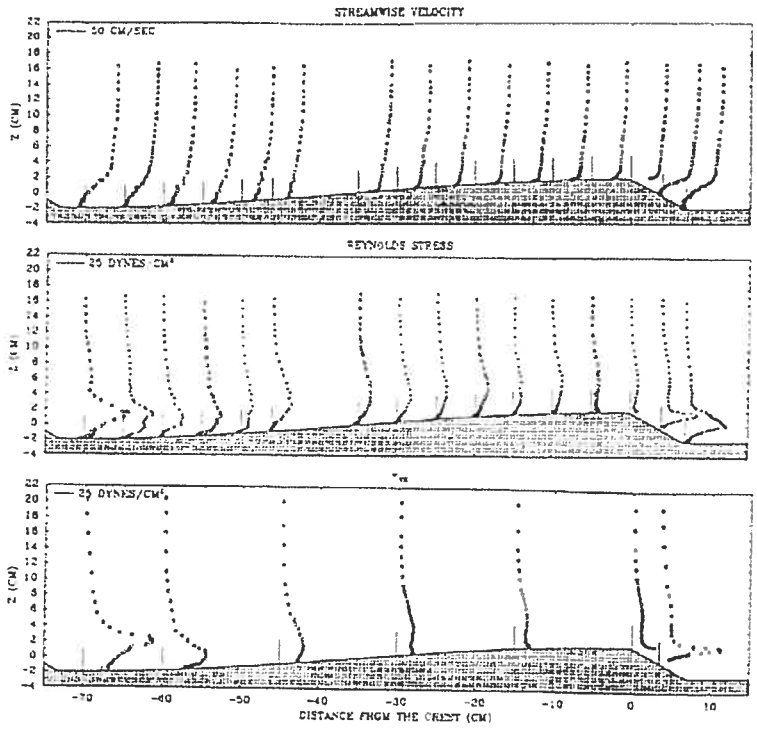

Figure 2.13 - Measured distributions of streamwise velocity, Reynolds shear stress, and normal stress (u'^2) over fixed dune forms [*Nelson et al.*, 1993]

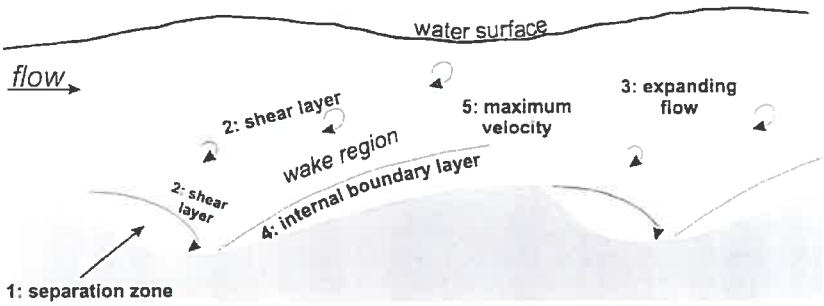

Figure 2.14 - Schematic diagram of the principal regions of flow over asymmetrical dunes [*Best*, 2005]

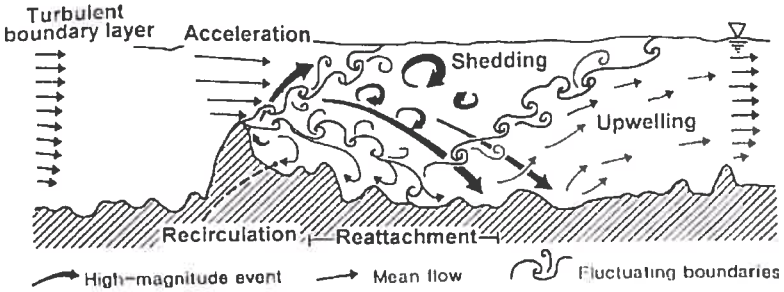

Figure 2.15 - Flow regions associated with the presence of a pebble cluster [*Buffin-Bélanger and Roy*, 1998]

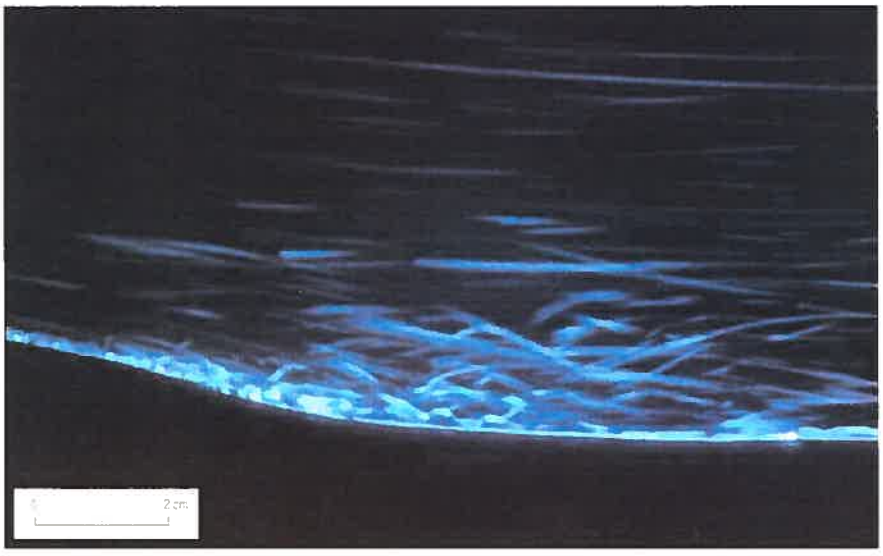

Figure 2.16 – Visualization of tracers in lower lee and trough of low-angled dune showing intermittent flow separation [*Best and Kostaschuk*, 2002]

2.2 Riffle-pool morphology

Riffle-pools are undulations of the river-bed expressed across the entire width of the channel. At low flow, they produce the characteristic pattern of alternate areas of shallow

and fast flow - the riffles - and deep and slow flow - the pools. Empirical studies have defined the necessary conditions for riffle-pool formation (Table 2.1). Slope is the most reliable predictor of channel morphology, with most riffle-pool reaches having overall slopes less than 1.5% [*Grant et al.*, 1990; *Montgomery and Buffington*, 1997; *Chartrand and Whiting*; 2000]. Forcing elements appear to induce the formation of pools in steeper channels where plane-bed morphology is more commonly observed [*Montgomery et al.*, 1995]. Other necessary conditions are related to the size and heterogeneity of the stream bed sediments [*Leopold and Wolman*, 1957; *Brush*, 1961], but no absolute ranges have been defined. *Grant et al.* [1990] and *Montgomery and Buffington* [1997] use the relative roughness as a criterion for riffle-pool formation. Although different definitions exist, $D_{90}/Y_{bf} \leq 0.30$ appears to define a useful criterion [*Montgomery and Buffington*, 1997]. Width-to-depth ratio is also a useful indicator of morphology, because wider channel tend to braid [*Leopold and Wolman*, 1957]. Although most studies in Table 2.1 do not list bankfull depths, a range of $Z_{bf}/Y_{bf} = 5\text{-}20$ was proposed by *Leopold* [1982] for riffle-pool streams. This range fits with *Richards* [1976] and *Buffington et al.* [2002], although relatively wider systems were considered in *Madej* [1999].

Source	Type	# rivers (reaches)	D_{50} (mm)	S (%)	Z_{bf} (m)	Y_{bf} (m)
Leopold and Wolman [1957]	straight, meandering	37 (51)	8 - 268	0.0095 - 3.6	0.20 - 100	n/a
Richards [1976]	straight, meandering	6 (8)	n/a	0.13 - 0.56	7.2 - 8.2	0.81 - 0.95
Keller and Melhorn [1978]	free, bedrock	11	n/a	0.10 - 0.89	3.7 - 29.3	n/a
Grant et al. [1990]	free, forced, cascade, steps	2	13 - 20	2.2 - 3.8	18.1	n/a
Lisle and Hilton [1992]	free, forced	8	n/a	1.3 - 4.4	n/a	n/a
Wohl et al. [1993]	cascade, free	3 (5)	60 -170	0.2 - 17.2	n/a	n/a
Montgomery et al.. [1995]	free, forced	n/a	n/a	0.2 - 8.5	2.7 - 38.1	n/a
Montgomery and Buffington [1997]	free, forced	4	≈ 10	≈ 0.5 - 2.5	n/a	n/a
Myers and Swanson [1997]	free, forced	17 (36)	n/a	0.3 - 19.3	1.1 - 6.8	n/a
Madej [1999]	free, forced	3 (7)	15 - 60	0.15 - 1.66	12 -110	1.0 - 2.2
Chartrand and Whiting [2000]	n/a	(25)	n/a	1.0 - 1.5	n/a	n/a
Thompson and Hoffman [2001]	forced	27	20 - 194	0.01 - 10	3.1 - 38.6	n/a
Buffington et al. [2002]	forced	18 (32)	16 - 153	0.17 - 4.1	4.6 - 29.1	0.32 - 1.59

Table 2.1 - Empirical studies of pool-riffle morphology

A typical representation of a riffle-pool bed form from *Church and Jones* [1982] is shown in Figure 2.17. There are four elements to the definition: the topographical sequence of highs and lows, the macro-scale of the form (wavelength $\lambda \propto Z$), sorting of sediment by size, and the formation of lateral bars. Topography yields the most objective methods of identification. *Richards* [1976] defined riffles as the positive residuals above the reach-averaged slope and the pools as the negative residuals. *O'Neill and Abrahams* [1984] modified this definition by including a tolerance about the mean slope to eliminate the definition of riffles that correspond to small deviations. An alternate approach is to consider the residual depths [*Lisle*, 1995; *Madej*, 1999]. Residual depth is defined as the distance from the stream bed to the elevation of a downstream control point and pools are those areas with a negative residual depth. In a detailed sedimentological analysis, *Sear* [1996] subdivided the pool as a function of the bed slope, with the pool-head, mid-pool and the pool-tail defined as the areas of negative, flat, and positive slopes in the downstream direction (Figure 2.18). These definitions are used in this study. Despite the need to distinguish smaller scale roughness from riffle-pools, there is no standard for the minimum size of a riffle-pool [*Buffington et al.*, 2002]. *Lisle and Hilton* [1992] required the residual depth of the pool to be at least twice the flow depth at the riffle crest during low flow. *Montgomery et al.* [1995] required pools to have residual depths at least 25% of the bankfull depth and allowed multiple pools to be defined in a cross section. In contrast, *Myers and Swanson* [1997] required pools to span the stream width. *Thompson and Hoffman* [2001] only measured pools with residual depths greater than 15 cm. Finally, *Buffington et al.* [2002] required that topographic depressions be wider than 1/10 and deeper than 1/20 of the active channel width. The variability of these definitions contributes to the variability of riffle-pool wavelength statistics.

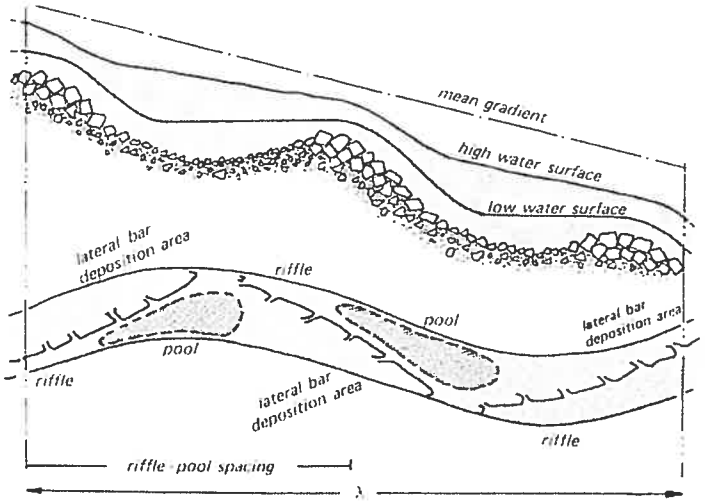

Figure 2.17 - Schematic diagram to define the riffle-pool sequence [*Church and Jones*, 1982]

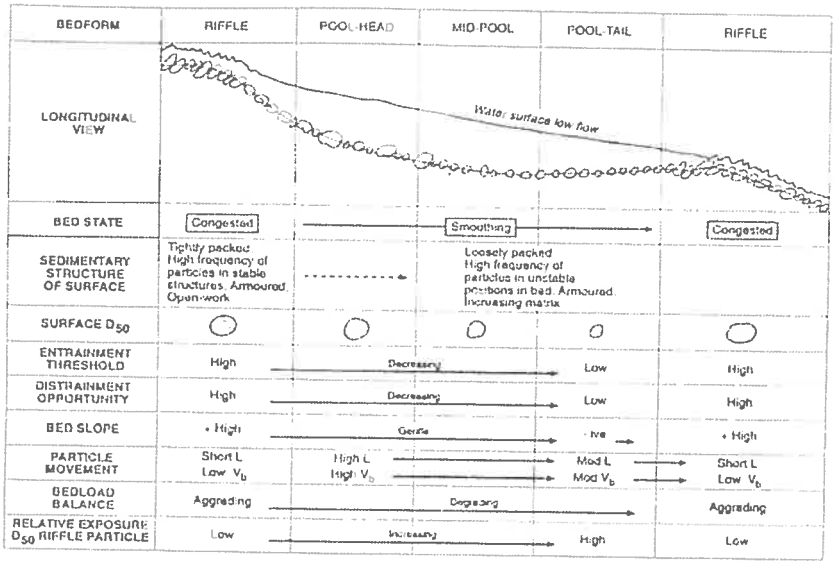

Figure 2.18 - A descriptive model of sediment transport processes in a riffle-pool [*Sear*, 1996]

Riffle-pools are commonly observed at a wavelength of 5-7 times the channel width [*Leopold and Wolman*, 1957; *Richards*, 1976; *Keller and Melhorn*, 1978; *Gregory et al.*, 1994; *Montgomery et al.*, 1995]. In their seminal work on river morphology, *Leopold and Wolman* [1957] found riffle-pools in both straight and meandering systems and observed that the wavelength is similar in both types of systems. *Keller and Melhorn* [1978] supported the generality of this relation when they observed no significant difference between the pools in alluvial and bedrock channels about a mean of 5.9 widths with individual units ranging from 1.5 to 23.3 channel widths. *Roy and Abrahams* [1980]

disagreed with the lack of a statistically significant difference but they did agree that mean bed form spacing for both types of channels were between 5 and 7 widths. Pool spacing was normally distributed. *Gregory et al.* [1994] reviewed a number of studies and also supported the robustness of this relation, although exceptions were noted associated with anthropogenic channel modifications and large pieces of woody debris. *Montgomery et al.* [1995] investigated this last effect in more detail and found that heavy loading of wood reduced the spacing between pools and increased the frequency of pools. This conclusion, however, is somewhat dependant on their relaxed definition of the minimum pool size in a riffle-pool system. *Thompson* [2001] demonstrated that, assuming pools that span the width of the creek and a minimum length between successive riffle-pool couplets, randomly placed forcing elements lead to mean wavelength statistics that agree with statistics in alluvial pool-riffle systems. This suggests that there is a common process underlying the formation of the different types of riffle-pool sequences. This process is distinct from that of dunes, which scale with flow depth [*Yalin and da Silva*, 2001], and step-pools, which are highly sensitive to particle size [*Chartrand and Whiting*, 2000; *Zimmerman and Church*, 2001].

Sediment sorting typically consists of larger particles on the riffle, especially on the downstream 'lee' face, and smaller particles in the pool [*Keller*, 1971; *Church*, 1972; *Hirsch and Abrahams*, 1981; *Sear*, 1996]. Inconsistent patterns have sometimes been reported due to the inclusion of bar sediments with pools [*Church and Jones*, 1982; *Milne*, 1982], large material associated with glacial lags that remains in the pool [*Richards*, 1976; *Heritage and Milan*, 2004], and temporal variability in the pool [*Lisle and Hilton*, 1992; *Madej*, 2001]. In the absence of these complicating factors, the model of *Sear* [1996] represents the typical sedimentology (Figure 2.18) and confirms the schematic diagram of *Church and Jones* [1982]. Unlike dunes, which form in mixed and unimodal sediments, riffle-pools appear to require heterogeneous sediment sizes. A large, relatively immobile fraction is particularly important for straight systems [*Leopold and Wolman*, 1957]. Flume tests in heterogeneous sediments found a coarse bar head to develop that stabilizes the position of the bar [*Lisle et al.*, 1991; *Pyrce and Ashmore*, 2005] (Figures 2.21-2.22). This coarse material is in close proximity to the riffle and appears to be part of the same sedimentological unit. Meandering is known to influence the degree of sediment sorting, as tighter radius meanders have larger sediment size differences between the pools and the

bars [*Milne*, 1982]. Finally, it is worth noting that sediment sorting may occur by other means than simply by size. *Hirsch and Abrahams* [1981] found that particle shape may also play a role. Although this factor could not be separated from the effect of size, shape differences do result in differences in terms of particle entrainment [*Carling et al.*, 1992]. Though they did not measure particle shape, *Clifford* [1993] and *Sear* [1996] both found that similarly sized particles tend to be more tightly held in riffle sections than in pools.

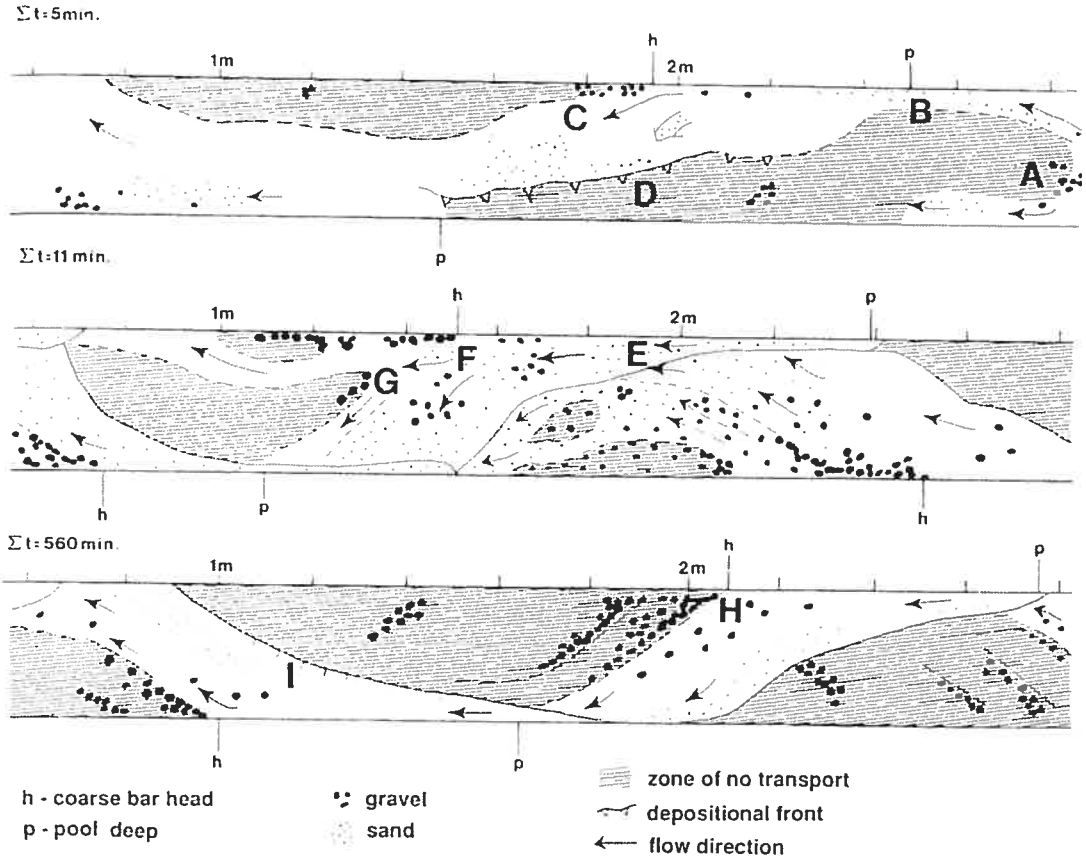

Figure 2.19 - Stages in formation of a bar showing the deposition of a coarse bar head at H [*Lisle et al.*, 1991]

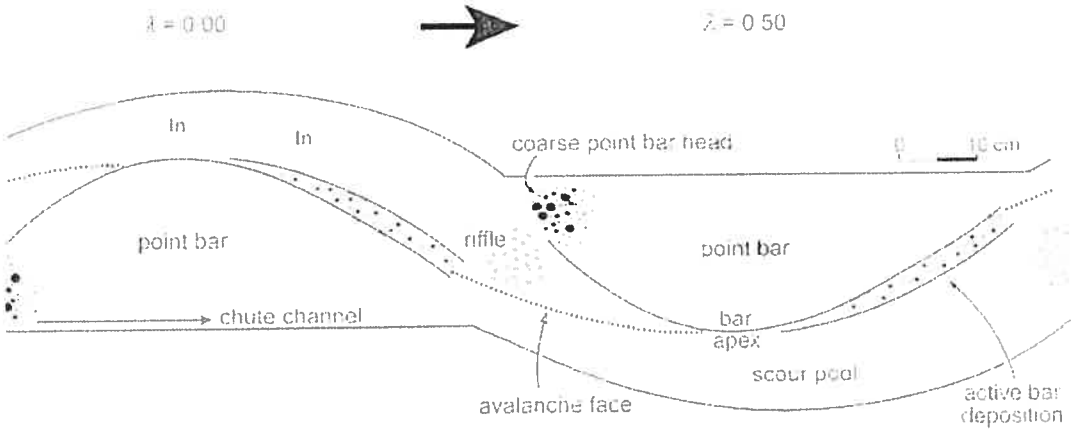

Figure 2.20 - Schematic diagram of the channel morphology [*Pyrce and Ashmore*, 2005]

Church and Jones [1982] suggested that bars should be included with any definition of riffle-pools. Bars are typically alternate bars in straight systems and point bars in meandering rivers. These forms have been associated with different stages of planform development (Figure 2.21) [*Keller*, 1972]. Even studies in bedrock channels have documented the development of point and alternate bars similar to what occurs in alluvial channels [*Keller and Melhorn*, 1978]. These bars result in asymmetric cross-sections in pools [*Leopold*, 1982] and systematically wider riffles at low flow [*Richards* 1976], which leads to complex stage-discharge relations [*Carling*, 1991]. These bars distinguish riffle-pools from step-pools, for which bar growth is not a requirement [*Montgomery and Buffington*, 1997]. The growth of bars also seems to activate lateral directions of movement in gravel-bed rivers as transverse structures do not remain stable in riffle-pool systems and diagonal forms are dominant [*Church and Jones*, 1982].

In summary, riffle-pool bed forms are defined by undulations of bed topography that scale with channel width, patterns of sediment sorting, and the development of bars. The bed forms are sensitive to channel width, slope, sediment size, sediment heterogeneity, and the supply of forcing elements. They are distinct from dunes because of the requirement for sediment heterogeneity and because they scale with width instead of flow depth. They are distinct from step-pools because they scale with channel width and because of their association with sediment bars. At least four types have been identified and include straight, meandering, bedrock, and forced riffle-pools. The similarity of scales in all types of riffle-pool systems suggests a common formative mechanism.

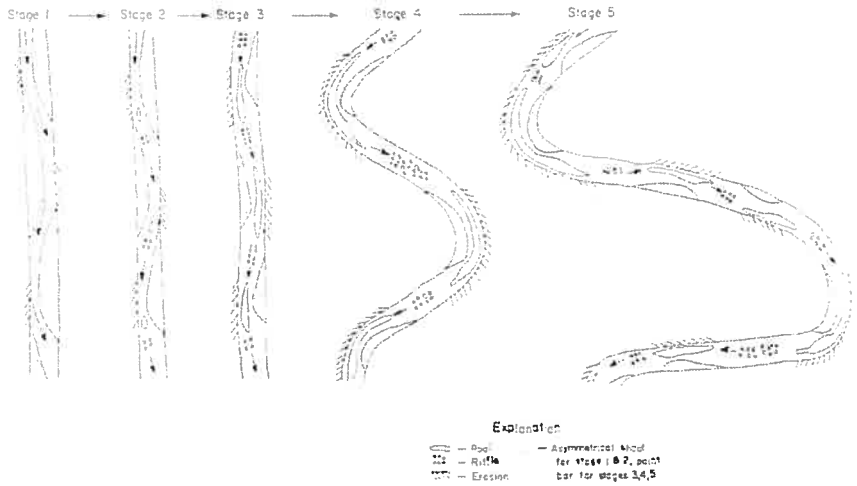

Figure 2.21 - A five-stage model of development that shows a progression from alternate bars to meandering [*Keller*, 1972]

2.3 Sediment transport in riffle-pools

Leopold et al. [1964] were perhaps the first to observe that, unlike dunes and bars, which are commonly observed to move downstream, riffle-pools tend to remain fixed in place. *Lisle* [1982] noted that the stability of riffles was related in part to the size of bars, which adjust to floods more slowly than smaller forms like ripples and dunes. However, *Church and Jones* [1982] identified a structural component to riffle-pool systems that provides additional stability. They use the term 'riffle' to distinguish the relatively immobile fraction on the lead edge of a bar that arrests the movement of the bar. *Brush* [1961] also observed a population of relatively immobile particles in the riffle, and *Leopold and Wolman* [1957] noted that this sediment fraction was particularly important in straight riffle-pools. Riffle-pools subject to extreme floods often show little change in their position [*Lisle*, 1986; *Eaton and Lapointe*, 2001]. *Madej* [1999] measured stream profiles over 20 years and found riffle-pools to remain stable in extreme events, although free riffle-pools did randomize to some extent during a 12-year return period event. *Lisle* [1982] reported some headward movement of riffle crests during flows below bankfull. These adjustments were associated with the reworking of sediments deposited at high flow and do not result in bed form translation. When disturbance does occur in riffle-pool systems, sediment supply appears to play a dominant role. Large sediment influxes tend to randomize bed topography by filling in the pools [*Lisle*, 1982; *Madej*, 1999; *Rathburn and Wohl*, 2001]. Degrading heterogeneous beds are capable of altering roughness through

sediment sorting and the development of bed forms [*Lisle et al.*, 1993; *Hassan and Church*, 2000; *Pender et al.*, 2001] and the systems become supply limited [*Bennett and Bridge*, 1995; *Lisle and Church*, 2002].

A two phase morphological model has been proposed for sediment transport where riffle-pools are present [*Jackson and Beschta*, 1982; *Meade*, 1985; *Sidle*, 1988]. In phase I, fine material is transported over a static bed [*Lisle and Hilton*, 1992]. *Meade* [1985] shows that the riffle typically degrades in this phase due to the winnowing of fines, material that subsequently deposits in the pool. Coarse material making up the armour layer of the bed is transported in phase II [*Jackson and Beschta*, 1982; *Sidle*, 1988] which results in riffle aggradation and pool scour (Figure 2.22) [*Meade*, 1985]. From measurements in riffle and step-pool systems, *Ryan et al.* [2002] identified a threshold in the relation between sediment transport that corresponds with the transport of larger clast sizes and the onset of phase II transport, as shown in Figure 2.23a. This figure, however, may be misleading because discharge and transport rate are more often plotted in log-log space due to the non-linear relation between them. This transformation removes the suitability of a two phase transport model [*Jackson and Beschta*, 1982], as shown in Figure 2.23b. *Hassan and Woodsmith* [2004] noted a decrease in the slope exponent between the two variables associated with a change in the relation between discharge and shear stress beyond the bankfull flow stage. Following *Shields* [1936], *Hassan and Woodsmith* [2004] chose to model entrainment using shear stress (Figure 2.24). Similar to flume results [*Wilcock and McArdell*, 1993] and in more uniform river environments [*Church and Hassan*, 2002], there is a gradual increase in the entrainment threshold with sediment size. Unlike the other studies, however, there does appear to be a threshold for full mobility. In the pool-center, for example, the three largest size fractions all reach full mobility at the same shear stress. This behaviour could be explained by the sorting of sediment into patches of relatively homogeneous sediment for which a clear threshold exists for local transport [*Lisle and Hilton*, 1992; *Garcia et al.*, 1999].

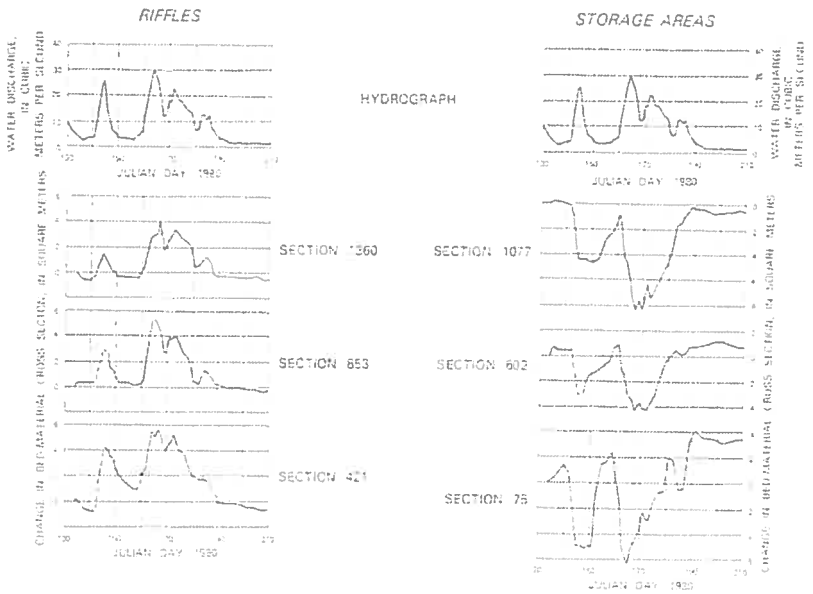

Figure 2.22 - Changes in storage of bed sediment in response to changes in water discharge on three major riffles (left) and three major storage areas (right) in the East Fork River [*Meade*, 1985]

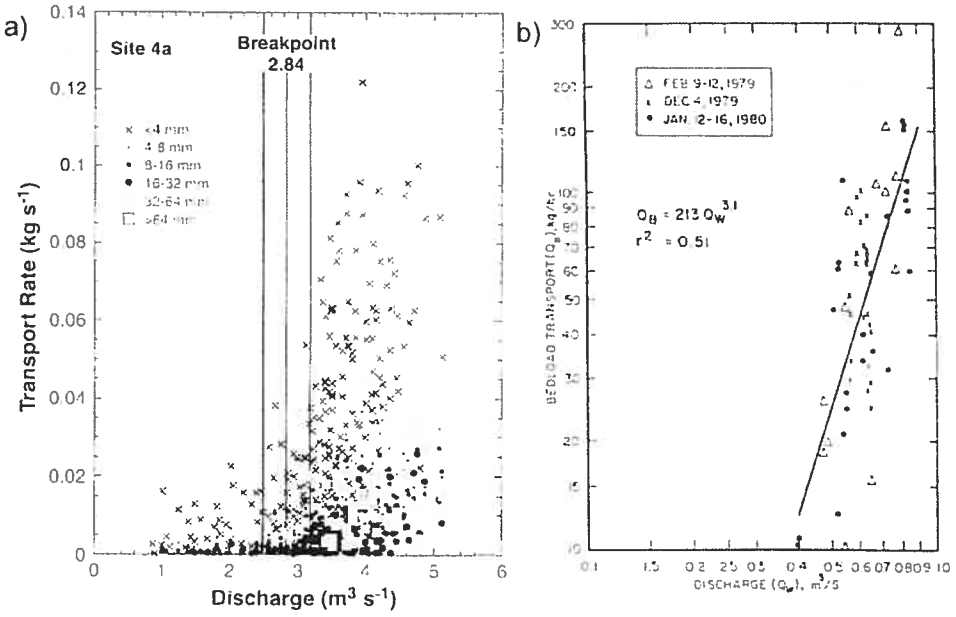

Figure 2.23 - Comparison of discharge versus sediment transport relations from (a) *Ryan et al.* [2002] and (b) *Jackson and Beschta* [1982].

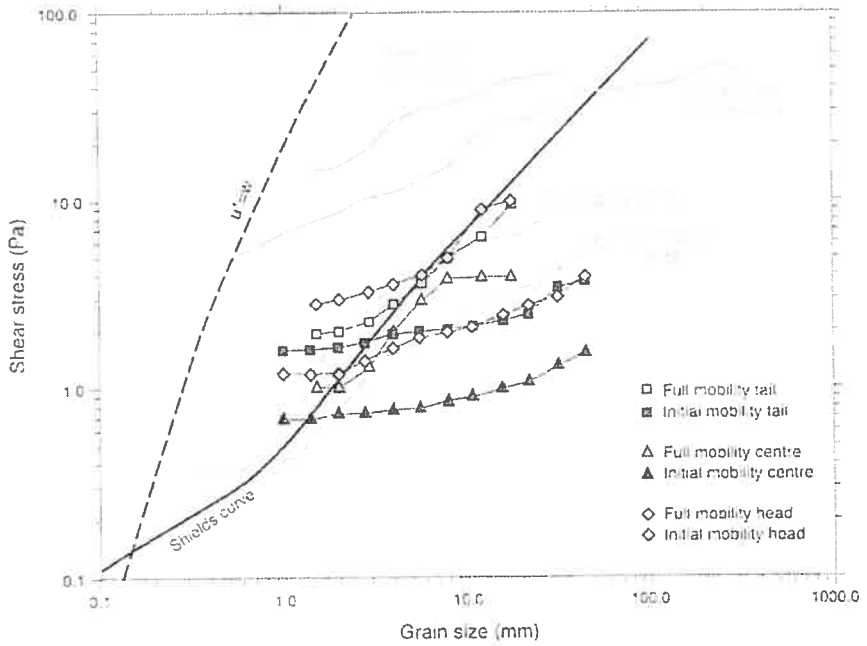

Figure 2.24 - Bed shear stress needed to initiate and to fully mobilize sediments in a pool versus grain size [*Hassan and Woodsmith*, 2004]. Also shown are results from flume experiments [*Wilcock and McArdell*, 1993], and Harris Creek [*Church and Hassan*, 2002].

2.4 Flow dynamics of riffle-pools

Table 2.2 summarizes field-based studies in which the hydraulic properties of pools and riffles have been measured. With a few exceptions, the streams meet the morphological criteria of *Montgomery and Buffington* [1997] for pool-riffle systems, as sediment is gravel sized, relative roughness is less than 0.3, and slopes generally range between 0.02 and 1.3 %. To examine the variability within this range, the measured streams are plotted in terms of their bankfull width (Z_{bf}) and slope (S) in Figure 2.25. In general, the relation follows a negative trend. A few sites are wider and steeper than the most common systems and these sites correspond with reaches in which riffles were artificially constructed. Within the negative trend, it appears that there is either a great deal of scatter around a single relation, or that there are different types of pool-riffle systems that can be separated using relations that follow a negative slope. Two relations following $S \propto Z^{-1}$ are shown (relation *a* and *b*). If we assume that $Z \propto Q^{-0.44}$ [*Kellerhals and Church*, 1989], the exponent on these relations is roughly equivalent to the well-known relation $S \propto Q^{-0.4}$ used to separate meandering and braided systems [*Leopold and Wolman*, 1957]. Similar to this classic approach, channel planform appears to be playing a role in the scatter

in Figure 2.25. Straight and forced systems generally plotting close to relation *a*, whereas pools in bends tending to plot close to relation *b*, although complete separation is not achieved. Forced pools generally plot above line a, a trend which was confirmed using the data set of *Buffington et al.* [2002], though these systems were not plotted because their hydraulics were not studied in detail. Sediment size is also playing a role, with smaller D_{50} values generally closer to relation *b*. Unfortunately, there is insufficient data to statistically examine all of the various factors that could be involved. Instead, the comparison of morphology is used here to contextualize the review of the various results. It is possible that the character of flow dynamics in a riffle-pool is at least partially dependant on its position within Figure 2.25, a factor that has not been considered in previous comparisons of hydraulic data in pools and riffles. In this vein, it is useful to note the relative positions of key studies. The streams studied by *Keller* [1971], *Clifford and Richards* [1992], *Thompson et al.* [1999], *Hassan and Woodsmith* [2004] all plot close to line *a*, as does Moras Creek, the stream examined in this study. In contrast, the streams studied by *Petit* [1987] and *Carling* [1991] plot close to line *b*.

Study	Site	Morphology: No of pools[a] +	x	+	,	Z_{bf} (m)	Y_{bf} (m)	S (%)	D_{50} (mm)	D_{84} (mm)	Experimental Design: Instrument	Var.	# of Sampling locations n_x[d]	n_y	n_z	desc.	Q_{max}/Q_{bf}
Leopold and Wolman [1957]	Middle R.	0	3	1	0	25[b]	n/a	0.17	n/a	n/a	staff gauge	Y	-	-	-	-	<< 1
	Popo Agie R.	4	0	0	0	30[b]	n/a	0.28	n/a	n/a	staff gauge	Y	-	-	-	-	<< 1
Keller [1971]	Dry Ck.	1	0	0	0	12[b]	3[b]	0.35	32	60	Price CM	U	5	1	1	near-bed	0.6
Richards [1976]	R. Fowey	1	1	0	0	8	1.1	0.13-0.56	64	n/a	staff gauge	Y	4	-	-	-	<< 1
Lisle [1979]	E. Fork R.	1	0	0	0	18	1.2	0.07	30[c]	46	staff gauge	Y	2	-	-	-	1.4
Bathurst [1979]	R. Severn A	0	3	0	0	18	n/a	0.052	19	45	Ott CM	U	3	18	n/a	section	n/a
	R. Severn B	3	0	0	0	29	n/a	0.16	28	47	Ott CM	U	3	29	n/a	section	n/a
	R. Swale	1	0	0	0	20	n/a	0.18	85	142	Ott CM	U	1	20	n/a	section	n/a
Bhomick and Demissie [1982]	Kaskaskia R.	1	1	0	0	50[b]	4.0[b]	0.13[b]	40	100	n/a	U	2	1	8	profile	1
Jackson and Beschta [1982]	Flynn Ck.	0	2	0	0	3.5	n/a	1	12	22	Price CM	U	3	6	1	y = 0.4Y	1.3
Petit [1987]	Rulles Ck.	2	6	0	0	3.5	0.75	0.3[b]	15	n/a	Ott CM	U	28	n/a	n/a	section	1.9
Carling [1991]	R. Severn A	2	0	0	0	37	3.4	0.034	19	35	Ott CM	U	4	18	34	section	1
	R. Severn B	1	0	0	0	80	4.4	0.02	31	51	Ott CM	U	2	40	40	section	1
Whiting and Dietrich [1991]	Solfatara Ck.	0	1	0	0	5.2	0.4	0.1	8	16.1	CM	U, V	11	23	≈ 0.1	section	0.45
Clifford and Richards [1992]	R. Quarme	1	0	0	0	8[b]	1[b]	0.7	50	n/a	Ott CM	U	4	5	2	y = 5cm,0.4Y	1
Clifford [1993a]	R. Quarme	1	0	0	0	8[b]	1[b]	0.7	50	n/a	ECM	u, v, w	4	1	1	y = 5 cm	0.5
Clifford [1993b]	R. Quarme	1	0	0	0	8[b]	1[b]	0.7	50	n/a	ECM	u, v, w	4	1	1	y = 5 cm	0.5
Clifford and French [1993]	Stiffkey R.	0	1	0	0	3	n/a	0.35	50	n/a	ECM	u, v	2	1	1	y = 2 cm	<< 1
Clifford [1996]	Langden Bk. A	1	0	0	0	2.5	n/a	n/a	50	n/a	ECM	u, v, w	5	1	3	profile	0.67
	Langden Bk. B	1	0	0	0	9.5	n/a	n/a	70	n/a	ECM	u, v, w	7	1	3	profile	0.67
Sear [1996]	R. N. Tyne	2	1	0	0	31	3	0.18	50	n/a	Ott CM	U	12	20	6	section	0.25
Robert [1997]	Little Rouge R.	0	2	0	0	8-10	0.75[b]	0.08	36	60	1D ECM	U	10	1	12	thalweg	0.67
Thompson et al. [1999]	N. St. Vrain Ck.	0	0	1	0	14	1.6	0.7	20[b]	n/a	ECM	U	5	10	4	section	0.5

Study	Site	Morphology: No of pools[a] +	x	+	.	Z_{bf} (m)	Y_{bf} (m)	S (%)	D_{50} (mm)	D_{84} (mm)	Experimental Design: Instrument	Var.	# of Sampling locations n_x[d]	n_y	n_z	desc.	Q_{max}/Q_{bf}
Wohl and Thompson [2000]	E. St. Louis Ck.	2	0	0	0	3	n/a	2.5-12	n/a	n/a	ECM	u	8	5	1	y = 0.4Y	1.1
Booker et al. [2001]	Highland Water	2	2	0	0	2.8	0.94	0.85	19	37	ECM	U,W	3	4	≈ 8	model verif.	0.86
Milan et al. [2001]	R. Rede	2	2	0	0	12[b]	1.5[b]	0.7[b]	101	n/a	staff gauge	Y	7	-	-	-	1
Emery et al. [2003]	R. Tern	0	1	0	0	3.5	0.4[b]	0.17	sand \gravel	n/a	ECM	U	45	5	1	y = 0.4Y	<< 1
	R. Cole	3	1	0	0	5.5	0.6[b]	0.36	gravel \cobble	n/a	ECM	U	65	5	1	y = 0.4Y	<< 1
Walker et al. [2004]	Beecher Ck.	0	0	0	9	4-5	0.65	2.1-2.4	80-90	320	staff gauge	Y	27	-	-	long profile	0.92
	Ouillet Ck.	0	0	0	8	12	0.65	2.4	59	237	staff gauge	Y	24	-	-	long profile	1.02
	Brunette R.	0	0	0	3	17	1.2	0.34	50	300	staff gauge	Y	9	-	-	long profile	0.33
	Chapman Ck.	0	0	0	7	25-29	1.30	1.2-1.8	110-120	600	staff gauge	Y	21	-	-	long profile	0.49
Wilkinson et al. [2004]	Steavenson R.	4	0	0	0	5	0.75[b]	1.3	75	n/a	staff gauge	Y	50	-	-	long profile	0.2
Hassan and Woodsmith [2004]	T. McDonald Ck.	0	0	1	0	10	0.6	0.6	9	30	Price CM	U	3	≈ 30	≈ 10	section	3

Notes: a symbols indicate (+) straight, (x) curved, (+) forced, and (,) constructed pools

b estimated from a figure shown in the study reference

c from *Andrews* [1979]

d n_x, n_y, and n_z refer to the number of sections, points in each profile, and number of profiles in each section, respectively

Table 2.2 - Morphology and experimental design of field-based studies on the hydraulics of riffle-pool systems.

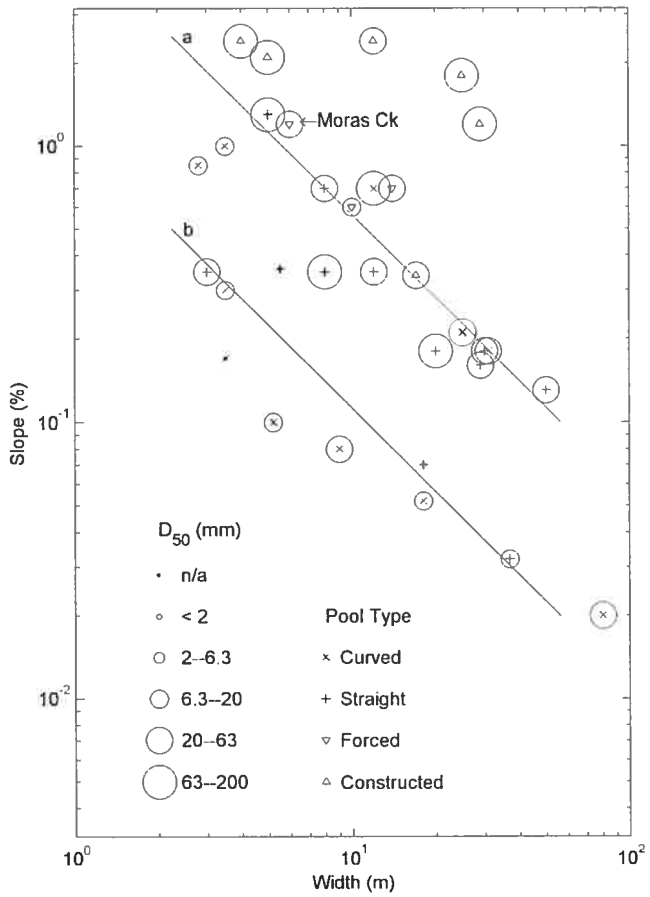

Figure 2.25 - Width versus slope for hydraulic studies of riffle-pools as listed in Table 2.2. Particle size (D_{50}) and pool type are shown for each site. Relations a and b following $S \propto Z^{-1}$ were fit by eye to the data. Moras Creek, the study site in this thesis, is also shown.

Existing studies can also be differentiated in terms of the sampling design, as characterized by measured parameters, sampling locations, sampling density, and maximum flow stage at which measurements were obtained. Measured variables have included water depth (Y), mean velocities (U, V, and W), and instantaneous velocities (u, v, and w). This choice has influenced the maximum flood level that could be sampled $Q_{max}/Q_{bf} > 1$ in 6 of 11 studies (55 %) that measured depth, 6 of 13 studies (46 %) that measured mean velocity, and only 1 of 6 (17 %) studies that measured instantaneous velocities. The main issue is personal safety in acquiring the velocity data at high discharge. Measurements can be made at bankfull flows by wading in very small streams [*Petit*, 1987], but alternate strategies are required in larger rivers. Strategies have included a fixed frame lowered to the stream bed [*Clifford and Richards*, 1992], boats [*Bhomick and Demissie*, 1982; *Carling*, 1991], and light bridges [*Jackson and Beschta*, 1982; *Wohl and*

Thompson, 2000; *Hassan and Woodsmith*, 2004]. Choices of sampling locations and density of measurement points vary widely between studies. $y = 0.4Y$ is commonly used, but this choice reflects an assumption that the mean velocity profile follows a uniform flow model. Measurements in flumes [*Kironoto and Graf*, 1995] and dunes [*Raudkivi*, 1963; *Nelson et al.*, 1993] have shown that velocity profiles deviate from those that are typical in uniform flow. In riffle-pools, profiles measured by *Bhomick and Demissie* [1982] found that the velocity is relatively high near the bed in their pool profile, especially at high flow (Figure 2.26). Interestingly, according to Figure 2.3, the profile in the pool is indicative of accelerating flow, but it is not clear whether the measurement was made in the pool-head or the pool-tail. The spatially averaged profiles measured by *Robert* [1997] show a similar variability between pools and riffles, with pool velocities lower than those in the riffle near to the surface but approximately equal near to the bed (Figure 2.27). Single profiles also suffer from questions of representativity. *Clifford and Richards* [1992] measured near-bed velocities at four sections and noted changing flow patterns with stage (Figure 2.25). This occurred despite the fact that the planform was straight, which makes it necessary to sample velocity profiles across the width of the channel. In all of the studies, the number of cross-sections where measurements were taken has varied from single cross-sections used to calibrate computer modeling as in *Wilkinson et al.* [2004], to those of *Keller* [1971] *Clifford and Richards* [1992], and *Thompson et al.* [1999], who used four to five sections to characterize a single riffle-pool unit. Based on the sedimentological model of *Sear* [1996], wherein the pool is subdivided into three regions, a minimum of five sections is needed to characterize the flow hydraulics of a pool and its neighbouring riffles.

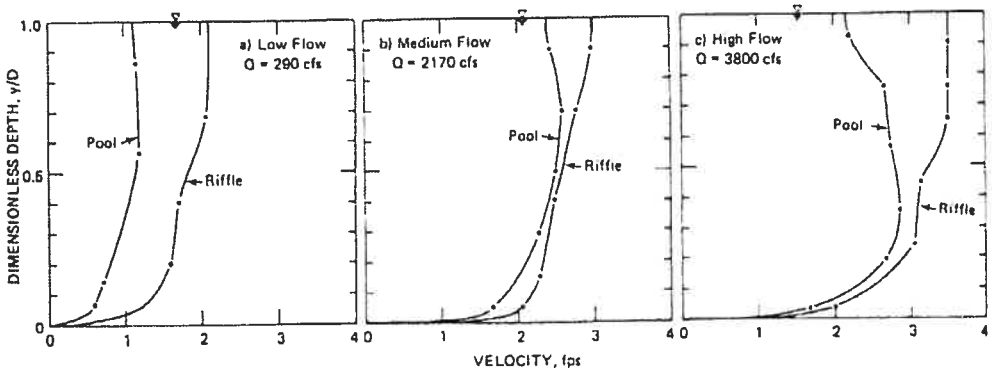

Figure 2.26 - Velocity profiles at pool and riffle cross-sections [*Bhomick and Demissie*, 1982]

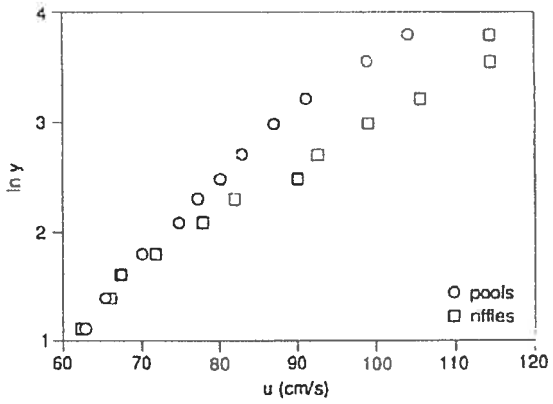

Figure 2.27 - Spatially averaged velocity profile for pools and riffles during high flow conditions ($Q = 2/3\ Q_{bf}$) [*Robert*, 1997]

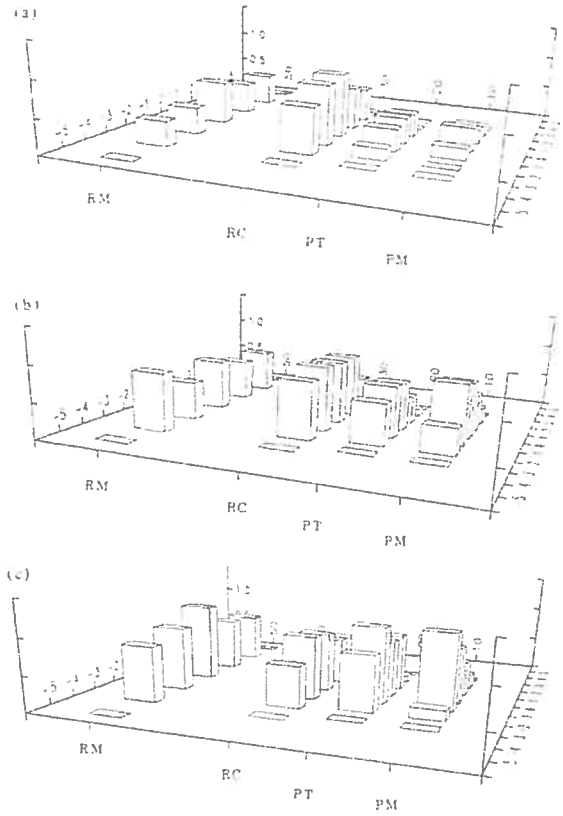

Figure 2.28 - Near-bed velocities measured at (a) low flow (b) moderate flow (c) high flow through a straight riffle-pool at RM - riffle midpoint, RC - riffle crest, PT - pool-tail, and PM - pool midpoint [*Clifford and Richards*, 1992]. Flow is from right to left and the height of the bar represents the velocity.

The work of *Nelson et al.* [1995] and *Sumer et al.* [2003] has demonstrated that sediment transport is sensitive to turbulent fluctuations. Focusing on the few studies that have measured instantaneous velocities, instrument parameters such as sampling frequencies and sampling volumes become important features to consider [*Soulsby*, 1980].

The most significant body of work used Colnbrook Electromagnetic Current Meters (ECM) with a 5.5 cm diameter discoidal sensor head sampling at 20 Hz [*Clifford*, 1993b; *Clifford and French*, 1993; *Clifford*, 1996]. Figure 2.29 shows the key results of *Clifford* [1996]. The RMS of the velocity is highest in the pool sections at high flow. This occurs despite the fact that mean velocities are often lower than those in the riffle, especially if pool sections E and F are compared to riffle section D. *Wohl and Thompson* [2000] were able to measure velocity during floods in streams with a slope greater than 2% using a one-dimensional Marsh-McBirney ECM model 2000 recording at 0.5 Hz. They documented areas of higher and lower turbulence associated with flow deceleration and acceleration, respectively. It is also useful to mention the study of *Thompson* [2004], who measured at 25 Hz using an ADV in a fixed pool built in a flume. He found high turbulent kinetic energy along a shear layer between the main 'core' of flow and a recirculation zone. There was a high correspondence of high turbulent energy with locations where the near bed velocity was faster than that higher up in the water column (Figure 2.30). Just recently, *Thompson* [2006] was able to measure instantaneous velocity signals up to the half bankfull discharge along the shear zone downstream of the constriction at the same site used in *Thompson et al.* [1999]. A principle conclusion from these experiments was that strong turbulent fluctuations in the pool appear to be capable of entraining sediment at higher flows. These fluctuations have not been quantified at bankfull discharges. Previous attempts in pools and other highly turbulent environments, such as the surf zone in oceans, have noted the negative influence of turbulence intensity on the quality of velocity measurements [*Thompson et al.*, 1999; *Rodriguez et al.*, 1999; *Wohl and Thompson*, 2000; *Bryan et al.*, 2003; *Thompson*, 2006]. Before turbulence measurements in riffle-pools can be reliably made at high flow, it will be critical to assess signal quality in these environments.

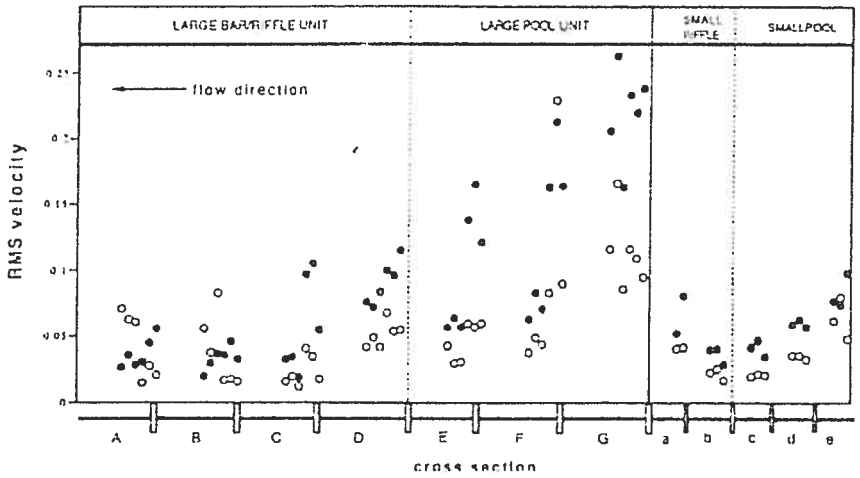

Figure 2.29 - Variation in absolute turbulence intensity (RMS in m/s) through two riffle-pools during moderate discharge [*Clifford*, 1996]. Flow direction is from right to left. Closed symbols refer to streamwise velocity components and open symbols refer to vertical velocity components.

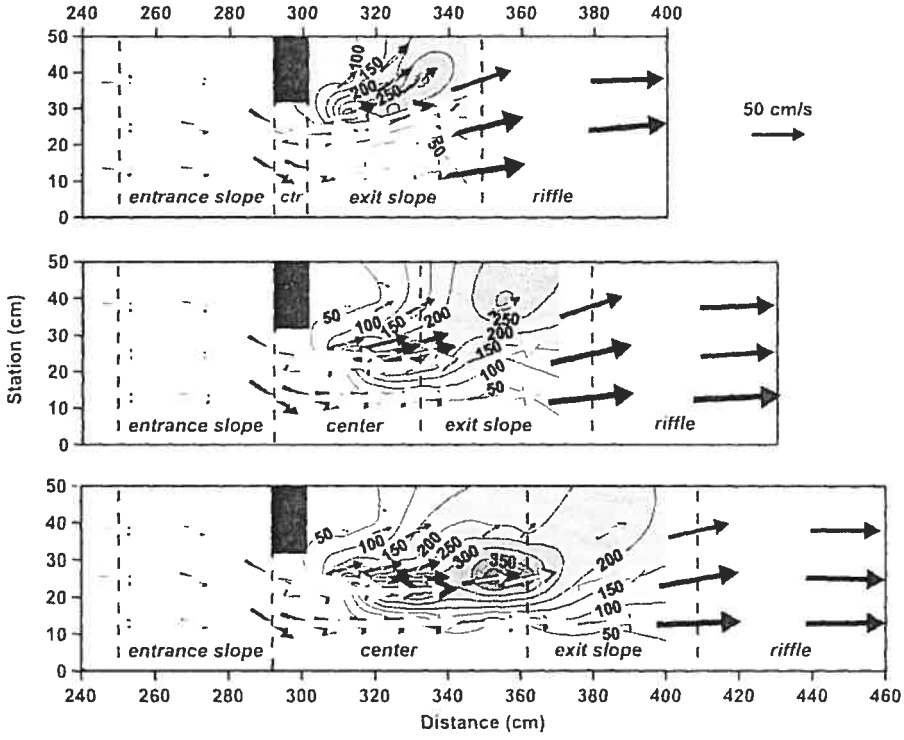

Figure 2.30 - Plan-view maps of 10 cm, 40 cm, and 70 cm long pools showing velocity vectors for the streamwise and lateral components of near-bed (black arrows) and 0.4Y (white arrows) velocities. The arrows are superimposed on turbulent kinetic energy (E_k) at 0.4Y [*Thompson*, 2004]

2.5 Formation of riffle-pools: theory and field evidence

The formation of riffle-pools is a geomorphic puzzle that has been the subject of debate in the literature for over 30 years. The major theories include kinematic wave theory [*Langbein and Leopold,* 1968], energy dissipation [*Yang*, 1971], the velocity reversal [*Keller*, 1971], and coherent turbulence [*Yalin*, 1971]. *Langbein and Leopold* [1968] considered the development of riffle-pools in rivers as a result of kinematic waves. This type of wave will occur when particles interact to decrease the effectiveness of fluid forces. A simple analogy is that of cars on a highway. They tend to concentrate into waves as cars between the waves interact less with other cars and move faster than the waves themselves. In many river systems, riffle-pool positions are fixed. If these bed forms are kinematic waves, sediment transport should largely be controlled by their positions and modes should show up in path length distributions that correspond with their dimensions. *Einstein* [1937] used painted tracers to investigate sediment transport in a relatively deep flume. Data from six of sixty experiments were plotted by *Pyrce and Ashmore* [2003] and are shown in Figure (2.31). The six plots correspond with increased run time and demonstrate an evolution from an exponential to a unimodal normal distribution, and an increase of mean path length with time. However, *Pyrce and Ashmore* [2003] also noted other simulations where the formation of sand bars apparently exerted a controlling influence on path length, which would support the kinematic wave model. The relation between channel width and path length modes from collected data sets is shown in Figure 2.32. Multiple modes were present in a number of cases. While there are cases in which the modal path length is consistent with riffle-pool spacing, there are also many cases where it is not.

Yang [1971] proposed that "the formation of pools and riffles is a means of self-adjustment that minimizes their time rate of potential energy expenditure per unit mass of water in accordance with the law of least time rate of energy expenditure". This theory was particularly concerned with aligning the occurrence of pool and riffles in accordance with the general laws of thermodynamics. The main weakness of this theory is that it difficult to test [*Carling*, 1991], as it is unclear how `self-adjustment' translates into measurable scour and deposition. *Yang* [1971] indicated that the water surface slope could typically be used as a measure of the energy gradient, meaning that slope breaks should be present and associated with the pools and riffles during formative discharges. Most studies concerned

with energy dissipation in pools and riffles have measured surface elevations [*Richards*, 1976; *Milan et al.*, 2001, *Walker et al.*, 2004]. A resulting difficulty is the common observation that the water surface slope tends to equalize over the entire reach at high flow [*Leopold and Wolman*, 1957; *Richards*, 1976]. *Yang* [1971] assumed this to indicate that riffles cease to exist, in a hydraulic sense, at high flows. The more recent study of *Walker et al.* [2004] found breaks in surface elevations over constructed riffles for a full range of flows. It is important to realize, however, that the use of surface elevation is a simplification of stream energetics. While few results at high flows are available, and no definitive test of the energy dissipation hypothesis has been completed, existing measurements in pools indicate that morphology also influences other energy components such as the kinetic and turbulent kinetic energy [*Clifford*, 1993b; *Clifford and French*, 1993; *Clifford*, 1996; *Thompson et al.*, 1998; *Wohl and Thompson*, 2000].

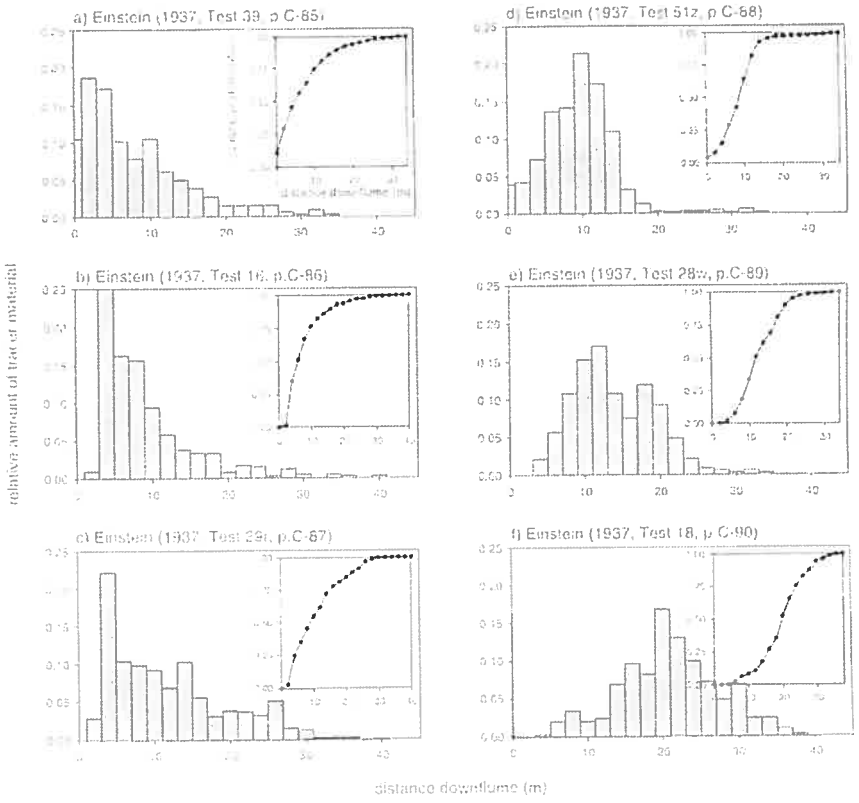

Figure 2.31- The effect of an increase of time on path length distributions [*Einstein*, 1937]. Time increases from a-f. [*Pyrce and Ashmore*, 2003]

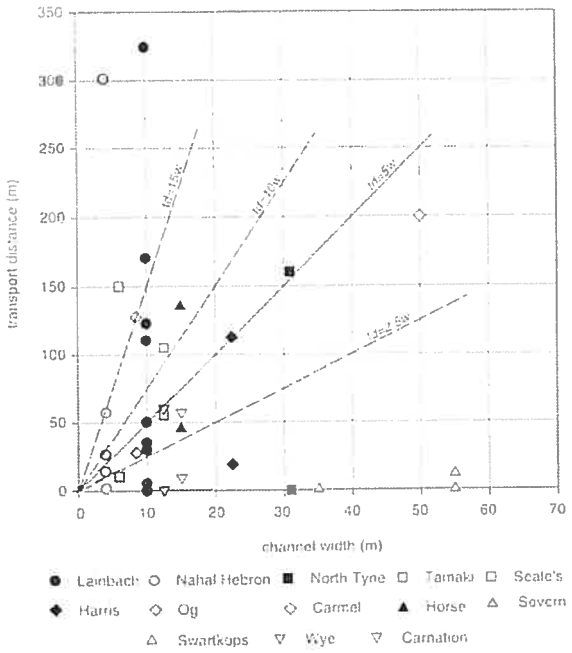

Figure 2.32 - Channel width versus modes of transport distance from studies compiled by *Pyrce and Ashmore* [2003]

Unlike Yang's concept of energy dissipation, the velocity reversal hypothesis is amenable to simple tests. As defined by *Keller* [1971], "with increasing discharge, the bottom velocity of the pool increases faster than that of adjacent riffles until at relatively high flow the bottom velocity of the pool exceeds that of the riffle." Such a reversal would explain how the pool, where deposition of fine sands is often observed at low and moderate discharges, maintains its depth during high discharges. Results of *Keller* [1971] did not demonstrate that a reversal occurred. Instead, the hypothesis was based on an extrapolation from measured values during low and moderate flow rates (Figure 2.33). A number of papers have critiqued or modified the concept of velocity reversal without extensive velocity measurements, relying instead on indirect arguments based on mean shear stress or bulk flow velocity [*Teleki*, 1972; *Lisle*, 1979; *Thompson et al.*, 1999; *Milan et al.*, 2001; *Wilkinson et al.*, 2004]. Without detailed knowledge of the structure of the boundary layer in pools and riffles at high discharges, measurements of mean properties cannot be used to infer near-bed conditions. Only six studies obtained measurements of U at bankfull flows. Of these, two did not obtain velocity measurements near the bed during the event [*Jackson and Beschta*, 1982; *Carling*, 1991], and one study measured only two velocity profiles [*Bhomick and Demissie*, 1982], meaning that data from these studies is not adequate to accept or reject the hypothesis. Of the remaining three cases, one site is a meandering

system [*Petit*, 1987], one is a relatively straight pool [*Clifford and Richards*, 1992], and one pool is forced [*Hassan and Woodsmith*, 2004]. *Clifford and Richards* [1992] measured near-bed velocity over a range of flows (Figure 2.34). Their results do not support the log-linear relations envisaged by *Keller* [1971] as the relation between velocity and discharge is erratic near to the bed. It is only the velocity in the pool-tail that always shows a positive relation with discharge and some areas such as the riffle crest decrease during high discharges. These results indicate that the pool cannot be considered a homogeneous zone. Flow dynamics in the pool-head, where bed slope is negative, and those in the pool-tail, where the bed slope is positive, must be considered separately. *Hassan and Woodsmith* [2004] observed that sediment moves at lower shear stresses (calculated from near-bed velocity profiles) in the pool than in other sections (Figure 2.24). They cite turbulent vortices as a possible secondary mechanism. The key result from this review is that, in spite of a theory that is conceptually simple to test, there is no unequivocal field evidence to support it. The pool has been shown to be a heterogeneous environment and it is not clear how near-bed velocities are distributed or what factors are responsible for the variability.

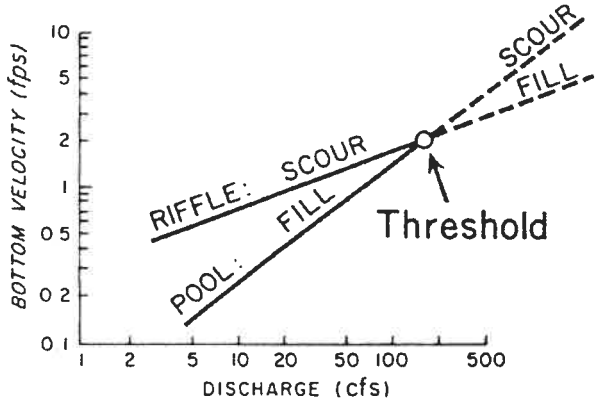

Figure 2.33 - Velocity reversal hypothesis for a riffle-pool in Dry Creek [*Keller*, 1982]. The data in *Keller* [1971] do not extend past the threshold point and the dashed lines have not been verified.

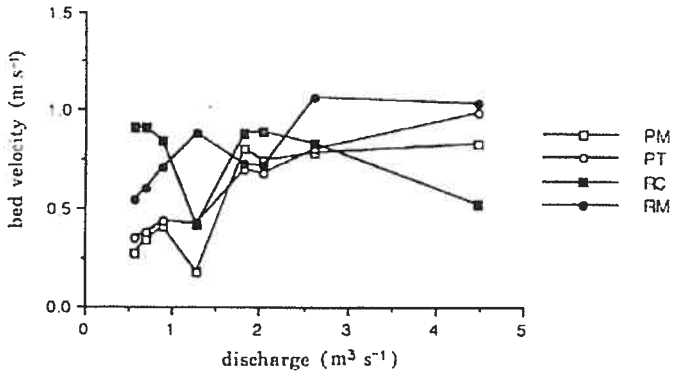

Figure 2.34 - Near-bed velocity at channel centerline in River Quarme at RM - riffle midpoint, RC - riffle crest, PT - pool-tail, and PM - pool midpoint [*Clifford and Richards*, 1992]. Only the pool-tail always increases with discharge.

Yalin [1971] related riverbed forms and plan form development to periodic turbulent oscillations within the flow: "sections separated from each other by the even multiples of the distance πZ are correlated by a positive coefficient of correlation." The coherent turbulent events required were proposed to develop from random discontinuities in the channel. *Clifford* [1993a] performed the only known field test of Yalin's theory as applied to pool-riffles, but results showed that dominant length of coherent structures scaled with particle roughness. The author did note that some larger scale events occurred during moderate discharges, but only conditions up to the half-bankfull event were measured in this study, thus leaving results open for interpretation. Large-scale coherent structures in the form of low and high-speed wedges are common in rivers [*Buffin-Bélanger et al.*, 2000; *Roy et al.*, 2004], but these flow structures scale with flow depth and have not been correlated with macro-scale bed forms. Coherent events have been visually observed in the shear zone formed downstream of obstructions [*Buffington et al.*, 2002; *Thompson*, 2004; *Hassan and Woodsmith*, 2004]. The flume study of *Thompson* [2004] found that these structures corresponded with zones of high E_k, (Figure 2.30) but the frequency, strength, and influence of these structures on bed form scale has not been established in natural rivers.

In conclusion, a review of available pool formation theories shows that we do not have the observations to properly test the theories, but neither does any theory seems to explain all the field observations. An additional element that has not been adequately considered is turbulence. *Nelson et al.* [1995] and *Sumer et al.* [2003] have found turbulence intensity to be important for sediment transport. The work of *Clifford* [1993a,

1996] and *Thompson* [2004, 2006] has demonstrated the variability of turbulence in pool environments. This variable needs to be considered if an adequate theory of pool formation is to be developed.

2.6 Modelling

Modelling allows field results of otherwise limited generality to be interpreted with greater confidence [*Richards*, 1978]. Modelling exercises relevant to the mechanics of riffle-pools are listed in Table 2.3. We list all published hydraulic models of pool-riffles, so far as we are aware, and examples of alternative approaches such as regime, stability, and discrete particle models. A more exhaustive discussion of discrete models is contained in Chapter 3. For each model we list the number of dimensions, how flow hydraulics and sediment transport are represented, whether they consider dynamic modelling where the bed form changes with time, and principle conclusions related to pool-riffle formation. There have been a number of models that attempt to reproduce the key hydraulic processes over riffle-pool sequences. Discussion in these models typically focuses on the velocity reversal hypothesis. They worked with simplified versions of the laws of continuity and the conservation of energy in one dimension or a depth-averaged plan view of the river. The only work that found reversal to occur was that of *Keller and Florsheim* [1993]. The subsequent efforts of *Carling and Wood* [1994] and *Cao et al.* [2003] concluded that a positive result was dependant on assumptions regarding channel width, and roughness. Assuming $\tau = \gamma R S_f$, where γ is the specific gravity, R is the hydraulic radius, and S_f is the water surface slope, *Wilkinson et al.* [2004] calculated a mean shear stress reversal. In general, the hydraulic models suffer from the same limitation as many field measurements. By modelling only the mean velocity, they make unfounded assumptions about the boundary layer in non-uniform flow that prevents them from being used with confidence. *Booker et al.* (2001) applied a fully three-dimensional hydraulic model to a sequence of pools and riffles. Calibrated results showed reasonable agreement with measured velocity profiles through the center of the channel. The principal results are shown in Figure 2.35. Once again, the results do not clearly support a reversal hypothesis. Sediment routing away from the deeper sections of the pool was proposed to account for pool maintenance, but limited sediment transport and morphological data were presented.

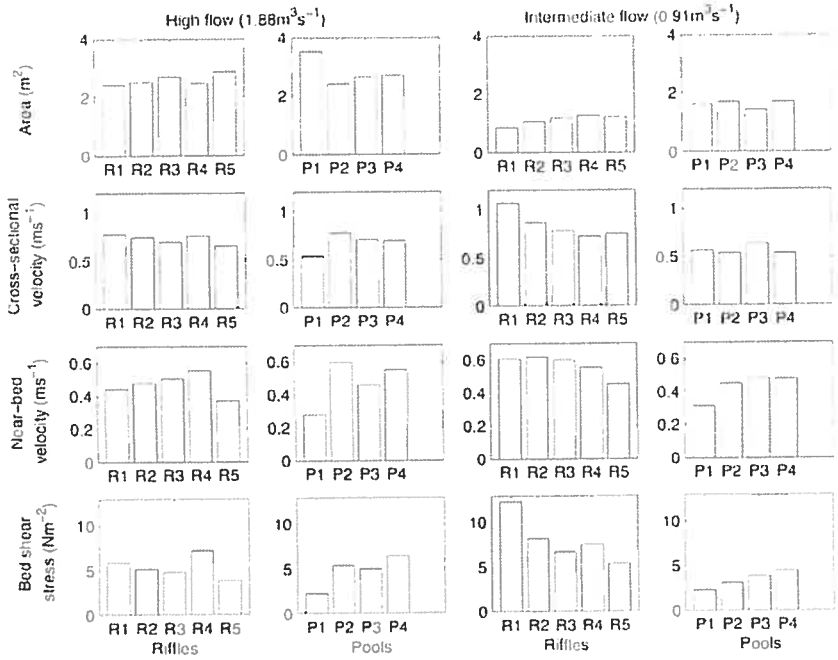

Figure 2.35 - Modelled cross-sectional area, velocity, average near-bed velocity, and shear stress at mid-riffle (R) and mid-pool (P) cross-sections [*Booker et al.*, 2001]

With one exception, the hydraulic models do not consider sediment transport or morphological change. *Wilkinson et al.* [2004] used shear stress to calculate the sediment balance from a single time step, but bed form evolution was not modelled. A successful model of pool formation and maintenance must account for bed form dynamics. Sediment transport modelling was undertaken by *Rathburn and Wohl* [2001] to predict system recovery after a large sediment release from a reservoir. This allowed them to predict scour and fill with some success, even if they applied a sediment transport relation that was developed for plane-bed, uniform flow conditions. As anticipated by *Gomez and Church* [1989], the authors could not recommend further application of the model without extensive calibration. Another approach, of which one example is included in Table 2.3, is regime modelling. *Davies and Sutherland* [1983] is the most relevant of the regime models to the formation of bed forms because it assumes a constant width and allows roughness to adjust to its equilibrium solution. While this approach anticipates the formation of bed forms, the bed forms themselves are poorly described, and neither the sediment transport nor the flow hydraulics equations adjust to the development of bed forms. These limitations also apply to the use of stability analyses. *Columbini et al.* [1987] present a theoretical basis for alternate bars in narrow channels using a weakly non-linear set of equations. Their results predict final bar dimensions that were corroborated with the data

from a large number of flume studies, an example of which is shown in Figure 2.36. A significant limitation of these studies is that they are dependant on sediment transport relations that were developed under controlled conditions where variability induced by bed forms was specifically avoided in order to improve predictability. To then apply these equations to the problem of bed form development places a significant limitation on the interpretability of the results. Sediment transport effectively blocks the development of an accurate model in the presence of bed forms because the feedback mechanisms between the bed morphology and flow on sediment mobility are not taken into account. A second limitation is the issue of equilibrium. Regime and stability models remove the historical dimension from the system. *Lane and Richards* [1997] have argued that non-linear relations in system dynamics imply sensitivity to initial conditions and to local scale processes. Examined more closely, statistical equilibrium of patterns such as meanders and braids can be seen to mask dynamic and non-equilibrium mechanics [*Furbish*, 1991; *Murray and Paola*, 1994]. Dynamic models are needed to demonstrate the development of bed forms and other patterns in river systems.

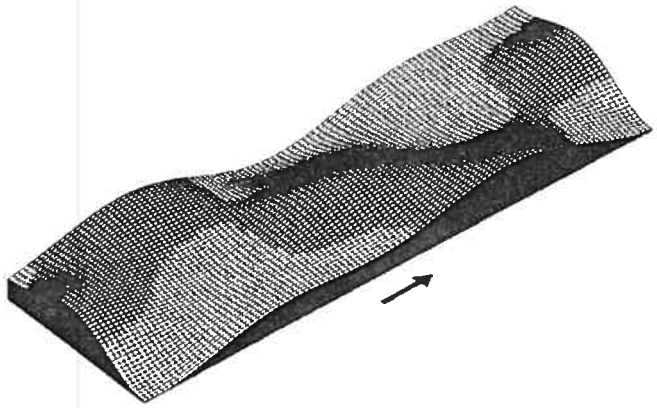

Figure 2.36 - A perpective view of bed topography of alternate bars predicted by the stability model of *Columbini et al.* [1987]

Two models that are capable of modelling system dynamics are shown in Table 2.3. These models work on the scale of individual 'discrete' particles. Because space and time are represented explicitly, it is possible to consider the local variability of flow and sediment dynamics and the systems can change with time. As shown in Table 2.3, *Naden* [1987] and *Schmeeckle and Nelson* [2003] both considered a force balance to calculate sediment entrainment, a method that accounts for the pocket geometry of individual particles and easily applied to mixed sediment sizes. Both models also adjust the fluid

forces on a given particle based on the protrusion of the particle from the bed. Simulated bed surfaces are shown in Figures 2.37 and 2.38. Both models are limited by the complexity of the problem, as discussed in section 2.1.2. There is continued uncertainty in a number of areas and accounting for dynamic changes is extremely expensive in terms of computing power, which has limited the extent and the duration of the studies, especially the three dimensional mechanistic models such as that of *Schmeeckle and Nelson* [2003]. Other similar models are listed in Table 3.1.

Progress in the characterization of sedimentary bed forms has been made in a variety of fields using discrete models by simplifying the representation of the processes into what is called a hierarchical [*Werner*, 1999], or exploratory model [*Murray*, 2003]. The use of these models is discussed in more detail in Chapter 3. The key step is the abstraction of 'fast' scale processes such as sediment transport, which are difficult to resolve from first principles, in order to investigate 'slow' scale processes such as bed form development. Notable among discrete models of sedimentary environments are those of aeolian dunes [*Anderson*, 1990; *Anderson and Bunas*, 1993; *Werner*, 1995; *Nino et al.*, 2002; *Baas*, 2002]. An example from *Anderson and Bunas* [1993] is shown in Figure 2.39. This type of model is not typically used to obtain quantitative predictions of such quantities as sediment transport because of the necessary simplifications, but they are useful because they can qualitatively reproduce many bed form dynamics. They are particularly useful for testing hypotheses.

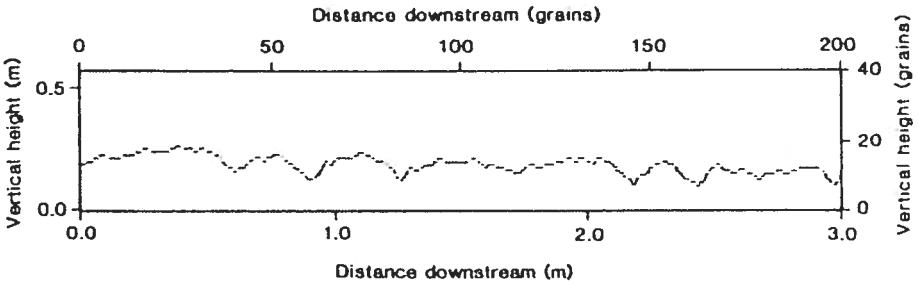

Figure 2.37 - An example of the bed topography generated by the discrete model of *Naden* [1987].

Figure 2.38 - Image of mixed sediment-size bed during modelled transport [*Schmeeckle and Nelson*, 2003]

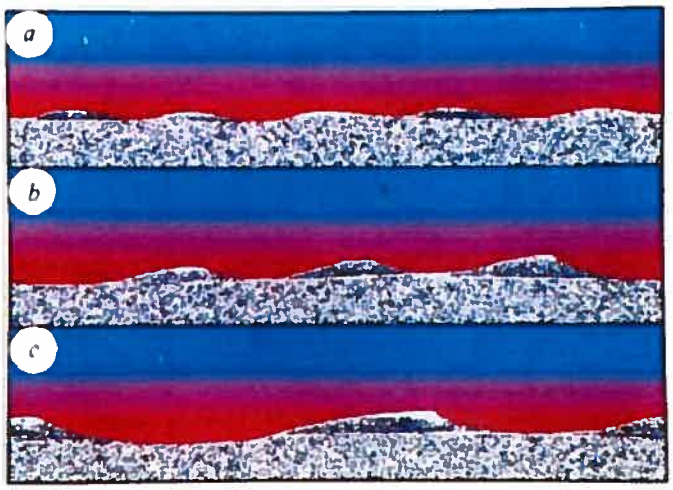

Figure 2.39 - Dune development in a dicrete particle model in which simple rules are used to represent aeolian transport [*Anderson and Bunas*, 1993]

Type	Author	Flow Hydraulics				Sediment Transport			Riffle-pool Formation
		dim[a]	equations	roughness/ turbulence	Δ ?[b]	equations	mixed sed?	Δ ?[b]	
Hydraulic	*Richards* [1978]	1	energy	Mannings n,	no	not modelled	n/a	n/a	no velocity reversal
	Keller and Florsheim [1993]	1	energy HEC-2	Mannings n, head loss	no	not modelled	n/a	n/a	velocity reversal
	Carling and Wood [1994]	1	energy, HEC-2	Mannings n, head loss	no	not modelled	n/a	n/a	reversal dependant on Z, n
	Booker et al. [2001]	3	SSIIM [Olsen, 1996]	k_s, eddy viscosity	no	not modelled	n/a	n/a	no systematic reversal, sediment routing
	Cao et al. [2003]	2	energy	Mannings n, eddy viscosity	no	not modelled	n/a	n/a	reversal dependant on Z
		1	energy	Mannings n	no	Meyer Peter-Muller	no	no	reversal dependant on D50 and Qs
	Wilkinson et al. [2004]	1	energy HECRAS	Mannings n, head loss	no	Du Boys	no	1 time step	shear stress reversal
	Rathburn and Wohl [2001]	1	energy HEC-6	Mannings n, head loss	no	14 options HEC-6	no	yes	not discussed
		2	energy, GSTARS	Mannings n	no	10 options GSTARS	no	yes	not discussed
Regime	*Davies and Sutherland* [1983]	1	steady	friction factor	no	function of shear stress	no	no	maximum friction factor
Stability	*Columbini et al.* [1987]	2	steady, perturbed	roughness length, eddy viscosity	no	Meyer Peter-Muller	no	no	harmonic analysis
Discrete	*Naden* [1987]	2	log-law	random	no	force balance	yes	yes	
	Scmeeckle and Nelson [2003]	3	energy	measured time series	yes	force balance	yes	yes	not discussed

Note a - dim refers to the number of dimensions in the model

b - Δ ? refers to the inclusion of feedback effects

Table 2.3 - Modelling studies relevant to riffle-pool mechanics

2.7 Problem Identification

The central problem to this thesis is the formation of riffle-pools in a gravel-bed river. Gravel-bed rivers are characterized by turbulent flow over a mobile bed. Riffle-pools are the characteristic form of a class of streams delineated by moderate slope ($S < 1.5$ %) and relative roughness values ($y/Y < 0.3$). They are undulations of the bed that are defined by the macro-scale of the form, sorting of sediment by size, and the formation of lateral bars. The similarity of scales across a range of systems suggests that there is a common formative mechanism and that this mechanism is related to the flow. A number of mechanisms have been suggested, but experimental results have been mixed. In general, there is a lack of adequate field data to test the significance of the proposed mechanisms. In addition, more recent research has highlighted the potentially important role of turbulence in sediment transport. Critically, there is a near complete lack of turbulence measurements in natural rivers at high discharge when sediment transport is active. Poor quality has been noted in a number of the key attempts to obtain such data and it is not clear that available instruments are capable of returning reliable signals in the types of flow environments that occur in riffle-pools during high flows. This thesis will test available instruments, address the flow turbulence data gap, and test theories of pool maintenance and formation at a field site.

Field data are limited in their generality due to local conditions and simultaneous interactions between flow, sediment, and morphology that make it difficult to isolate the key mechanisms. Numerical models, while unable to capture local variability, are suitable for testing hypotheses, an attribute that makes them complementary to field studies. It would be useful to be able to model the interactions between turbulent flow, sediment transport, and bed form development in order to test specific feedback mechanisms. Modelling strategies that utilize spatially-averaged steady state solutions are limited in this regard because they are not able to simulate dynamic behaviour. An alternate approach will be utilized in this thesis that models the movement and entrainment conditions around discrete particles. This approach has been utilized in other sedimentary environments may be useful for the investigation of riffle-pool development.

2.8 Objectives

The objectives of this thesis are:

1. To develop a discrete particle model to simulate the flow and sediment dynamics in a gravel-bed river in order to examine the mechanisms that lead to bed form development, demonstrate how feedback mechanisms operating on a local scale can lead to large scale features of the bed, and test the role of turbulence in bed form development;
2. To assess the quality of velocity time series measured in highly turbulent flows using an Acoustic Doppler Velocimeter (ADV) and an Electromagnetic Current Meter (ECM);
3. To characterize the flow, sediment, and morphological dynamics in a forced riffle-pool over a range of flow levels up to the bankfull stage. We measure and describe mean velocity and turbulence intensity distributions, the size and scale of coherent turbulent events, the interrelation between the scaling of coherent turbulent events, bed morphology and discharge, mechanisms of enhanced turbulence production, morphological adjustments in response to floods, the relation between particle size and transport distance, and spatial patterns of sediment entrainment and deposition in relation to the mean and instantaneous shear stresses; and
4. In both the numerical simulations and analysis of the field data, to identify the mechanisms that lead to the formation of riffles and pools in gravel-bed rivers.

2.9 Methodology

The objectives were met in four major steps. In the first step we developed a numerical model based on research contained in this background chapter on river and riffle-pool mechanics. The second step was to develop and test the appropriate field sampling to ensure high quality data and allow us to measure during high flows. The third step was to collect and analyse the field data. The field data allowed some refinement of specific rules in the numerical model and this information was incorporated back into the model in the final step of this thesis.

Model development was the first major step. Criteria for the model emerged from the literature review. In order to have the flexibility to test different factors that may be involved in pool-formation, we designed the model to handle heterogeneous sediment, size selective transport, local feedbacks between particles to emulate hiding and imbrication,

flow separation, flow acceleration, and changes to turbulence intensity associated with flow acceleration. These criteria meant that all modeling approaches using empirical relations developed under conditions of spatially averaged sediment transport were not applicable. A discrete particle model was necessary in order to reduce system dynamics to the process scale. At the current time, the desired model is beyond the capabilities of a fully parameterized physical model. The model was therefore constructed using simplified rules to govern the interaction between the sediment and the flow. This approach borrowed from the interdisciplinary field of complex systems, where local and non-linear effects have been found to lead to the emergence of patterns on a global scale. The model and results are presented in Chapter 3. Results highlight the potential importance of turbulence for the formation of large-scale bed forms. This meant that accurate measurements of instantaneous velocity at a range of discharges in the field campaign were required. The model also encouraged us to examine sediment transport from the perspective of spatially distributed individual grains in order to establish the behavior of discrete sediment particles of various sizes in the study site.

The field campaign of this thesis was reliant on three methods: a safe manner in which to measure turbulence in a riffle-pool during floods, velocity measurements in highly turbulent flows, and a new technique to track sediments. Appropriate strategies and techniques were completed in the second major step of this thesis. Many previous studies in riffle-pools have been limited by practical difficulties during high flows. Working with Echafauds Plus ®, a construction company specializing in scaffolding equipment, we were able to construct a leveled grid of supports above the riffle and pool. This grid allowed us to measure the flow at any point and at any flow level up to bankfull while providing a local coordinate system to quickly position the measurements during floods. The design is detailed in Chapter 5. The characterization of flow hydraulics relies on accurate velocity measurements. There have been few tests of available technologies in highly turbulent flow environments [*Buffin-Bélanger and Roy*, 2005]. Those that attempted to measure in locations such as the ocean surf zone have suffered due to the poor quality of the data [*Rodriguez et al.*, 1999; *Bryan et al.*, 2003]. It was therefore imperative to assess the accuracy of flow measurements. We undertook a comparative test of Electromagnetic Current Meters (ECMs) and Acoustic Doppler Velocimeters (ADV) in a highly turbulent environment. Full analysis and results are detailed in Chapter 4. Surprisingly, despite a

slight reduction of spatial and temporal resolution, the older ECM technology was found to be the most reliable in highly turbulent environments and were used in the rest of our field campaign. The third method was the development of a new sediment tracking technique. We worked with other members of the Canada Research Chair in Fluvial Dynamics at the Université de Montréal to develop the use of Passive Integrated Transponder (PIT) tags for sediment transport research. The initial test of the method has been published [*Lamarre et al.*, 2005] and this article highlights many of the advantages that made it attractive for this thesis. Most importantly, each PIT tag has a unique code. This means that sediment transport data can be associated with details of size, shape, and initial location. Also, the reading is taken remotely so that the bed is not disturbed and sediment movement can be followed over a number of floods. Finally, recovery rates are typically above 85% and because the tags do not require a battery, long term study is possible.

The third major step was the collection of flow, sediment transport, and morphological data at our field sites. We concentrated on a small number of field sites because there is a need for spatially distributed process-scale data on flow turbulence and sediment dynamics in riffle-pools. This data is difficult to obtain and necessitates significant investment of time and money, which precluded a large number of sites. The original design of the project was to compare a forced riffle-pool with a 'free' or autogenetic riffle-pool. In the results presented in this thesis, only the forced pool was retained due to a number of advantages at that site. First, the stream with the forced-pool is smaller, which allowed us to construct a more stable set of platforms from which to sample flow conditions during floods. Second, a series of large floods occurred in the forced pool during the study period. The first of these floods rotated a large tree that controls the location of the pool, an event that effectively reset pool geometry and initiated a period of active pool formation. Field data was used to characterize flow properties at seven discharges including the bankfull discharge. During the bankfull event we were also fortunate because continual rain during the day meant that the water level stayed high throughout the measurement period. Full methodology, analysis, and results of the hydraulic component to the study are detailed in Chapters 5 and 6.

We used two deployment strategies of tagged particles to sample sediment transport. The first strategy was to obtain as much spatial coverage as possible by placing tagged particles of all sizes in all areas of the studied riffle and pool. A pressure transducer

and a meteorological station were installed to allow us to estimate flood levels, which were compared with spatial patterns of sediment entrainment and deposition. This allowed us to characterize sediment dynamics in response to floods of various magnitudes. The second deployment strategy was to place a wide range of particle sizes upstream of the site so that they would feed into the site as part of the sediment supply. From this we could examine path length distributions of particle transport and discuss patterns of deposition in the riffle-pool. The morphology of the pool was surveyed using a total station at frequent intervals through the study period. Erosion and deposition was calculated in order to characterize the morphological response of the forced riffle-pool to floods of various magnitudes. Results on the morphology and sediment dynamics of the site are presented and discussed in Chapter 7.

The final step of this thesis was to use the field results to refine the numerical model. This was an iterative process that continued throughout the study as more field data became available. The best example of this process was the development of the rule for flow separation. Flow separation was not originally included in the model because it is not generally observed in riffle-pools due to the relatively mild lee side angle of the bed form. Flow separation occurs over dunes where the lee side angle is > 10° [*Best and Kostaschuk*, 2002] whereas the angle of the riffle in our study site is closer to 5°. However, during the analysis of the coherent turbulent structure of the flow in chapter 6, it became apparent that intermittent flow separation was playing an important role in turbulence generation near the bed. We then developed a flow separation rule for the model and this appears to be a key mechanism for the stability of the riffle-pool bed form.

2.10 Thesis Statement

The formation of riffle-pools is a geomorphologic puzzle. The key elements of this puzzle are the macro-scale of the bed form, the sorting of sediments by size, and the stability of the form in extreme floods. The central hypothesis of this thesis is that turbulence plays a key role in the formation of riffle-pools. We argue that turbulence and riffle-pools are linked by three key mechanisms. First, the shape of mean velocity profiles is modified by flow acceleration or deceleration. Near the bed, low velocities occur in decelerating flow and fast velocities occur in accelerating flow. Second, intermittent flow separation occurs near the bed in decelerating flow such that large turbulent fluctuations are generated. These fluctuations dominate the transfer of shear stress to the bed in the pool-

head. Third, the turbulent fluctuations appear to preferentially transport the smaller particles. This means that large particles transported into the riffle and pool-head are effectively trapped in this area. We use these three mechanisms to explain the initiation of riffle-pools, their stability, and the requirement of heterogeneous particle sizes.

Liason Paragraph A

Field-based studies of riffles and pools have identified a number of factors that play a role in their formation. These factors operate at a range of spatial and temporal scales and they include sediment size heterogeneity, selective sediment transport, flow turbulence, and flood stage variability. At present, there exists no model that can be used to examine and isolate the effects of these factors and allow for the development a coherent view of riffle-pool formation. The lack of such a model is the result of our incomplete understanding of central processes such as sediment transport and turbulence effects. In addition, modelling approaches have concentrated on equilibrium solutions that do not incorporate feedback effects between particles, flow and bed morphology. In this chapter[1] we present a flexible model that considers a gravel-bed river as a complex system in which simplified local rules describe the sediment and flow dynamics including turbulence. From these rules emerge bed forms of various scales and dynamics. In the model, sediment clasts are represented as discrete elements and space and time are represented explicitly. Using a trimodal sediment distribution, irregular forms that scale with particle diameter develop without explicit feedback mechanisms due to the tendency of large particles to roll along the bed surface and collect into chains. Feedback mechanisms such as imbrication increase the effective entrainment threshold of groups of large particles and increase the stability of these imbricate forms. A second type of bed form is associated with saltating grains, and emerges where particles are transported at a preferred distance. The development and maintenance of larger scale bed forms require feedback between the bed and flow properties. By allowing mean velocity to adjust to bed morphology and considering the effect of acceleration on turbulence generation and mean velocity profiles, we demonstrate the emergence of forms similar in morphology to gravel sheets, dunes, and riffle-pools. In the context of this thesis, the model is used to complement field-based studies because of its suitability for testing hypotheses of streambed behavior. The rules were also refined based on results from the field campaign that comprises the bulk of the thesis.

---

[1] MacVicar, B. J., L. Parrott, A. G. Roy (2006) A 2-D discrete particle model of gravel-bed river systems, *Journal of Geophysical Resesarch*, 111, F03009, doi:10.1029/2005JF000316.

3 A 2-D DISCRETE PARTICLE MODEL OF GRAVEL-BED RIVER SYSTEMS

3.1 Introduction

Malanson [1999] defines complex systems as those characterized by non-linear behavior, with feedbacks that lead to the emergence of global properties from interactions between finer-scaled elements. Gravel-bed rivers fit this system classification, as the interaction between flow and transported sediment particles is characterized by a non-linear relation [*Gomez and Church*, 1989], and the development of bed forms is a feedback mechanism that alters the sediment transport regime [*Laronne and Carson*, 1976; *Hassan and Reid*, 1990] and the surrounding turbulent environment [*Clifford*, 1996; *Buffin-Bélanger and Roy*, 1998]. Established techniques for modeling river morphology include regime [*Yang*, 1976; *Chang*, 1979] and stability analyses [*Smith, 1970*; *Colombini et al.*, 1987; *Seminara et al.*, 1996]. These approaches necessarily remove the spatial and historical context of river behavior and are limited to the prediction of equilibrium and statistically averaged states. As argued by *Lane and Richards* [1997], observed non-linear behavior in river systems implies sensitivity to initial conditions and local-scale processes. Examined closely, river systems are frequently unstable, with statistical equilibrium masking the dynamic behavior [*Furbish*, 1991; *Murray and Paola*, 1994]. In this article we present a new model for the analysis of flow and sediment dynamics in a gravel-bed river that treats the river as a complex system.

Complex systems research is a rapidly developing cross-disciplinary field, within which new approaches have been developed for the study of system behavior. One such approach is the individual-based model [*Judson*, 1994], already applied successfully to such varied problems as the study of social insects [*Theraulaz et al.*, 2003], World Wide Web access efficiency [*Guha and Wang*, 2002], ecosystem population dynamics [*Parrott and Kok*, 2001], and the workings of the brain [*Soucek*, 2001]. The common principles behind the respective models are that the systems are represented by discrete elements, be they insects, people, plants, or neural agents etc., and that global behavior is allowed to emerge from local interactions of the discrete elements. Systems modeled with individual-based models have been shown to exhibit a richness of non-linear behaviors, including

evolution and chaos [*Wolfram*, 1984]. This capacity is possible because of the explicit representation of space and time.

In fluvial geomorphology, a number of researchers have investigated the transport of individual sediment grains, both in laboratory environments [*Abbott and Francis*, 1977; *Sekine and Kikkawa*, 1992; *Nino et al.*, 1994], and in natural rivers [*Laronne and Carson*, 1976; *Hassan and Church*, 1992; *Habersack* 2001]. This research has allowed the development of a number of discrete particle sediment transport models (Table 3.1). Two approaches for the development of discrete particle models exist. Mechanistic models apply mathematically detailed physical descriptions of sediment transport in two [*Naden*, 1987; *Jiang and Haff*, 1993] and three dimensions [*McEwan et al.*, 2000; *Drake and Calantoni*, 2001; *Schmeeckle and Nelson*, 2003]. However, continued uncertainty in the calculation of lift forces, the resolution of collisions between moving grains, the feedback effects of developing bed forms, and the inclusion of turbulence restrict these models from being applied to investigate bed form development. *McEwan et al.* [2000] suggest that, for the foreseeable future at least, abstraction is necessary for the problem.

Author	Type	Matrix Length (grains)	Flow	Entrainment	Particle Interactions	Turbulence	Bed forms (length in grains)
Naden [1987]	mechanistic 2D (profile)	1000	normally distributed	flow drag and lift	friction angle	not considered	clusters (6-15)
Jiang and Haff [1993]	mechanistic 2D (profile)	100	slab model	flow drag	equations of motion	not considered	none
Tribe and Church [1999]	hierarchical 2D (plan)	200	none	monte carlo	neighbour rule	not considered	transverse (~30)
McEwan et al. [2000]	mechanistic 3D	not given	steady, uniform	flow drag	equations of motion	not considered	none
Drake and Calantoni [2001]	mechanistic 3D	15	slab model	flow drag	equations of motion	not considered	none
Malmaeus and Hassan [2002]	hierarchical 2D (plan)	200	none	monte carlo	resistance fields	not considered	transverse, clusters (~30)
Schmeeckle and Nelson [2003]	mechanistic 3D	40	measured time series	flow drag	equations of motion	not considered	none

Table 3.1 - Discrete particle models in fluvial environments

The use of abstraction requires the deduction of a set of qualitative or semi-quantitative rules from observed system interactions, producing what are alternatively called "hierarchical" [*Werner*, 1999], "exploratory" [*Murray*, 2003], or "toy" models [*Tufillaro*, 1993]. This simplified approach offers two main advantages. First, it is possible to represent "fast-scale" processes such as sediment transport, whose precise physical formulation remains elusive, in order to investigate "slow-scale" processes such as bed form development [*Werner*, 1999]. For example, the effect of imbrication on sediment transport is relatively difficult to parameterize in physical terms, yet a simplified rule can be readily developed based on visual observations and field-experiments. The second advantage is simplicity itself. Because extraneous dynamics are minimized, hierarchical models produce clear demonstrations of system behavior [*Murray*, 2003], which allows hypotheses to be tested [*Werner*, 1999].

Hierarchical models of sedimentary environments have been applied to simulate the development of stone cells [*Anhert*, 1994]; squares, hexagons and other shapes in shake table simulations [*Shinbrot*, 1997]; stone rings and stripes on frozen ground [*Kessler and Werner*, 2003]; and eolian sand ripples and dunes [*Anderson*, 1990; *Anderson and Bunas*, 1993; *Landry and Werner*, 1994; *Werner* 1995; *Momiji et al.*, 2000; *Nino et al.*, 2002; *Baas*, 2002]. In fluvial environments, two models have been used to simulate transverse cobble ribs in rivers [*Tribe and Church*, 1999; *Malmaeus and Hassan*, 2002], details of which are also included in Table 3.1. In spite of strong evidence of feedback between the bed and hydraulic parameters such as flow turbulence [*Nelson et al.*, 1995; *Buffin-Bélanger and Roy*, 1998; *Thompson et al.*, 1998; *Best*, 2005], there is no model that considers these effects. The objective of this article is to present a flexible model of river processes in which a gravel-bed river is considered as a complex hierarchical system. We demonstrate that simple rules governing flow and sediment dynamics can lead to the emergence of commonly observed bed form types.

3.2 Gravel bed forms

Gravel bed forms represent a considerable challenge for modeling. Many feedback mechanisms are active between flow, sediment transport, and bed forms [*Leeder*, 1983], such as imbrication [*Hassan and Reid*, 1990; *Sear*, 1996], changes to mean velocity [*Best*, 2005; *Keller*, 1971], and turbulence generation [*Nelson et al.*, 1993; *Wohl and Thompson*, 2000]. Sediment and flow dynamics are sensitive to flow stage [*Jackson and Beschta*,

1982; *Warburton*, 1992; *Ryan et al.*, 2002], particle size distributions [*Wilcock and McArdell*, 1997; *Lisle et al.*, 2000], and slope [*Wohl et al.*, 1993, *Montgomery and Buffington*, 1997; *Thompson and Hoffman*, 2001]. Many different bed forms have been identified in gravel-bed rivers including pebble clusters, bed load sheets, dunes, bars, and pool-riffle sequences (Table 3.2). In this study we consider the longitudinal profile of a river and will not discuss forms such as transverse ribs, stone cells, and stone stripes, which require explicit representation of the lateral dimension. Similarly, forms with forcing mechanisms such as woody debris and bedrock controls, and bed forms on steep slopes with rapidly varying plunging flow such as step-pools and cascades are beyond the scope of this work. Simulation results will be compared to natural bed forms on the basis of three characteristics: (i) the length scale that determines the size and frequency of the form, be it the sediment size (d), flow depth (y), or channel width (Z); (ii) the dominant sediment sorting pattern, predominantly identified by the behavior of the largest sediment fraction; and (iii) the nature of the bulk movement of the bed form.

Type	Reference	Scale	Sorting	Bulk Movement
Pebble clusters	*Hassan and Reid* [1990]	$\propto d$	dominated by large	by individual particles
Gravelsheets	*Whiting et al.* [1988]	$\propto d$	large in front	downstream
Dunes	*Dinehart* [1992]	$\propto y$	variable	downstream
Bars	*Church and Jones* [1982]	$\propto Z$	variable	downstream
Riffle-pools	*Sear* [1996]	$\propto Z$	large on lee slope	stable

Table 3.2 - Gravel bed forms

3.3 Model Description

3.3.1 Conceptual Approach

We developed the model ROQ-B (les ROches Qui Bougent - translation: Rocks That Move) using the software Matlab (©Mathworks Inc.). In terms of existing models, the approach is most similar to that of *Naden* [1987], as a two-dimensional vertical matrix oriented longitudinally along the centerline of a channel represents the riverbed, and sediment particles are represented as discrete clasts of varying size within the matrix. The interaction of flow and sediment in Naden's model, however, is controlled by a set of empirical equations that determine the calculation of velocity profiles, erosion thresholds, particle trajectories, etc. Feedbacks are limited and bed forms develop only on small scales. To allow its application to a wide range of stream types and flow conditions, we

designed ROQ-B as a hierarchical model, with simplified rules for entrainment and transport that increased its flexibility in heterogeneous environments.

A central algorithm determines the interaction between flow and sediment in the model (Figure 3.1). The entrainment of a particle and its mode of transport at a given time are determined by comparing a randomly sampled value from the appropriate flow velocity distribution to the entrainment and movement mode thresholds. A grain will move when this instantaneous velocity is greater than its entrainment threshold, and the degree to which the entrainment threshold is exceeded determines the type of movement. We used near-bed velocity because it determines the local shear stress [*Wilcock*, 1996] and drag forces on the particle [*Schmeeckle and Nelson*, 2003]. Experimental results in turbulent flows demonstrated the importance of the instantaneous flow velocity on sediment transport [*Nelson et al.*, 1995; *Sumer et al.*, 2003]. In uniform flow, instantaneous flow velocities tend to follow a normal probability density function [*Naden*, 1987]. Transport modes are rolling (↻) (equivalent to sliding in modeling terms) and saltation (↗). Transport mode thresholds increase with particle size [*Drake et al.*, 1988]. Unlike what is observed in eolian transport, saltating grains do not dislodge bed grains upon collision [*Nino et al.*, 1994]. Particles move individually in partial transport, which is considered to be the dominant mode of transport in gravel-bed rivers [*Andrews*, 1994; *Church and Hassan*, 2002].

Feedback rules allow the relation between velocity and particle movement to vary in time and space. Two types of feedback are possible: particle feedback, which alters the entrainment and transport mode thresholds by considering the effects of hiding and imbrication; and flow feedback, which alters the velocity distributions by considering the effect of changes in mean velocity on turbulence generation. Figure 3.2 is a conceptual diagram of the feedback mechanisms simulated in this model. The computer code of the model is available from the corresponding author on request. The following sections detail model algorithms and operation.

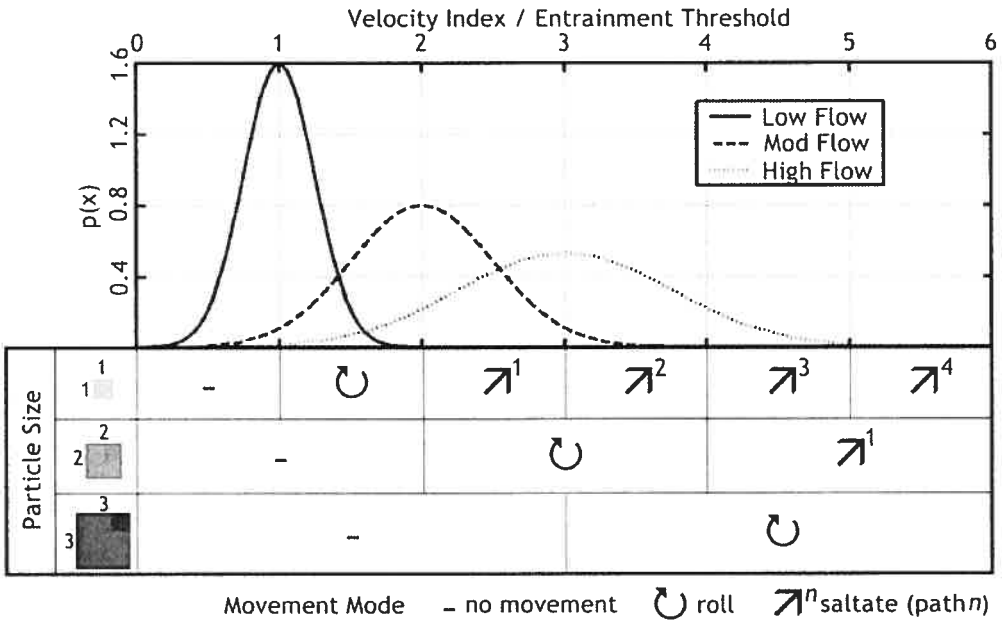

Figure 3.1 - Relation of velocity probability distributions to movement mode thresholds at three flow stages for three particle sizes. This figure represents equations 3.1 and 3.2 when feedback rules are inactive. Saltation paths are shown in Figure 3.5 Medium and large particles have a 'handle' on the upper right corner, and this handle is darkened slightly to aid the distinction of individual particles.

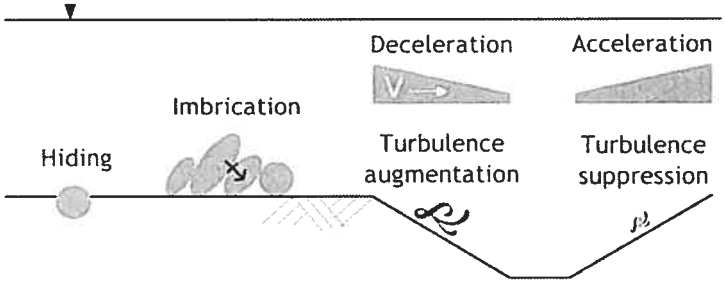

Figure 3.2 - Schematic diagram of modeled flow and particle feedback mechanisms.

3.3.2 Initial Conditions

3.3.2.1 Simulation Matrix

Three parameters are required to specify the initial bed: the bed slope, the size of the simulation matrix, and the particle size distribution. The initial bed surface varies by ± 1 grid square around the specified slope for initial roughness. The bed is constructed by filling the matrix to the surface with randomly placed particles according to the size distribution. In the simulations presented here, initial parameters were specified to mimic natural river systems in which lateral meandering is not dominant and macro-scale features such as pools, riffles and bars are commonly found. A bed slope of 1% was chosen

because it is a common value for pool-riffle streams [*Montgomery and Buffington*, 1997]. A large simulation matrix of 10,000 by 250 grid squares was used to allow bed forms to develop at a scale much greater than the size of individual particles. Three particle sizes were used to represent heterogeneous sediment. Small, medium and large particles occupy 1 (1x1), 4 (2x2), and 9 (3x3) grid squares, respectively, at proportions of 20, 60, and 20%. Initial parameters are summarized in Table 3.3 and the default matrix is shown in Figure 3.3. Initial parameter values were tested in sensitivity simulations.

Parameter	Role	Range	Default values	Sensitivity test values
Matrix length	sets overall size of matrix in grid squares	> 100	10 000	7 500, 12 500
Bed slope (S)	sets initial surface slope	> 0	0.01	0.005, 0.015
Particle size distribution	sets proportions of each particle size by % [small/medium/large]	[100/0/0] - [0/0/100]	[20/60/20]	[10/60/30], [30/60/10]
Hydrograph	controls duration of simulation and sequence of flood stages	any hydrograph	6 'pyramids' (Figure 3.4)	6 'falling', 6 'rising' [a]

a – Hydrographs are sawtooth patterns composed of floods either rising or falling from stage 1 to 3 or from 3 to 1 for each floods of 500 time intervals.

Table 3.3 - Initial Parameters

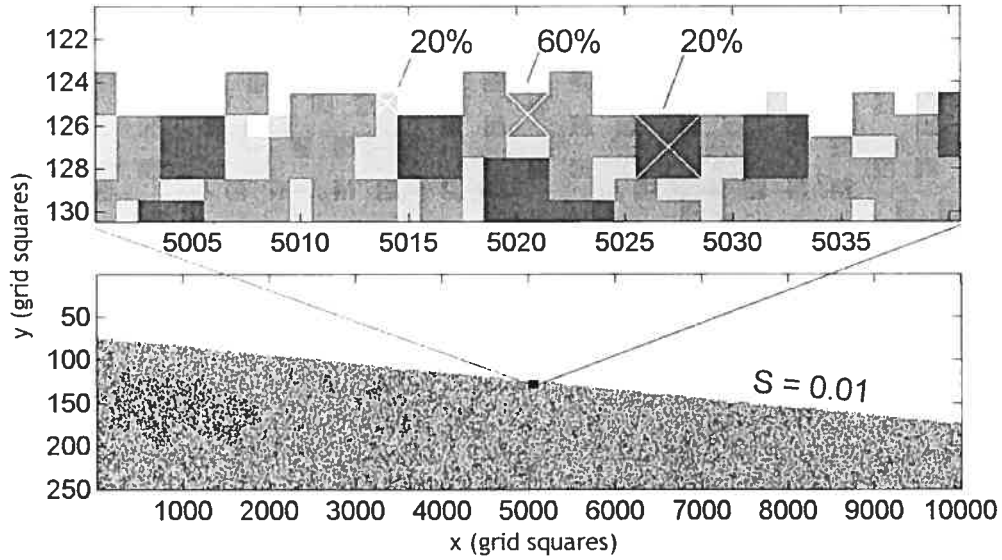

Figure 3.3 - Initial simulation matrix showing default matrix dimensions, particle size distribution (percentages of each size class indicated by *Í*), and bed slope (*S*). Flow is from left to right.

3.3.2.2 Flow Stage

Flow variables are calculated at each time interval from the flow stage (q). For ease of calculation, q is represented numerically in the model but is conceptually similar manner

to the classification of hurricanes on an arbitrary scale because it does not represent a measurable parameter. For these simulations, three flow stages were used to allow gravel transport in three phases [*Jackson and Beschta*, 1982; *Warburton*, 1992; *Ryan et al.*, 2002] and the flow hydrograph consisted of a series of six floods with symmetrical rising and falling limbs and had a total duration of 3000 time intervals (Figure 3.4). When feedback rules were inactive, small particles had a 50% chance of moving at low flow, for the most part by rolling, while large particles were unlikely to move (Figure 3.1). At high flow, small particles had a high probability of entrainment and moved by rolling and saltation, while large particles had a 50% probability of moving and moved almost exclusively by rolling. The effect of the shape of the hydrograph was tested in sensitivity simulations (Table 3.3).

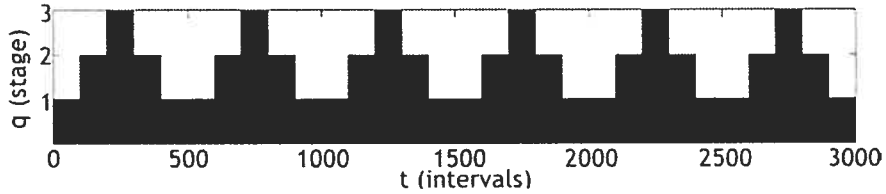

Figure 3.4 - Default hydrograph showing six pyramid-shape floods.

3.3.3 Model Algorithms

3.3.3.1 Particle Entrainment and Movement

The entrainment threshold of a particle (E) is calculated by adding the effects of hiding (H) and imbrication (I) to that of particle size (d):

$$E = d+H+I \tag{3.1}$$

When particle feedback rules are inactive ($H=I=0$), the threshold is a simple function of d. A given particle will be entrained when the local instantaneous velocity (v) exceeds the entrainment threshold ($v \geq E$). Velocities and entrainment thresholds are non-dimensionalized using the size of the grid so that $v=1$ is the velocity at which a particle that is one grid cell in diameter is entrained. The transport mode (M) is calculated as follows:

$$M = \left(\frac{v-E}{d}\right) + 1 \tag{3.2}$$

where M {<1, 1, 2, 3, 4...} = {no movement,↻, ↗, ↗^{2}, ↗^{3}...}. This equation has the structure of an entrainment function, as the shear stress (here represented by the excess

velocity) is in the numerator and the particle diameter is in the denominator. The exponent on the saltation icon refers to saltation trajectories (Figure 3.5). The trajectories rise at a steep angle to the horizontal, and then fall at a gentler angle to mimic the motion of saltating gravel sediment [*Nino et al.*, 1994]. Rolling particles translate horizontally within the matrix until blocked by a downstream particle. When not supported from below, rolling particles fall at an angle of 45° until making contact with the bed surface.

Three rules governing deposition are necessary to produce physically realistic bed surfaces. First, saltating particles roll after making contact with the bed. This prevents the development of unrealistic stacks of sediment particles. Second, off-balance particles topple into surface depressions. This ensures that large and medium sized particles are supported by at least two occupied grid squares when they come to rest. Third, a particle that comes to rest at the edge of a vertical drop greater than its diameter moves to the base of the drop. This prevents the formation of depositional slopes at unrealistic angles of repose but does not affect steep slopes that form as a result of erosion.

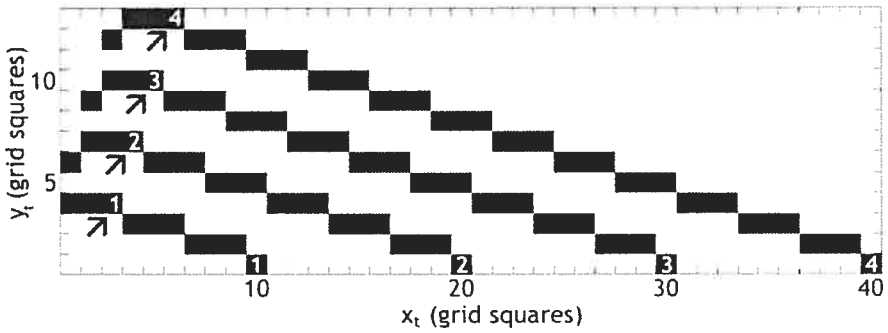

Figure 3.5 Saltation paths for $\nearrow^1$ - $\nearrow^4$. The paths are those followed, from left to right, by the particle handle (the upper right corner of medium and large particles). The occupation of a grid square in the path of any part of the particle will terminate saltation and induce deposition.

3.3.3.2 Particle Hiding

Sediment particles partially or completely buried within the bed are hidden from the full forces of the flow and held in place by increased friction angles according to their pocket geometries [*Andrews*, 1994]. Particles at or below the local bed surface will therefore be transported less easily than those exposed on a flat surface. This effect is modeled by increasing entrainment thresholds as a function of the burial depth (y_b):

$$H = k_H\, y_b \tag{3.3}$$

where k_H is the hiding rule control parameter with default and test values as listed in Table 3.4. If the upstream burial depth is not equal to that downstream, the minimum burial depth is used. Examples demonstrating how y_b is specified are shown in Figure 3.6.

Parameter	Role	Range	Default values	Test values
k_V	mean velocity	> 0	1 (2[a])	[1.0[b], 2.0]
k_H	particle hiding rule	≥ 0	0	[0.5, 1.0, 2.0, 3.0[b]]
k_I	particle imbrication rule	0 - 1	0	[0.4, 0.6[b], 0.8, 1.0]
k_T	flow turbulence rule	≥ 0	0 (5[c])	[1, 2, 3[b], 5]
k_A	flow acceleration rule	0 - 1	0	[0.0001, 0.0004[b],0.001, 0.01]

Note a value used to test hiding and imbrication rules

b values selected for variability, sensitivity simulations, roughness calculations, and pool dimension versus time plots.

c value used to test acceleration rule

Table 3.4 - Control parameters

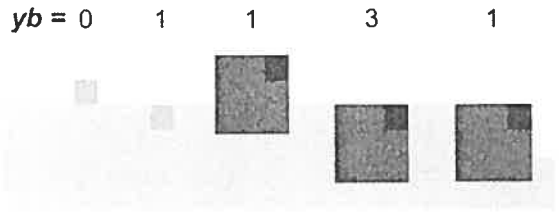

Figure 3.6 - Five examples, two for small particles (1x1) and three for large particles (3x3), showing the calculation of burial depth (y_b) for determination of hiding factor. Particles are shaded as for Figure 3.1.

3.3.3.3 Particle Imbrication

In gravel-bed rivers, large particles have a structuring influence on the bed. Whether because they tend to be less spherical than small particles [*Hirsch and Abrahams*, 1981], or because they typically maintain contact with the bed during transport [*Laronne and Carson*, 1976], large particles tend to form imbricate structures such as pebble clusters, transverse ribs [*de Jong and Ergenzinger*, 1995], and stone cells [*Church et al.*, 1998]. These structures impart stability to their members by increasing their effective weight [*Clifford and Richards*, 1992].

The effect of imbrication was added to the model by increasing the entrainment threshold of large particles in contact with other large particles. The imbrication factor is calculated as a function of all the members in an unbroken chain of large particles:

$$I = d\sum_{i=m}^{n} k_I^{|i|} \qquad (3.4)$$

where k_I is the imbrication rule control parameter, m is the number of particles upstream in the chain, and n is the number of particles downstream in the chain. k_I controls the proportion of a particle's weight that is transmitted to neighboring particles. Figure 3.7 shows an example of how the imbrication rule is implemented.

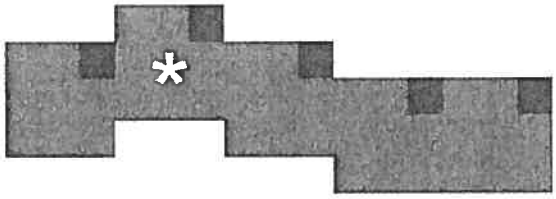

Figure 3.7 - Calculation of imbrication. For particle indicated by *, particles in chain upstream (m) = 1 and particles downstream in chain (n) = 3. Using Equation 3.4 and k_I = 0.5: I = $3(0.5 + 0.5 + 0.5^2 + 0.5^3) = 4.125$

3.3.3.4 Local Instantaneous Velocity

The local instantaneous velocity is determined by randomly sampling one value from a normal probability distribution defined by the mean and standard deviation [V, σ]. The mean velocity at any location is calculated as a function of the velocity immediately upstream (V_{x-1}) and the acceleration factor (A), where the initial velocity at the upstream end of the matrix (V_0) is a function of a control parameter (k_V) and the flow stage (q):

$$V = V_{x-1} + A \text{; where } V_0 = k_V q \qquad (3.5)$$

The velocity standard deviation is a function of V and the turbulence factor (T):

$$\sigma = \frac{V}{4} + T \qquad (3.6)$$

When feedback rules are inactive (A=T=0), V and σ are constant in space and time. As a note, we also tested the denominator of the standard deviation function as a control parameter, but the simulations presented here use a constant value.

3.3.3.5 Turbulence

When considering the development of bed forms, *Bagnold* [1980] reasoned that bed irregularities produce flow turbulence at a local scale, which necessarily leads to a release of kinetic energy in the form of excess turbulence, inducing further scour. Measurements over bed forms have confirmed the link between morphology and turbulence in pool-heads [*Clifford*, 1996; *Wohl and Thompson*, 2000], in laboratory studies of pools [*Thompson et al.*, 1998; *Thompson*, 2004], and downstream of pebble clusters and dunes [*Nelson et al.*,

1993; *Buffin-Bélanger and Roy*, 1998; *Best*, 2005]. We included this phenomenon via a rule that increases turbulence when the local depth is greater than the normal depth. This requires the estimation of flow variables that include local depth and backwater effects. The normal depth (y_n) is calculated as a multiple of flow stage:

$$y_n=10q \tag{3.7}$$

Control points are then identified as the topographical high points on the streambed (Figure 3.8a). At low and medium discharges, water pools upstream of control points and the local water surface is flat. At high flows we assumed that the water surface slope will tend to equalize throughout the river [*Richards*, 1976], but that large bed forms will continue to function as control points [*Walker et al.*, 2004], and the minimum water surface slope is fixed at one half the initial bed slope. Based on continuity, the local depth averaged velocity (V_{DA}) is calculated using a ratio between the normal and the local depth (y_d):

$$V_{DA}=V\frac{y_n}{y_d} \tag{3.8}$$

The turbulence factor is a function of the control parameter (k_T) and the difference between the mean and the depth-averaged velocity:

$$T=k_T\left(V-V_{DA}\right) \tag{3.9}$$

Figure 3.8b demonstrates the effect of the turbulence rule on flow parameters and samples from the local velocity distributions are shown in Figure 3.8d.

3.3.3.6 Flow Acceleration

Applied in isolation, the turbulence rule can produce physically unrealistic effects when bed forms are large because the mean flow velocity remains constant. We developed an acceleration rule to allow the mean velocity to increase or decrease as a function of the difference between the depth-averaged and upstream velocities. A parameter (k_A) controls the rate at which the mean velocity adjusts towards the depth-averaged velocity:

$$A=k_A\left(V_{DA}-V_{x-1}\right) \tag{3.10}$$

Controlled flume studies [*Kironoto and Graf*, 1995; *Song and Chiew*, 2001] have demonstrated that the standard deviation of the streamwise velocity component increases

during flow deceleration but decreases during acceleration. This effect is achieved by activating the turbulence and acceleration feedback rules (Figure 3.8c-d).

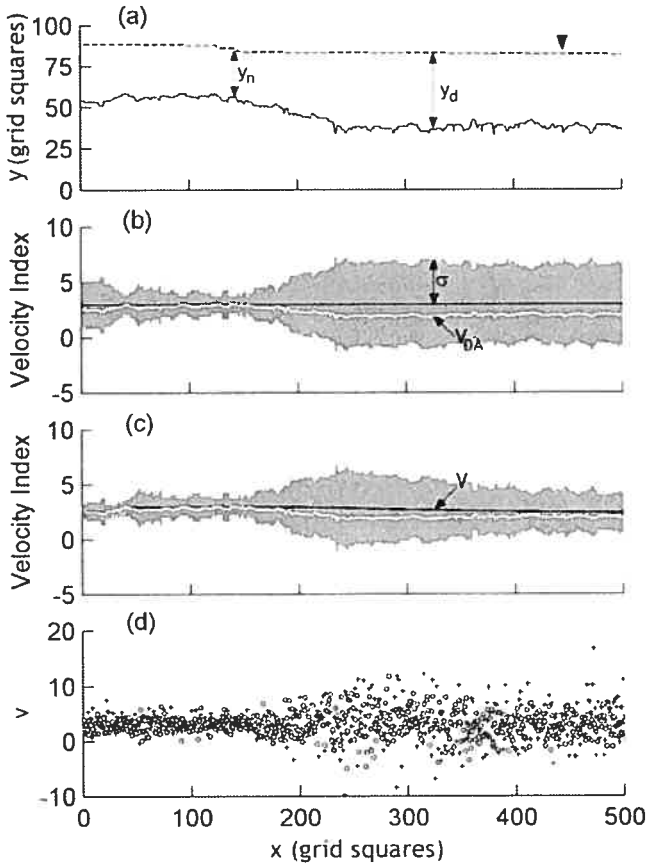

Figure 3.8 - Example to demonstrate flow feedback rule calculations. (a) dashed line - water surface; solid line - bed surface; (b) turbulence rule with control parameter (k_T) = 3.0 (black line - mean velocity V; white line - depth averaged velocity V_{DA}; grey bars - standard deviation σ); (c) acceleration rule with control parameter (k_A) = 0.003, and k_T = 3.0; and (d) instantaneous velocity samples; (+ turbulence rule; " acceleration rule).

3.3.4 Summary of Model Execution

Model execution is represented schematically in Figure 3.9. Required inputs are the initial bed parameters and a flow hydrograph (Table 3.3). Control parameters and their roles as described in the previous sections are summarized in Table 3.4. Without feedback rules, entrainment thresholds are a function of particle size, and instantaneous water velocities are sampled from a probability density function, which is a function solely of flow stage. The activation of control parameters initiates feedback mechanisms whereby bed configuration is also considered when entrainment thresholds and water velocities are calculated. For each particle where the local instantaneous velocity exceeds the entrainment threshold, the type and distance of movement is calculated. Particles are

moved and deposited, one at a time, starting from the downstream end of the matrix. Particles that move out of the matrix are dropped randomly in a 50 grid square sediment feed section at the upper end of the matrix in a manner similar to a flume with recirculating sediment. Calculations are repeated for each time interval. Analysis is based on the section from x = 1000-9000 grid squares to avoid edge effects.

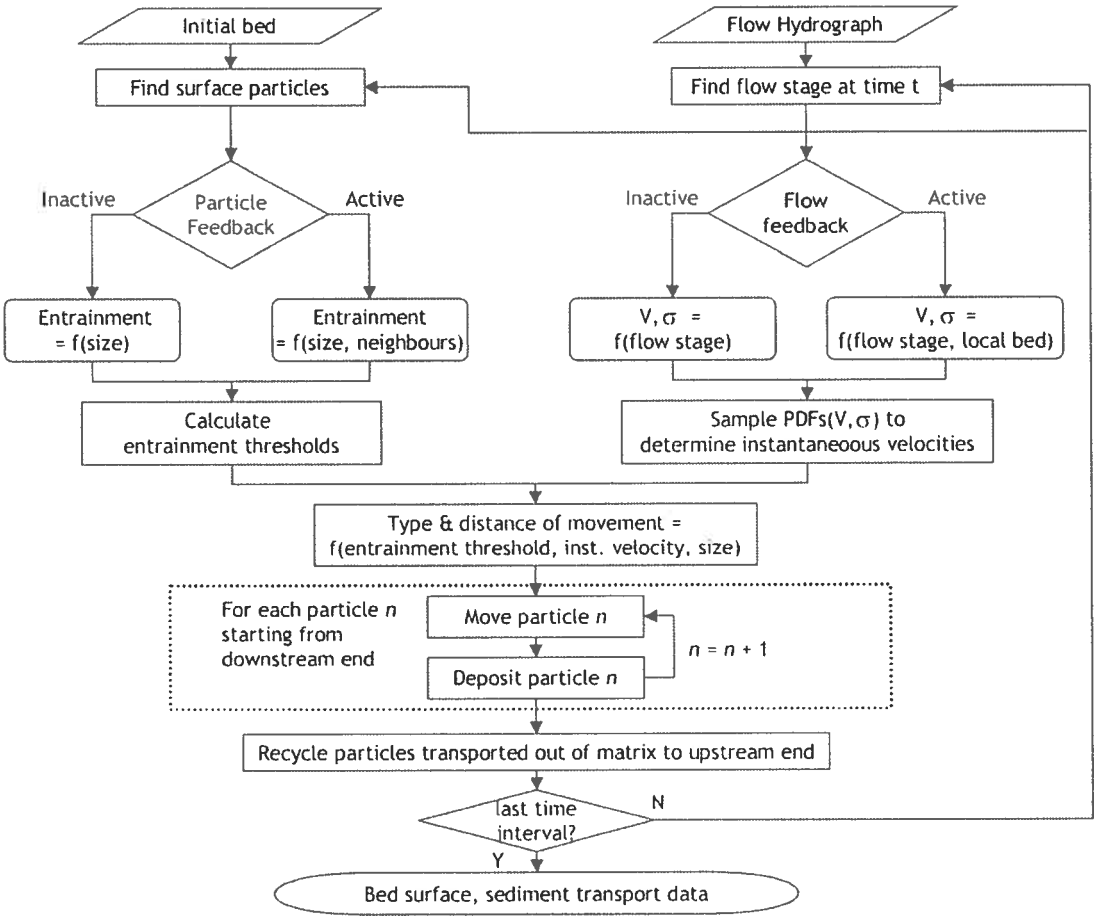

Figure 3.9 - Flow chart of model execution.

3.4 Model Simulations

We present four sets of simulations:

1. Basic model simulations - to ensure proper model function and serve as a control for simulations in which feedback rules were active. We varied the mean velocity control parameter (k_l values are listed in Table 3.4), and set all other control parameters to 0.
2. Feedback simulations - to test the effects of the hiding, imbrication, turbulence, and acceleration rules. We varied the control parameters one at

a time, with the exception of the acceleration rule, which requires the activation of the turbulence rule (values are listed in Table 3.4).

3. Variability simulations - to estimate the error associated with random variability in results. Six repetitions of one simulation case from each from the basic model and four feedback simulation series (selected cases are given in Table 3.4).
4. Sensitivity simulations - to test the sensitivity of results to initial parameters of bed slope, matrix length, particle size distribution and hydrograph shape. We tested each the sensitivity of each parameter (values are listed in Table 3.3) for each of the cases for which variability was assessed (selected cases are given in Table 3.4).

3.5 Results

3.5.1 Space-Time Plots

Space-time plots are grayscale images that show the evolution of bed surface elevations during a simulation run (Figure 3.10). For both cases of the basic model simulations, bed forms are small with no dominant periodicity. In Figure 3.10a, strong vertical lines are notable, meaning that bed forms do not translate up or downstream, and some forms remain through several floods (e.g. the accumulation indicated by a white vertical line at $x = 6000$). Periods of high flows are clearly distinguished by changes in the bed surface, which indicates that particles are frequently entrained. In the second case (Figure 3.10b), the mean velocity and standard deviation are doubled at all flood stages. This change results in frequent entrainment during high and moderate flows, but still no significant bed forms develop.

The hiding rule simulations (Figure 3.11) use mean velocity control parameter $k_{U^*} = 2$. We present these simulations instead of those where $k_{U^*} = 1$ because hiding reduces entrainment frequency and results are sensitive to the rule when initial transport rates are high. As shown by comparing Figures 3.11a-b with Figure 3.10b, the hiding rule has little impact when $k_H \leq 1.0$. When $k_H \geq 2.0$, however, occasional forms are present at low and moderate flows, as shown in Figures 3.10c-d. The forms do not translate upstream or downstream and are occasionally stable through multiple floods, as shown by a dark vertical line in Figure 3.11c from $t = 1250$ to 2750 at $x = 8000$. Another bed form in Figure

3.11d from $x = 5000$ to 6000 increases in magnitude through the last three flood peaks (t = 1500 - 3000).

Using a similar rationale to that for the hiding rule, we also set $k_{I'} = 2$ for the imbrication rule simulations (Figure 3.12). No bed forms are clearly distinguished in Figure 3.12a when the control parameter k_I is small, and the space-time plot is similar to the basic model simulation shown in Figure 3.10b. When k_I is increased, moderately sized bed forms develop (Figure 3.12b). The forms do not translate upstream or downstream. They appear and are washed out during periods of high flows, although some remain stable through multiple floods (e.g. at $x = 4600$ from $t = 1750$ to 2750). Stable, regularly spaced structures appear for large values of k_I, as shown in Figures 3.12c-d. These forms are often discernable after the first high flows. The most prominent structures grow with time, as shown by the dark area in Figure 3.12c at $x = 6600$ from $t = 750$ to 3000.

We set $k_{I'} = 1$ for the turbulence rule simulations (Figure 3.13, compare with Figure 3.10a). Contrary to the hiding and imbrication rules, the turbulence rule selectively increases sediment transport, and simulations are more sensitive when initial transport rates are low. Large bed forms develop when the rule is activated. Bed forms increase in magnitude through the flood sequence for all simulations, as shown in Figure 3.13a from t = 1250 to 3000 at $x = 8000$; and in Figure 3.13d from $t = 250$ to 3000 at $x = 5500$. When the control parameter k_T is large (Figures 3.13c-d), bed features develop into prominent waves. The waves translate upstream, competing with each other such that large forms increase in magnitude at the expense of smaller forms, increasing the overall wavelength. An example of this type of competition is shown in Figure 3.13d where two small forms between $x = 5500$ to 6500 at $t = 1000$ are washed out in favor of two large forms at x = 5000 and 7000 at $t = 3000$. Bed form spacing is not consistent. Figure 3.13c shows six dominant forms at $t = 3000$ more or less evenly spaced over the length of the matrix, while Figure 3.13d shows only three dominant forms and all three occur from $x = 4000$ to 7000.

Following a similar rationale as that for the turbulence rule, we set $k_{I'} = 1$ for the acceleration rule simulations (Figure 3.14). As the acceleration rule modifies the turbulence rule, a value for k_T was also required. We set $k_T = 5$ because the acceleration rule selectively reduces velocity standard deviations and results are more sensitive when initial transport rates are high. The acceleration rule produces forms that are similar to the turbulence rule forms, except that the dominant wavelength appears to be more consistent.

The wavelength decreases as k_d is increased and the forms translate upstream. New forms sometimes emerge after three to four floods from initially inconspicuous surface deviations (e.g. Figure 3.14c at $x = 4000$ from $t = 1750$ to 3000). In Figure 3.14d, the mean velocity closely follows the depth-averaged velocity and bed forms are small, irregular, and transient.

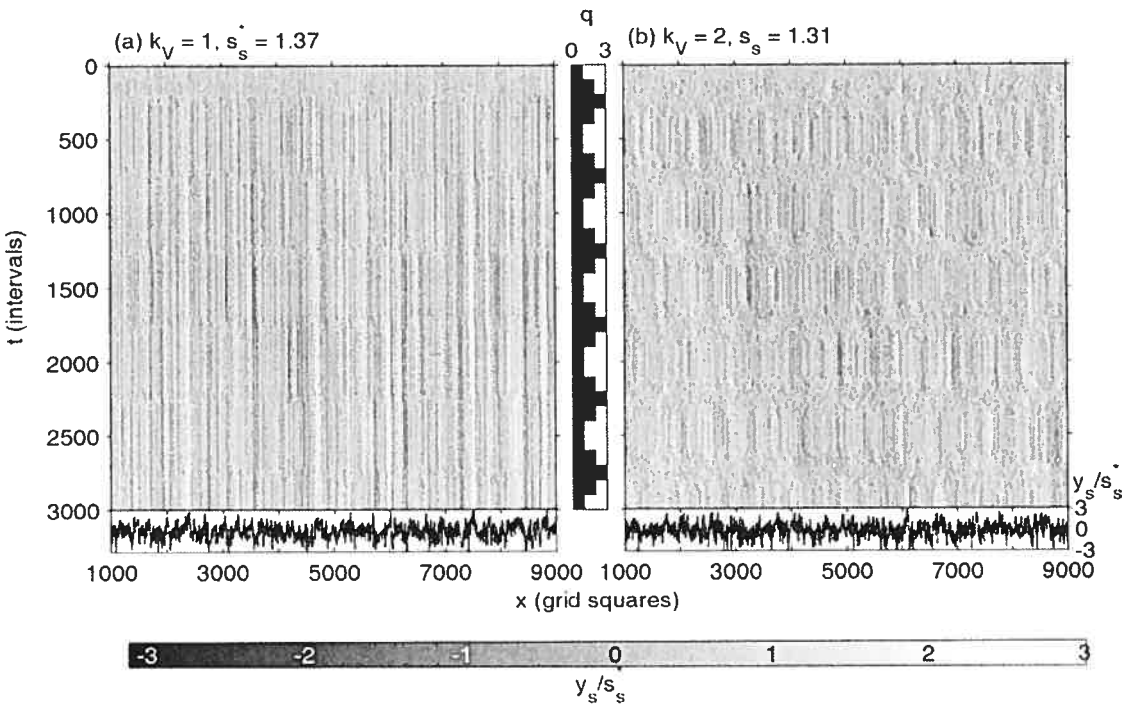

Figure 3.10 - Space-time plots of bed surface elevations for basic model simulations. Bed surface elevations have been normalized by removing the mean slope and dividing by the largest standard deviation of the final bed surfaces in the series (y_s/s_s*). Accumulations of particles above the mean slope appear white, while pools are dark. Final surface profiles are included for each simulation run to aid interpretation of the graphics. Flow direction is from left to right.

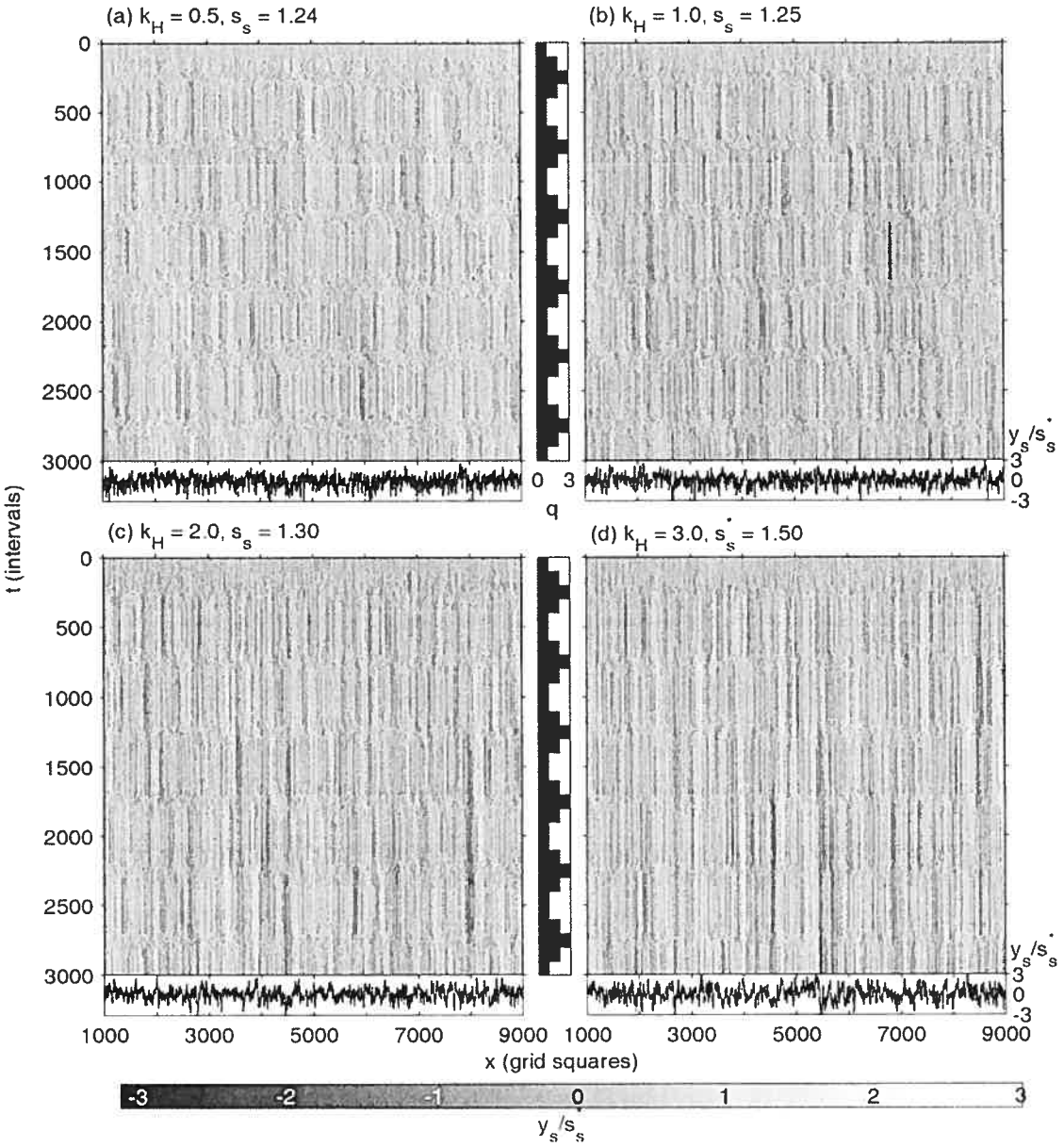

Figure 3.11 - Space-time plots of y_s/s_s^* for hiding rule simulations. See caption of Figure 3.10 for more detailed explanation.

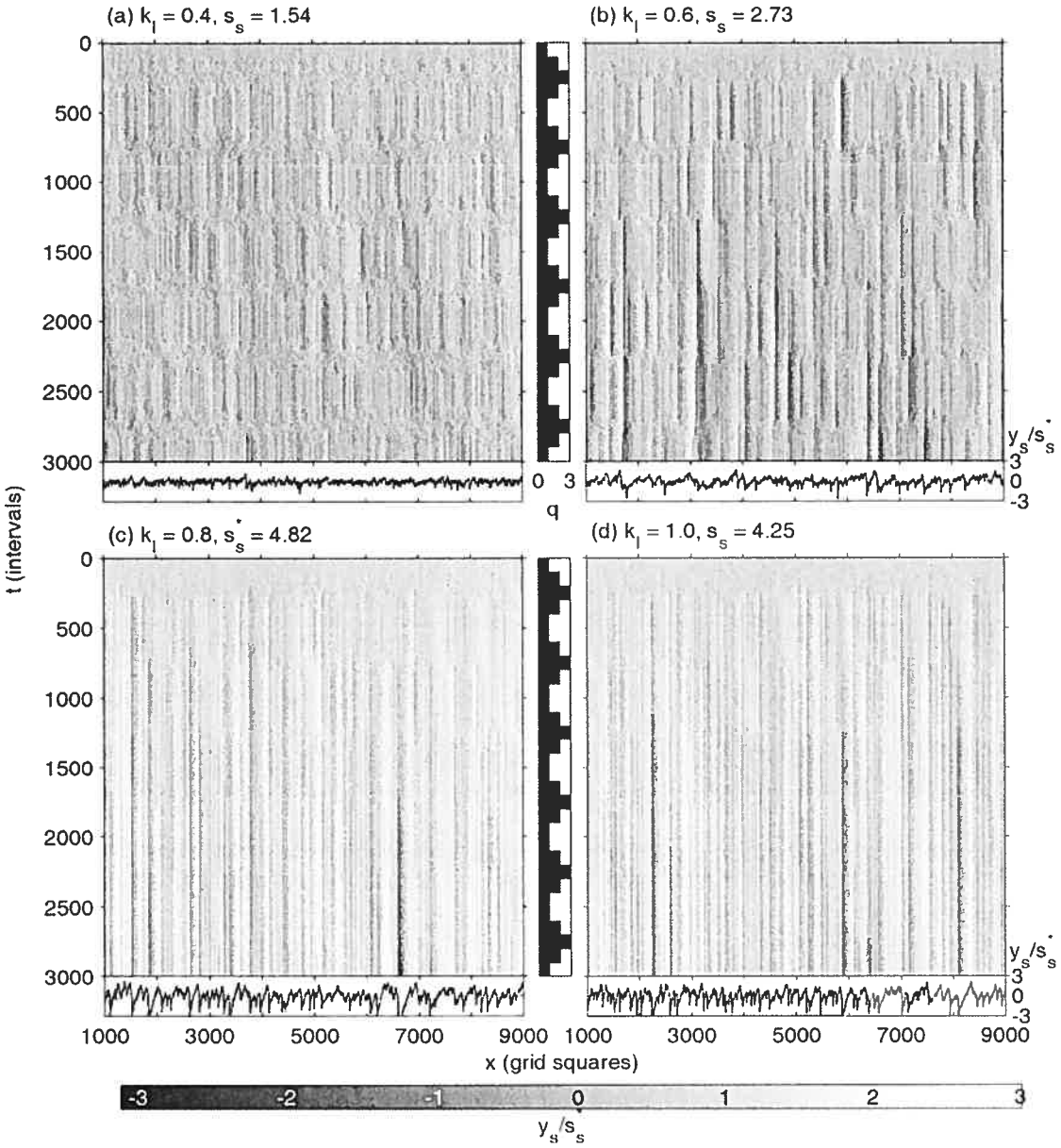

Figure 3.12 - Space-time plots of y_s/s_s^* for imbrication rule simulations. See caption of Figure 3.10 for more detailed explanation.

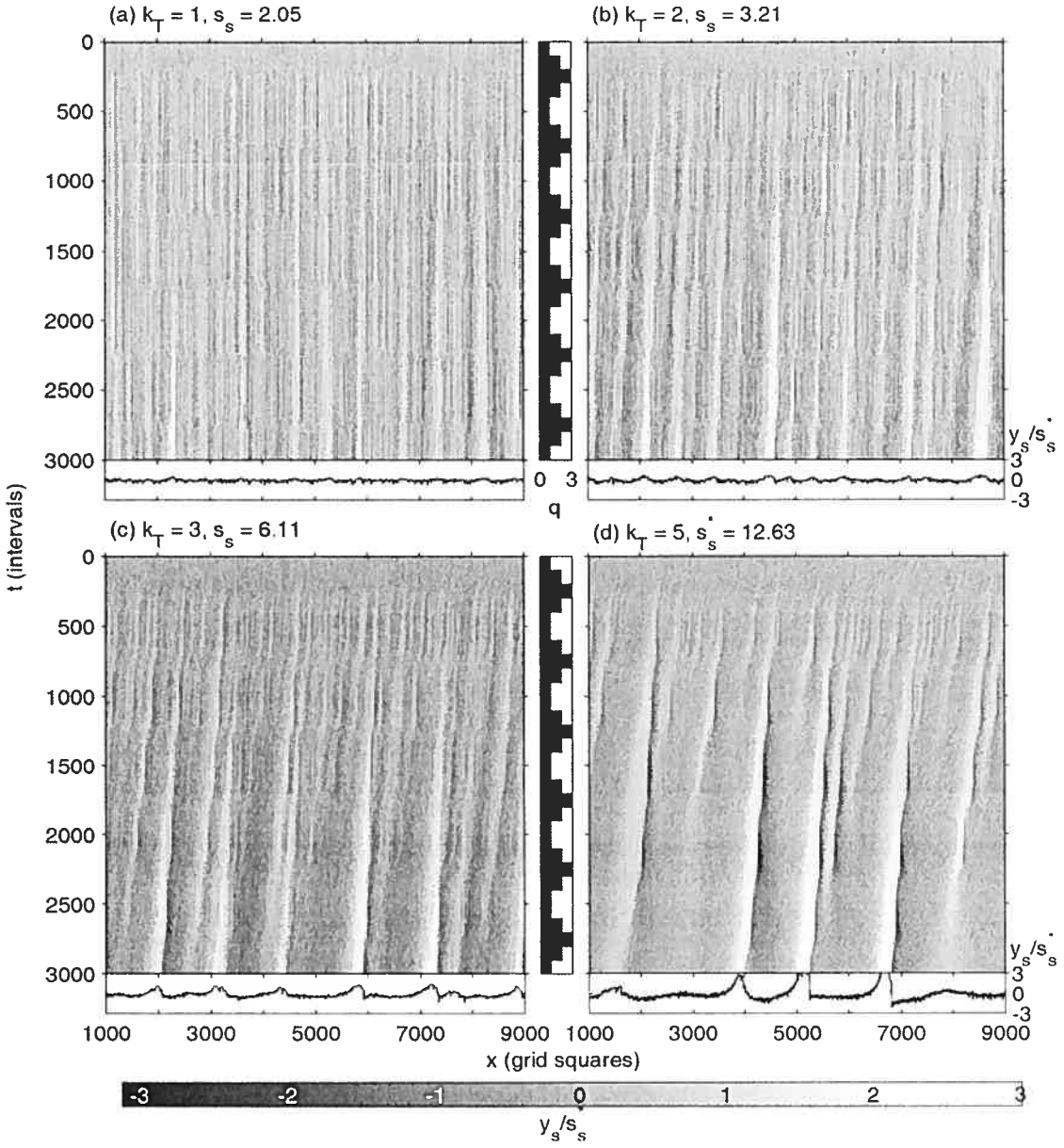

Figure 3.13 - Space-time plots of y_s/s_s* for turbulence rule simulations. See caption of Figure 3.10 for more detailed explanation.

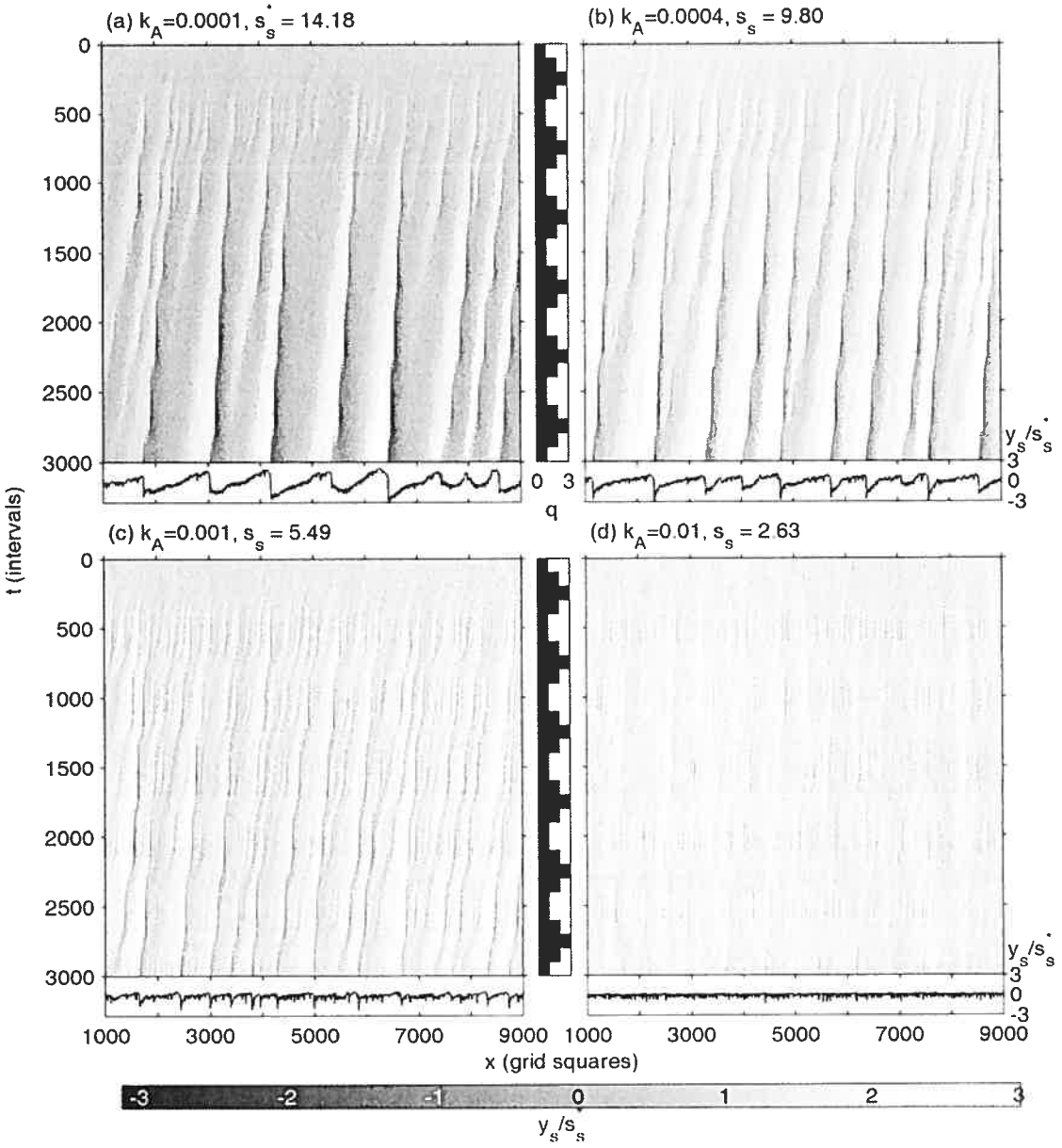

Figure 3.14 - Space-time plots of y_s/s_s* for acceleration rule simulations. See caption of Figure 3.10 for more detailed explanation.

3.5.2 Profile plots

Profile plots zoom in on side views of simulation matrices at specific times in order to highlight typical examples of bed forms (Figure 3.15). The matrix is plotted at a 1:1 scale and particles are colored by size. The plot from a basic model simulation confirms the small amplitude and irregularity of typical bed forms (Figure 3.15a). The most prominent accumulation occurs at x = 500-550 on the profile plot scale and we zoomed in further on this section to show particle sorting. The form is composed of small and medium particles and supported at the downstream toe by a chain of four large particles. Similar accumulations were noted in Figure 3.15b, a section taken from a hiding rule simulation. The surface structures are small and irregularly spaced, with the most prominent accumulations at x = 430 and 620. The blow-up section confirms the occurrence of large particle chains, but it is interesting to note the sorting of sizes, with large particle beneath the smaller sizes, which indicates that the smaller particles deposited after the large particles. Three prominent forms with chains of large particles are noted in Figure 3.15c, a section taken from an imbrication rule simulation. The shape of the characteristic bed form is asymmetric, with a long stoss slope and a short lee slope. The stoss slopes are dominated by small and medium sized particles, while the lee slopes are comprised exclusively of large particles.

Figure 3.15d shows a typical structure from a turbulence simulation at low flow when the control parameter is large (k_T = 3). The wavelength of this large bed form is greater than the limits of the plot. The bed forms have a long stoss slope and a short lee slope. Small particles concentrate at bed form crests at low flows (Figure 3.15d) but this is not evident at high flows (Figure 3.15e). A secondary bed form appears at high flows, with a typical example between x = 600-700. These symmetrical forms occur in the deepest areas of the pool, where instantaneous velocities can be very high and many particles saltate at the maximum modeled distance of 60 grid squares - the approximate length of the observed bed forms. Figure 3.15f shows a typical structure at low flow when the acceleration rule is active. The shape of the form is asymmetric, with a very steep lee slope and a long stoss slope. This shape is the result of size selective transport during moderate and low flows. Small particles concentrate just upstream of bed form crests while large particles remain and are exposed in the deepest sections of the pools.

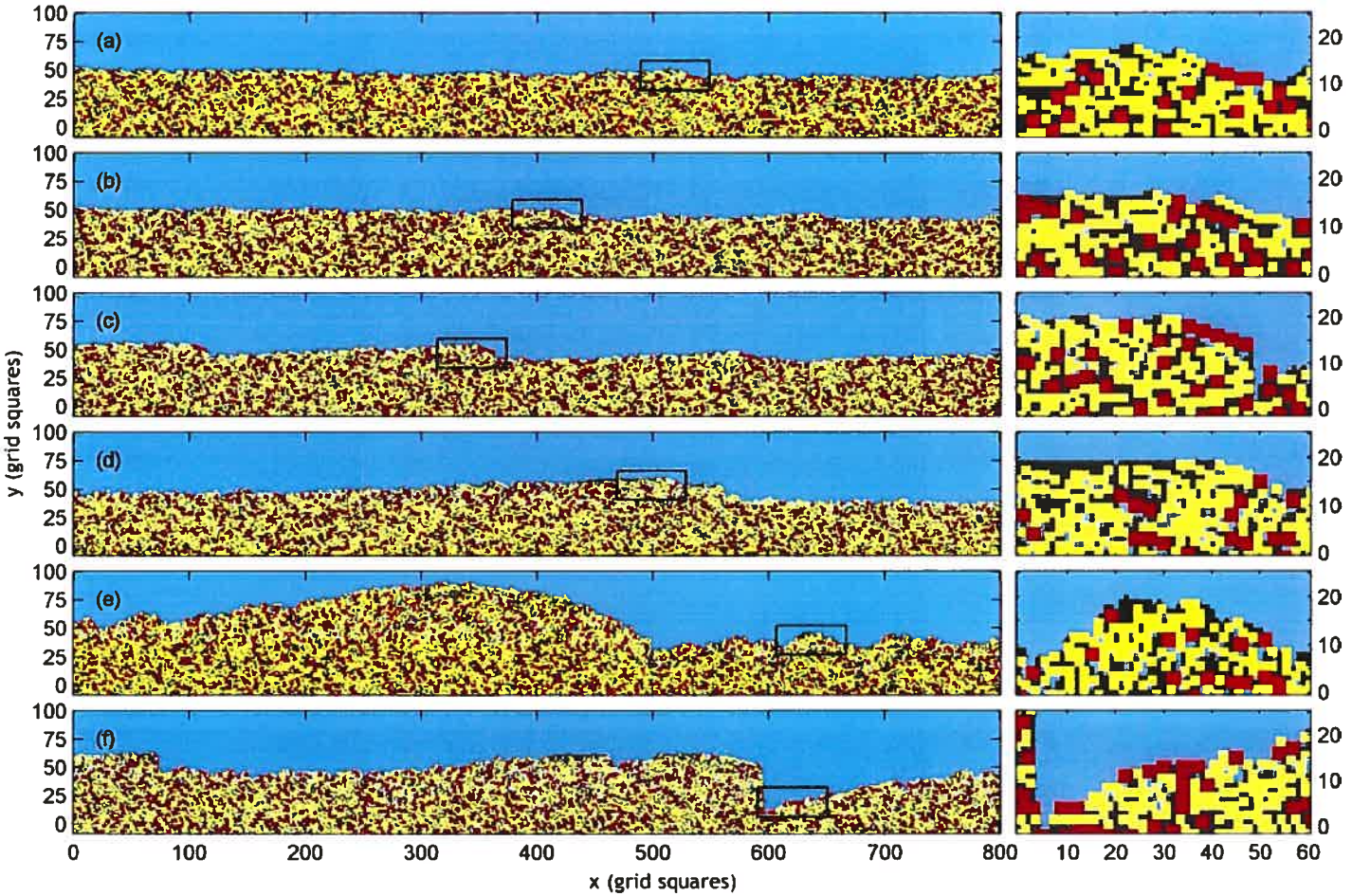

Figure 3.15 - Profile plots at two different scales. Small, medium, and large particles are colored grey, yellow, and red, respectively. (a) basic model ($k_I = 1$, $t = 2000$, $x = 7000$ - 7800); (b) hiding rule ($k_H = 3$, $t = 3000$, $x = 5000$ - 5800); (c) imbrication rule ($k_I = 0.60$, $t = 2500$, $x = 4500$ - 5300); (d) turbulence rule ($k_T = 3$; $t = 3000$; $x = 1500$ - 2300); (e) turbulence rule ($k_T = 5$, $t = 2750$, $x = 4850$ - 5650); and (f) acceleration rule ($k_A = 0.0004$, $k_T = 5$, $t = 3000$, $x = 7000$ - 7800).

3.5.3 *Roughness*

Since particle size distributions are the same, variations in roughness can be used to compare the organization of the bed for various simulations. Overall bed roughness can be quickly assessed using the standard deviation of surface elevations (σ_s) as shown on the space-time plots (Figures 3.10-14). This measure is related to hydraulic roughness in flow resistance equations [*Smart et al.*, 2002]. Roughness increases with bed form development. The hiding rule results in only marginal increases, but the imbrication rule increases σ_s to approximately three times the basic model value, and the turbulence and acceleration rules produce changes in the order of magnitude.

We were also interested in the spatial distribution of this roughness to help characterize the patterns observed in Figures 3.10-14. Spatially distributed bed roughness (r) can be calculated using the equation:

$$r = \frac{1}{w} \sum_{i=0,w,2w,\ldots}^{w} (y_x - y_{x-1})^2 \qquad (3.11)$$

where y is the elevation of the bed surface with the overall slope removed, and w is a window length over which r will be averaged. High frequency roughness - i.e. that occurs within a window - results in a high r-value. Low frequency roughness - i.e. differences between windows - will produce spatial variability in the r-value, which can be measured with the skewness. Using a window size of 20 grid squares, spatially distributed roughness was calculated for one simulation case from each series as indicated in Table 3.4 (Figure 3.16). The spatial quality of the measure allows us to confirm the regular size and frequency of bed forms for the acceleration rule simulation (Figure 3.16c). Overall statistics of the bed roughness parameter are shown by means of box plots in Figure 3.17. Means and standard deviations of roughness decreases when feedback rules are activated, which means the high frequency roughness decreases. Skewness increases for the imbrication, turbulence, and acceleration simulations, because larger and fewer bed forms contain a greater proportion of the roughness.

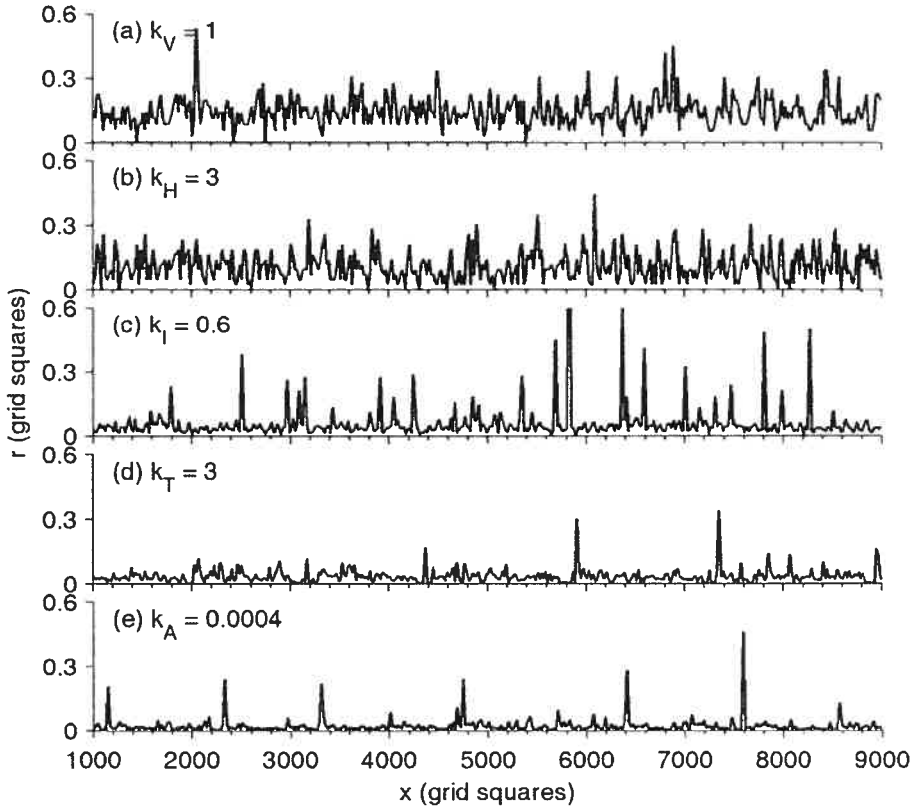

Figure 3.16 - Spatial roughness as calculated using Equation 3.11 and a window size of 20 grid squares. Selected cases are as in Table 3.4.

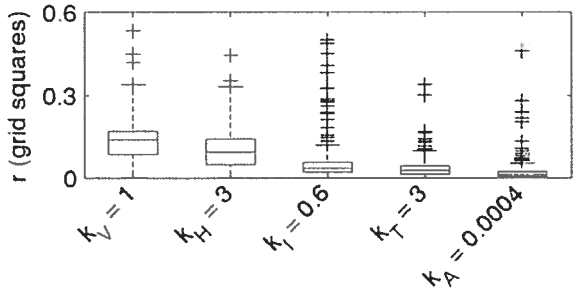

Figure 3.17 - Box plots of spatially distributed roughness values. The horizontal lines through the boxes represent the medians and the limits of the box are set at the inter-quartile ranges. The whiskers are twice the quartile ranges and + markers indicate values beyond these limits.

3.5.4 Pool dimensions

To further assess the organization of gravel bed profiles, we used pool dimensions calculated from residual depths, defined as the depth of water in a pool below the elevation of a downstream control point [*Lisle*, 1995; *Madej*, 1999]. We calculated residual depths by subtracting the local bed surface from the highest downstream bed surface elevation.

Positive residual depths indicate a pool, and the pool volume (assuming a unit width) is calculated by summing residual depths defined by the same control point. An average depth (y_p) is calculated by dividing the unit pool volume (v_p) by the length (l_p). The weighted mean pool dimensions (L_p' and Y_p') are calculated for the final bed surface as follows:

$$L_p' = \frac{\sum(l_p v_p)}{\sum v_p} \tag{3.12}$$

$$Y_p' = \frac{\sum(y_p v_p)}{\sum v_p} \tag{3.13}$$

Weighting the pools by their volume means that large pools have a greater influence on the statistics than smaller pools.

The evolution of pool dimensions over time is shown in Figure 3.18 for five selected cases, one from each simulation series (as indicated in Table 3.4). These results confirm the trends observed in the space-time plots. Pool dimensions using the basic model react to the onset of high flow during the first flood peak and then quickly stabilize. Subsequent high flows produce slight changes to the dimensions, but no long-term trend is evident. Using the hiding rule, the dimensions first increase during moderate flows. In subsequent floods, pool dimensions decrease during high flows and then recover during the moderate flows after the peak. Dimensions are then stable until the next high flows. The activation of the imbrication rule increases the pool dimensions during both moderate flows and the high flows of the first event. During subsequent events, pool dimensions are unpredictable, sometimes increasing, sometimes decreasing with the passage of peak flows, but again do not show a long-term trend. Dimensions are stable during low flows. The activation of the turbulence rule results in a steady increase in pool depth over the six modeled flood events. Overlain on this trend is a within-flood cycle, with the maximum depth occurring at the end of the low flow period on the rising limb and the minimum at the end of high flows on the falling limb. Pool length increases irregularly, with floods 1, 3, and 5 resulting in increases in pool length, and the other floods resulting in minimal change. The addition of the acceleration rule results in an asymptotic trend for both depth and length, which corresponds with the visual observation of the formation of equilibrium dimensions of the pools for these simulations. While the peak pool depths always occur on

the rising limb, they occur at the end of the moderate flows in the first two floods and at the end of the low flow stage in the later floods. Pool lengths show a similar shift in behavior after the second flood, with the largest increases occurring on the rising limb in the final three floods, whereas the increases mostly occurred on the falling limbs in the first two floods.

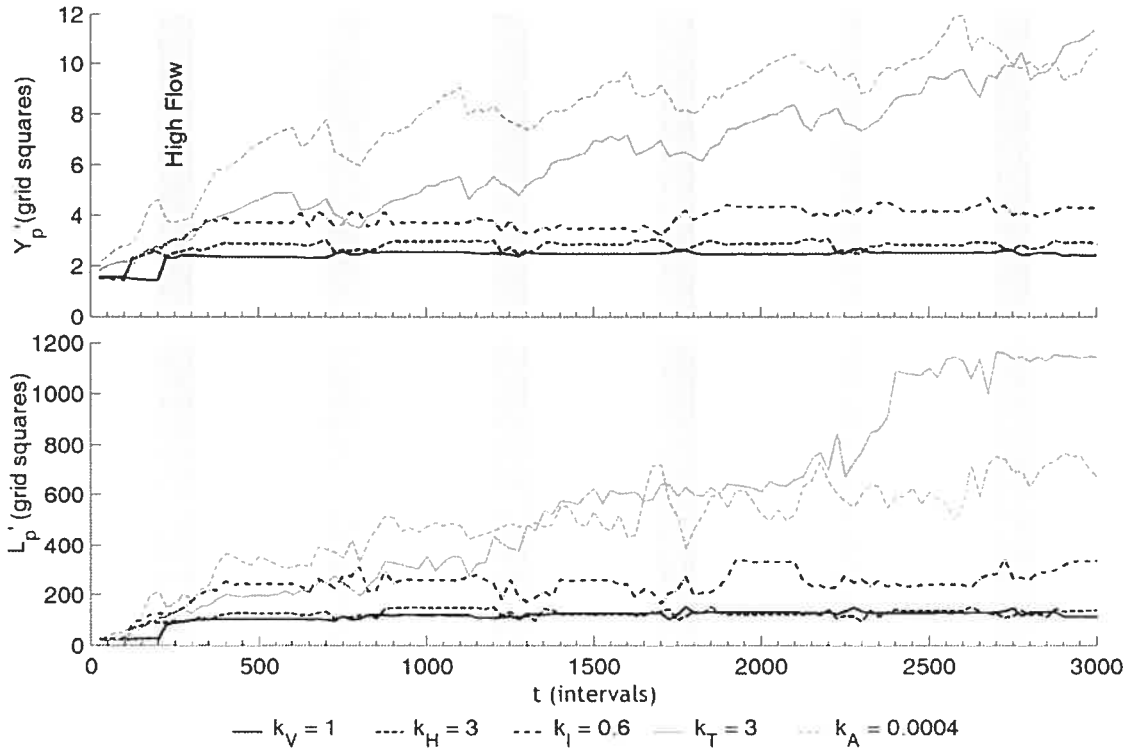

Figure 3.18 - Pool dimensions (*Lp'* and *Yp'*) versus time for the five simulations as selected in Table 3.4.

Final pool dimensions for all simulations are shown in Figure 3.19. This figure confirms the qualitative observations made from the space-time and profile plots. The randomly generated initial bed roughness results in a weighted average pool length and depth of 20 and 1.6 grid squares, respectively. The basic model simulations produce longer and deeper pools that reach dimensions of 110 x 2.5 grid squares. Pool dimensions decrease slightly when the mean velocity control parameter is increased. Pool size decreases again when the hiding control parameter is small, indicating the infilling of pools with sediment, but increases as k_H is increased, although the maximum of 140 x 3.0 grid squares remain close to basic model pool dimensions. Pool dimensions are larger when the imbrication rule is active, reaching dimensions of 300 x 8.4 grid squares. Pool length is relatively constant at larger values of the imbrication control parameter, indicating a

maximum pool length with particle feedback rules. Flow feedback rules increase pool dimensions by an order of magnitude. Increasing the turbulence rule control parameter steadily increases pool dimensions, reaching a maximum of 1500 x 33 grid squares. The acceleration rule introduces a negative feedback on pool dimensions, and the size of pools steadily decrease as k_A is increased until pools are similar in length to those of the basic model simulations, although they remain relatively deep. As shown, error bars for all the selected cases are small relative to the differences in pool dimensions between the cases. This allows clear interpretation of results, as simulations with specific control parameter values occupy distinct regions within the pool dimensions plot.

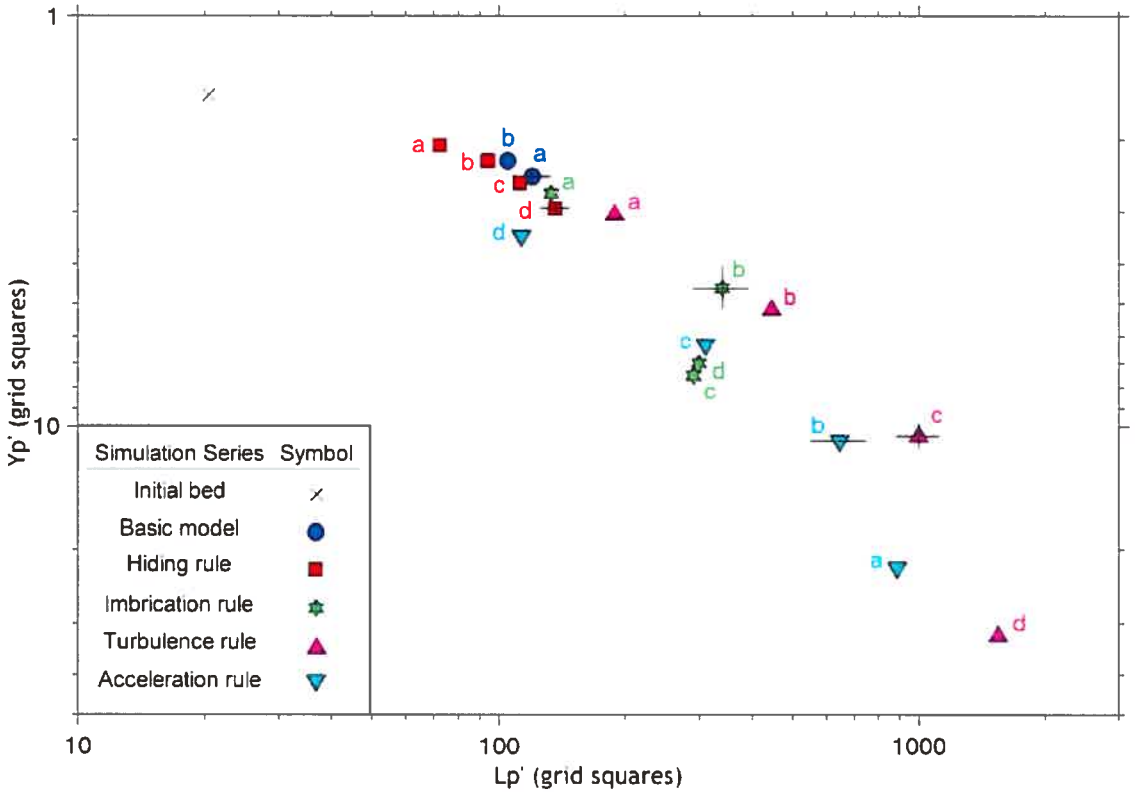

Figure 3.19 - Pool dimensions plot showing weighted mean lengths (*Lp'*) and depths (*Yp'*) of residual pools on the final bed surface ($t = 3000$) of basic model and feedback simulations. The control parameter value increases from a - d (values are listed in Table 3.4). Note that the y-axis is reversed so that longer and deeper pools plot towards the bottom right-hand corner. Error bars are shown in black for cases selected for repeat simulations. Error bars were set at 1.64 times the standard deviation of the weighted mean pool dimension to encompass 95% of the variability.

3.5.5 Sensitivity

As shown in Figure 3.20, all simulations are sensitive to the initial bed slope. A gentler slope results in longer and deeper pools for the basic model, hiding rule, and

imbrication rule simulations; and shallower pools for the turbulence and acceleration rules. Particle feedback simulations are sensitive to particle size, with a higher proportion of large particles resulting in deeper and longer pools. Flow feedback simulations are sensitive to the shape of the hydrograph, with the falling hydrograph resulting in larger pools. The length of the matrix was found to be significant for the imbrication rule and the acceleration rule simulations, indicating edge effects of the matrix to be important in these cases.

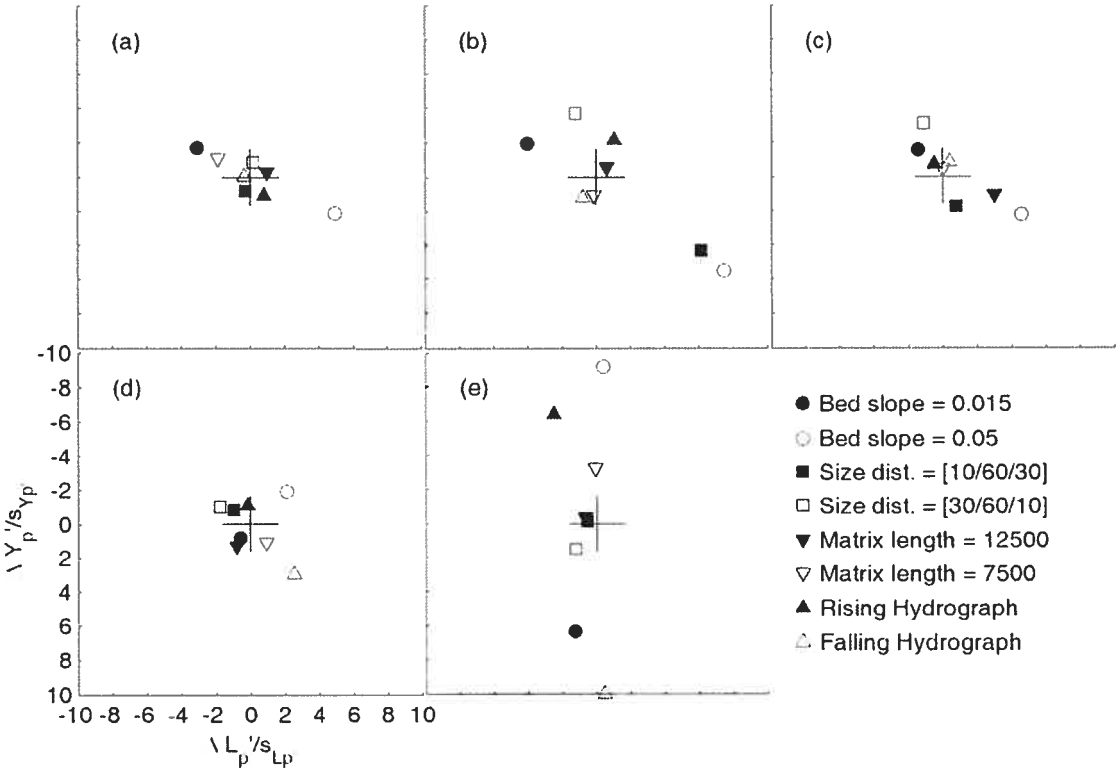

Figure 3.20 - Sensitivity to initial parameters: (a) $k_{I'} = 1$, (b) $k_{II} = 3$, (c) $k_I = 0.60$, (d) $k_T = 3$, and (e) $k_A = 0.0004$. Axes represent the difference between mean pool dimensions (Lp' and Yp') calculated from the final beds of the sensitivity simulations and the average dimensions calculated from the repeatability simulations. The differences are normalized by the standard deviations of the dimensions as calculated from the repeatability simulations (s_{Lp}'). Simulations were considered sensitive to the indicated parameter where the difference was greater than the error bars ($\alpha = 0.05$). Initial parameter values used in these simulations are listed in Table 3.4.

3.6 Emergent Bed forms

Three types of bed forms emerge during ROQ-B model simulations. The first type consists of an accumulation of medium and fine particles supported downstream by a chain of large particles (Figures 3.15a, 15c). We think this is the result of large particles that move by rolling or small hops. Figure 3.21 shows the effect of the imbrication rule on the occurrence of high saltations of large particles. High saltations are defined as those greater

that the diameter of the particle. Simulations in which less high saltations occur show more organization (Figure 3.12), have larger pool dimensions (Figure 3.19), with well-developed examples approximately 250 grid squares long (Figure 3.15c). These chains of large particles do not move, as they are formed and destroyed at a given location (Figure 3.12b). Pools of this nature are sensitive to the concentration of large particles and the overall slope (Figure 3.20), both of which are geometrical properties that alter the probability of large particles forming chains and saltating over each other.

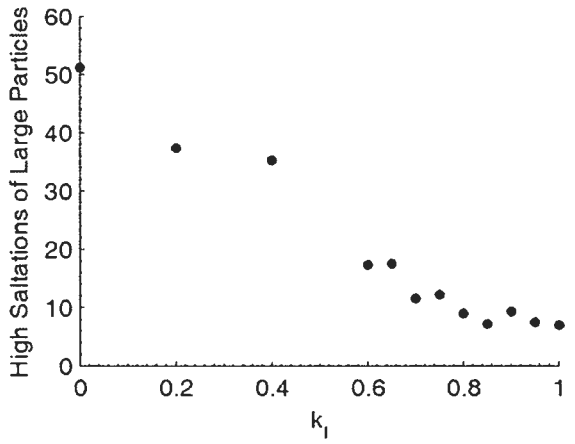

Figure 3.21 - High saltation of large particles versus the imbrication rule control parameter (k_1). $k_{1'} = 2$ for all simulations in this figure. High saltations of large particles are defined as those which are sufficient for a large particle to saltate over another large particle ($\geq \nearrow^2$).

The second type of bed form is a wave-like structure that formed in deep pools at high flows (Figure 3.15e). This type of wave occurred frequently during the model development tests. They appeared relatively quickly, and at low flow, during tests with very small standard deviations on the velocity distributions and only small particles in the simulations. The use of a range of transport distances largely eliminated their occurrence (Figure 3.5). In this mixed sediment version of the model, the waves occur only at high flows after large bed forms develop that significantly modify the flow environment. Their wavelength is approximately 60 grid squares, which is equal to the maximum transport distance used in the model. These structures translate quickly upstream as sediment is preferentially deposited on the stoss slope and eroded from the lee slope.

The third type of bed form is dependent on feedback mechanisms between the bed and the flow field. These bed forms develop on scales much larger than both individual grain sizes and transport distances (Figures 3.13 and 14), and the size of the forms is not sensitive to particle size distributions (Figure 3.20d-e). Instead, the forms are sensitive to

the shape of the flow hydrograph, and their dimensions are controlled by the relation between mean velocity and the generation of turbulence. At high flows, the entrainment of a particle depends on its position with respect to macro-bed forms and no sorting by size is evident (Figure 3.15e). Sorting does occur during medium and low flows, with fine sediment deposited on bed form crests and large sediment exposed in the deep sections (Figure 3.15f). Without the acceleration rule, instantaneous velocities in deep areas can be very high, even at low flow, which erodes the bed, increases velocity values, and results in large structures that grow indefinitely (Figure 3.18d). The flow acceleration rule allows high mean velocities to decay towards the depth-averaged flow velocity (Figure 3.8). This results in deposition and the emergence of new structures at an equilibrium wavelength (Figure 3.18e).

3.7 Discussion

The key result from this study is the emergence of bed forms in a model based on local interactions between discrete particles and with the flow environment including turbulence. Bed forms have been simulated with other models, however. What is unique to this study is the variety of forms that have been simulated, the control and flexibility that the central algorithm permits, and the feedback between the morphology and flow properties that leads to the emergence of meso- and macro-bed forms. In this discussion we compare results with existing models, identify possible natural analogs, and present a test of the effect of flow separation on bed form celerity. We also discuss limitations associated with the parameterization of simplified rules and directions for new research.

According to *Langbein and Leopold* [1968], kinematic waves will develop on a river bed when particles interact to reduce the effectiveness of fluid forces. This interaction can occur in a number of ways, the simplest being the geometric effect of the bed on rolling particles, as an irregular surface will induce deposition when particles are trapped in surface depressions. Large particles are particularly effective in generating this type of wave because they (a) provide a physically larger barrier to particles moving on or close to the bed; (b) move less frequently; and (c) move slowly and primarily by sliding, rolling, and short hops that are not sufficient to pass other large particles. There is thus a tendency for them to group into chains and form the loci for particle accumulations. In the ROQ-B model, particle feedback rules can further decrease the effectiveness of fluid forces, which results in more numerous and longer chains. The typical form, on the order of 10 to 50 grid

squares (Figure 3.15a), is similar in scale to structures generated in the models of *Tribe and Church* [1999] and *Malmaeus and Hassan* [2002], for which bed form lengths of approximately 30 grain diameters were estimated from simulation results. The model of *Naden* [1987] also generated forms on this order of magnitude, with typical lengths of 6-15 grain diameters. *Naden and Bradshaw* [1987] showed this scale to be close to lengths of pebble clusters measured in a natural river. The importance of large clasts, the similarity of length scales, and the lack of bed form translation support the conclusions that a) the models operate on similar principles; and b) that the forms are analogous to natural pebble clusters.

Longer forms were developed in the simulations here using the imbrication feedback rule. A possible natural analog is bed load sheets [*Whiting et al.*, 1988; *Dietrich et al.*, 1989]. These forms are distinguished from clusters by their larger scale, on the order of 100-600 grains, and by their mobility, as they have been found to translate downstream. Large particles are typically found on the front of these forms. The forms in the simulations presented here are approximately 250 grains in length, which is within the range of bed load sheets, and large particles are invariably seen on the front of these forms (Figure 3.15c). Critically, however, the modeled forms are imbricate forms that are fixed in a given location. This contrasts with observations that shows gravel sheets to translate downstream. There is clearly something missing from our model, as will be discussed later in this discussion.

The appearance of wave-like gravel bed forms in deep pools at high flows is related to particle saltation. Accumulations form a physical barrier to the saltating particles, decreasing saltation distances and controlling deposition. The resulting forms are symmetrical in shape, which is similar to results from the simpler eolian models [*Anderson*, 1990; *Landry and Werner*, 1994; *Nino et al.*, 2002]. In these models, the initial bed forms that appeared were found to be related to the splash length or creeping distance. This is similar to what occurs in the ROQB model, because the length of the symmetrical wave forms is a function of the maximum saltation distance assumed in the model. A possible natural analog is gravel dunes [*Dinehart*, 1992; *Carling*, 1999], although some key differences exist. Gravel dunes have been measured at 200 to 500 grain diameters in length [*Dinehart*, 1992], which is larger than those modeled here. Individual saltation distances on these scales have not been observed in laboratory [*Abbott and Francis*, 1977; *Sekine and*

Kikkawa, 1992] or field studies *Habersack* [2001], which suggests that the simulated forms are a transient feature of bed form initiation that may be an artefact of model assumptions. The other feature that does not follow with accepted dune morphology is the fact that the forms again translate upstream.

The introduction of flow properties is similar to the use of wind speedup [*Anderson and Bunas*, 1993; *Momiji et al.*, 2000], and vegetation growth on dunes [*Baas,* 2002] in aeolian models. These models were able to simulate larger scale aeolian forms by considering feedback mechanisms other than particle interactions. These results are mirrored in this study, as flow feedback mechanisms led to the development of macro-scale forms on the scale of pools, riffles, and bars. In contrast to activating particle feedback rules, which produces shallower pools at steeper slopes, flow feedback leads to deeper pools at steeper slopes (Figure 3.20), which is in agreement with empirical studies [*Wohl et al.*, 1993]. These key results suggest that the relation between turbulence generation and changes to mean velocity is central to the generation of macro-scale forms in gravel-bed rivers such as bars, pools, and riffles. Before meaningful conclusions can be drawn, however, it is necessary to consider bed form celerity.

The formation of ripples and dunes that translate downstream is a common feature of aeolian environments, and many models have successfully simulated this behavior [e.g. *Anderson*, 1990; *Landry and Werner*, 1994]. To do so they implemented the concept of a shadow zone downstream of developing bed forms. These shadow zones are the geometric result of transport being initiated by the impact of saltating particles arriving at low angles to the horizontal. In rivers, transport is more commonly initiated as a result of fluid shear. We developed a hiding rule to attempt to model the reduction of fluid forces on particles at or beneath the bed surface, but the rule only accounts for immediate neighbors, and the effect of the rule is weak. It does not account for the alteration of mean velocity profiles in response to acceleration [*Kironoto and Graf*, 1995] or flow separation near sudden increases in depth such as in the lee of dunes [*Nelson et al.*, 1993]. In the current model, flow properties are represented in one dimension. It is clear that a more sophisticated treatment of the flow environment is necessary.

As a preliminary attempt we introduced a profile factor to model increased mean velocity near the bed in accelerating flow and decreased velocity in decelerating flow, with flow separation occurring where the expansion of the bed was greater than 10° [*Best*,

2005]. Two simulations from this test are shown in Figure 3.22. In both examples, bed forms translate downstream. The first example shows results from the trimodal sediment used in the other simulations and the large material is shown to collect in the lee of bed forms. Smaller bed forms translate downstream during moderate and high flows, but the positions of the dominant bed forms remain fixed through the series of floods. Particle sorting and the stability of the modeled bed forms is very similar to pool-riffle sequences [*Sear*, 1996]. Imbrication is not necessary to produce these forms, which means that the greater degree of imbrication observed in riffles by [*Clifford*, 1993b] and [*Sear*, 1996] may be a consequence of the flow environment rather than a formative mechanism of pools and riffles. The second example demonstrates the effect of replacing the large sediment fraction with the smallest size of sediment. The bimodal forms translate in a downstream direction in a similar manner to gravel sheets, bars, and dunes.

Simplified rules have been used to represent physical processes in the ROQ-B model. This modeling choice creates uncertainties in model parameterization. This problem is not critical when rules are tested one at a time. *Nino et al.* [2002] noted that similar results could be obtained using different rules, provided that the fundamental aspect of the physical process is represented. However, mature bed forms such as dunes, gravel sheets, and pool-riffle sequences require the simultaneous activation of rules to control turbulence generation, changes to mean velocity, and changes to the velocity profile. Two approaches are possible to deal with this issue. The first approach, already illustrated in Figure 3.22, involves extensive simulations with which any number of system types can be generated. This approach negates the advantage of transparency, as multiple control parameters need to be activated, and is made more difficult due to the immense quantity of results that are generated. The second, more selective approach would use experimental work to identify parameter ranges for particular system types. In this spirit, field research is planned in a pool-riffle unit to improve the characterization of flow hydraulics and sediment transport in order to test and refine the model for this application.

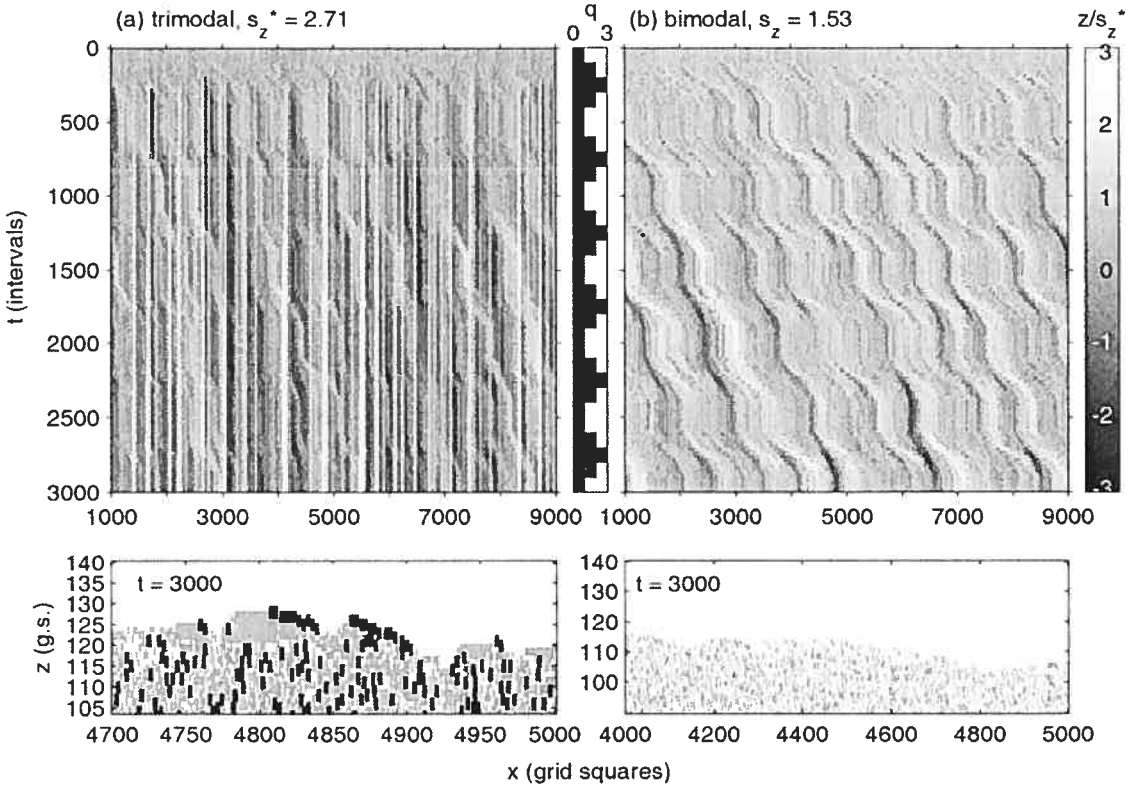

Figure 3.22 - Space-time and profile plots of two simulations to demonstrate the velocity profile/flow separation rule. The trimodal sediment is that used in the other simulations. The bimodal sediment consists of 40% small and 60% medium sized particles. All other parameters are held constant in the two simulations. Particles are colored by size on the profile plots (small - light gray; medium - dark gray; and large - black).

Other improvements are possible. It is not clear how the control parameters used in this study will relate to the limiting scales in river channels of flow depth and width. For instance, the length of dune and riffle-like forms is controlled by the rate at which mean velocity adjusts to the depth-averaged velocity. Based on considerations of momentum, it is likely that a relation exists between the control parameter and channel width, but future research should test this link. It may ultimately be possible to replace the control parameters with measurable morphological parameters. Another unresolved issue is the importance of coherence in turbulent flow. Large-scale forms were found to develop in the absence of coherence - i.e. turbulence was uncorrelated in time - which runs counter to some hypotheses of macro-form development [*Yalin*, 1971], and measured coherent structures over dunes [*Kostaschuk and Church*, 1993]. Model tests could be developed to test the role of flow coherence on bed form development. The sensitivity to initial parameters also needs further investigation. Simulations dominated by particle feedback

rules were found to be sensitive to the effects of slope and particle size. This result matches the conclusions of *Wohl et al.* [1993], who found these two parameters to control pool dimensions in steep rivers. The two parameters are typically correlated, however, with large particles occurring in systems with high slopes. The ROQ-B model can be used as a tool to assist research in gravel-bed rivers on such problems.

3.8 Conclusions

We have presented and tested a hierarchical model of a gravel-bed river system in which simple rules govern flow and sediment dynamics. This model clearly demonstrates the emergence of commonly observed bed form types in response to feedback mechanisms. Small-scale imbricate forms such as pebble-clusters were simulated by considering feedbacks between the bed and transported particles. Flow field heterogeneity is required to generate larger scale forms. This heterogeneity appears to be controlled by mean velocity acceleration and deceleration. In the model, non-uniform flow alters both the amplitude of turbulent fluctuations and the near-bed velocity such that powerful feedback mechanisms are generated and bed forms with similar scale, sorting, and celerity to gravel sheets, dunes, and riffle-pools emerge. Further research to establish the relation between modeled control mechanisms and morphological parameters of channel width, depth and sediment size would be useful. Nevertheless, this simple model reproduces much of the complexity observed in gravel-bed river system dynamics and offers a new and useful approach to resolving geomorphologic problems.

Liason Paragraph B

The previous chapter presents the model that we used to simulate flow and sediment dynamics in riffle-pools. Based on a number of flume studies that found turbulence intensity to increase in zones of flow deceleration and a few field studies that found increased turbulence intensity in pool-heads, we tested the effect of linking turbulence intensity to mean flow acceleration. We found that the activation of this mechanism resulted in the formation of large scale bed forms. More field data are needed to determine if this accurately represents what occurs in riffle-pools. This chapter[2] is the first of four resulting from a field campaign to study flow and sediment dynamics of a forced riffle-pool. It represents a critical step in this thesis because of the need to test the reliability of measurements of instantaneous velocity in highly turbulent flow environments such as riffle-pools in flood. We compared the performance of an Electromagnetic Current Meter (ECM) with that of an Acoustic Doppler Velocimeter (ADV). Measurements were made at two field sites, one at moderate flow velocities (up to 0.70 m/s) and moderate turbulence intensities (10-20% of mean flow), and the other in an area of non-uniform flow that included locations with fast mean velocities (up to 1.75 m/s) and high turbulent intensities (up to 50% of mean flow). Comparisons of common statistics confirm the general agreement between the ECMs and ADVs. This agreement is subject to limitations associated with the sample volume and frequency response of the instruments, and only applies within restricted velocity (up to $\approx$ 1.25 m/s) and velocity rms ranges (up to $\approx$ 0.125 m/s). Outside of these ranges, spectral analysis, error estimates, and a quadrant analysis showed anomalous behavior of the ADV signal, especially in the vertical velocity component in the very fast and turbulent flows. For this thesis, the key conclusion is that the older ECM technology provides the more reliable estimates of flow parameters in high turbulence. We used ECMs to characterize the flow hydraulics of a riffle-pool in the subsequent chapters.

---

[2] MacVicar, B. J., E. Beaulieu, V. Champagne, and A. G. Roy (*accepted July 2006*), Measuring water velocity in highly turbulent flows: Field tests of an Electromagnetic Current Meter (ECM) and an Acoustic Doppler Velocimeter (ADV), *Earth Surface Processes and Landforms.*

4 MEASURING WATER VELOCITY IN HIGHLY TURBULENT FLOWS: FIELD TESTS OF AN ELECTROMAGNETIC CURRENT METER (ECM) AND AN ACOUSTIC DOPPLER VELOCIMETER (ADV)

4.1 Introduction

The measurement of flow velocity and turbulence is critical for understanding the dynamics of rivers. In shallow river flows, two types of instruments - Electromagnetic Current Meters (ECMs) and Acoustic Doppler Velocimeters (ADVs) - have been predominantly used over the past decade [*Buffin-Bélanger and Roy*, 2005]. These instruments are commercially available, physically robust, and capable of sampling at rates up to 20 and 25 Hz , respectively. The two types of instruments operate on different principles. An ECM uses the Faraday principle of electromagnetic induction, which states that the water moving in a magnetic field will produce a voltage that is proportional to the velocity of the water. It is intrusive, in that it samples the velocity of water surrounding the probe, and has a sampling volume with a diameter that is typically 2 to 3 times the diameter of the probe [*Marsh-McBirney*, 1994]. Instantaneous measurements of the voltage difference between two electrodes are taken once every cycle of an AC electromagnet that generates the magnetic field. Voltage measurements need to be calibrated to water velocity, are sometimes prone to zero-drift, and are sensitive to electronic interference and improper grounding. ADVs operate on the principle of Doppler shift. Two pulses of sound are transmitted, separated by a time interval, and the acoustic energy reflected off particulate matter in a sampling volume at a short distance from the probe tip is recorded. The velocity is then calculated as a function of the phase lag between the return signals [*Sontek/YSI*, 2001]. ADVs are seen as an improvement for both lab and field investigations because they measure three-dimensional velocity components, are non-intrusive, and calibration is invariant. ECMs are still in use, however, and nearly all of the progress in the study of turbulence in natural rivers up until 1998 relied on their deployment [*Buffin-Bélanger and Roy*, 2005]. It is necessary to establish whether the library of data within the existing literature can be directly compared irrespective of instrument choice and if conclusions obtained using ECMs still hold. It has also been observed that low quality ADV signals

sometimes occur, a problem that forces data to be discarded and has hampered studies in high turbulent areas such as surf zones [*Rodriguez et al.*, 1999; *Bryan et al.*, 2003]. It is possible that the ECM may still give superior performance in some sampling situations. This study was particularly motivated by the need to assess the reliability of available instruments for the characterization of high velocity, highly turbulent, and non-uniform flow environments such as rough step-pools, cascade rivers, and gravel-bed rivers in flood.

The performance of ECMs has been previously tested in the laboratory [*Aubrey and Trowbridge*, 1985; *Lane et al.*, 1993], and in coastal [*Soulsby*, 1980; *Guza et al.*, 1988] and riverine environments [*Lane et al.*, 1998; *Roy et al.*, 1996a]. Similarly, ADVs have been tested in the lab [*Rodriguez et al.*, 1999; *Voulgaris and Trowbridge*, 1998; *Finelli et al.*, 1999], in the ocean [*Elgar et al.*, 2001; *Smyth and Hay*, 2003; *Elgar et al.*, 2005], and in rivers [*Lane et al.*, 1998]. Only two of these tests, *Aubrey and Trowbridge* [1985] and *Voulgaris and Trowbridge* [1998], were able to control their flow environment such that the performance of the instrument could be assessed against known values. These laboratory experiments, however, were typically conducted in still water tanks or smooth-walled flumes and cannot be directly applied to quantify sensor accuracy in field deployments due to the significant effects of turbulence scales and intensity [*Guza et al.*, 1988]. *Garcia et al.* [2005] used simulated flow series to develop performance curves for the ADV under various flow conditions. Although the performance curves are based on mean velocity and depth, the study also looked at turbulence. They found that the ADV will overestimate signal variance when turbulence is low due to the presence of noise, but will underestimate signal variance when turbulence is high due to the sampling protocol. The more common approach has been to compare the performance of two or more instruments in a particular flow environment in order to identify discrepancies. Few direct comparisons between ADVs and ECMs have been reported, and the range of mean velocities and turbulent intensities over which they have been tested is usually small (Table 4.1). *Lane et al.* [1998] found mean velocity values to be highly correlated, although some offset errors up to 10 cm/s were noted. In a set of flume experiments by *Rodriguez et al.* [1999] the ECM consistently reported higher mean velocities, lower standard deviations, and lower integral time scales than the ADV. *Elgar et al.* [2001] simultaneously deployed ADVs and ECMs sampling at lower frequencies and found the signals to be highly correlated at velocities up to ± 300cm/s, confirming the ability of both instruments to

characterize low frequency turbulence. *Buffin-Bélanger and Roy* [2005] were not able to compare measurements from the same location, and while they did compare some general turbulent characteristics and found reasonable agreement, they highlighted the need for a more detailed investigation in rivers. The objective of the work presented here is to compare and test the quality of velocity time series simultaneously sampled with an ADV and an ECM in a riverine environment characterized by a wide range of mean velocity and turbulence intensities.

Source	Experimental Design			ECM			ADV		Key Observations
	Environment	ΔU (cm/s)	Strategy	Type	Diam.r	Hz	Type	Hz	
Lane et al. (1998)	River/Flume	0-70	replacement	MM	0.013	20	Sontek	25	10 cm/s U offset
Rodriquez et al. (1999)	Ocean/Flume	30-80	simultaneous	Delft p-s	0.038	25	Sontek	25	poor agreement in U, u'
Elgar et al. (2001)	Surf zone	±300	simultaneous	MM	0.04	1.5	Sontek	16	low frequency agreement
Buffin-Bélanger and Roy (2005)	Rivers	2-50	statistical comparison	MM	0.013	20	Sontek	25	good agreement in turbulence intensity

Table 4.1 - Past studies comparing the performance of ADVs and ECMs.

4.2 Methodology

4.2.1 Field Site and Experimental Design

The instruments were tested in the Eaton-Nord and the Nicolet Rivers, both of which are located in southeastern Quebec, Canada. The Eaton-Nord River has an average width of 17 m and a median bed particle size (D_{50}) = 40 mm. At the time of sampling, flow depths (Y) varied from 40-70 cm and mean velocities (U) varied from 30-60 cm/s. We also sampled in a slack water zone behind a boulder where $U \approx 0$ cm/s. The section sampled is characterized by relatively uniform flow (Figure 4.1). The Nicolet River is 30 m wide with D_{50} = 40 mm, Y = 40-120 cm , and U = 50-175 cm/s at the time of sampling. To restore fish habitat, large boulders have been placed across the full width of the channel to form a rock weir. The sampling section is characterized by rapidly varying flow that accelerates between two large boulders, passes through a hydraulic jump induced by a submerged boulder, and then decelerates in a scour pool downstream (Figure 4.2). The water level was at low stage during both field tests.

The instruments compared were a Marsh-McBirney ECM Model 523 [*Marsh-McBirney*, 1994] with a spherical head diameter of 0.013 m, and a Sontek ADV

[*Sontek/YSI*, 2001] with a cylindrical measurement volume of 6 x 9 mm located 10 cm below the probe tip. Streamwise (u) and vertical (v) velocities were measured at a sampling frequency $f_s = 20$ Hz with the ECM, while the ADV measured three-dimensional velocity components at $f_s = 25$ Hz. ADV parameters can be varied to encompass different velocity ranges. In the field tests described here, the user-set velocity range $u_{beam} = \pm 100$ cm/s was used as the standard range. This range was increased to $u_{beam} = \pm 250$ cm/s in fast and turbulent areas of the Nicolet River. ECMs are designed to have a range of ± 300 cm/s. Three ECMs and one ADV were mounted on a single wading rod as shown in Figure 4.3. Due to the intrusive nature of ECMs, it is not possible to simultaneously sample the same fluid volume with the two instruments. It is thus necessary to strike a compromise in the experimental design, either by measuring the flow at same location at different times or at different locations simultaneously. In this study, the latter approach was chosen because it removes differences that can arise due to longer frequency pulsations of the flow. The ADV was positioned to measure a volume 25 cm upstream of the ECM. Both sampling volumes were centered at an elevation of 25 cm above the bed to ensure that the probe tip of the ADV was below the water surface at all locations and that interference with the bed was minimized. The data set consists of 120 s time series collected at 16 and 12 locations in the Eaton-Nord and Nicolet Rivers, respectively.

Figure 4.1 - Eaton-Nord River field site looking upstream.

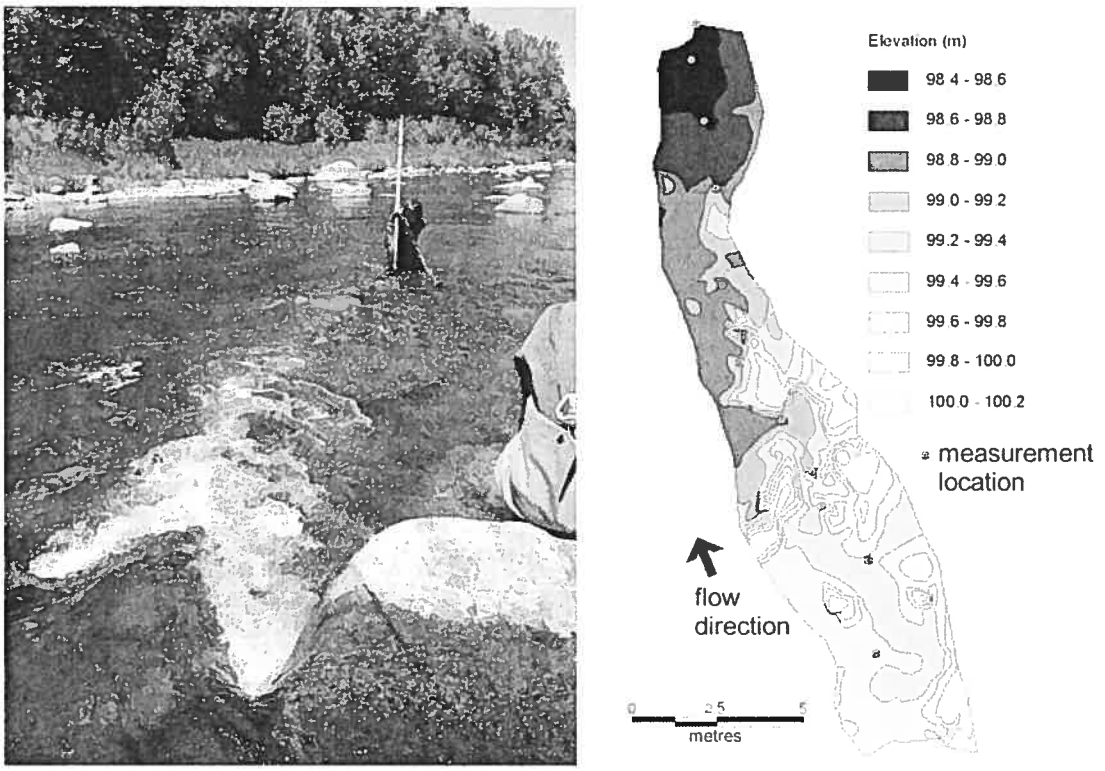

Figure 4.2 - Nicolet River field site looking downstream and sampling section bathymetry. Note jet of water as a result of constriction of flow between two large boulders. Sampling locations are shown.

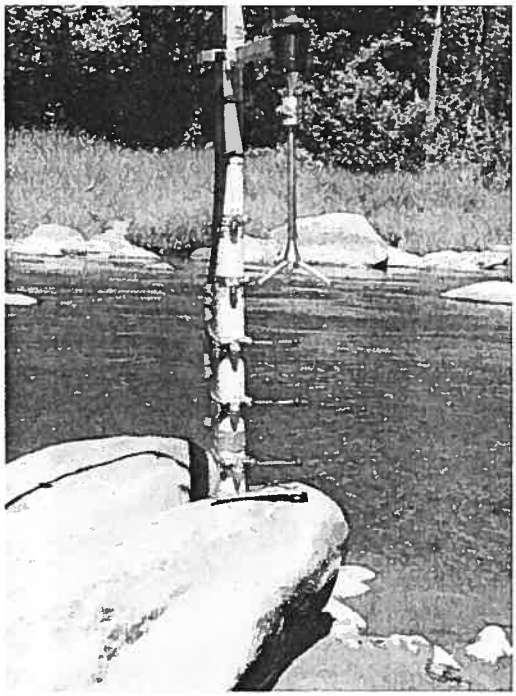

Figure 4.3 - Wading rod with ADV and three ECMs. Only the top ECM (at 25 cm) was used for this study.

4.2.2 *Signal Processing*

Raw ADV signals are often contaminated by electronic errors, Doppler noise, and errors due to velocity shear [*Voulgaris and Trowbridge*, 1998], and may contain spikes due to air bubbles traveling within the fluid [*Rodriguez et al.*, 1999], aliasing of the return signal above the Nyquist frequency ($f_N = f_s/2$) [*Goring and Nikora*, 2002], or other signal interference. ECM signals also suffer from errors due to electronic noise at high frequencies, although this error is mostly removed by an internal low-pass filter [*Roy et al.*, 1997], velocity shear within the sample volume, wake generation [*Aubrey and Trowbridge*, 1985], and spikes due to debris or other signal interference. Extensive use in the field has not found zero-drift to be a problem with the ECM probes utilized, and this was confirmed with zero tests before and after sampling. We processed the data series to minimize the effects of these sources of noise. Processing can also introduce bias into statistics, whether through filtering [*Roy et al.*, 1997], or spike removal [*Lane et al.*, 1998], making it necessary to process the data prior to analysis in a consistent manner. As a note, the convention used in this article is the definition of x, y, and z as the streamwise, vertical, and lateral dimensions, respectively, with corresponding velocity components defined as u, v, and w. U, V, and W represent mean velocities, while u_i, v_i and w_i represent the detrended fluctuations about the mean.

Data series were processed in three steps. An example of data processing showing the velocity signals and spectral plots from each is presented in Figure 4.4. To compare agreement in the inertial subrange with the Kolmogorov -5/3 law [*Kolmogorov*, 1941], lines at a -5/3 slope are included on the spectral plots. A line labeled f_v is also shown. The sampling volume of the utilized ECM is 70-140 times that of the ADV, and f_v indicates the frequency at which this larger volume is expected to result in a 10% decrease in spectral energy measured by the ECM as compared to the true spectral energy [*Soulsby*, 1980]

$$f_v = \frac{U}{7d_x} \tag{4.1}$$

where d_x is the dimension of the sampling volume in the direction of the flow. This line corresponds with a break in the spectral slope of the ECM (Figure 4.4a).

Following the recommendations of *Roy et al.* [1997], the first step of data processing was to remove the effect of the internal filter from the ECM velocity series. The

internal filter is an analog resistor/capacitance design that acts to dampen velocity fluctuations by applying a series of exponential weights to the measured data. This can be removed using deconvolution algorithms in such programs as Matlab in order to obtain the 'real' raw signal. This procedure slightly flattens the spectral slope in the inertial subrange, which tends to improve agreement with the Kolmogorov -5/3 law at frequencies up to f_s (Figure 4.4 a-b). In the second step, we removed spikes from both the ADV and ECM signals using the phase-space thresholding method developed by *Goring and Nikora* [2002]. While developed for spikes caused by aliasing of the Doppler signal, this method is based on turbulent flow properties rather than on specific ADV characteristics and was found to reliably remove spikes from ECM signals. In the third step of data processing we removed all high-frequency variance using a low-pass third order Butterworth filter with half-power frequencies calculated as a function of the sampling frequency ($f_{50} = f_s/2.93$), as recommended by *Roy et al.* [1997]. The effect on the ECM signal of this final step is negligible. The effect on the ADV signal is to effectively cut off the signal at the frequency where the spectral slope begins to deviate strongly from Kolmogorov's -5/3 law. Signals were not rotated to remove mean vertical components, because streamlines were not always parallel to the stream bed [*Roy et al.*, 1996b].

4.2.3 Data Quality Analysis

In order to examine the quality of the data obtained with the two instruments, we compared spectral plots of the velocity-time series, inspected internal ADV parameters, and calculated error estimates for the ADV using the methods proposed by *Voulgaris and Trowbridge* [1998], *McLelland and Nicholas* [2000], and *Smyth and Hay* [2003]. Spectral analysis is a powerful tool for assessing signal quality. Following the recommendations of *Lapointe et al.* [1996], electronic interference in the signals was identified by the presence of spikes in the power spectra. There is also an extensive literature on the typical form of spectral plots in turbulent flows (for e.g. *Kolmogorov* [1941]; *Frisch* [1995]; *Nikora and Goring* [1998]). In particular, the -5/3 first postulated by Kolmogorov and supported by numerous studies in a variety of turbulent flows is useful to identify deviations from expected results in the inertial subrange. The power spectra of the streamwise velocity component (S_{uu}) have been noted to systematically deviate from the -5/3 slope as a result of a noise floor [*Nikora and Goring*, 1998; *Voulgaris and Trowbridge*, 1998; *Kim et al.*, 2000]. We used this characteristic to estimate additional variance due to noise (σ_t^2) in a

manner similar to that utilized by *Voulgaris and Trowbridge* [1998]. The method can be understood with reference to Figure 4.5. The noise term (S_N) is equal to the difference between S_{fit} and the -5/3 law extended from the frequency range over which the Kolmogorov -5/3 law is applicable (f_k). σ_t^2 was then obtained by integrating S_N over the frequency range. This method, referred to as the noise floor technique, is relatively easy to apply when f_k is large and S_N is low, but is more subjective when f_k is small and S_N is large.

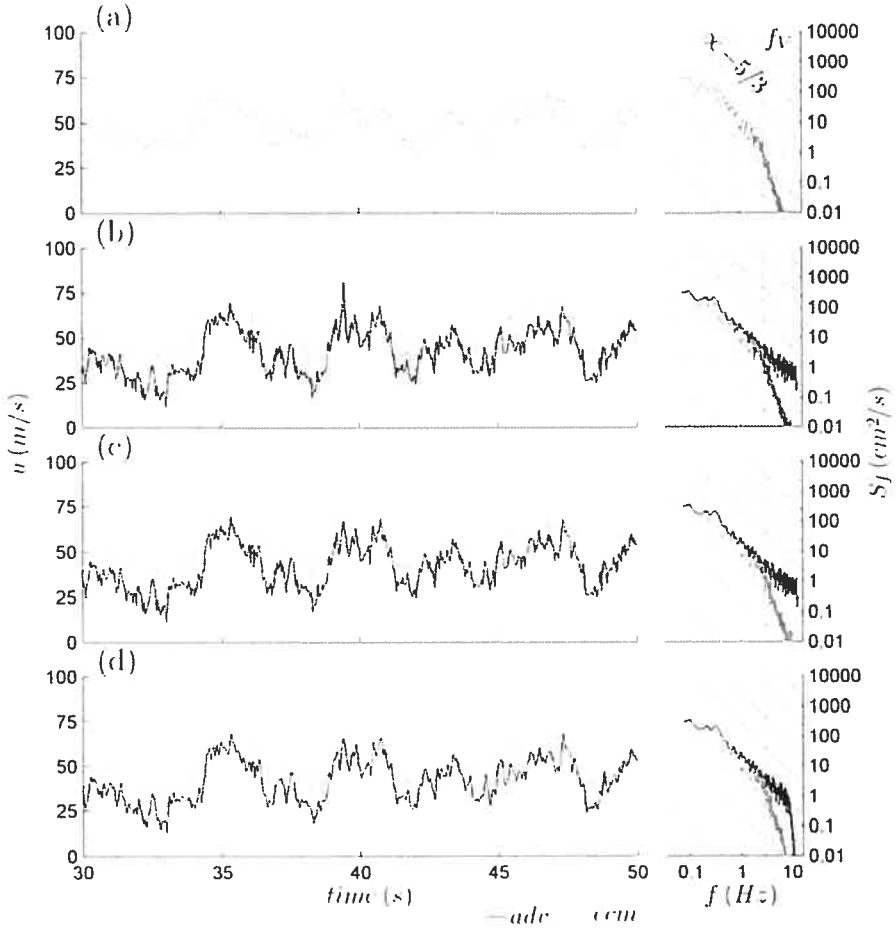

Figure 4.4 - Effect of quality assurance procedure on typical signal. Dashed lines facilitate comparison with Kolmorgorov's -5/3 law and f_v, the frequency at which the larger sampling volume of the ECM should reduce S_f by 10%. a) ECM signal output; (b) ECM signal after removal of internal filtering (note small increase of S_f near f_v) and the raw ADV signal; (c) ECM and ADV signals after de-spiking procedure; (d) ECM and ADV signals after filtering with third order Butterworth filter.

Internal ADV data quality parameters include the signal to noise ratio (*SNR*) and the correlation coefficient (R^2), a measure of the correlation between acoustic return signals. When measuring at 25 Hz, it is recommended by the manufacturer that $SNR \geq 15$ dB and $R^2 \geq 70$, although it may not be possible to achieve these levels in a highly turbulent flow

[*Sontek/YSI*, 2001]. These threshold values have largely been adopted as criteria to filter or discard data series [*Lane et al.*, 1998; *Elgar et al.*, 2001; *Bryan et al.*, 2003; *Schindler and Robert*, 2005], although other studies have used thresholds of $R^2 \geq 60$ [*McLelland and Nicholas*, 2000] and $R^2 \geq 50$ [*Nicholas*, 2001]. *Lane et al.* [1998] found a bias of the mean statistics of the velocity time series to occur when $R^2 \leq 85$. *Smyth and Hay* [2003] used R^2 to obtain a direct measurement of the variance due to noise (σ_t^2) :

$$\sigma_t^2 = -\ln R^2 \frac{c^2}{8\pi^2 t_a^2 f_{adv}^2} \tag{4.2}$$

where c is the speed of sound, t_a is the pulse duration, and f_{adv} is the operating frequency of the ADV (10 MHz). We will refer to this method as the correlation technique.

While a number of authors have attempted to quantify the sub-factors of the noise terms [*Cabrera et al.*, 1987; *Lemmin and Lhermitte*, 1994; *Zedel et al.*, 1996], the methods proposed by *Voulgaris and Trowbridge* [1998] and *McLelland and Nicholas* [2000], henceforth referred to as the VT98 and MN00 methods, were utilized in this study. These methods estimate the total variance due to noise (σ_t^2) as a function of phase shift (σ_s^2), Doppler noise (σ_d^2), and velocity shear (σ_u^2):

$$\sigma_t^2 = \sigma_s^2 + \sigma_d^2 + \sigma_u^2 \tag{4.3}$$

Phase shift is the sampling error due to the inability of the system to resolve the phase shift of the return pulse [*Zedel et al.*, 1996]:

$$\sigma_s^2 = \begin{cases} \dfrac{c^2}{16\pi^2 f_{adv}^2 t_a (f_s^{-1} - t_O)} K^2 \sigma_\phi^2 & [VT98] \\ \dfrac{c^2}{16\pi^2 f_{adv}^2 M (t_c^2 - t_b^2)} K^2 \sigma_\phi^2 R^2 & [MN00] \end{cases} \tag{4.4}$$

where K is a constant, σ_φ is the phase uncertainty, f_s is the sampling frequency, t_O is the overhead time used by the sensor (0.002 s), M is the number of pulse pairs measured during the sample period, and t_b and t_c are the durations of the first and second pulses in a dual pulse probe. Both VT98 and MN00 estimated $K^2\sigma_\varphi^2$ empirically from still water tests (Table 4.2). MN00 selected the points with $SNR > 15$ and $R^2 > 99$ to estimate $K^2\sigma_\varphi^2$ and it is for this reason that the MN00 estimates are much less than those of VT98. Instrument parameters M, t_a, t_b, and t_c are also listed in Table 4.2.

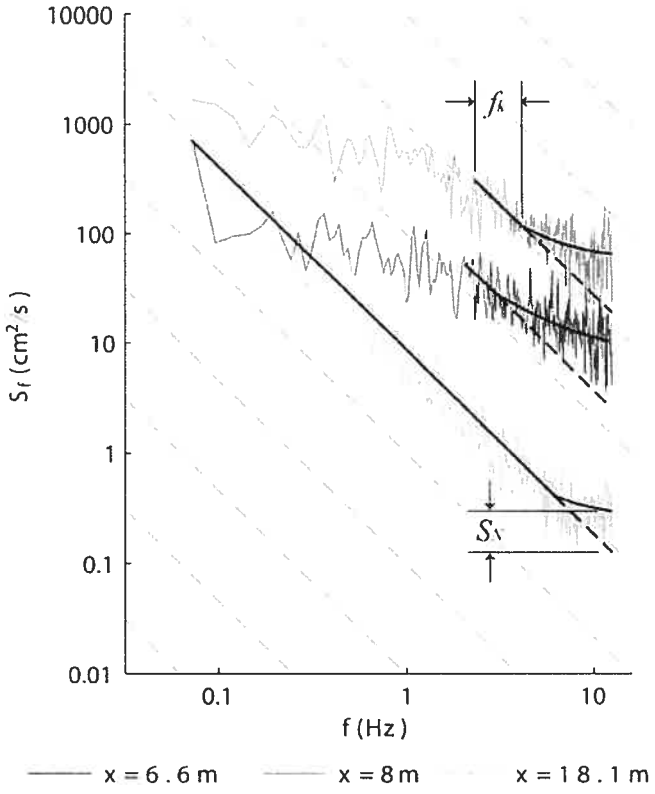

Figure 4.5 - Estimation of total variance due to noise (σ_t^2) using the noise floor technique. f_k is the frequency range over which the Kolmogorov -5/3 scaling law is applicable and S_N is the spectral noise calculated from the difference between the actual spectral density and the projected value. σ_t^2 is calculated by integrating S_N over the total frequency range.

Parameter	Method	Beam Velocity	
		± 100 cm/s	± 250 cm/s
$K^2\sigma_\varphi^2$	VT98	11.6	7.4
	MN00	0.0057	0.0057
M	VT98	9	9
	MN00	9	10
t_m (ms)	MN00	3.89	3.79
t_a (ms)	VT98	4.00	3.85
t_b (ms)	MN00	0.48	0.4
t_c (ms)	MN00	0.128	0.104

Table 4.2 - Parameters for estimation of ADV measurement errors. Values reported are from *Voulgaris and Trowbridge* [1998] (VT98) and *McLelland and Nicholas* [2000] (MN00).

Doppler noise (σ_d^2) is related to three factors: the residence time (B_r), turbulence decorrelation (B_t), and beam divergence (B_d). VT98 calculated the Doppler noise sub factors as:

$$B_r = 0.2\frac{U}{d_x} \tag{4.5}$$

$$B_t = 2.4\frac{f_{adv}}{c}(\varepsilon d_x)^{1/3} \tag{4.6}$$

$$B_d = 0.84\sin\theta\frac{f_{adv}U_h}{c} \tag{4.7}$$

where ε is the turbulence dissipation rate, θ is the bistatic angle (30°), and U_h is the mean cross beam velocity. From *McLelland and Nicholas* [2000]:

$$U_h = \sqrt{U^2+W^2}\cos\frac{\theta}{2} - V\sin\frac{\theta}{2} \tag{4.8}$$

The coefficients in Equations 4.5-4.7 are based on the geometry of the sensing volume [*Voulgaris and Trowbridge*, 1998]. These equations were derived in an unpublished manuscript [*Brumley et al.*, 1987, cited by *Cabrera et al.*, 1987] and their applicability to field situations has not been demonstrated. MN00 eliminated the need for coefficients in Equations 4.5-4.7 by assuming a uniform cylindrical sampling volume, and removed the assumptions about boundary layer structure implicit in the calculation of ε by relating B_t to the standard deviation of the radial velocity (σ_{vr}) such that:

$$B_r = \sqrt{\frac{U^2+W^2}{d_x^2}+\frac{V^2}{d_y^2}} \tag{4.9}$$

$$B_t = \frac{f_{adv}}{c}\sigma_{vr} \tag{4.10}$$

$$B_d = \sin\theta\frac{f_{adv}U_h}{c} \tag{4.11}$$

where d_y is the sample volume height. σ_{vr} is related to R^2 as:

$$\sigma_{vr} = \sqrt{\frac{c^2}{8\pi^2 f_{adv}^2}\frac{-\ln R^2}{(t_b+t_c+t_D)^2}} \tag{4.12}$$

where t_D is the dwell time that separates the pulses ($t_D = 560\text{x}10^{-6}$ s). The total Doppler noise is calculated as:

$$\sigma_d^2 = \begin{cases} \dfrac{c^2}{16\pi^2 f_{adv}^2}\dfrac{B}{Mt_a} & [VT98] \\ \dfrac{c^2}{16\pi^2 f_{adv}^2}\dfrac{B}{Mt_M}R^2 & [MN00] \end{cases} \tag{4.14}$$

where B is the root mean squared of the total Doppler bandwidth broadening $\left(B=\sqrt{B_r^2+B_t^2+B_d^2}\right)$, and t_m is the velocity measurement time (Table 4.2).

Velocity shear is related to the variation of velocity across the dimensions of the sampling volume. This term requires a number of assumptions about the form of the boundary layer that limit its application to uniform flows. Assuming linear variation of U over the height of the volume and no lateral or streamwise gradients, σ_u^2 is given by:

$$\sigma_u^2=\frac{\Delta U^2}{3} \tag{4.15}$$

where ΔU can be estimated from the law of the wall:

$$\Delta U=\frac{u^*}{\kappa}\ln\left(1+\frac{d_v}{y}\right) \tag{4.16}$$

where u* is the shear velocity (estimated using $u^*=\sqrt{0.2E_k}$, where E_k is the turbulent kinetic energy), κ is the Von-Karman constant ($\kappa \approx 0.4$), and y is the distance of the measurement volume above the bed.

4.2.4 Comparison of Turbulence Statistics

Common turbulent flow properties and quadrant analyses of the Reynolds shear stress as determined using both instruments were directly compared. Compared statistics included mean velocities of streamwise and vertical velocity components (U, V), the respective standard deviations (u', v'), turbulent kinetic energy in two dimensions $\left(E_k=0.5\rho\left(\overline{u_i^2}+\overline{v_i^2}\right)\right)$, where ρ = 1000 kg/m^3, and the Reynolds shear stress $\left(\tau_r=-\rho\overline{u_i v_i}\right)$. Quadrant analysis is useful for assessing the contribution of different types of turbulent events to the overall shear stress [*Lu and Willmarth*, 1973]. Quadrants (q) are defined as:

$$q=\begin{cases}1 \text{ if } u_i>0 \ \& \ v_i>0\\ 2 \text{ if } u_i<0 \ \& \ v_i>0\\ 3 \text{ if } u_i<0 \ \& \ v_i<0\\ 4 \text{ if } u_i>0 \ \& \ v_i<0\end{cases} \tag{4.17}$$

The contribution of each quadrant to the total Reynolds shear stress $\left(-\rho\overline{u_i v_{i,q}}\right)$ is calculated as:

$$-\rho\overline{u_i v_{iq}} = -\rho \lim_{T\to\infty} \frac{1}{T} \int_0^T u_i v_i(t)\, \eta(t,H)\, dt \qquad (4.18)$$

where H is the hole size, t is the time interval, T is the total number of time intervals, and:

$$\eta = \begin{cases} 1 & \text{if} \quad |u_i v_i(t)| \le H u' v' \\ 0 & \text{otherwise} \end{cases} \qquad (4.19)$$

Summary diagrams are typically presented in terms of the contribution of the various quadrants to the total shear stress (τ_r). This was slightly modified in this study as a result of near zero or negative total shear stresses in some locations, and we normalized $-\rho\overline{u_i v_{iq}}$ by the total shear stress from the positive quadrants q2 and q4 $\left(-\rho\overline{u_i v_{i24}}\right)$.

4.3 Results

4.3.1 Internal ADV Parameters

Mean *SNR* values ranged from 23 to 31 dB in the Eaton Nord with *SNR* standard deviations between 2.5 and 5.5 dB. Mean *SNR* values in the Nicolet River ranged from 37 to 48 dB with *SNR* standard deviations between 2.4 and 4.2 dB. Based on these values and the manufacturer's recommendation that $SNR \ge 15$ dB, signal strength was not considered to be an important factor in these tests, especially considering the strong signals obtained at Nicolet River, where mean velocities and turbulence intensities were higher. R^2 values were always greater than 90 in the Eaton-Nord River, indicating the measurements to be of excellent quality. R^2 values for the Nicolet River data were more variable, with values as low as 50 in fast and turbulent flows. To investigate the spatial variability, we plotted R^2 against a profile of water and bed surface elevations (Figure 4.6). Common statistics from ADV and ECM measurements are also included. To facilitate the presentation of results, the sampled river profile is separated into four distinct regions based on the character of the flow. In the upstream region, from 0-6 m, flow is moderately fast but relatively uniform, and $70 \le R^2 \le 85$. There is good agreement between the statistics derived from both instruments, although we note a difference between u'(adv) and u'(ecm). In the lateral constriction, R^2 decreases as the standard deviations and average flow velocity increase, and the differences between the estimates of the means, standard deviations, and E_k increase. This divergence continues in the lateral expansion section, where large differences are especially noted in v' and τ_r. In the deeper downstream section, from 13-20

m, R^2 value are larger than 90, and the agreement between all parameters is good, although again with a slight offset in u', with the ADV values being larger than those of the ECM.

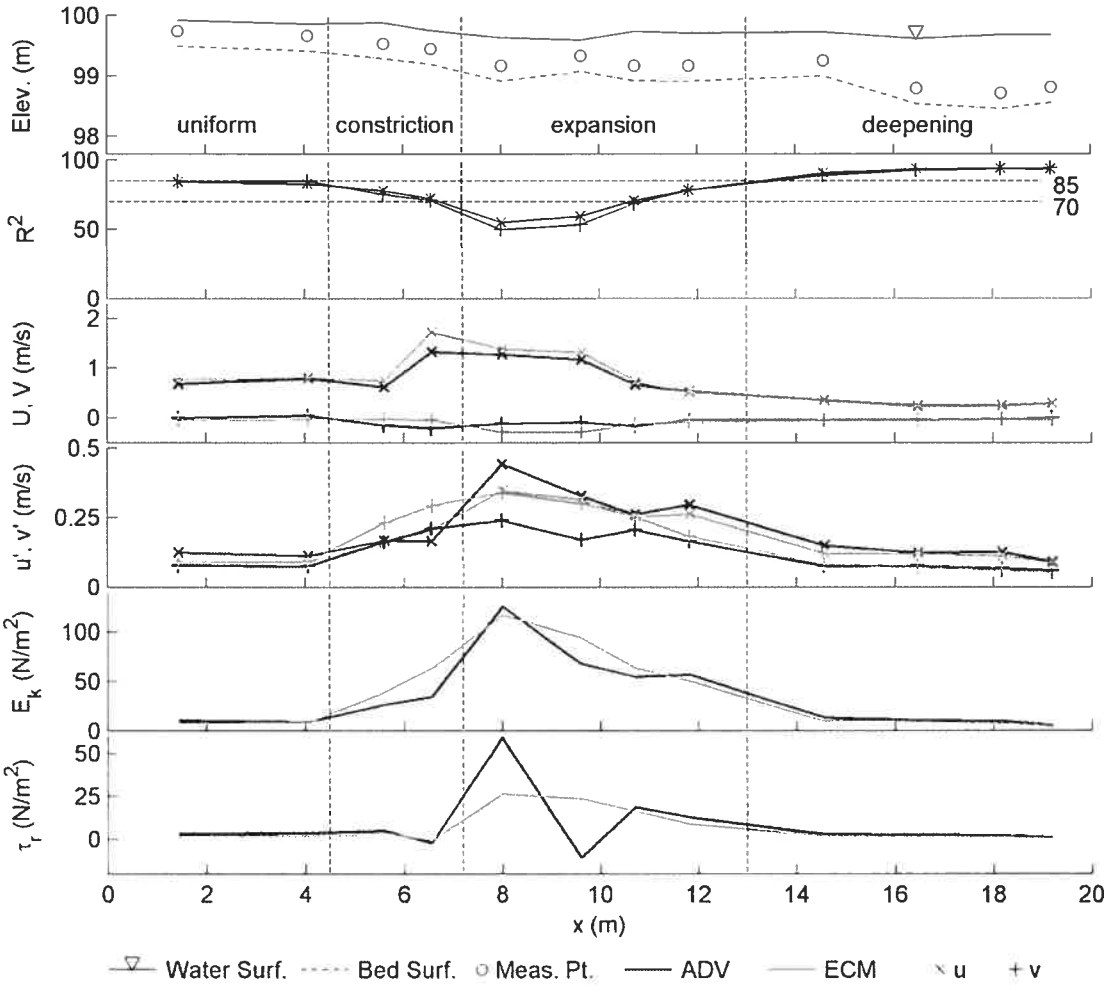

Figure 4.6 - Spatial plot of representative statistics in the Nicolet River. The sampled transect has been has been separated into four sections based on observed morphological control on flow dynamics.

4.3.2 Spectral Analysis

Spikes in the power spectra of ECM data, indicative of some electronic contamination of the signal, occur in 4 of 16 data series from the Eaton-Nord River, examples of which are shown in Figure 4.7. The source of the contamination is not known, although errors can occur due to low batteries, nearby electronic devices or power sources, and poor grounding [*Guza et al.*, 1988; *Lapointe et al.*, 1996]. Electronic contamination is not observed in the ECM data collected in the Nicolet River (Figure 4.8). At both the upstream and downstream limits of the test section in the Nicolet River, spectral slopes are in agreement with previous observations reported for gravel-bed rivers, as $S_{fu} \approx S_{fv}$ within

the inertial subrange of S_{fv}, the low-frequency boundary of the inertial region occurs at a lower frequency for S_{fv} than for S_{fu}, and the Kolmogorov -5/3 law is applicable to the inertial region of flow [*Sukhodolov and Rhoads*, 2001; *Nikora*, 2005]. Differences between the two instruments are largely restricted to the high frequency range at $f > 4$ Hz, where spectral densities are affected by the difference in sampling volumes. There is a tendency for S_{fu}(adv) to flatten out in the higher frequencies, a phenomenon that is the result of Doppler noise levels that are greater than signal variance close to the Nyquist frequency [*Lhermitte and Lemmin*, 1994; *Nikora and Goring*, 1998]. These errors are typically negligible in the vertical spectra as a result of probe configuration [*Lemmin and Lhermitte*, 1999].

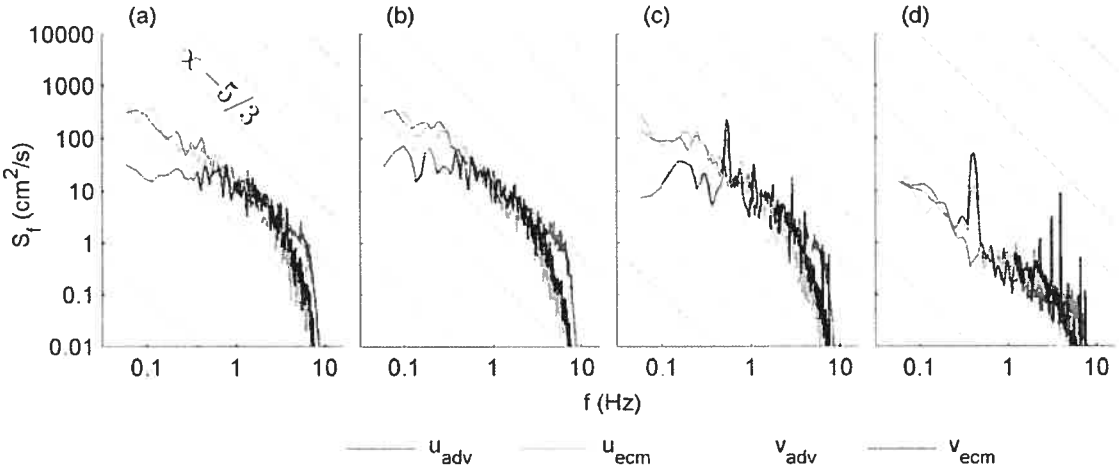

Figure 4.7 - Selected spectral plots of signals from the Eaton-Nord River. Spectra have been smoothed using the Welch technique to facilitate comparison between the signals [*Welch*, 1967]. Signal (a) and (b) are representative of twelve of the sixteen measured time series. Contamination is evident in (c) and (d). This occurred at four locations. Lower spectral energy is noted in plot (d), which was measured in a slack water area in the river.

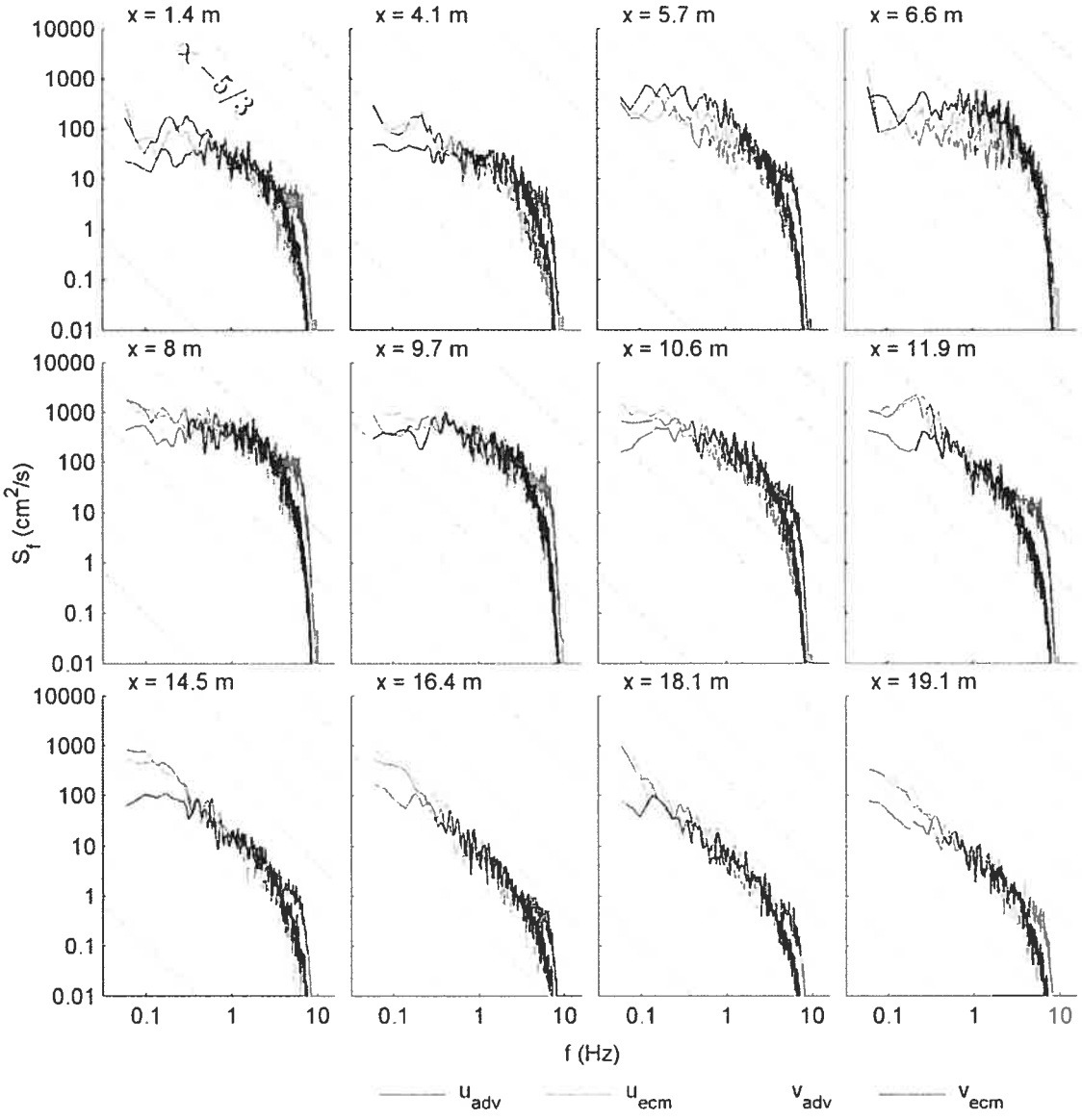

Figure 4.8 - Spectral plots of signals from the Nicolet River. Spectra have been averaged by subdividing the time series using the Welch technique to facilitate comparison between the signals.

Within the high velocity and high turbulence section of the flow constriction and expansion (x = 5.7-11.9 m), a number of observations are not in agreement with typical results from gravel-bed rivers. For the ECMs we note that $S_{fv} > S_{fu}$ at the measurement locations x = 5.7-6.6 m between the frequencies f = 0.1-1 Hz, and the presence of a broad peak in S_{fu} and S_{fv} between x = 5.7-8 m that reduces the range over which the slope of the spectra follow the -5/3 law. Broad peaks can form as a result of shedding eddies [*Venditti and Bennett*, 2000], which may originate in the separation zone in the lee of the ECM probe

[*Aubrey and Trowbridge*, 1985]. We used the Strouhal number (N_s) to estimate the frequency of vortex shedding (f_e) from the probe head:

$$f_e = N_s \frac{U}{d} \tag{4.20}$$

where Ns is the Strouhal number (from *Achenbach* [1974], $N_s \approx 0.2$ for $Re > 2x10^5$), and d is a length scale (in this case d = 0.013 m - the probe diameter). Based on this calculation, f_e = 15 and 23 Hz for average velocities of 1.0 and 1.5 m/s, respectively, which is higher than the Nyquist frequency of 10 Hz. An alternate explanation is therefore required to explain the occurrence of broad peaks in the energy spectra. The derivation of the Kolmogorov -5/3 law assumed no energy production or dissipation [*Frisch*, 1995]. Close to the source of turbulence generation such as jets, wakes, and very close to the wall, these assumptions break down [*Yahkot*, 1998] and spectral peaks can occur [*Grinstein and Devore*, 1996] as is observed over dunes [*Venditti and Bennett*, 2000]. In laboratory tests on accelerating fluids, *Kironoto and Graf* [1995] observed broad peaks in spectral energy at frequencies close to f = 1 Hz, especially in the vertical component. It thus appears that flow non-uniformity is the likely source of the spectral anomalies identified in the ECM signal.

For the ADVs we note that: spectral slopes are flatter than -5/3 over all frequencies from x = 5.7-6.6 m; $S_{fv} > S_{fu}$ in the measurement locations x = 5.7-6.6 m between the frequencies f = 0.1-1 Hz; and $S_{fu} > S_{fv}$ over all frequencies in the measurement locations x = 8-9.7 m. Flat spectral slopes at high frequencies occur as a result of Doppler noise. In this case, however, S_{fu} is flat at low frequencies and S_{fv} is also relatively flat. One possible explanation is that flatter slopes are related to the suppression of turbulence in the lower frequencies as a result of acceleration. It is interesting to note how S_{fu}, in particular, is reduced right at the maximum constriction (x = 6.6 m) in the low frequencies while higher frequencies increase. This explanation is not supported, however, by limited observations in accelerating flows. *Kironoto and Graf* [1995] found a -5/3 slope to be applicable to the inertial subrange in both decelerating and accelerating flows. Also problematic is the second observation, the separation between S_{fv} and S_{fu} within the inertial subrange. Within this range, turbulent structures are typically three-dimensional, which means that S_{fv} should be greater than S_{fu} [*Monin and Yaglom*, 1981], although in natural rivers, it is more frequently observed that $S_{fv} \approx S_{fu}$ [*Sukhodolov and Rhoads*, 2001; *Nikora*, 2005]. S_{fv}(adv) is clearly an outlier in this area, consistently below S_{fu}(adv), S_{fu}(ecm), and S_{fv}(ecm), which

suggests that there is a failure in the measurement of v with the ADV when turbulence is high.

4.3.3 Error Analysis

The error terms responsible for noise in the ADV signals were estimated using both the VT98 and the MN00 methods (Figure 4.9). We present both the sub factors that contribute to Doppler noise (turbulence, residence time and beam divergence) and the errors that contribute to total noise (phase uncertainty, Doppler noise, and velocity shear). In the Eaton-Nord River, $\sigma_t^2 = 0.1\text{-}0.2$ cm^2/s^2, which is in agreement with *Voulgaris and Trowbridge* [1998] and *McLelland and Nicholas* [2000]. In the Nicolet River, absolute errors increase as velocity and turbulence increase and the maximum error of $\sigma_t^2 \approx 0.9$ cm^2/s^2 occurs in the expansion zone. Beam divergence and velocity shear are the most significant contributors to overall noise. These factors are related to the mean flow velocity, and overall error estimates at high velocity will be similar, regardless of the level of turbulence. There is a lack of response in the turbulence error (σ_d^2) to increasing turbulence. σ_d^2 is a function of shear velocity using the VT98 method, but contributions are never more than a few percent of the overall noise. MN00 attempted to reduce the reliance on calibrated constants and prior knowledge of the structure of the boundary layer by incorporating R^2, but these changes reduce σ_d^2 to negligible levels in our field tests. In addition, as is most evident in the difference in σ_s^2 between the two methods, the effect of the introduction of R^2 to Equations 4.3 and 4.14 is to reduce these sources of error when R^2 is low, a direction of change that is counter intuitive.

A comparison of the four methods used to estimate the total signal variance due to noise (σ_t^2) is shown in Figure 4.10. σ_t^2 is normalized by the total variance $(u')^2$ and plotted versus U(adv) for both the Eaton Nord and Nicolet Rivers. A single point with negative velocities and for which the relative error was high was not plotted. The main observation is that overall noise as estimated with the VT98 and MN00 has a neutral or slightly negative relation with U. This is contrary to the positive relation between noise and U that is expected based on theoretical grounds [*Lemmin and Lhermitte*, 1999] and the estimates of total error from the noise floor and the correlation techniques. This result is in agreement with *Garcia et al.* [2005], who argued that the VT98 and MN00 techniques will provide a lower bound of the instrument noise level. They do not account for uncontrolled variables in the field such as levels of seeding and the presence on bubbles in the water due

to the entrainment of air within the flow, and cannot predict a reduction in signal variance as a result of the ADV sampling protocol.

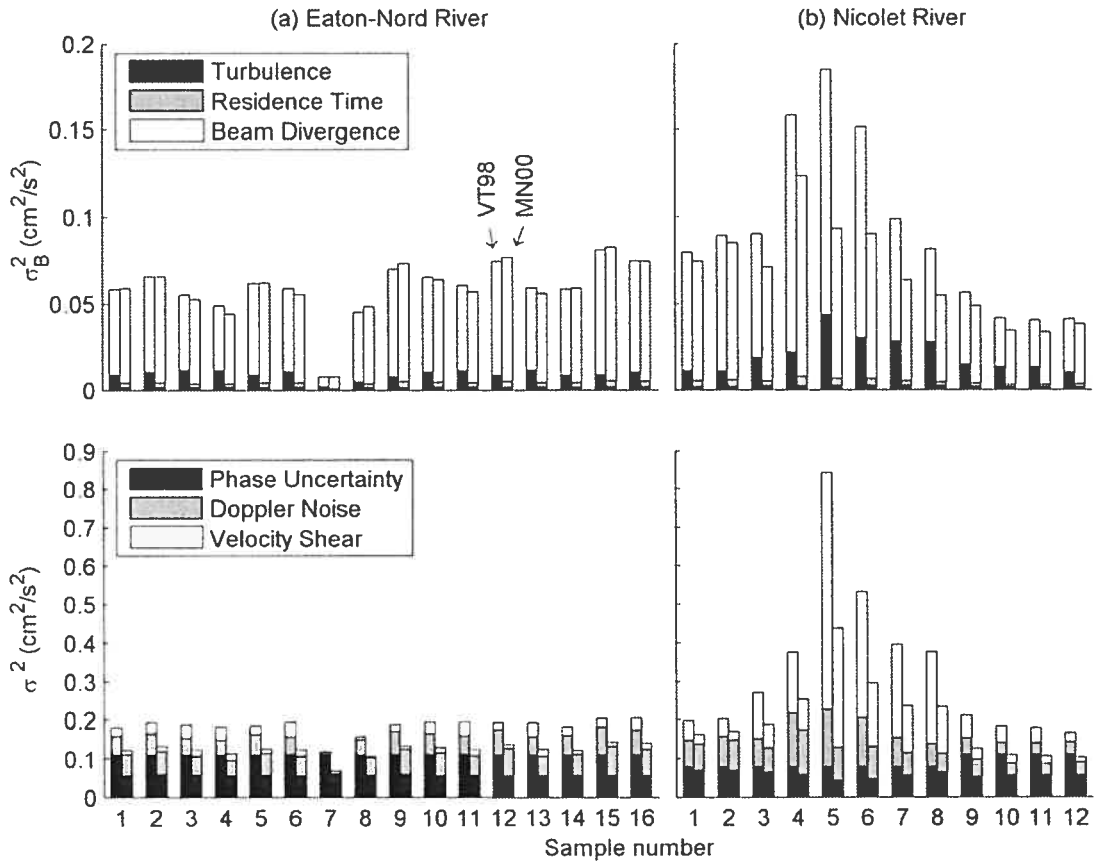

Figure 4.9 - Variance in the ADV signal due to noise as estimated using the *Voulgaris and Trowbridge* [1998] (VT98) and *McLelland and Nicholas* [2000] (MN00) techniques: (a) subcomponents contributing to Doppler noise, and (b) components contributing to total noise.

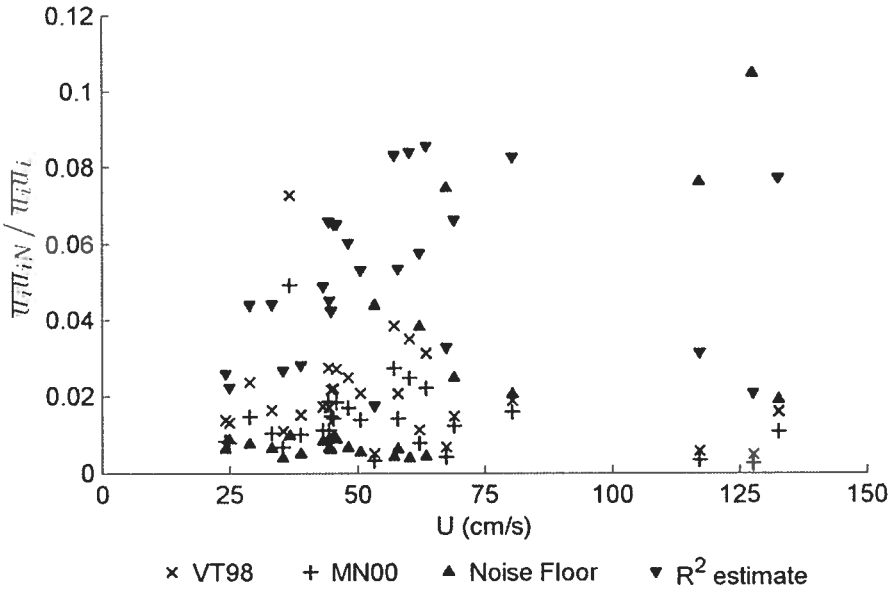

Figure 4.10 - Variance due to noise in the streamwise normal shear stress (σ_t^2) normalized by the total variance in streamwise normal shear stress ($\overline{u_i^2}$) and plotted against mean downstream velocity. Error estimates using the VT98, MN00, the noise floor, and the correlation methods are shown.

4.4 Comparison of Turbulent Flow Parameters and Discussion

Figure 4.11 shows the comparisons of means, standard deviations, E_k, and τ_r as obtained from each instrument in both rivers. Data points of potentially poor quality due to contamination and low correlation ($R^2 \leq 70$) are highlighted. Lines of perfect agreement are shown and the variance explained by these lines (p^2) for all data and with poor quality data points removed, is listed in Table 4.3. Overall, the most important result from Figure 4.11 and Table 4.3 is the strong agreement shown by the two instruments. Means of velocity components are in agreement near to the origin, although offset differences on the order of 2-3 cm/s are visible. Relative to the ADV, the ECM recorded higher U and lower V. These offset errors are less than the 10 cm/s reported by *Lane et al.*, [1998], and much better than the discrepancies found by [*Rodriguez et al.*, 1999]. The larger differences found by *Rodriguez et al.* [1999] could be at least partially explained by the larger (0.038 m) diameter ECM probe used in their study. Sources of error that lead to an offset include differences in instrument alignment and/or poor calibration of the ECM [*Lane et al.*, 1998]. Voltage differences captured by the ECM probes are relatively weak, and these voltages are amplified prior to data storage. Amplification can be adjusted during calibration, but differences between sites mean that small offset errors are difficult to eliminate [*Aubrey*

and Trowbridge, 1985], especially for measurements in natural rivers [*Guza et al.*, 1988]. At higher values of U, the ECM recorded higher values than the ADV, although only one point has an error larger than 10%. ECMs have been shown to have good low-frequency response up to 300 cm/s [*Elgar et al.*, 2001]. *Aubrey and Trowbridge* [1985] tested for the occurrence of flow separation around the spherical head and found a non-linear behavior in the streamwise component of the flow, with a point of inflection close to $U = 0.80$ m/s. However, this error was only 1.2% at $U = 2.0$ m/s and the probes used in that study were three to seven times larger than those utilized for these field tests. For V, the relation is inconsistent, as the ECM recorded both higher and lower values away from the origin. Of all the parameters investigated, V is the most likely to be strongly affected by the spatial error inherent in the distance between the sampling volumes. These points in the extreme ranges of the plots are from the Nicolet River, and they typically correspond with low internal correlation coefficients ($R^2 \leq 70$). The values of p^2 increase for all parameters when these points are removed from the analysis (Table 4.3). ECM signals affected by electronic noise plot close to the lines of agreement and p^2 decreases when these values were removed, indicating that this problem did not bias the mean velocities in this test.

The agreement between the values obtained from the two instruments for u' is similar to what has been observed for U with only one or two points that show significant discrepancies. These points occur when u' is large and R^2 is low. There is an offset error noted for the full range of values, with the ECM recording systematically lower values than the ADV. This offset error is no more than 3 cm/s and can be explained by the ability of the ADV to capture a larger proportion of the actual variance by resolving more of the inertial subrange, and by the Doppler noise in the ADV measurements that produces the noise floor. p^2 increases when points with low R^2 values are removed from the analysis. The removal of points with evident contamination has the inverse effect, indicating that this source of noise does not bias estimates of standard deviation in this test. It would be useful to know if there is a relation between U and the error in u'(ecm) or v'(ecm), but these values were not reported in laboratory studies published in the literature. *Guza et al.* [1988] did look at u' and v' in an oscillating flow environment and found that a spherical and an open frame ECM were within a range of ± 5%, indicating that the intrusive nature of the head only has a minor effect on flow dynamics in the vicinity of the probe.

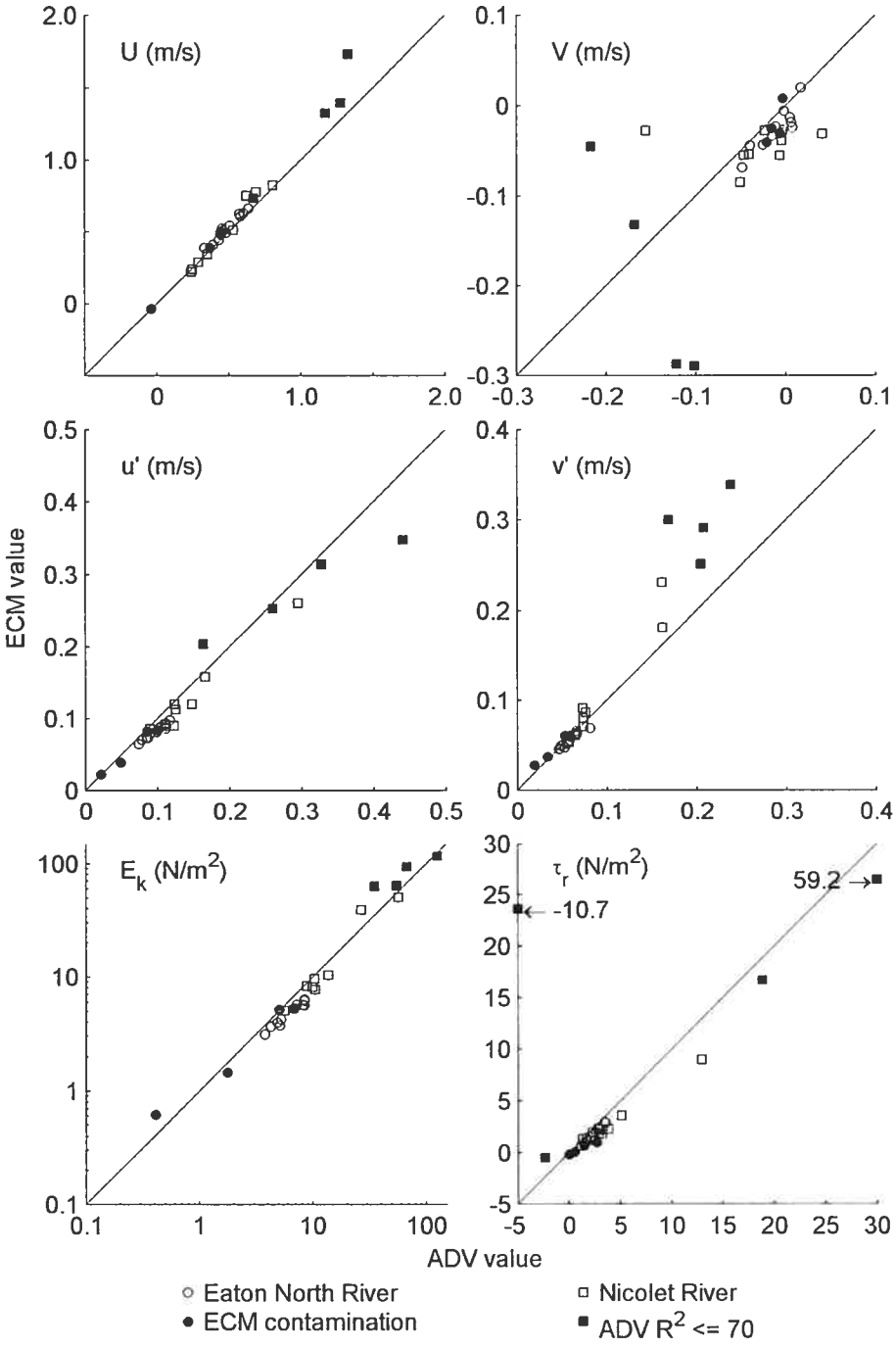

Figure 4.11 - Comparison of mean velocities (U, V), standard deviations (u', v'), turbulent kinetic energy (E_k), and Reynolds shear stress (τ_r) of velocity time signals measured using an ADV and an ECM.

Parameter	p^2		
	all data	without •	without ■
U	0.979	0.949	0.992
V	0.874	0.841	0.933
u'	0.969	0.946	0.97
v'	0.808	0.693	0.923
E_k	0.938	0.931	0.949
τ_r	0.78	0.764	0.914

Table 4.3 - Variance explained by the line of agreement (p^2) for all data, without points where ECM series were contaminated with electronic noise (•), and without points where low R^2 values (■) were recorded by the ADV.

No systematic offset between the two instruments is visible for v'. This is the result of less Doppler noise in the vertical velocity component [*Lemmin and Lhermitte*, 1999]. At high v' values there is a trend of increasing discrepancy between the estimates of v' from the two instruments, with a point of inflexion around 15 cm/s. v'(adv) is about 10 cm/s less than v'(ecm) when v'(ecm) $\approx$ 35 cm/s. One possible explanation is the more limited sampling range in v inherent in ADV probe design, which for beam velocity $u_{beam} = \pm 250$ cm/s is $v = \pm 90$ cm/s. Aliasing will occur sooner in the vertical component and, because V typically fluctuates around zero, incorrect data points are not likely to appear in a distinct range, as often occurs for U. This diminishes the efficiency of the spike detection and removal schemes. As a test, we replaced all values in the ECM signals where $|v| > 90$ cm/s with $v = 0$. This replacement reduced the peak v' from 33.9 to 31.2 cm/s and had no effect for $v' \leq 23$ cm/s, which means that this explanation is not sufficient to account for the observed difference between instruments. *Sontek/YSI* [2001] recommends that turbulence should not exceed 5% of the velocity range, which corresponds with $v' = 12.5$ cm/s for $u_{beam} = \pm 250$ cm/s. This value agrees with the observed point of inflection of v' (Figure 4.11). No discussion of this 5% limit was found in other studies. Additionally, contrary to expectations from the error analysis techniques, this error appears to affect v more than u. The observed error is not the result of an additive error, or noise. Instead, the sensitivity of v compared to u and the reduction of spectral density indicate suggest a subtractive error. This is thought to be related to the inability of the ADV to measure all of the true variance in high turbulence due to the filtering effects of the ADV sampling methodology as identified by *Garcia et al.* [2005].

The E_k estimates from the two instruments seem to agree over the range of values obtained in this test (Figure 4.11). The log scale, however, appears to hide the tendency of the ECM to overestimate E_k relative to the ADV where E_k is high. Also, an offset difference is present in the midrange of the plot, with the ECM tending to underestimate E_k relative to the ADV. p^2 increases slightly when signals with low R^2 values are not considered. The removal of points with electronic contamination does not improve the agreement in E_k. τ_r estimates are more variable. Very large errors are associated with two points for which R^2 is low, and p^2 increases markedly when these points are removed (Table 4.3). Similar to E_k, the removal of points with electronic contamination does not improve the agreement in τ_r.

Average contributions of the various quadrants to the shear stress $\left(\overline{u_i v_{iq}}/\overline{u_i v_{i24}}\right)$ are shown for both the ECM and the ADV in Table 4.4. Event structure agrees well with other studies, as quadrants 2 and 4 contribute more to τ_r than the other two quadrants, which results in a net positive shear stress, and $\overline{u_i v_{i2}} > \overline{u_i v_{i4}}$ [*Lu and Willmarth*, 1973; *Luchick and Tiederman*, 1987; *Roy et al.*, 1996a]. Quadrant 1 contributes a larger percentage when measured with the ECM, and while contributions from quadrants 2 and 4 are slightly reduced in comparison with the ADV, these differences are minor. In addition to the mean statistics, the mean and standard deviation of the difference (Δ) between ECM and ADV measurements are shown for both the Eaton-Nord and the Nicolet Rivers. In comparing the two rivers, the most striking observation is the large standard deviations of the quadrants 1 and 3 in the Nicolet compared to the Eaton-Nord River. The standard deviation of $\Delta\overline{u_i v_{iq}}/\overline{u_i v_{i24}}$ also increases by 50% for quadrants 2 and 4 in the Nicolet River, but this difference is small compared to the order of magnitude change observed for quadrants 1 and 3.

To examine the differences in the structure of the Reynolds shear stress in more detail, we have plotted the quadrant contributions at various hole sizes for all measurement positions in the Nicolet River (Figure 4.12). A broad agreement exists in terms of the contributions of positive and negative events between the two instruments. Contributions from quadrants 1 and 3 increase from x = 1.4 m toward the flow constriction at x = 6.6 m, but this result is consistent with observed shifts in the Reynolds shear stress as Reynolds number increases [*Lu and Willmarth*, 1973; *Priyardarshana and Klewicki*, 2004]. From x

= 8 to 9.7 m, a strong disagreement exists in the total Reynolds shear stress. Very small contributions from quadrants 1 and 3 result in a large ADV estimate of τ_r at x = 8 m and vice-versa at x = 9.7 m. In contrast, ECM estimates are similar to the values upstream and downstream of this expansion zone. These observations indicate that disagreement between the two instruments is largely restricted to the quadrants 1 and 3 in the highly turbulent zone and that the performance of the ADV is erratic in this case.

Quadrant	Eaton - Nord			Nicolet
	ECM	ADV	Δ	Δ
1	-0.18 (0.064)	-0.14 (0.037)	0.038 (0.042)	0.0017 (0.21)
2	0.51 (0.045)	-0.53 (0.042)	0.013 (0.033)	0.012 (0.053)
3	-0.16 (0.054)	-0.15 (0.045)	0.013 (0.038)	-0.027 (0.44)
4	0.49 (0.045)	0.47 (0.042)	-0.013 (0.033)	-0.012 (0.053)

Table 4.4 - Summary of contributions by quadrant to the overall Reynolds shear stress . Results for the Eaton-Nord River are averaged to give mean values for the ECM and ADV measurements. Standard deviations are shown in parentheses. Also shown is Δ - the mean and standard deviations of the difference between ECM and ADV measurements. Only Δ is shown for the Nicolet River as the non-uniform flow environment did not allow for spatial averaging.

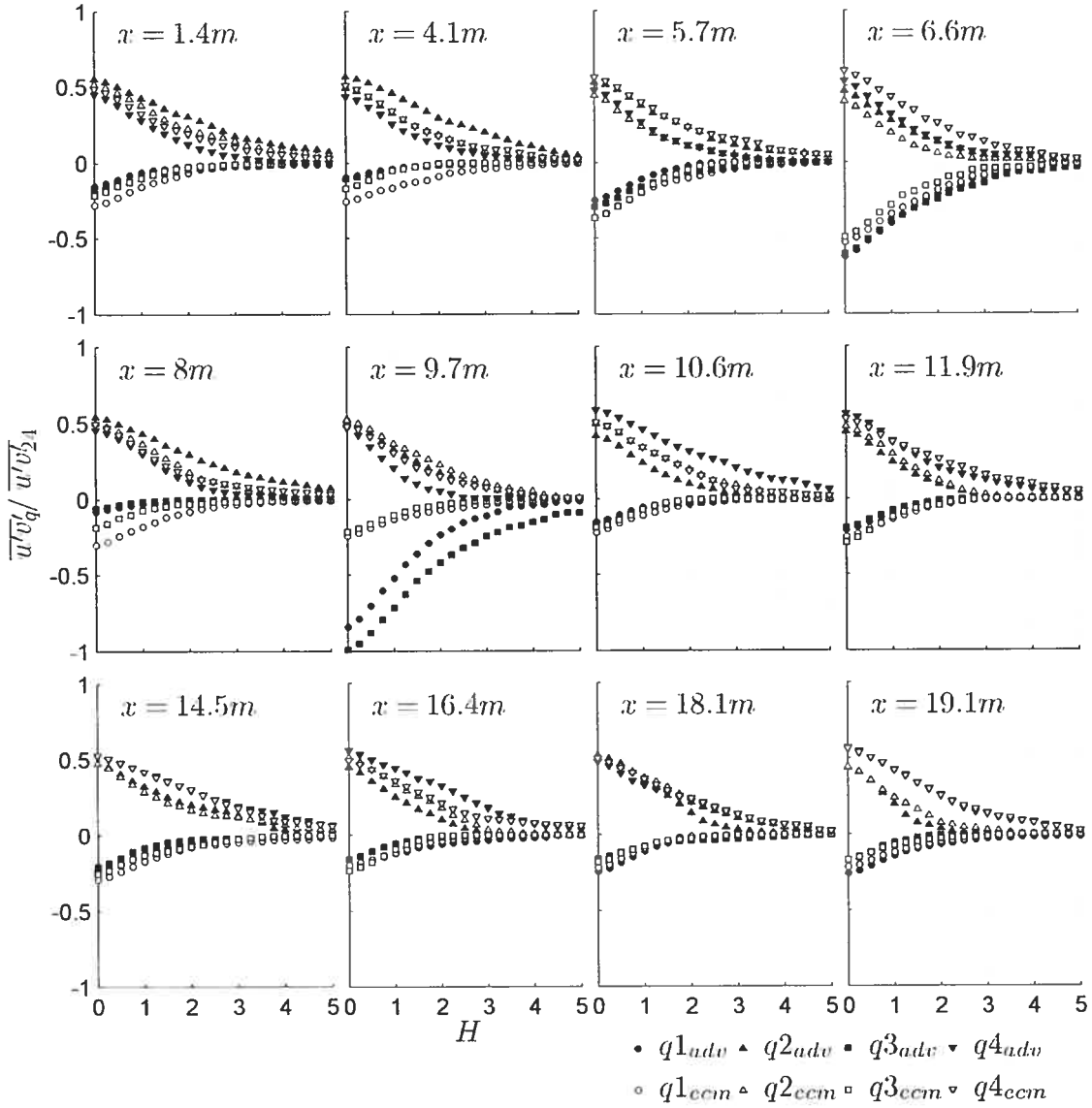

Figure 4.12 - Hole size analysis of Reynolds shear stress contributions by quadrant for measured time series in the Nicolet River for both the ADV and the ECM measurements. The Reynolds shear stress of each quadrant has been normalized by the total Reynolds shear stress in quadrants 2 and 4 $\left(\overline{u_i v_{iq}}/\overline{u_i v_{i24}}\right)$

4.5 Conclusion

ECMs and ADVs are designed to measure the same phenomenon, namely the velocity of water at high frequencies in more than one dimension. Under most conditions and subject to certain limitations, the instruments perform generally as expected. For the common turbulent statistics measured here, the agreement between the ECM and the ADV is > 90% if points with $R^2 \leq 70$ are not considered, an important result given that previous

comparative tests have not been conclusive. This allows results from ECM and ADV measurements to be discussed interchangeably in most cases. A more difficult situation arises when the measurements are carried out in highly turbulent flows. ECMs capture less of the inertial subrange than ADVs. This limitation is related to well-known differences in internal filtering, sampling frequency and sampling volume. ECMs have the significant advantage, however, that measurements are taken at a time instant rather than over a time interval. We have found no evidence of instrument failure as velocities and turbulence levels increase and they are thus suitable for characterizing turbulent river environments such as step-pool systems and rivers in flood. ADVs are non-intrusive, do not require calibration, and measure at higher frequencies, in three-dimensions, and with a smaller sampling volume than the ECM. These features have led to the rapid acceptance and utilization of the ADV in a wide range of environments. Nevertheless, spectral anomalies, measured increases in noise from the power spectra, and decreasing correlations indicate that ADV error increases as a result of turbulence, particularly in the vertical component. This problem manifests itself as a decrease in signal variance and appears to be related to the sampling protocol in that single recordings require correlated measurements over a time interval. High turbulence decorrelates measurements over the time interval and prevents accurate measurement. More testing of the subcomponents of Doppler noise, particularly turbulence, is needed before available error estimation techniques can be applied with confidence.

Linking Paragraph C

The modeling exercise in Chapter 3 demonstrated that a link between flow acceleration and turbulence intensity could lead to the development of large-scale bed forms. This link was hypothesized from flume studies, observations over dunes, and a few exploratory investigations of turbulence in pools. Spatially intensive field data from a riffle-pool that measures flow properties at a range of discharges is needed. This article[3] presents the first results from the main field site. The objectives of this article are to characterize the mean velocity and turbulence intensity during floods up to and including bankfull discharge and, from this, to refine existing conceptual models of flow hydraulics in a pool. The dataset we gathered is unique in terms of instrumentation, sampling density, and the measured range of discharges. Flow hydraulics in the forced pool are shown to be dominated by deceleration and acceleration in the pool-head and pool-tail, respectively. While this fact is evident from a simple consideration of flow continuity, the implications of non-uniform flow on the distribution of mean velocity and turbulence intensity have not been considered in explanations of riffle-pool formation. The measurements presented here support the velocity reversal mechanism, which is often invoked as an explanation for the formation and maintenance of riffle-pools, but only in the pool-tail, where topographically induced acceleration and high velocities near the bed occur. In the pool-head, deceleration means that high flow velocities are concentrated near the center of the channel close to the water surface. Mean velocities near the bed are close to zero and cannot account for sediment transport and pool maintenance in this area. A secondary mechanism is necessary. It was found that large differences in mean velocity create steep velocity gradients in the outer flow region. This appears to generate large amounts of turbulence in the pool-head and strong turbulent intensities occur near to the bed. It suggests that turbulence may account for sediment transport and scour in the pool-head. The agreement with modeling results in Chapter 3 suggests that, although non-uniform flow and turbulence generation may be induced by a forcing element, the general model may also apply to autogenetic bed forms.

---

[3] MacVicar, B. J., and A. G. Roy, (*submitted*), Flow dynamics of a forced pool in a gravel-bed river Part A: Mean velocity and turbulence intensity, *Water Resources Research.*

5 FLOW DYNAMICS OF A FORCED POOL IN A GRAVEL-BED RIVER PART A: MEAN VELOCITY AND TURBULENCE INTENSITY

5.1 Introduction

Pools occur in a wide variety of riverine environments, ranging from gently sloped meandering systems in which pools tend to form in the bends, to steep step and cascade systems in which pools form in zones of plunging flow. Pool-riffle systems occupy a middle ground, occurring at slopes of less than 1.5 %, relative roughness values (D_{90}/Y) of less than 0.3 at bankfull stage [*Montgomery and Buffington*, 1997], and heterogeneous gravel-bed sediments [*Lisle and Hilton*, 1999; *Thompson and Hoffman*, 2001]. The forms are known to be stable through a range of flow stages [*Church and Jones*, 1982; *Eaton and Lapointe*, 2001], a property that is important for fish habitat [*Inoue and Nunokawa*, 2002; *Edo and Suzuki*, 2003]. An understanding of how these forms develop and are maintained is necessary for stream restoration and management [*Newbury and Gaboury*, 1993; *Buffington et al.*, 2002].

In spite of a number of studies, there is a lack of consensus on the mechanism that is responsible for the formation and maintenance of pools and riffles [*Clifford and Richards*, 1992; *Milan et al.*, 2001; *Wilkinson et al.*, 2004]. Proposed mechanisms can be separated into two groups, the first consisting of mechanisms arising from particle interactions, and the second being related to the flow. Particle interactions are related to the kinematic wave theory [*Langbein and Leopold*, 1968], which states that sediment waves form when particles interact to reduce the effectiveness of fluid forces. *Clifford* [1993a] and *Sear* [1996] confirmed that this process occurs in riffles. However, unlike step-pools, which scale with particle sizes [*Chartrand and Whiting*, 2000], pools and riffles generally scale with channel width [*Leopold and Wolman*, 1957; *Richards*, 1976; *Madej*, 1999], a parameter that is strongly related to the discharge [*Kellerhals and Church*, 1989]. In addition, recent modeling results suggest that, in order to account for bed forms at the scale of pools and riffles, the effects of a non-uniform bed on turbulence generation must be considered (*see Chapter 3*). Flow mechanisms that have been proposed include energy dissipation [*Yang*, 1971; *Walker et al.*, 2004], velocity reversal [*Keller*, 1971; *Lisle*, 1979;

Wilkinson et al., 2004], and turbulent vortices [*Yalin*, 1971; *Clifford*, 1993a; *Sear*, 1996; *Hassan and Woodsmith*, 2004; *Thompson*, 2004]. Interestingly, the three types of flow mechanisms were originally proposed in the same year and, in spite of a number of mutations of the original theories, all three are still invoked to this day.

While a number of studies have been undertaken, the review work of *Clifford and French* [1992] demonstrated that many studies suffer from inadequate field data to convincingly demonstrate or reject any of the competing theories. Common limitations are the assumption of a logarithmic shape for the velocity profile in non-uniform flows [*Teleki*, 1971; *Lisle*, 1979, *Petit*, 1987; *Milan et al.*, 2001; *Walker et al.*, 2004], inadequate spatial coverage [*Keller*, 1971; *Bhomick and Demissie*, 1982; *Robert*, 1997], and instrument failure or an inability to measure critical points during flood conditions [*Carling*, 1991; *Whiting and Dietrich*, 1991; *Sear*, 1996; *Thompson et al.*, 1998]. In addition, only a few studies have considered the role of turbulence [*Clifford*, 1993a; *Clifford*, 1996; *Thompson*, 2004; *Thompson*, 2006]. The result of these problems is that contradictory results are common [*Clifford and French*, 1992]. More field research is needed that meets minimum standards of spatial density, characterizes high flood stages, and measures turbulent flow parameters.

We undertook an intensive field-based study of the flow hydraulics in a single riffle-pool unit. The pool location is 'forced', as it is associated with a large tree with its root wad intact that has slid into the channel as a result of a bank failure. This limits the applicability of the results in 'free' pools. Flow dynamics are resolved to a finer scale than what has been possible in other studies, however, and we hope to generalize the results by considering the physics of riffle-pools with and without forcing elements. The objectives are to (a) characterize the mean velocity and turbulence intensity in a forced-pool over a range of flood levels up to and including bankfull flow, and (b) assess the relative merits of existing conceptual models of flow hydraulics in riffle-pools. In this article we revisit and refine the velocity-reversal hypothesis by reconciling apparently contradictory evidence, incorporating the variable of turbulence intensity, and supporting our field data with results from laboratory studies of non-uniform flows. In a companion article we analyze the structure of turbulent events and discuss the role of coherent vortices in pool formation and possible sources of pool-riffle scaling.

5.2 Methodology

5.2.1 Field Site

Moras Creek is a gravel-bed river located in eastern Quebec, Canada. A Trimble 5700 GPS system with a vertical and horizontal accuracy of 5 mm was used to survey the topography of the channel and floodplain of the surrounding area (Figure 5.1). The channel is slightly sinuous but does not exhibit a regular meandering pattern. Impingement on the valley wall is common and a heterogeneous glacial till contributes a wide range of particle sizes to the creek. Land cover in the watershed is forest with limited open fields and pasture. Anecdotal references indicate the channel was straightened in the early part of the 20th century to transport cut logs. The riparian area at the site is forested.

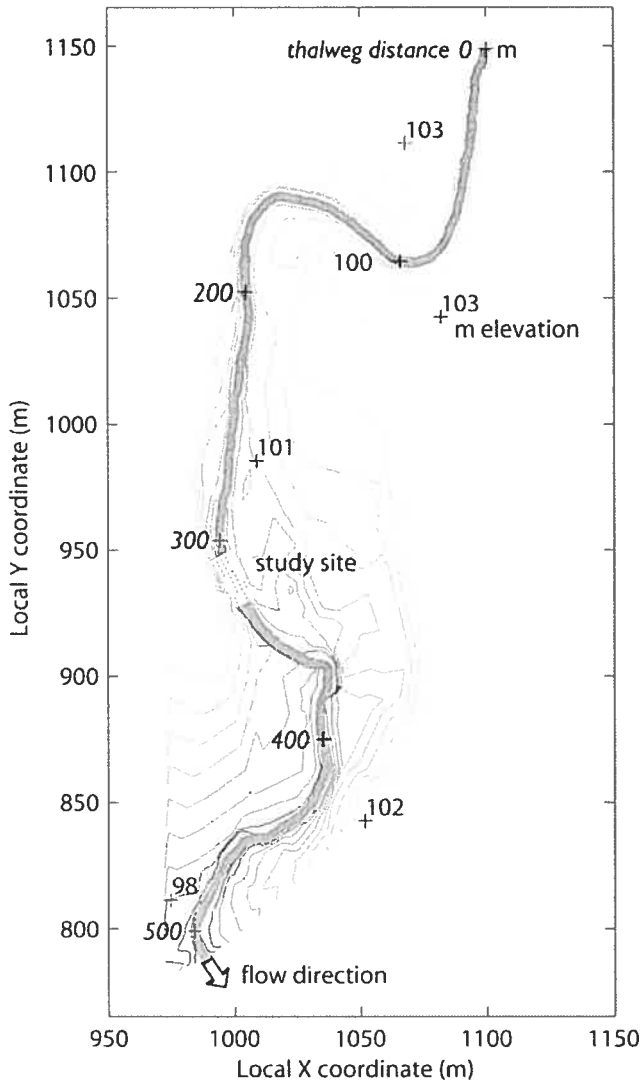

Figure 5.1 - Topography of area surrounding Moras Creek field site.

A longitudinal profile of the channel thalweg is plotted in Figure 5.2. The bed is composed of long runs with occasional steps and typically shallow pools. Deeper pools also occur and are invariably associated with forcing mechanisms such as boulders, sharp bends, or wood debris. Bankfull channel width, depth and slope are Z_{bf} = 6 m, Y_{bf} = 0.7 m, and S =1.2%, respectively. Based on a Wolman pebble count (n = 800) the representative particle sizes are D_{16} = 18 mm, D_{50} = 60 mm, and D_{84} = 190 mm. Large boulders are present in both the riffles and the pools. *Sear* [1996] showed that pools can be divided into sub-units where the bed slope of the pool-head is negative in the downstream direction, flat in the mid-pool, and positive in the pool-tail. Large particles tend to be imbricated in the riffle and pool-head and isolated in the mid-pool and pool-tail. Loose sand frequently deposits in the pool. The field site was selected because it fits within the classification of *Montgomery and Buffington* [1987], is straight enough that meander processes are not dominant, and is narrow enough that the scaffold platforms described below could span the width of the river and allow flow measurements during bankfull flows. We chose a forced pool because they are deeper in the systems that we surveyed, and deeper pools were expected to result in stronger differentiation of flow hydraulics between zones of acceleration and deceleration.

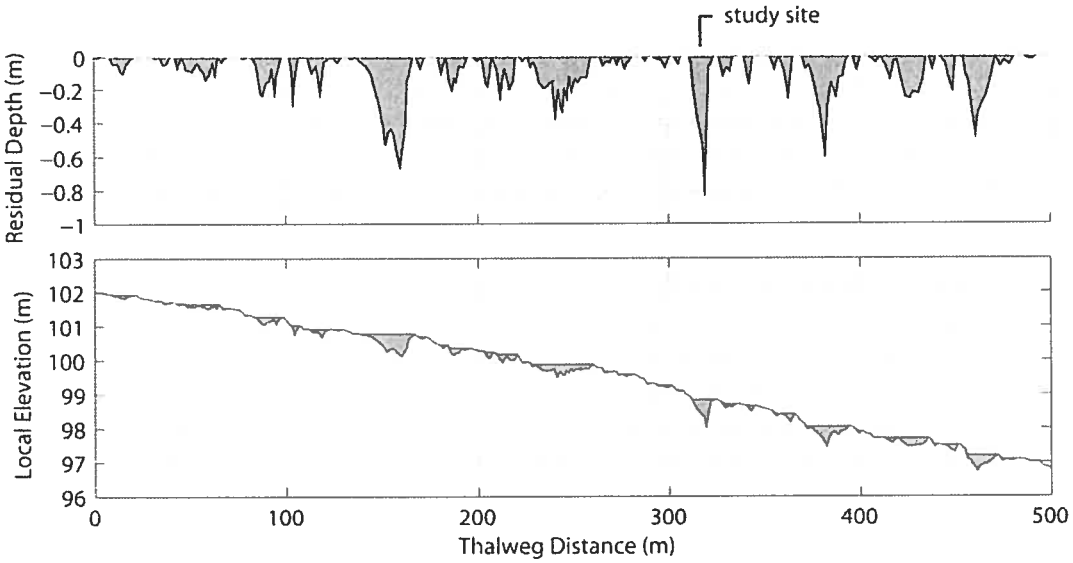

Figure 5.2 - Moras Creek thalweg profile and residual pools.

The study site is at the downstream end of a relatively long straight reach (Figure 5.1). As a note, the convention used in this article is the definition of x, y, and z as the streamwise, vertical, and lateral dimensions, respectively. The pool spans the width of the

channel, is 10 m long, and has a residual depth of 0.8 m (Figure 5.3). The location of the pool is controlled by a 60 cm diameter tree with an intact root wad approximately 200 cm in diameter that slid into the river. The root bole rests on the channel bed. Flow passes under the tree and around the root bole during normal flows and over the trunk of the tree at floods near the bankfull level. The roots at the top of the bole remained exposed during all the floods measured in this study. The tree moved immediately prior to the period of study when an above-bank level flood forced it to rotate from a position in which the root bole was upstream of the trunk, to one in which the roots were downstream of the trunk. This movement, coupled with a series of high flow events through 2003-04, induced changes in pool morphology that allowed us to study a period of active pool formation. Bed topography was repeatedly surveyed using a Trimble 5600 Total Station. Sediment transport data were also collected and these results will be presented in future work. The thalweg flows to the left side of the channel upstream of the tree and to the right side downstream of the tree. Lateral bars occur on the right side of the channel upstream of the tree and to the left side downstream. Isolated boulders and pebble clusters are visible as lighter circles on the topographical map. The most prominent cluster occurs on the left side of the channel on the upstream riffle at x = 2 m. Boulders are also visible to the left side in the pool-head between x = 8-12 m and in the pool-tail from x = 16-20 m on the sides and top of the downstream lateral bar. Underlying till has been exposed during pool scour and a resistant outcrop is visible to the right side of the channel at x = 18 m.

5.2.2 Flow Measurements

Velocity time signals were sampled using Marsh-McBirney 523 Electromagnetic Current Meters (ECMs). The reliability of this instrument in fast and turbulent flows has been assessed by comparing signals obtained simultaneously with an ECM and an Acoustic Doppler Velocimeter (ADV) in a range of flow environments (*see Chapter 4*). Results showed that, although the ECM does not capture all of the variance because of sampling volume and sampling frequency limitations, it does yield more reliable measurements than the ADV in highly turbulent flows. The ECMs are also suitable for simultaneous measurement of an array of point values, which allowed a high sampling density. For this article, instantaneous velocity components are defined in the streamwise and vertical dimensions as u, and v, U and V represent mean velocities, u' and v' are the standard deviations; and u_i and v_i represent the detrended instantaneous fluctuations about the mean.

Each point measurement consisted of a 120 s time series of u and v sampled at 20 Hz. Data were logged to a CR5000 Campbell Scientific micrologger. As recommended in *Roy et al.* [1996b], the signals were not rotated due to expected variability of V associated with non-uniform flow and topographical forcing.

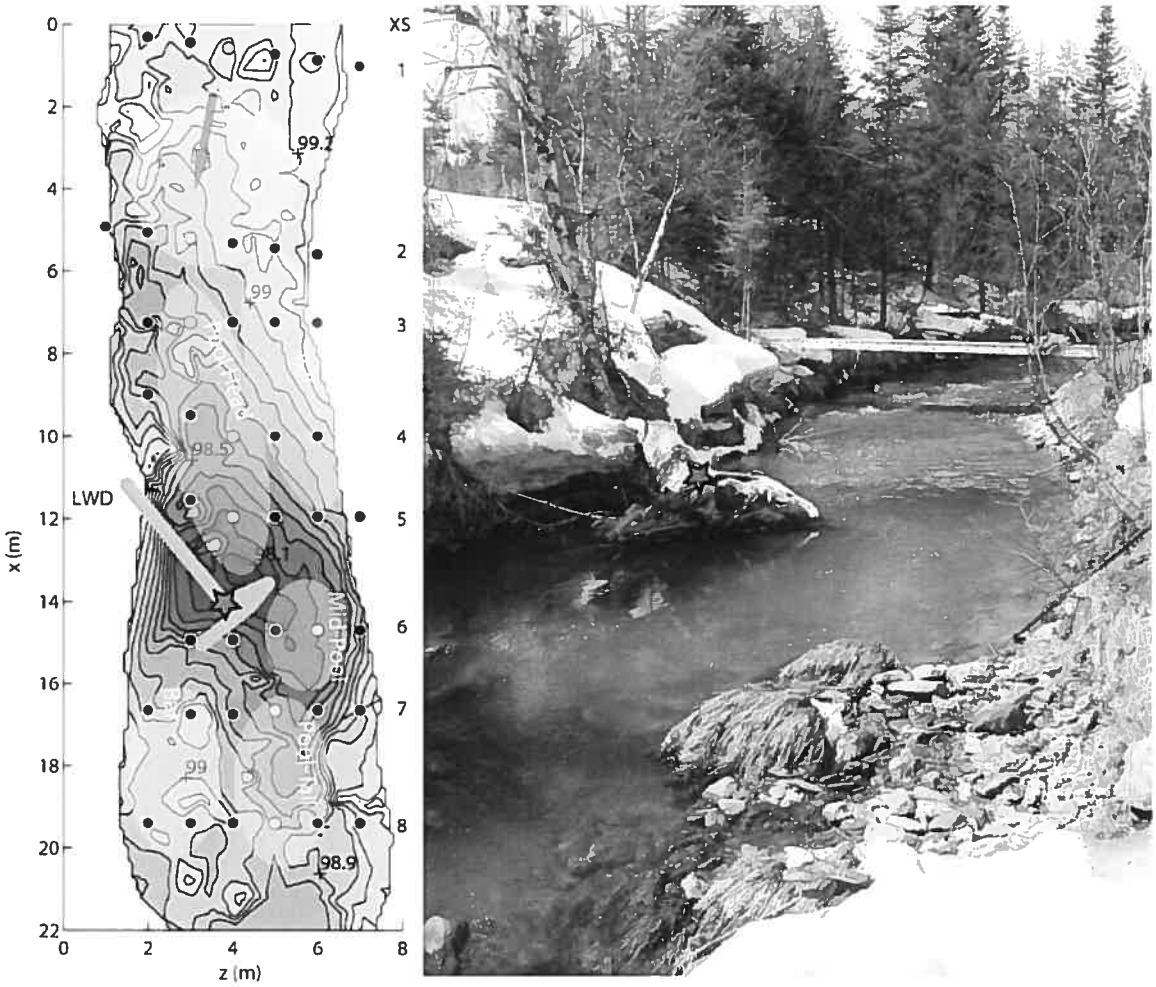

Figure 5.3 -Bed topography of study site on August 6, 2004 and photo from spring of 2004 during low flow. Measurement locations are black circles, and yellow circles distinguish the thalweg. Cross-section numbers (XS) are also shown for reference, the blue stars indicate the location of the tree, and light ellipses have been overlain to indicate morphological subunits.

Five bridges consisting four 8.5m Echafauds Plus® aluminum I-beams and one 10 m Werner Task-Master® aluminum scaffold plank were installed on leveled bases above the bankfull flow level. Bases were constructed from standard scaffolding parts. During storm events, two movable 5 m aluminum scaffold planks were placed on the beams. Using this system, flow measurements could be made from above the water surface at any position within a 20 m section of the river. Eight cross-sections were established and

vertical profiles were measured with a lateral spacing of 1 m (Figure 5.4). Some sampling locations appear outside the topographic map due to the difficulty of topographic surveying close to forested banks. Sampling was done using a vertical array of four ECMs with the probes fixed at vertical intervals of 10 cm starting at 5 cm from the streambed. A two-piece wading rod was utilized that allowed the ECM array to be slid vertically in order to measure higher in the water column while the base of the rod remained in contact with the stream bed. This design, combined with a wading-rod support attached to the bridges, ensured proper probe orientation and stability during high flood events. Figure 5.4 shows the system of bridges, a typical bridge base, the ECM array and wading rod, and sampling conditions during a flood.

A total of seven sets of water velocity measurements were made at different flood levels. Discharge was estimated at each cross-section and compared to flood stage data obtained from a pressure transducer. Relevant details of the measured floods are listed in Table 5.1. As shown, earlier floods were measured in less detail. Longer daylight hours and improved technique allowed more measurements to be made in later floods. Section 1 could not be measured during the largest event due to the failure of the bridge at this location during an earlier above-bankfull event. Minor flooding in overbank areas occurred during flow measurements on August 12, 2004, which means that the flow conditions during this event represent bankfull conditions in the channel. Intermittent rain occurred throughout the sampling day and the water level at the end of the sampling period was only a few centimeters below that at the beginning of the sampling period. The fluctuations that occurred do prevent calculation of convective acceleration/deceleration and the analysis of water surface elevations. For reference, profile statistics for the bankfull event are shown in Table 5.2. The maximum Froude number (*Fr*) of 0.71 occurs over the bar in section 2, which confirms subcritical flow throughout the pool, and *Fr* decreases in the deeper section of the pool. In contrast, the Reynolds number (*Re*) reaches a maximum in the deepest part of the pool. In the thalweg, it is useful to note that depth-integrated velocities ($\overline{U}$) remain relatively constant through sections 3 to 6 in spite of the changes to depth. This is accomplished through the concentration of flow in the thalweg as the pool deepens, evident from a comparison of velocities and depths across each cross-section, as $\overline{U}$ values for profiles adjacent to the thalweg are shown to decrease from sections 3 to 6.

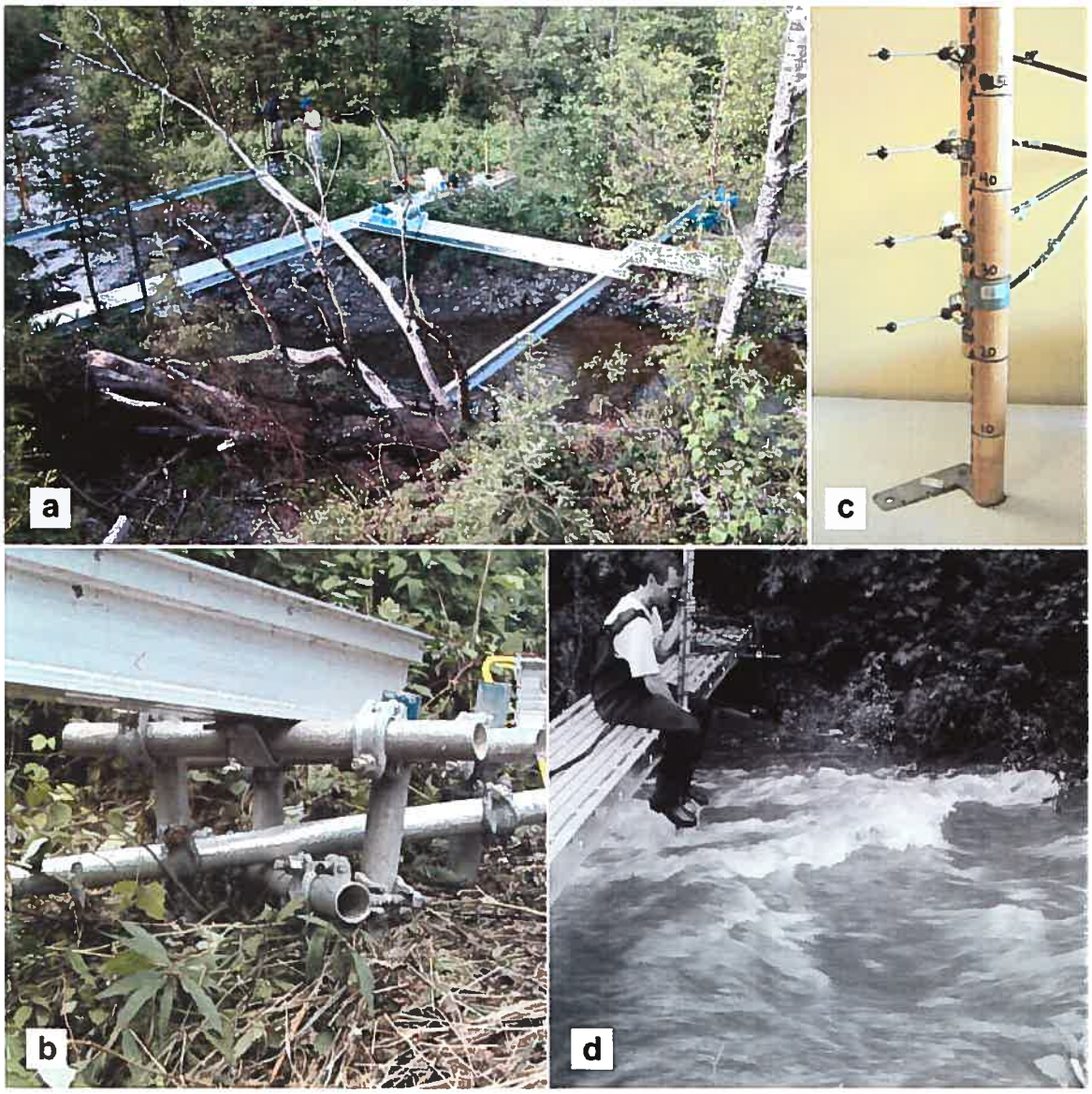

Figure 5.4 - Setup photos showing (a) the system of bridges as installed looking upstream (the tree is on the near bank, (b) a typical bridge base installed on the floodplain, (c) the wading rod with a 20 cm split and the array of four ECMs, (d) sampling conditions at XS 2 and z = 3 m during the bankfull flood.

Date	Q (m^3/s)	Sections	Points	ΔY (m)
28-Nov-03	2.73	1,2,4,5,6	119	n/a
12-Apr-04	3.55	1-6	119	n/a
27-Apr-04	0.84	1-8	136	n/a
02-Jun-04	1.64	1-8	180	-0.095
09-Jun-04	0.10	1-8	88	0
23-Jul-04	0.36	1-8	155	0
01-Aug-04	0.90	1-8	155	-0.02
12-Aug-04	5.10	2-8	270	-0.09

Table 5.1 - Summary of Flow Sampling Dates. ΔY refers to the changes in water level during the sampling period.

XS	z (m)	Y (m)	Points	U (m/s)	Fr	Re (x 10^3)
2	1	0.2	2	-0.08	0.05	15.2
	2	0.83	7	1.04	0.37	866
	3	**0.81**	**6**	**1.5**	**0.53**	**1210**
	4	0.7	6	1.59	0.61	1120
	5	0.51	4	1.59	0.71	812
	6	0.46	4	1.45	0.68	668
3	2	0.87	8	0.56	0.19	489
	3	**0.92**	**8**	**1.13**	**0.38**	**1040**
	4	0.78	7	1.17	0.42	912
	5	0.58	4	1.15	0.48	664
	6	0.49	4	0.05	0.02	22.3
4	2	0.72	7	0.37	0.14	268
	3	0.9	8	1.05	0.35	945
	4	**1.18**	**11**	**1.22**	**0.36**	**1440**
	5	0.89	8	1.2	0.41	1070
	6	0.73	7	-0.03	0.01	25.5
5	3	1.12	11	0.51	0.15	571
	4	**1.34**	**12**	**1.05**	**0.29**	**1410**
	5	1.12	11	0.99	0.3	1100
	6	0.86	8	0.38	0.13	327
	7	0.64	6	-0.3	0.12	191
6	3	0.71	7	0.42	0.16	298
	4	1.02	8	0.13	0.04	131
	5	1.25	12	0.64	0.18	801
	6	**1.34**	**12**	**1.13**	**0.31**	**1520**
	7	0.94	8	0.53	0.17	499
7	2	0.66	6	0.5	0.19	327
	3	0.46	4	0.34	0.16	158
	4	0.9	8	0.36	0.12	325
	5	**1.3**	**11**	**1.11**	**0.31**	**1440**
	6	1.15	11	1.46	0.43	1670
	7	0.71	6	1.01	0.38	716
8	2	0.55	4	0.89	0.38	490
	3	0.58	4	1.09	0.46	631
	4	0.51	4	1.5	0.67	765
	5	**0.79**	**7**	**1.83**	**0.66**	**1440**
	6	0.62	6	1.55	0.63	958
	7	0.35	3	0.9	0.49	315

Table 5.2 - Parameters of flow profiles measured during the bankfull flood. Bold values indicate the position of the thalweg as determined from the depth and mean velocity.

5.2.3 Data Quality and Post-Processing

To ensure the quality of the measured velocity signals, a four-step quality assurance procedure was followed:

1. The signal was visually inspected to identify discontinuities or irregular data (Figure 5.5a). Discontinuities were most often associated with leaves or floating debris on the probes. Where discontinuities occurred, sections of the data were eliminated unless at least one minute of good data was not available, in which case the data set was eliminated from further analysis. Electronic interference was the occasional result from low battery power and interference from connected power sources. Electronic noises are typically identifiable on power spectra plots [*Lapointe et al.*, 1996]. Signals where this was observed were eliminated from further analysis.
2. The raw signals were de-filtered to remove the analog filter in ECM measurements according to recommendations in *Roy et al.* [1997]. The effect of this step is most clearly observed in the spectral density plot (Figure 5.5b) where a slight increase in spectral density is evident for frequencies above 3 Hz. The de-filtered signals follow the *Komolgorov* [1941] -5/3 scaling law up to the vertical line labeled f_v. This is the frequency at which the sampling volume is expected to reduce measured spectral density (S_f) by 10% [*Soulsby*, 1980]. This frequency was calculated as $f_v = U/7d_v$, where d_v is the length of the sampling volume (~ 2.5 cm for the ECM used in this study). f_v corresponds with a point of inflection in the spectral density curve, above which spectral densities drop off more steeply than would be expected from the -5/3 scaling law.
3. A spike removal program was developed from the Goring-Nikora criteria for ADV data [*Goring and Nikora*, 2002]. Under normal conditions, this program successfully removed signal outliers and replaced them with an interpolated value between successive points in the time series. This is demonstrated by the removal of a prominent spike in the data at 47 s (Figure 5.5c).
4. High frequency electronic noise above the Nyquist frequency was filtered using a third order Butterworth filter according to recommendations in *Roy*

et al. [1997]. The effect on the overall signal is again not large, but the difference can be seen in the power spectra above a frequency of 7 Hz (Figure 5.5d).

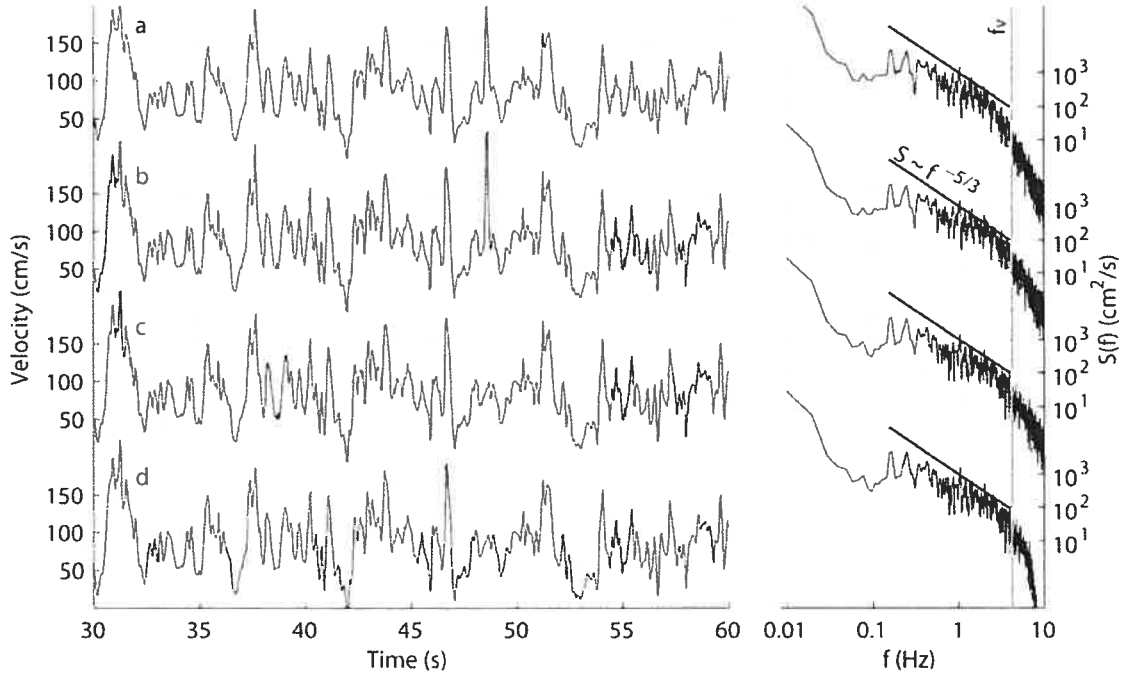

Figure 5.5 - Filtering and despiking operations illustrated with a 30 s segment and power spectra from a time signal at moderate velocity (U = 0.74 m/s) and moderate turbulence (u' = 0.39 m/s). (a) The measured ECM output, (b) the de-filtered signal, (c) the de-spiked signal, (d) the re-filtered signal and output from the quality assurance procedure. Reference lines are included on the spectral plots for identification of intermediate and inertial subranges, and the frequency above which sampling volume effects are significant.

5.2.4 Turbulence intensity in non-uniform flow

Pools and riffles are most consistently classified based on topography [*Richards*, 1976]. For morphologies similar to Moras Creek, where the width is relatively constant, the morphology necessarily results in bulk flow deceleration and acceleration in the pool-head and the pool-tail, respectively. In the sampled pool, the tree also forces deceleration due to backwater effects. This is most evident at high flow, when a steep water surface slope is observed at the constriction. Bulk velocity changes, however, are counteracted in the thalweg by converging and diverging flow in the pool-head and pool-tail, respectively. To get around the morphological complexity and limitations in the sampled data, we utilized an indirect method to determine whether flow was accelerating or decelerating in the thalweg. *Kironoto and Graf* [1995] measured the effects of topographically induced

acceleration and deceleration on mean velocities and turbulence intensities in flume experiments. They found acceleration to lead to a 'fuller' mean velocity profile, with fast relative velocities occurring close to the bed, while deceleration produced a strong gradient throughout the flow depth so that near-surface velocities were much faster than those near the bed. The change in velocity profiles had a strong effect on turbulence intensity. In order to determine if the flow was accelerating or decelerating in Moras Creek, we normalized u' and v' profiles by the shear velocity (u^*) and compared our results with these laboratory studies:

$$u^* = \sqrt{\frac{\tau}{\rho}} \tag{5.1}$$

where τ is the shear stress (N/m^2), and ρ is fluid density (kg/m^3). *Kironoto and Graf* [1995] obtained the following turbulence intensity profiles in uniform flow:

$$\frac{u'}{u^*} = 2.04e^{-0.97y/Y} \tag{5.2}$$

$$\frac{v'}{u^*} = 1.14e^{-0.76y/Y} \tag{5.3}$$

Relative to the uniform condition, acceleration reduced turbulence intensities in the outer layers, and deceleration increased turbulence in both the streamwise and vertical directions. *Kironoto and Graf* [1995] also found that the vertical position of the peak turbulence intensity changes in non-uniform flow. While peak intensities occur close to the bed in accelerating flows, this peak tends to be higher in the water column in decelerating flows. These results have been confirmed by *Song and Graf* [1994], who also noted a slight tendency for negative vertical velocities in accelerating flows, by *Afzalimehr and Anctil* [1999] for decelerating flows, who observed a strongly convex profile for the Reynolds shear stress, and by *Song and Chiew* [2001], who noted that the changes to mean velocity and turbulence intensity profiles are sensitive to the width-to-depth ratio.

5.2.5 Shear stress in non-uniform flow

Various methods exist to estimate the shear stress. It is not clear what method is the most representative of forces transmitted to the bed in non-uniform flows. Morphological parameters of the reach can be used to calculate a spatially averaged value:

$$\tau_o = \rho g R S_e \tag{5.4}$$

where τ_o is the bed shear stress, g is acceleration due to gravity, R is the hydraulic radius, and S_e is the energy slope. This method will be of limited use in riffle-pools due to the perturbation that the non-uniform boundary will have on mean velocities and turbulence intensities that were observed at this site. *Wilcock* [1996] discusses three methods to estimate a local value of shear stress based on mean velocities using (a) the near-bed point measurement of U and an estimate of the roughness length (k_s), (b) the slope of the near-bed relation between U and y, and (c) the depth averaged velocity. Of these three methods, method (a) makes the least restrictive assumptions about the shape of the velocity profile [*Wilcock*, 1996] and was used in this study to normalize turbulence intensities for comparison with *Kironoto and Graf* [1995]. We used $k_s=D_{84}/10$ [*Wilcock*, 1996], and the following equation for the near-bed velocity shear stress (τ_u):

$$\tau_u=\rho\left(\frac{\kappa U}{\ln(10y/D_{84})}\right)^2 \tag{5.5}$$

where κ is the Von-Karman coefficient (≈ 0.40). To compare with existing studies in riffle-pools [for e.g. *Clifford and Richards*, 1992; *Bathurst*, 1979] we also used method (b) of *Wilcock* [1996] based on the two lowest measurements in the profile to estimate the near-bed velocity gradient shear stress ($\tau_{\Delta u}$):

$$\tau_{\Delta u}=\rho\left(\frac{\kappa(U_2-U_1)}{\ln(y_2/y_1)}\right)^2 \tag{5.6}$$

For both of the methods based on mean velocities, all parameters except velocity can be reduced to a constant if fixed probe heights are used, as was the case in this study ($y_1 = 5$ cm and $y_2 = 15$ cm).

Kironoto and Graf [1995] found that the relation between mean velocity and turbulence intensity is perturbed in non-uniform flow. Areas of flow deceleration are subject to high amplitude fluctuations in spite of low mean velocities. These fluctuations are likely to be significant for sediment transport [*Nelson et al.*, 1995; *Sumer et al.*, 2003]. Two methods have been used in previous studies to estimate local bed shear stress using the fluctuating part of the velocity signals. *Carling et al.* [2002] and *Biron et al.* [2004] used the Reynolds stress (τ_r):

$$\tau_r=\rho\overline{u_i v_i} \tag{5.7}$$

Alternatively, *Kim et al.* [2000] and *Biron et al.* [2004] estimate local bed shear stress from an empirical relation with turbulent kinetic energy (E_k):

$$E_k = 0.5\rho(\overline{u_i^2}+\overline{v_i^2}+\overline{w_i^2}) \tag{5.8}$$

The ECM only measures in two dimensions and an assumption was required to estimate the lateral component $\overline{w_i^2}$. We used the simplest assumption, based on the common observation that $\overline{u_i^2}>\overline{w_i^2}>\overline{v_i^2}$ [*Nezu and Nakagawa, 1993*] and set $\overline{w_i^2}=0.5(\overline{u_i^2}+\overline{v_i^2})$. This allowed us to calculate local shear stress from the turbulent kinetic energy (τ_k) as:

$$\tau_k = 0.75\rho K_1(\overline{u_i^2}+\overline{v_i^2}) \tag{5.9}$$

where constant $K_1 \approx 0.19$ [*Kim et al.*, 2000; *Biron et al.*, 2004]. This method has been found to be more accurate than other estimates in complex flows [*Biron et al.*, 2004].

5.3 Results and Analysis

5.3.1 Spatial and Flow Stage Variability

The mean of the streamwise and vertical velocity components (U and V) and the respective standard deviations (u' and v') are presented in a series of contour plots (Figure 5.6-Figure 5.9). These figures show the streamwise, lateral, and vertical variability and the variability with flow stage of flow statistics. In these figures, flow is from the top to the bottom and right and left sides of the channel are defined looking upstream. Due to space limitations, only three flood stages are shown, consisting of one relatively low stage (Q = 0.9 m^3/s), one moderate stage (Q = 2.0 m^3/s) and the bankfull flow (Q = 5.1 m^3/s). These events occurred within a 2-month period during which morphologic change was minor.

From Figure 5.6, it is immediately apparent that it is difficult to interpret streamwise variability of U without considering the lateral and vertical variability. The pool is characterized by convergence of flow marked by a core of high U values at the channel center in sections 1 to 5 and by flow divergence as U values become similar across the width of the channel between sections 7 and 8. This pattern is common to all flow stages, though convergence in sections 2 to 4 is less pronounced at high flow than at low flow. U is negative near the right bank upstream of the tree at all flow stages, an area in which a recirculating eddy was consistently observed. U is also relatively low downstream of the tree in section 6 from x = 1 – 4 m at all flow stages, an area in which flow patterns included

boils, flow separation and plunging flow over the tree at high flow. Concentration of flow in the vertical direction also occurs in sections 1 to 5 as U is high near the water surface and low near the bed at all flow stages. As discharge increases, velocities near the bed do not increase noticeably in these sections, but large increases do occur near the water surface. In sections 6 through 8, vertical gradients are reduced, as near-bed values are approximately equal to those at the surface. Velocities at all points in the profiles increase with flow stage in these sections.

V is plotted on Figure 5.7. Upstream of the tree in section 1-5, V tends to be negative in the thalweg. This is true for all flood levels, and the amplitude of vertical velocity vectors increases with discharge. V is largest in section 6 at high discharge, where strong downwelling in the thalweg is matched by strong upwelling in adjacent profiles. Mean vertical velocities were greater than 60 cm/s in one location and strong shearing and boils were observed. Upwelling is also strong near the bed in sections 7 and 8. This pattern is visible during low discharge, but is most evident at high discharge. Upwelling is also characteristic of the eddy zone on the right bank upstream of the tree and on the left bank downstream of the tree. Considering U and V together, these results indicate that converging flow in the pool-head is associated with downwelling in the thalweg and upwelling in the channel margins, while diverging flow over the pool-tail corresponds with areas of upwelling near the bed.

u' is shown in Figure 5.8. At low discharge, high u' values are concentrated in the center of the channel of the pool-head, similar to the mean velocity values, except that peak u' values occur closer to the bed than peak U values. u' decreases in a downstream direction at lower flows, and are very low downstream of the tree. At moderate discharge, larger values are observed through the entire length of the pool. High u' zones typically extend from the water surface right down to the bed. At high discharge, higher u' values occur, with the highest values typically observed near to the bed. The most extreme values occur near to the bed in the pool sections 3 to 5, 7 and 8. These results show that instantaneous velocities can be very high even where U is low. v' is shown in Figure 5.9. Though similar in terms of near-bed values, lateral variability and variability with flow stage, v' and u' differ in terms of their vertical distribution, with v' generally larger near to the water surface. This effect is most evident at high flow and in the pool-head (sections 2-5) at moderate and low discharge.

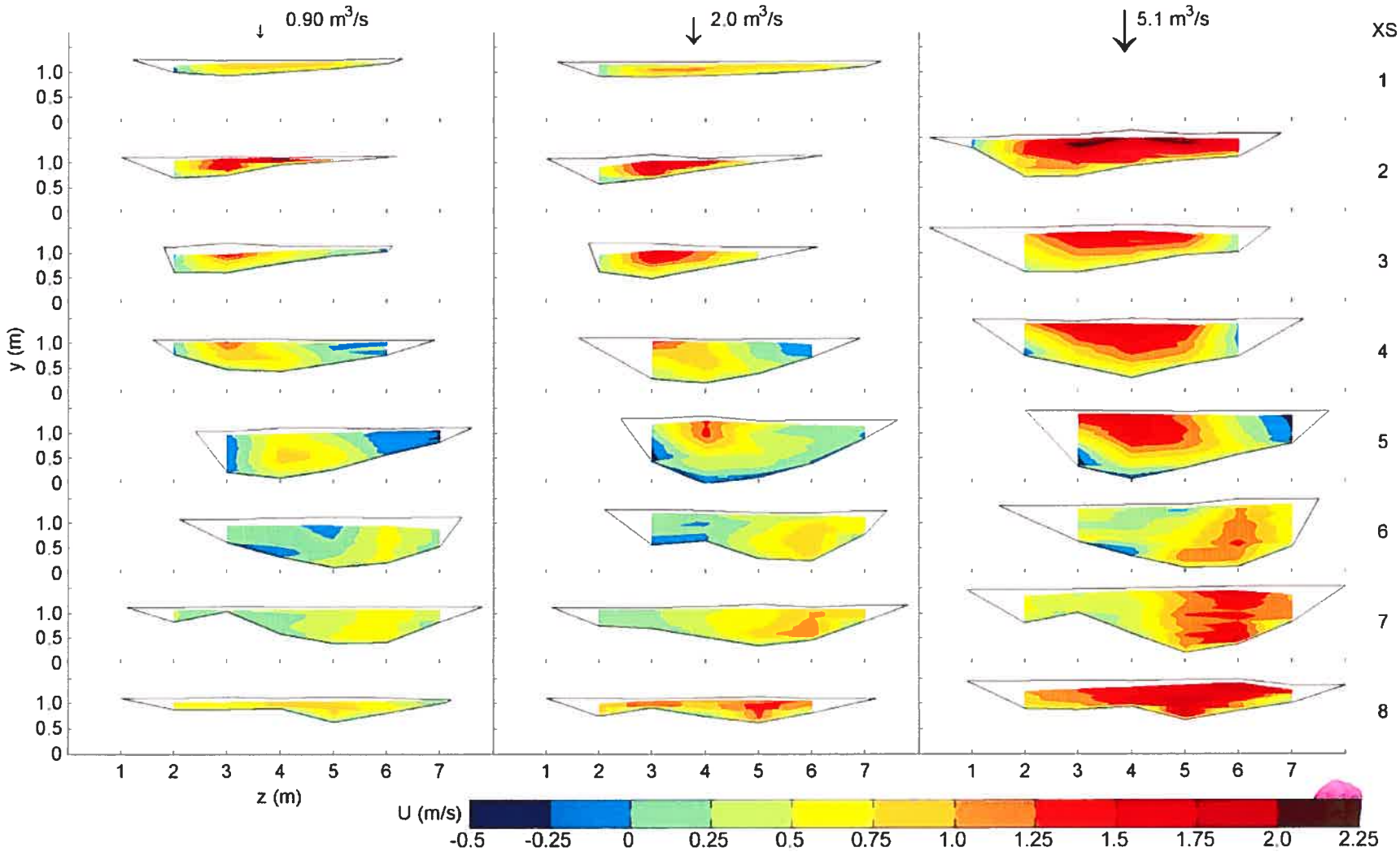

Figure 5.6 - Mean streamwise velocity (U) contours during three events including bankfull. Flow direction is from top to bottom. The tree that forces the pool is located between sections 5 and 6 on the left bank out to a distance of approximately 5 m.

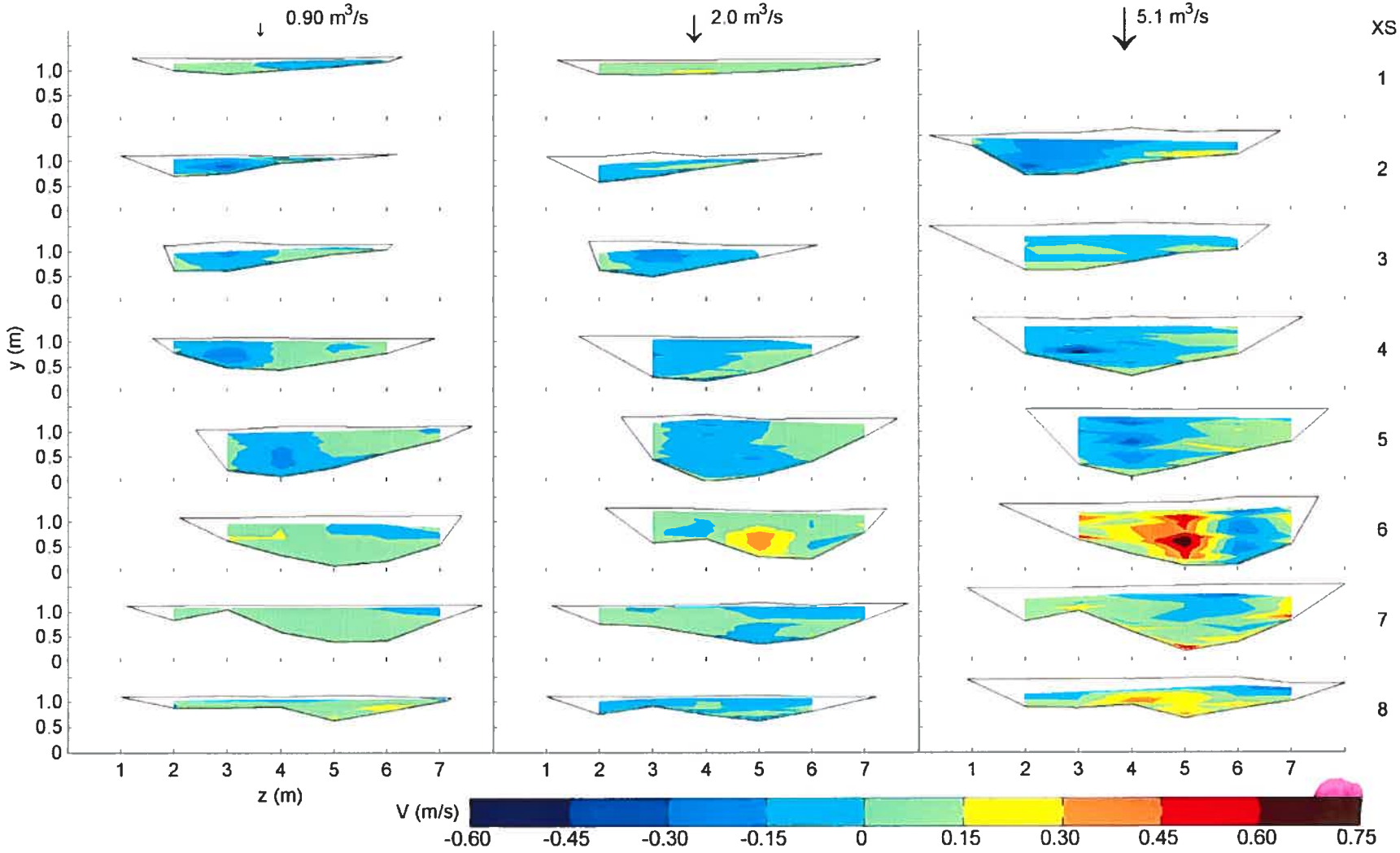

Figure 5.7 - Mean vertical velocity (V) contours. Flow direction is from top to bottom. The tree that forces the pool is located between sections 5 and 6 on the left bank out to a distance of approximately 5 m.

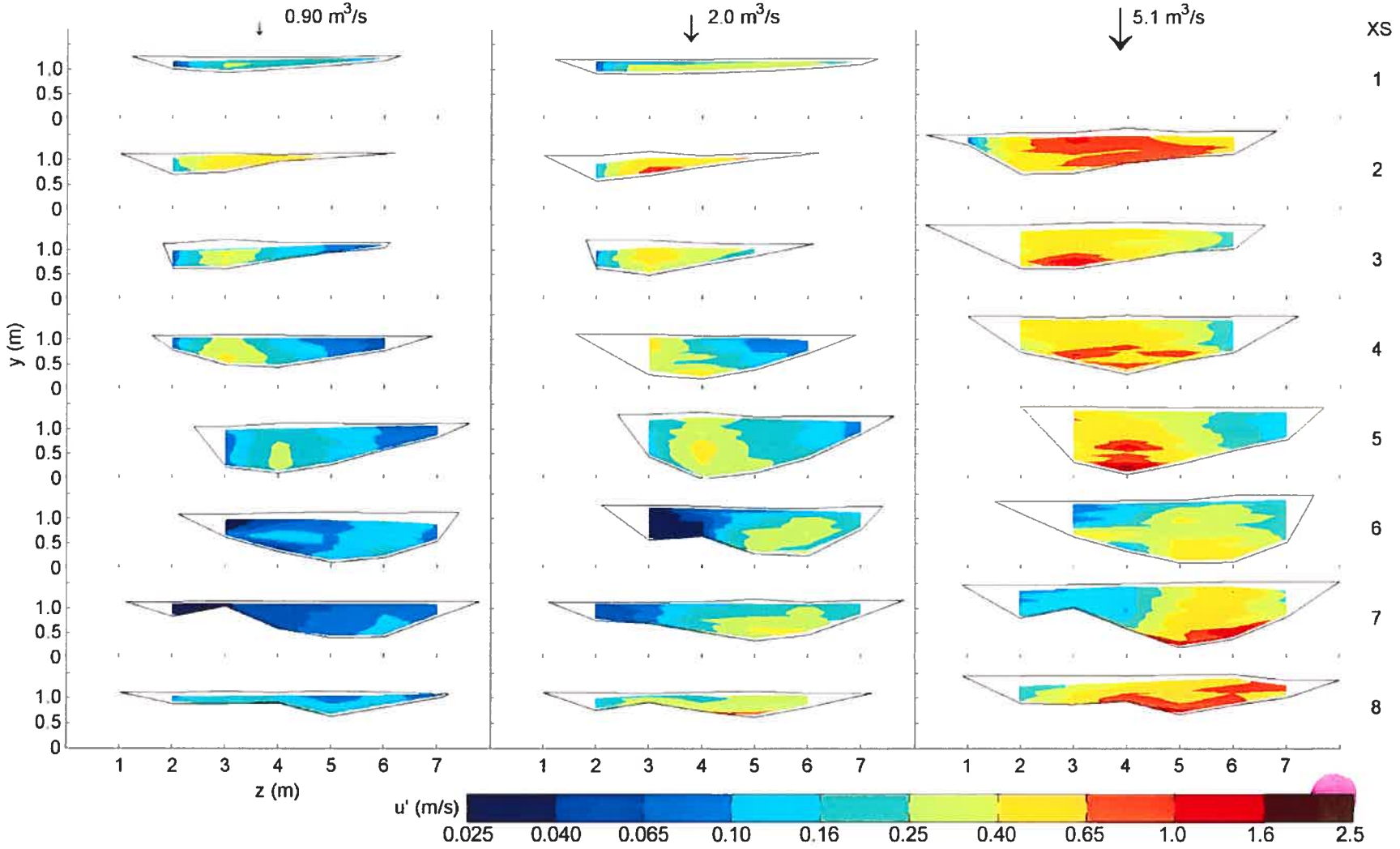

Figure 5.8 - Standard deviation of streamwise velocity (u') contours. Flow direction is from top to bottom. The tree that forces the pool is located between sections 5 and 6 on the left bank out to a distance of approximately 5 m.

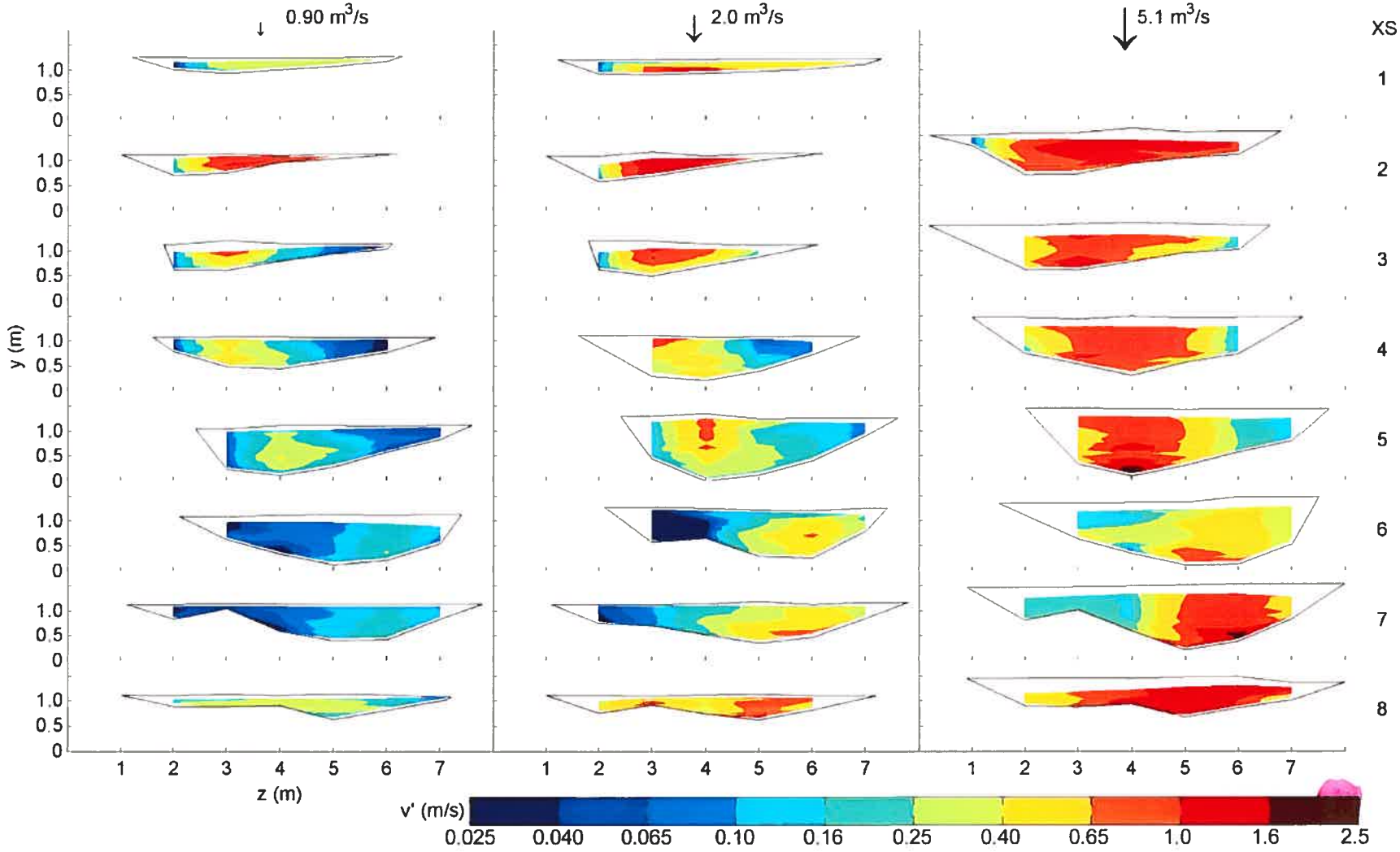

Figure 5.9 - Standard deviation of vertical velocity (v') contours. Flow direction is from top to bottom. The tree that forces the pool is located between sections 5 and 6 on the left bank out to a distance of approximately 5 m.

5.3.2 *Mean velocity profiles at bankfull flow*

Mean velocities in the thalweg during the bankfull discharge (Q = 5.1 m^3/s) are presented for the seven sections measured during this event in Figure 5.10. Profiles adjacent to the thalweg are included in order to avoid misinterpretations associated with lateral variability. To facilitate the presentation of the results, we define the inner flow region (y/Y = 0-0.2), the intermediate region (y/Y = 0.2-0.6), and the outer region (y/Y = 0.6-1.0) (definitions from *Nezu and Nakagawa* [1993]). It is clear that the shape of the velocity profile changes with streamwise position, which confirms the observations from Figure 5.6. Velocity profiles in sections 2 to 5 are generally 'kinked', with decreasing values near to the bed, while U in sections 6 to 8 is nearly constant throughout the water column. Also evident are a few, more subtle points that were not obvious in the previous presentation of the data. The first is the vertical position of the maximum U value in the profile. As shown, this position descends through the pool, occurring close to the surface in sections 2 to 3, at the limit between the outer and intermediate zones in sections 4 to 5, in the intermediate zone in sections 6 to 7, and finally at the limit between the inner and intermediate zones in section 8. The absolute value of this maximum U value decreases through sections 2 through 7, but increases in section 8. It is also interesting, and relevant to the interpretation of results from other field-based studies, to note that velocities at the depth used to estimate the depth-averaged velocity in uniform flow ($y = 0.4Y$) are relatively similar, and only the faster flow velocities in sections 2 and 8 are clearly different. This result follows that of the depth-averaged velocity ($\overline{U}$) as shown in Table 5.2. If near-bed measurements were not taken they would indicate a relatively homogeneous pool environment where the effects of the topographical changes are not critical to flow parameters. However, because of its importance for sediment entrainment, it is important to note the changes in near-bed velocity. Overall, U decreases near the bed through sections 2 to 5 and increases through sections 6 to 8. Near-bed velocities are lowest in section 5, and highest in section 8. These results demonstrate that bed sediments in the pool-head are subject to entirely different hydraulics than those in the pool-tail. In addition, there is a strong acceleration of flow near the bed between sections 5 to 6 that confirms that there is a hydraulic effect of the forcing by the tree in this location.

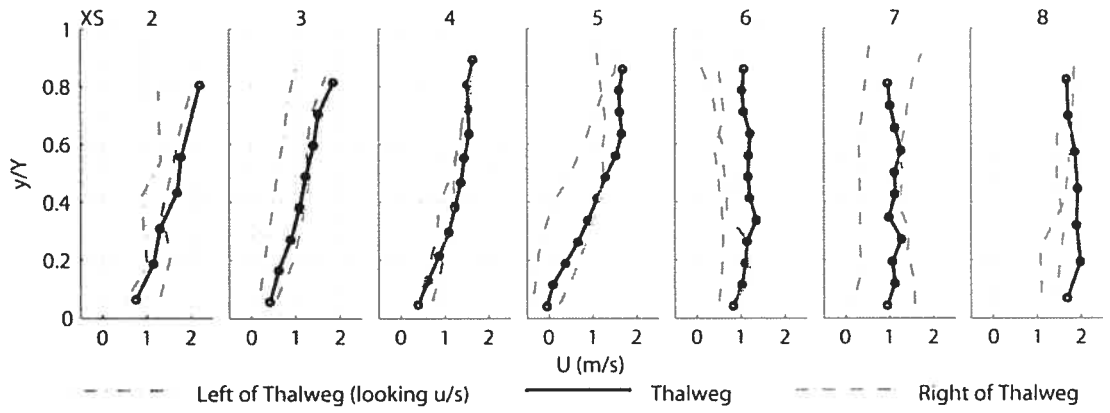

Figure 5.10 - Profiles of U during the bankfull flow event.

5.3.3 Effect of flood stage on inner flow region

Figure 5.11 plots the averaged values of U and u' for all probes in the inner zone at all seven sampled flood stages and at each cross-section. Similar to the previous figure, the thalweg and its adjacent points have been isolated in order to concentrate on streamwise trends while retaining some information about lateral variability. The lack of data at the lowest flood levels in sections 1, 2 and 8 is a result of a minimum sampling depth of 5 cm, which is not in the inner zone for flow depths less than 25 cm according to the criteria used here. Missing data points include section 1 at the maximum flow as a result of a bridge washout, and section 3 at $Q = 2.7$ m^3/s and sections 7 and 8 at $Q = 2.7$ m^3/s and $Q = 3.5$ m^3/s due to reduced sampling densities in these earlier events.

The relation between near-bed U and Q does not appear to follow a consistent pattern. Up to $Q \approx 1$ m^3/s, near-bed velocities increase at all positions. As discharge continues to increase, however, there is a diverging trend in near-bed velocities. The slowest velocities, which occur upstream of the tree, are flat or decreasing with discharge while the fastest velocities, which occur in the pool-tail, are increasing. Upstream of the tree, it appears that there is a backwater effect from theA near-bed velocity reversal occurs at $Q \approx 3$ m^3/s (about 3/5 of the bankfull discharge) between the upstream riffle (sections 1 and 2) and the mid-pool and tail (sections 6 to 8). Changes in flow patterns with Q are illustrated by the frequent occurrence of peak velocities in a location other than the thalweg. It is only in section 8 that the highest near-bed velocity occurs in the thalweg at high flow.

The relation between near-bed u' and Q is also variable. One general trend is that u' increases with discharge until $Q \approx 2.0$ m^3/s. This is true for all positions including the points adjacent to the thalweg. Above this value, u' is more erratic and spatially variable. At moderate discharge (Q = 2-3.5 m^3/s), u' is highest in sections 1,2 and 8. It appears, however, that u' does not continue to increase near bankfull discharge ($Q > 3.5$ m^3/s) in these sections. u' is lower in sections 3 to 7 at moderate flows, sometimes exhibiting decreasing values in the range Q = 2-3.5 m^3/s, but sharp increases are notable at higher flows. This is particularly true in sections 3 to 5, which experience large increases in near-bed turbulence as the discharge approaches bankfull.

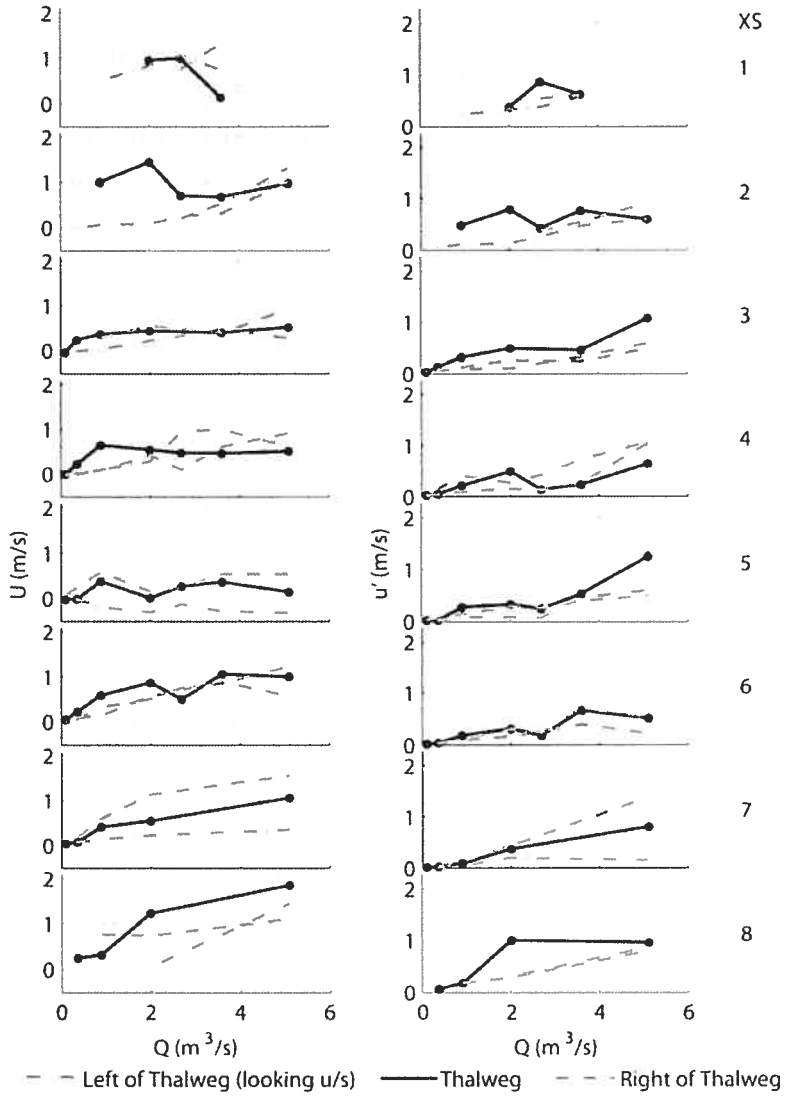

Figure 5.11 -Effect of discharge (Q) on near bed mean velocity (U) and standard deviation (u'). Plotted values represent the mean of all probes in the inner zone ($y/Y < 0.20$).

5.3.4 *Turbulence intensity and shear stress*

Profiles of the turbulence intensities in the thalweg at bankfull discharge (normalized using τ_u) are compared with uniform flow profiles calculated by *Kironoto and Graf* [1995] in Figure 5.12. These results confirm the contrast between flow dynamics upstream and downstream of the tree. Upstream of the tree, normalized u' profiles plot far to the right of the uniform flow line, and peaks occur away from the bed near to the division between the inner and outer layers. These results demonstrate that, despite flow convergence in the pool-head, the flow is hydraulically decelerating in this region. In contrast, downstream of the tree, u' plots to the left of the uniform flow line and there is no inner zone peak. These results show that, despite the expansion of flow through the mid-pool and over the pool-tail, the flow is hydraulically accelerating in this region. v' profiles are essentially the same as u' profiles in terms of near-bed values and the occurrence of peaks within the inner flow region. The main difference between u' and v' is that, in sections 2 to 5, strong positive gradients are observed in the outer zone of v' profiles and v' is generally greater than u' in the intermediate and outer zones. It is also clear that the v' measurements in both decelerating and accelerating flows plot to the right of the empirical relation for uniform flow. This fact is not anticipated by flume studies of non-uniform flows and will be examined in the discussion of results.

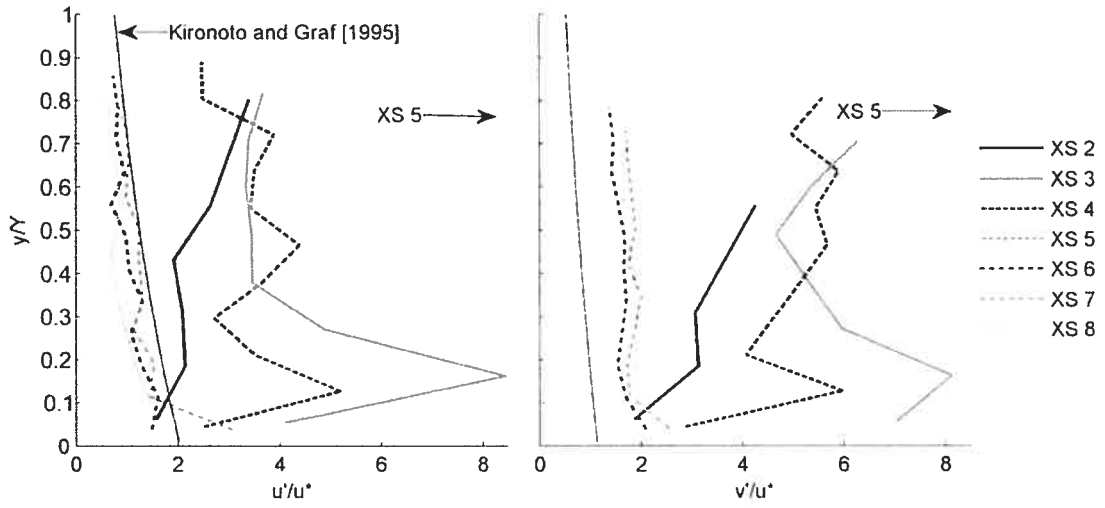

Figure 5.12 - Normalized turbulence intensity profiles during the bankfull flow event. Thin black lines indicate uniform flow relations from *Kironoto and Graf* [1995]. In their laboratory studies, accelerating flow plotted to the left of this line and decelerating flows plotted to the right. In section 5, values of $u^* \approx 0$ meant that normalized values of u' and v' approached infinity and are not plotted.

Local bed shear stresses calculated using the four different methods (Equations 5.5 to 5.7 and 5.9) are shown for the bankfull discharge in Figure 5.13. For comparison, the reach-averaged bed shear stress (τ_o) calculated using the bankfull dimensions and overall slope of the channel is 67 Pa. We also calculated the slope between cross-sections to estimate the variability between cross sections, but the calculation of slope is sensitive to elevation measurements that were measured over four hours and unsteady discharge precluded their use for shear stress calculations. Local shear stresses during the bankfull flood are both lower and higher than τ_o depending on the measurement location and the calculation method. $\tau_{\Delta u}$ is always less than the reference value of τ_o. Though always positive, $\tau_{\Delta u}$ is close to zero in the deep areas of the pool both upstream and downstream of the tree. The highest values are obtained in the channel margins in sections 2 and 8. In contrast, τ_u is highly variable through the pool, with peak values in the thalweg of sections 2, 7, and 8. Moderate values are also observed over the bar to the right of the channel in sections 3 to 5 and in the thalweg of section 6. τ_u and τ_k give very similar estimates of local shear stress at most locations. The only area where the estimates strongly disagree is in the thalweg of the pool-head. In this area, sections 3, 4 and 5 all show $\tau_k >> \tau_u$. Local values of τ_u and τ_k are often greater than the reference value of τ_o, with peak local estimates over 500 Pa in the pool-head as estimated with τ_k, and in the pool-tail as estimated with both τ_k and τ_u. τ_r was negative in many locations. It is interesting to note that in the three sections with the largest shear stresses (sections 5, 7, and 8), the τ_r estimate, while opposite in sign from the result calculated by the other methods, is often of similar magnitude to the τ_k estimate in section 5, and to both the τ_k and τ_u estimates in sections 7 and 8. This indicates that the assumption of a dominance of positive Reynolds shear stress events may not apply in such non-uniform flows. This result is relevant to interpretations of coherent flow structure and is discussed in greater detail in the companion article.

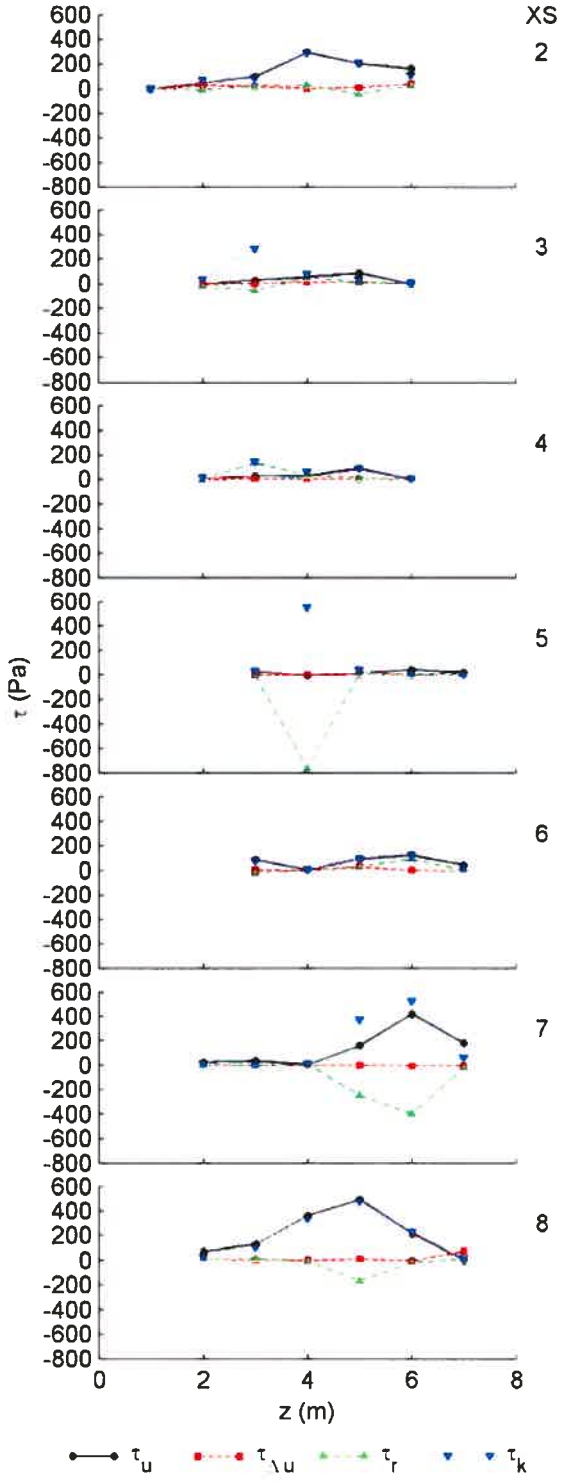

Figure 5.13 - Local estimates of shear stress during the bankfull flow event using four methods: near-bed velocity (τ_u); near-bed velocity gradient ($\tau_{\Delta u}$); Reynolds stress (τ_r); and turbulent kinetic energy (τ_k). The reach-averaged shear stress τ_o = 67 Pa.

5.4 Discussion

In terms of instrumentation, sampling density, and range of flows, the results obtained for this study may represent the most comprehensive data set of flow hydraulics yet measured in a riverine pool environment. The picture of flow hydraulics that emerges is an environment dominated by flow deceleration and turbulence generation over both the riffle and pool-head and flow acceleration past the constriction and over the pool-tail. A conceptual model of a forced-pool was developed to synthesize and discuss the results (Figure 5.14a). Based on comparison with other studies and theoretical considerations, we also seek to extend the results to a more general model (Figure 5.14b). There are three key elements to both versions of the model: (1) systematic alteration of streamwise velocity profiles, (2) laterally-converging flow and secondary circulation, and (3) increased turbulent energy in the inner zone of flow in the pool-head at high flows. We discuss these elements in this section in terms of the support from other studies and flume experiments, the importance of the forcing element, and directions for future research. The calculation of shear stress in non-uniform flows is also addressed.

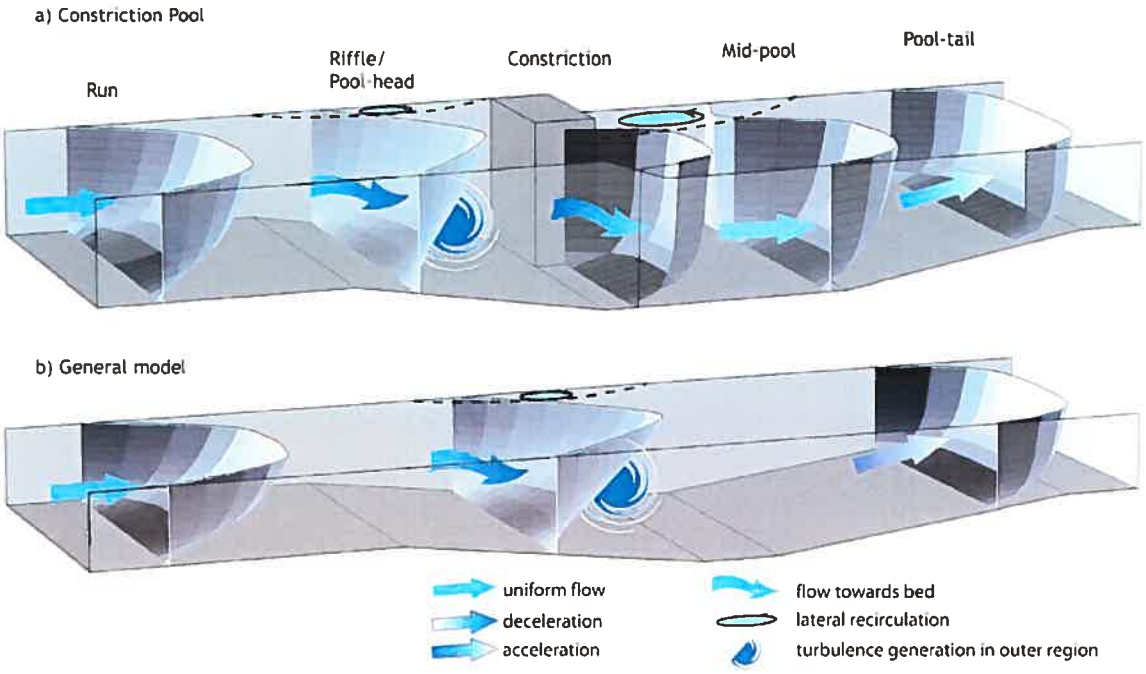

Figure 5.14 - Conceptual model of flow dynamics in (a) a forced riffle-pool such as the Moras Creek study site and (b) a straight pool without a constriction. Surfaces represent streamwise velocity vectors in uniform, decelerating, and accelerating flows, respectively. These surfaces are shaded as a function gradient and demonstrate the formation of a high velocity core in decelerating flows and the occurrence of high mean velocities close to the boundary in accelerating flows.

5.4.1 Streamwise velocity profiles

In the presence of macro-bed forms, streamwise velocity profiles systematically deviate from the log law. In the pool-head, near-bed velocities are less and near-surface velocities are greater than predicted. This profile shape is characteristic of deceleration [*Kironoto and Graf*, 1995; *Song and Chiew*, 2001]. In the pool-center and pool-tail, profiles show the inverse deviations from the log law, and the peak velocities often occur close to the bed. This profile shape is characteristic of flow acceleration [*Kironoto and Graf*, 1995; *Song and Chiew*, 2001]. In the pool-tail, the flow cross-sectional area decreases in a streamwise direction and flow acceleration occurs. In the center of the pool, the tree constricts the width of the stream, which induces lateral acceleration of the flow and produces a sharp discontinuity in the shape of the velocity profile between sections 5 and 6.

Comparison with existing studies is rarely straightforward because few studies have distinguished between the pool-head and the pool-tail. In the studied pool, we have shown that the two areas are hydraulically distinct. This distinction may explain some apparent discrepancies among previous studies. *Bhomick and Demissie* [1982] compared one velocity profile measured in a riffle with one measured in a pool. Lower near-bed velocities occurred in the pool during low flow, but at bankfull discharge, near-bed velocities were found to equalize. The velocity profile gradient in the pool was low and the maximum velocity occurred near to the bed. These observations fit with characteristics of profiles in sections 6 and 7 (Figure 5.10), which suggests that this profile was measured in the relatively deep portion of the pool-tail where flow acceleration occurs. *Jackson and Beschta* [1982] measured a single profile in the pool and also found the maximum velocity to occur close to the bed at bankfull flow. Judging from a bed profile of the study site, the measurement also appears to have been made in the pool-tail. *Robert* [1997] spatially averaged the velocity profiles obtained over two riffle-pool units. Riffles and pools were defined as positive and negative residuals from a linear trend using the technique of *Richards* [1976]. This technique is based on elevation, not bed slope, which means that areas with both positive and negative bed slopes are mixed into each morphological unit. It is perhaps for this reason that near-bed velocities from the defined riffles and pools were similar, even at low discharge. *Carling* [1991] measured profiles in three riffle-pools and found surface and mean velocities to roughly equalize at high flow. Equalization of

velocities higher up in the profile does not contradict the results from the current study, but the current study also shows that these values cannot be used to infer near-bed conditions.

Clifford and Richards [1992] were not able to measure velocity profiles using their experimental set-up. They did obtain, however, the most complete information available on the behavior of near-bed velocity with flow stage. It is interesting to compare their Figure 2.8 with Figure 5.11. Similar to our results, the relation between U and Q was found to vary with streamwise position. The only location where the U always increased with Q was the pool-tail. Velocities at the riffle-crest, in contrast, decreased at high flood stages, while those in the center of the pool tended to flatten out so that U remained constant with increases in Q at high flood stages. All of these key results are reproduced in this study. This agreement confirms the conclusion of *Clifford and Richards* [1992] that the log-linear model of velocity discharge relations as hypothesized by *Keller* [1971] is too simple, a conclusion also reached from the field studies by *Petit* [1987] and *Hassan and Woodsmith* [2004], who were also able to measure mean velocity during bankfull flow.

The velocity reversal hypothesis can be significantly refined as a result of the observations in this study. A near-bed velocity reversal occurs between the riffle and the mid-pool through the pool-tail (Figure 5.11). However, such a reversal does not occur between the riffle and the pool-head, which means that an alternate explanation for pool maintenance is required in this area. It is also useful to speculate on the maintenance of free pools in gravel-bed rivers. In Moras Creek, the transition between deceleration and acceleration is forced by the tree that constricts the width. Downstream of this structure, near-bed velocities are accelerated, a downwelling component is added to the velocity vector, likely due to the difference in water surface elevation upstream and downstream of the tree, and boils and vortices are produced in the shear zone that may capable of inducing scour of the bed. In free pools, there is no such forcing mechanism. A general model of pool formation and maintenance therefore cannot include this element. We have shown that deceleration and acceleration dominate flow hydraulics in the pool-head and pool-tail, respectively. We have also shown that our results agree with those obtained at field sites where the pool was not forced. Based on these considerations we propose a general model of riffle-pool hydraulics in Figure 5.14b and discuss the occurrence of laterally converging flow and the link between flow deceleration and turbulence generation in the following sections.

5.4.2 Laterally converging flow and secondary circulation

In Moras Creek, the flow is progressively concentrated in the middle of the channel in the pool-head and then diverges over the pool-tail. This lateral convergence is encouraged by a slight bend in the channel planform, which produces a recirculating eddy, even at high discharge, and the tree, which strongly constricts the channel width. However, there are two reasons to suggest that lateral convergence and expansion is a product of non-uniform flow. First, our results fit with the common observation of a high velocity core in other natural pool sites. This term has most often been used to describe flow through meanders [*Leopold and Wolman*, 1960; *Dietrich et al.*, 1979; *Markham and Thorne*, 1992] and constrictions [*Thompson et al.*, 1999], but converging flow is also evident in the pool-heads of straight sections in the reach studied by *Petit* [1987]. *Clifford and Richards* [1992] also showed that velocities were less uniformly distributed in their straight pool than in the neighboring riffle. The second reason to suspect a general model of lateral convergence and expansion is that the shape of velocity profiles in laboratory flumes has been found to be a function of the width-depth ratio (Z/Y) [*Kironoto and Graf*, 1995; *Song and Chiew*, 2001]. This means that the degree of perturbation to velocity and turbulence intensity caused by non-uniform flow is dependant on the shape of the cross-section. This is highly relevant to the discussion of riffle-pool formation because it suggests that non-uniform flow induces a lateral component to the flow. More tests are needed in a variety of systems, and laboratory experiments may help to clarify the relation between non-uniform flow and lateral convergence. Such a mechanism is satisfying, however, because flow properties are thereby sensitive to channel width, which is broadly accepted as the morphological scaling factor for riffle-pools, and because it provides a unifying mechanism for free, forced and meandering pools to exhibit a similar scaling relation.

Closely related to lateral convergence is the generation of secondary circulation in the pool. The strongest V values observed in the study occurred just downstream of the tree. An increase in water surface slope was observed in this area where water flowed past the tree. This steeper slope produces downwelling flow in the thalweg downstream of the constriction. Strong vortices and boils are present in the adjacent shear flow and are likely to have a strong influence on the size and shape of the downstream pool [*Thompson,* 2004; *Thompson*, 2006]. Secondary circulation also occurs upstream of the tree, however, with velocity generally toward the bed in the thalweg and toward the surface in the channel

margins. We were not, unfortunately, able to measure the three-dimensional flow vectors, as it would be useful to know the lateral flow. Some assistance with this problem is available from flume experiments and numerical modeling. *Booker et al.* [2001] advanced the theory that lateral near bed-flows are directed away from the deepest part of the pool and that what we observe as scour may in fact be the routing of sediment away from the pool. This may be occurring upstream of the tree in Moras Ck, as near-bed velocities over the bar are much faster than in the thalweg. Near surface flows concentrate in the thalweg, but because they are directed toward the bed, conservation of mass dictates that lateral flows are directed away from the deepest part of the channel upstream of the tree. Boils were observed in the channel margins. Three dimensional velocity time series were obtained in a forced pool constructed in a flume by *Thompson* [2004]. Similar to the results in this study, they found vertical velocities to be directed towards the bed in the pool-head and center within the thalweg and away from the bed in the pool-tail. Near-bed lateral velocity vectors were directed away from the center of the pool. Future research using tracer particles to measure directions of near-bed sediment transport vectors could assess the role of this mechanism.

5.4.3 Turbulence generation and energy dissipation

Turbulence is generated as a result of velocity gradients [*Nezu and Nakagawa*, 1993]. Where velocity gradients are greater than what occurs in uniform flow, it is expected that turbulence intensity will also increase. Laboratory studies confirmed this in decelerating flows [*Kironoto and Graf*, 1995; *Song and Chiew*, 2001]. Results from the present study fit this general model, as u' and v' are high where deceleration occurs upstream of the tree, both in an absolute (Figure 5.8, Figure 5.9) and a relative sense (Figure 5.12). Additionally, u' and v' are sharply reduced at section 6, where the constriction has induced strong acceleration of the near-bed velocities. The dominant role of flow acceleration is confirmed by the collapse of u' and v' profiles when normalized by the shear velocity (Figure 5.12). While the v' values are higher than those predicted by *Kironoto and Graf* [1995], the u'/u^* values are consistent with those expected in accelerating flows.

Turbulence intensity equations universally predict $u'>v'$ [*Nezu and Nakagawa*, 1993; *Kironoto and Graf*, 1995], and this result has been supported by a number of natural rivers [*McQuivey*, 1973; *Clifford*, 1996]. This model of turbulence generation is strictly

2D, however, with all turbulence resulting from near-bed processes. The studied pool is a rough environment in which lateral velocity gradients and secondary circulation are additional elements that may account for higher than expected v' values. Surface waves were observed at all flow levels in the thalweg of the pool-head, a factor that is known to strongly influence v' values [*Nezu and Nakagawa*, 1993], and the occurrence of large turbulence intensities near to the surface was predominant in the pool-head. Turbulence is expected to be more isotropic under these conditions, in which case theory predicts that $v'>u'$ [*Monin and Yaglom*, 1981].

There is some support from other field and flume experiments for the spatial variability of turbulence intensities observed here. *Clifford* [1993b] measured up to half-bankfull stage and found turbulent kinetic energy to increase with stage in the pool compared to the riffle. These results were confirmed by *Clifford* [1996], who measured higher E_k in the pool despite lower mean velocities, and *Clifford and French* [1993], who measured particularly large values in the pool-head. *Wohl and Thompson* [2000] also observed a general suppression of turbulence in accelerating flows and an augmentation of turbulence in pools during deceleration. Laboratory experiments have shown that variations in turbulence intensity can be significant for sediment transport. *Nelson et al.* [1995] found the transport of individual sand grains to be positively correlated with instantaneous velocity. *Sumer et al.* [2003] found a general increase of transport with turbulence intensity including one case involving sand in which a 20 % increase in the turbulence level led to a 600 % increase in transport. Turbulence intensity thus appears to be a significant variable with strong spatial variability that cannot be predicted from the mean velocity.

5.4.4 Shear Stress in Non-Uniform Flow

It is very difficult to measure shear stress directly, even in the laboratory, and it is typically estimated from the flow geometry and/or measurements of velocity [*Wilcock*, 1996]. There are a number of methods available for this exercise and four have been applied in this study (Figure 5.13). The methods often give widely different estimates, and while it is not possible to know which estimate most accurately reflects the forces transmitted to bed sediment, it is important to understand how the methods will vary, especially when interpreting previous studies. *Lisle* [1979], *Petit* [1987], and *Teleki* [1972] relied upon the mean shear stress (τ_o). This is not suitable for the calculation of local scour

due to the changes in the boundary layer structure and will be of limited use in non-uniform flow environments [*Robert*, 1990].

Most studies of shear stress in pools and riffles have used the slope from the near-bed velocity profile [*Bathurst*, 1979; *Carling*, 1991; *Whiting and Dietrich*, 1991; *Clifford and Richards*, 1992; *Robert*, 1997; *Sear*, 1996; *Hassan and Woodsmith*, 2004]. This method does not rely on an empirical estimate of bed roughness, but it does assume a logarithmic boundary layer and its utilization in situations other than in wide straight channels is not recommended [*Wilcock*, 1996; *Biron et al.*, 2004]. Typically, shear stress calculated in this manner is inadequate to account for pool maintenance due to the transport of pool sediments at relatively low shear stresses [*Whiting and Dietrich*, 1991; *Robert*, 1997; *Sear*, 1996; *Hassan and Woodsmith*, 2004]. In this study, two methods were used to calculate shear stress from the near-bed velocity measurements (τ_u and $\tau_{\Delta u}$). Both methods calculated low values in the pool-head but only $\tau_{\Delta u}$ was low in the pool-tail. In decelerating flow, velocities are all low near the bed and the slope of the profile is also low, which means that both τ_u and $\tau_{\Delta u}$ are low. In accelerating flow, the near-bed velocity is high and τ_u is high, as is confirmed by our results. Our results also show that $\tau_{\Delta u}$ is often low in the pool-tail. This is likely because the logarithmic layer is compressed in accelerating flows [*Kironoto and Graf*, 1995]. This means that even the near-bed probes can be above the logarithmic layer, as was the case in this study, and erroneous interpretations of low mean velocity shear stress from $\tau_{\Delta u}$ may result.

To avoid the assumptions necessary in the calculation of shear stress from the velocity profile, *Kironoto and Graf* [1995] used the Reynolds shear stress τ_r. This method has not been applied in other studies of pool riffle systems, likely due to the scarcity of the required instantaneous velocity measurements. This method is sensitive to sensor misalignment [*Kim et al.*, 2000] and assumes of two-dimensional flow [*Nezu and Nakagawa,* 1993; *Biron et al.*, 2004]. In our study, the Reynolds shear stress was frequently negative, especially in the pool-head. A quadrant analysis was performed in the companion article to examine the source of this divergence from expected behavior.

Only *Booker et al.* [2001] has estimated shear stress from E_k in a pool-riffle environment. Although, τ_k was calculated within a fluid dynamics model and not measured at their field site, they found that τ_k decreased in riffles at discharges close to the bankfull level and, unlike other estimation methods, to increase in pools. This conclusion is

matched by the results from this study, as very high τ_k values were measured near to the bed in the pool-head at bankfull flows. These results suggest that the stress as a result of turbulence should be considered in an explanation of sediment transport in a pool. There are two components to these fluctuations, the first being their amplitude as discussed here. The second component to the fluctuations is their coherence. The coherence of the instantaneous flow signal and its potential for affecting sediment transport processes in a pool are analyzed in the companion article.

5.5 Conclusions

This study has shown that the flow hydraulics in a forced riffle-pool are dominated by acceleration and deceleration. Non-uniform flow occurs as a result of lateral constriction of the forcing element and topographical changes. In accelerating flow, weaker velocity gradients occur in the vertical direction, except near the bed, where high mean velocities just a few centimeters above the bed apply large mean shear stresses at high discharges. Mean velocity reversal occurs in the mid-pool due to the lateral constriction and on the pool-tail as a result of the topographically induced acceleration. However, a second mechanism is needed to explain the maintenance of depth in the pool-head where mean velocities are insufficient to transport sediment. Decelerating flow is dominant in this area. Strong vertical and lateral velocity gradients are produced in decelerating flow as a high velocity core forms in the center of the channel near the surface. These gradients produce high turbulence intensities, especially near the bed, and this turbulence transfers high instantaneous shear stresses to the bed. Turbulence may account for the maintenance of depth in the pool-head.

Linking Paragraph D

In the previous chapter we presented mean velocity and turbulence intensity statistics at a range of discharges. It was shown that pool morphology perturbs the boundary layer from what is observed in uniform flows. The shape of mean velocity profiles is systematically altered as a result of deceleration and acceleration in the pool-head and the pool-tail, respectively, which strongly affects the distribution of turbulence. This chapter[4] consists of an article that will be submitted as a companion to Chapter 5 of this thesis. Using the same data set, we seek to characterize the coherent structure of turbulent events. The objective is to describe the structure of turbulence in a forced riffle-pool in a gravel-bed river. We were particularly interested in the sources of turbulence generation and possible links between the scales of macro bed forms and coherent turbulent flow structures. Coherence was found to decrease with velocity and discharge. A number of techniques were used to confirm this important conclusion. At low flows, the high velocity flow entering the pool is decelerated by the low momentum of water already in the pool. Turbulence increases in the shear zones and larger scale structures develop as energy decays. At high flows, turbulent exchanges in the pool-head are dominated by a zone of intermittent separation that produces powerful events of short duration. This feature appears to alter the structure of the outer layer and generates a large amount of turbulent energy in the pool-head. The boundary layer is perturbed and contributions to the Reynolds shear stress are frequently high in quadrants *q1* and *q3*. Further study of other systems would be useful to compare interrelations between morphology, mean velocity, turbulence intensity, and the coherence of turbulent events.

---

[4] MacVicar, B. J., and A. G. Roy (*submitted*) Flow dynamics of a forced pool in a gravel-bed river Part B: The structure and scale of turbulent events, *Water Resources Research.*

6 FLOW DYNAMICS OF A FORCED POOL IN A GRAVEL-BED RIVER PART B: THE STRUCTURE AND SCALE OF TURBULENT EVENTS

6.1 Introduction

In the companion article it was concluded that a model of flow hydraulics in a forced riffle-pool must include both the mean flow velocity and turbulent intensity (*see Chapter 5*). The analysis found that non-uniform flow perturbs mean velocity profiles such that low velocities occur near the bed in decelerating flow. Acceleration produces the opposite effect such that the fastest mean velocities occur near to the bed. Turbulence intensity distributions show high amplitude turbulent fluctuations occur within the pool-head, particularly at high discharge. We argued that turbulence intensity appears to be an important control on sediment transport in this area and may be important for pool formation and maintenance. In this article we detail the properties of turbulence in order to document how the production of turbulence changes with discharge and how coherent turbulence interacts with bed morphology.

The possibility that bed form and coherent turbulence scales could be connected was realized early on by authors such as *Matthes* [1947] and *Jackson* [1976], who visually observed links between bed forms, spatially heterogeneous sediment transport, and coherent turbulent flow structures such as boils. There have been many detailed studies that explore the interactions between coherent flow and smaller scale bedforms such as sand-streaks and micro-scale ripples [*Grass*, 1982; *Best*, 1992; *Ha and Chough*, 2003; *Venditti et al.*, 2005], meso-scale dunes [*Kostaschuk and Church*, 1993; *Bennett and Best*, 1995; *Venditti and Bennett*, 2000; *Carling et al.*, 2000; *Best and Kostaschuk*, 2002; *Venditti and Bauer*, 2005], and pebble clusters [*Robert et al.*, 1996; *Buffin-Bélanger et al.*, 1998; *Lawless and Robert*, 2001]. Riffle-pools are distinct from these bed form types because they are macro-scale features that scale with channel width [*Leopold and Wolman*, 1957], are uniquely associated with heterogeneous sediments [*Lisle and Hilton*, 1999; *Thompson and Hoffman*, 2001], and can remain stable through extreme floods [*Madej*, 1999; *Eaton and Lapointe*, 2001]. Coherent vortices have been hypothesized to be responsible for the emergence of the characteristic spacing of 5 to 7 channel widths in riffle-pools [*Yalin*,

1971; *Yalin and da Silva*, 2001] and have been observed downstream of constrictions in forced riffle-pools [*Buffington et al.*, 2002; *Thompson*, 2004; *Hassan and Woodbridge*, 2004], but relatively few measurements of turbulence in riffle-pools exist [*Clifford*, 1996; *Thompson et al.*, 1998], and fewer still have attempted to establish the size and structure of coherent events [*Clifford*, 1993b]. More field studies are needed to characterize the structure and scaling of coherent turbulent flow structures in riffle-pools at a range of discharges and especially when sediment transport is active.

Research on the mechanics of smaller bed forms provides a useful context from which to interpret turbulence data obtained in a pool-riffle unit. Over asymmetrical dunes, coherent structures in the form of Kelvin-Helmholz instabilities develop in the region downstream of the flow crest as a result of flow separation [*Best*, 2005a]. This structure leads to eddy shedding, a mechanism that is responsible for the production of turbulence many times the strength of what is generated near the wall and appears to initiate the transition from ripples to dunes [*Bennett and Best*, 1995]. Shedding eddies propagate toward the surface [*Venditti and Bennett*, 2000] where they produce the commonly observed boil structures [*Jackson*, 1976; *Best*, 2005b]. High shear occurs at the reattachment point and sediment is transported up towards the next dune crest [*Kostaschuk and Church*, 1993; *Nelson et al.*, 1995]. The forms develop on scales related to flow depth because of the depth limitation in maximum eddy size [*Yalin and da Silva*, 2001; *Sukhodolov et al.*, 1998].

Symmetrical dunes present a problem to the theorized role of Kelvin-Helmholz instabilities in the development of dunes because they are often characterized by a reduced angle of the lee slope (<10°) where only intermittent separation occurs [*Simpson*, 1981; *Carling et al.*, 2000; *Best and Kostaschuk*, 2002]. *Simpson* [1989] performed a series of experiments in low-angled, smooth wall expansions to characterize intermittent separation. Similar to what occurs in full flow separation, shear stress at the channel boundary is a function of turbulence generated in a shear zone away from the wall. Large eddies from the shear zone bring momentum toward the channel boundary. Velocity fluctuations are greater than or equal to mean velocities in this region and, unlike separated flow, near-wall fluctuations are not related to a Kelvin-Helmholz shear layer. Instead, the turbulence occurs in the form of vortices that fill the near-wall zone and quickly grow in scale before being ejected back into the main flow. This work is supported by an extensive literature on

intermittent separation in low-angle diffusers used for various purposes in hydraulic engineering (see *Azad* [1999] for review). The work of *Best and Kostaschuk* [2002] shows that the lee-side of a low-angle dune is characterized by shedding eddies, which may account for the similarity of the scaling between symmetrical and asymmetrical dunes [*Best*, 2005a].

Yalin [1971] and *Yalin and da Silva* [2001] consider meanders in the plan form of a river to be equivalent to horizontal dunes. They theorize the periodicity of any defect in a stream boundary to recur at a spacing of $2\pi d$, where d is a length scale. Assuming the channel width is the relevant length scale, this relation is close to that between plan form wavelength and channel width [*Leopold and Wolman*, 1957], provided that the wavelength is doubled as recommended by *Richards* [1976] due to the association of a full meander wavelength with two pool-riffle wavelengths. It is not clear, however, whether coherent turbulent flow structures occur in riffle-pools with either the necessary scale or strength to support Yalin's hypothesis. Large-scale coherent structures in the form of low and high-speed wedges are common in rivers [*Buffin-Bélanger and Roy*, 2000; *Roy et al.*, 2004], but these flow structures scale with flow depth and have not been correlated with macro-bed forms. Coherent events have been visually observed in the shear zone downstream of obstructions [*Buffington et al.*, 2002; *Hassan and Woodbridge*, 2004] and in flume experiments [*Thompson*, 2004; *Thompson*, 2006], but turbulent scales were not estimated in these studies. *Clifford* [1993a] performed the only known field test of Yalin's theory as applied to pool-riffles. Results showed that dominant length of coherent structures corresponded with low multiples of bed roughness. The author did note that larger scales were associated with higher stages, and only conditions up to the half-bankfull event were measured, leaving results open for re-interpretation if a more complete data set were to be obtained.

In this study we present the results of an intensive field-based study of the flow hydraulics in a forced riffle-pool unit. The objectives of this article are to (a) measure and describe the spatial and temporal variability of the size, scales and types of turbulent events in a forced riffle-pool and (b) assess the relation between the scaling of coherent turbulent events and discharge (c) look at the type and mechanisms of turbulence production in the pool. Our results provide new information on the nature of the turbulent flow environment in riffle-pools and how that environment changes as discharge increases. This significantly

improves our understanding of the flow conditions that are present in a forced-riffle when sediment transport is active and what role coherent turbulent flow events might play in bed form dynamics.

Figure 6.1 -Bed topography of study site on August 6, 2004 and photo from spring of 2004 during low flow. Measurement locations are black circles, and yellow circles distinguish the thalweg. Cross-section numbers (XS) are also shown for reference, the blue stars indicate the location of the tree, and light ellipses have been overlain to indicate morphological subunits. Red circles indicate measurement points for which time series visualizations and hole size analyses are included in this article.

6.2 Methodology

6.2.1 Field Site and Data Collection

In this article we provide a summary of the field site, data collection methods, and the quality assurance procedure. Refer to the companion article in this issue for a more detailed description. We collected the data in Moras Creek. At the study site, the bankfull width (Z_{bf}) is 6 m, bankfull depth (Y_{bf}) is 0.7 m, the slope (S) is 1.2 %, and representative

particle sizes D_{50} and D_{84} are 60 and 190 mm, respectively. The layout of the pool and the position of the tree that forces the location of the pool are shown in Figure 5.3. The lee side angle of the riffle/pool-head (θ) varies between 4.5° and 7°. A set of light movable bridges installed above the bankfull water level allowed for the characterization of flow properties up to the bankfull stage. We obtained profiles of instantaneous velocity time series in the streamwise (u) and vertical (v) directions using an array of Electromagnetic Current Meters (ECMs) with a vertical spacing of 10 cm starting at 5 cm above the bed surface. We measured 5 to 6 profiles per cross-section and 6 to 8 cross-sections through the pool for a total of 90 to 270 point measurements, depending on flow depth. Profile locations are shown in Figure 5.3. Time series were sampled at 20 Hz for two minutes. The quality assurance procedure removed the effects of an internal filter, replaced data spikes, and filtered all signal variance above the Nyquist frequency (f_N = 10 Hz). In addition to six floods at low to moderately high levels, we were able to obtain high quality velocity signals during a bankfull flood in August of 2004.

6.2.2 Model of mean velocity and turbulence intensity

In the companion article, we developed a model that describes a time-averaged flow hydraulics in the forced riffle-pool. A brief summary is presented here to facilitate the discussion of the results presented in this article. Despite lateral flow convergence, the topographical expansion in the pool-head and the backwater created by the constriction result in deceleration. Deceleration perturbs mean velocity profiles such that relatively low velocities occur near to the bed. Turbulence intensities are relatively high in decelerating flows. Near to the bed there is a tendency for a peak at $y/Y \approx 0.15$ and this peak can be many times that which is observed elsewhere in the profile. Flow is accelerated past the width constriction presented by the tree. This process produces the opposite perturbation to mean velocity profiles such that near-bed velocities increase relative to near-surface velocities, and the peak velocity occurs closer to the stream bed. Secondary circulation is very strong in the center of the pool and flow towards the bed in the thalweg is balanced by strong boils downstream of the tree and near the channel banks. Vertical contraction of the flow in the pool-tail was shown to result in flow acceleration. Peak velocities occur close to the bed at $y/Y \approx 0.2$. Peak turbulence intensities occur very close to the bed and turbulence production away from the bed surface is suppressed.

6.2.3 Data Analysis

Two main types of analyses are presented in this article to quantify the structure of turbulence in the pool-riffle unit. The first group of analyses considers the velocity series in their entirety. We look for instances of flow separation from the boundary, explore the spectral plots, and calculate mean correlations of velocity signals in space and time. All analyses are described in more detail in the sections following. The second group of analyses refines the characterization of coherence in turbulence by quantifying only conditionally-sampled events from the velocity series. We use a visualization technique based on quadrant analysis to detect coherent turbulent events in instantaneous velocity time series. We also estimate the frequencies and durations of the turbulent events and the contributions of these events to the overall Reynolds shear stress. As a note, the convention used in this article is the definition of x, y, and z as the streamwise, vertical, and lateral dimensions, respectively. Instantaneous velocity components are defined in the streamwise and vertical dimensions as u, and v. This signal is broken down into mean (U, V) and instantaneous fluctuations about the mean (u_i, v_i) such that $u = U + u_i$ and $v = V + v_i$ Standard deviations are represented as u', and v'.

6.2.3.1 Flow Separation

The detachment of the flow from the boundary layer alters the nature of turbulent exchange near the wall [*Simpson*, 1981]. Flow separation is identified using the streamwise velocity, and mean detachment occurs when the mean streamwise velocity is negative. Mean detachment is characteristic of steep-angled dunes [*Best*, 2005a] and pebble clusters [*Buffin-Bélanger and Roy*, 1998]. Intermediate conditions were identified by *Simpson* [1981] based on the intermittency of the instantaneous streamwise velocity (γ_u), defined as the percentage of time for which the streamwise velocity is negative. The three stages of intermediate detachment are incipient detachment (γ_u = 1-20%), intermittent transitory detachment (γ_u = 20-50%), and transitory detachment (γ_u = >50%). These stages have been identified over other bed forms such as low-angled dunes [*Carling et al.*, 2000; *Best and Kostaschuk*, 2002]. We used the mean velocity and the fluctuating signal to identify zones of mean and intermediate detachment in the riffle-pool unit during the measured floods.

6.2.3.2 Spectral analysis

Spectral analysis is a powerful tool in the analysis of turbulent velocity signals [*Kolmogorov*, 1941; *Soulsby*, 1980; *Frisch*, 1995; *Nikora*, 2005]. As outlined in *Nikora* [2005], the frequency domain can be divided into three or four ranges that are characterized by specific exponents in the relation between spectral density (S_f) and frequency (f). From lower to higher frequencies, these are: (a) the large-scale energy production frequency range, where the spectral energy has a flat slope ($S_f \propto f^0$); (b) the "-1" scaling range, which *Nikora* [1999] proposed to be the result of superimposed energy production and energy cascades ($S_f \propto f^{-1}$); (c) the inertial subrange ($S_f \propto f^{-5/3}$); and (d) the dissipative range, which occurs at higher frequencies than what is measured by the ECMs used in this study and will not be discussed.

Spectral plots have also been used to identify dominant frequencies in the velocity signals, both as a means of identifying frequencies contaminated by electronic or other interference [*Lapointe et al.*, 1996] and the frequencies of shedding eddies in the lee side of bedforms [*Kostaschuk and Church*, 1993; *Venditti and Bennett*, 2000; *Best and Kostaschuk*, 2002; *Venditti and Bauer, 2005*]. We identified signal contamination by the presence of sharp peaks in the data quality assurance procedure summarized in the companion article. In this article we identified eddy shedding frequencies by the presence of broad peaks in the spectral density. The frequency of spectral peaks (f) can be related to a length scale (d) using the Strouhal relation:

$$N_s = fd/U \tag{6.1}$$

where N_s is a constant referred to as the Strouhal number. *Levi* [1991] found the Strouhal number to be consistent across a wide range of systems, and suggested $N_s = 1/2\pi = 0.16$. Over sand dunes *Venditti and Bauer* [2005] suggested a range of $N_s = 0.10$-0.25 where d is the dune height. In gravel-bed rivers, *Clifford et al.* [1992] used the Strouhal relation to explain the link between the sediment size of the bed and the roughness of the flow. They used a value of $N_s = 0.2$ to relate the dominant particle size (D_{84}) to dominant frequencies in the turbulent flow.

6.2.3.3 Space-time correlation and auto-correlation

In our measurements we simultaneously sampled water velocity at four points in a profile. This design allowed us to calculate the correlation between the signals as a means

of assessing both the size and the character of coherent turbulence structure. We estimated the correlation coefficient (r_{mn}) between the simultaneously measured time signals from two probes m and n at two heights and over a range of time lags (l). From this, we extracted the maximum correlation coefficient (r_{max}) and the lag at the time of maximum correlation (l_{max}). l_{max} has been used in other studies as a means of estimating the angle of the front of the structure in order to determine whether a given event is first expressed in the inner or outer flow region [*Buffin-Bélanger et al.*, 2000; *Roy et al.*, 2004]. This type of analysis is important for understanding the momentum exchange dynamics in the boundary layer.

To obtain a second estimate of the average size of coherent events and compare with values calculated using spectral analysis, we derived the auto-correlation function (r_{nn}) at different time lags (l). From this we obtained the integral time scale (*ITS*)

$$ITS = \int_0^L r_{nn}(l)\, dl \tag{6.2}$$

where L is the time lag at which r_{nn} is no longer significantly different from zero. There have been limited tests of the behavior of *ITS* in gravel-bed rivers. Some data have been published in *Roy et al.*, [1996] and *Roy et al.* [2004], but there is little information on the variability of this parameter. This study provided new data on the spatial variability of *ITS* over bed forms and its relation with the mean velocity.

6.2.3.4 Event Analysis

In their seminal works on structure in turbulent flows, *Kline et al.* [1967] and *Corino and Brodkey* [1969] showed that intermittent sweeps and ejections are responsible for the majority of the momentum exchange between the inner and outer regions of the flow in the turbulent boundary layer. There are a number of techniques used to identify the occurrence and strength of these events (see reviews in *Bogard and Tiederman* [1986] and *Roy et al.* [1996a]). In this study, event classes were determined by a quadrant analysis [*Willmarth and Lu*, 1972] because it allowed comparison with other studies of coherent turbulent events over bed forms [*Sano and Shirakashi,* 1994; *Bennett and Best*, 1995; *Buffin-Bélanger and Roy*, 1998; *Venditti and Bennett*, 2005; *Aubertine and Eaton*, 2005]. A selection of the data is presented using space-time velocity matrices to help visualize the

event structure [*Buffin-Bélanger et al.*, 2000]. In this technique, each pixel in a space-time velocity matrix is shaded a color (q_c) according to the detrended velocity fluctuations:

$$q_c = \begin{cases} \text{dark grey} & \text{if } u_i > 0 \;\&\; v_i > 0 \quad (q_1 \text{ - outward interaction}) \\ \text{white} & \text{if } u_i < 0 \;\&\; v_i > 0 \quad (q_2 \text{ - burst}) \\ \text{light grey} & \text{if } u_i < 0 \;\&\; v_i < 0 \quad (q_3 \text{ - inward interaction}) \\ \text{black} & \text{if } u_i > 0 \;\&\; v_i < 0 \quad (q_4 \text{ - sweep}) \end{cases} \tag{6.3}$$

Here, space refers to the points along a vertical profile where flow velocities have been measured simultaneously. This color scheme allows the distinction of the four quadrants. In addition, faster streamwise velocities are represented by the two darker shades, which means that areas of low and high-speed flow can also be distinguished as it was first used by Buffin-Bélanger and Roy (2000).

The relation between the frequency and duration of turbulent coherent events was investigated following the method of *Paiement-Paradis et al.* [2003]. This technique is useful because, unlike spectral analysis and integral time scales that calculate event scales for the entire signal, it is sensitive to intermittent coherent events. Similar to *ITS*, however, there is little information in the literature concerning the variability of this parameter in rivers. We present frequency-duration plots of high-speed events ($u_i > 0$) to allow a direct comparison with *Paiement-Paradis et al.* [2003] and because turbulent fluctuations for which the streamwise velocity is greater than the mean have been found to be significant for sediment transport [*Nelson et al.*, 1995]. The frequency and duration of individual events were computed from the velocity records and the slope of the log-log frequency-duration relationship (s_u) was estimated. We did not use a threshold value in event detection because $H>0$ decreases the frequency of short events and introduces a point of inflection in the relation [*Roy et al.*, 2004].

Shear stress calculations in the companion article found that the Reynolds shear stress ($\tau_r = -\rho\overline{u_i v_i}$) was often negative, especially near to the bed in the pool-head. In order to better understand this result, we calculate the contributions to the Reynolds shear stress by quadrant (χ_q) using the technique of *Willmarth and Lu* [1972]. Shear stress contributions by quadrant are typically normalized by the net Reynolds stress. However, in

order to avoid normalizing by negative values, we used the sum of the two quadrants that contribute to positive shear stress $\left(\overline{u_i v_{i24}}\right)$ such that:

$$\chi_q = \frac{\overline{u_i v_i}(H)}{\overline{u_i v_{i24}}} = \frac{1}{T\overline{u_i v_{i24}}} \int_0^T u_i v_i(t)\eta(t,H)dt \tag{6.4}$$

$$\text{where } \eta = \begin{cases} 1 & \text{if } |u_i v_i(t)| \le Hu'v' \\ 0 & \text{otherwise} \end{cases} \tag{6.5}$$

and the point (u_i, v_i) is in the quadrant q, t is time, T is total time, and H is the hole size.

6.3 Results

6.3.1 Flow Separation

Figure 6.2 presents a contour plot of the streamwise velocity intermittency (γ_u). We subdivided the category of incipient detachment from *Simpson* [1981] into classes of γ_u = 1-5% and γ_u = 5-20% for added detail. Three flow rates are presented and contours are shown for all eight cross sections except for the largest flood, where damage to our bridge grid during an above-bank flood event prevented us from measuring at the upstream-most cross-section. Flow is from top to bottom and the right and left sides of the channel are defined looking upstream. There are small areas in sections 1, 2, 7, and 8 where γ_u > 5%. These areas occur near the bank in section 1, where bank interference may be playing a role; at the surface in the thalweg of section 2 at high flow, where large standing waves were observed; and close to the bed in sections 7 and 8, where separation zones behind large clasts may be playing a role. Overall, however, γ_u is generally less that 5% in sections 1, 2, 7, and 8. This characterization strongly contrasts with what is observed in sections 3 to 6. In sections 3 to 5, upstream of the tree and in an area characterized by flow deceleration, there is a trend towards increasing separation of flow in a downstream direction. This is true even at high flow where areas with mean flow separation (γ_u > 50%) are present. γ_u is less than these values in the near-bed zone of the thalweg, but sections 3 to 5 all show γ_u > 20%, which means that they are characterized by intermittent transitory detachment [*Simpson*, 1981]. Mean flow separation does not occur in the thalweg, a result that was expected based on the relatively mild value of 4.6° for the lee side angle of the riffle and pool-head. In section 6, γ_u > 5% over the bar and downstream of the tree in the near-bed region of flow in the thalweg. However, γ_u is generally less than 5% in the thalweg in this region, which suggests the dynamics of flow separation are not as important in this area.

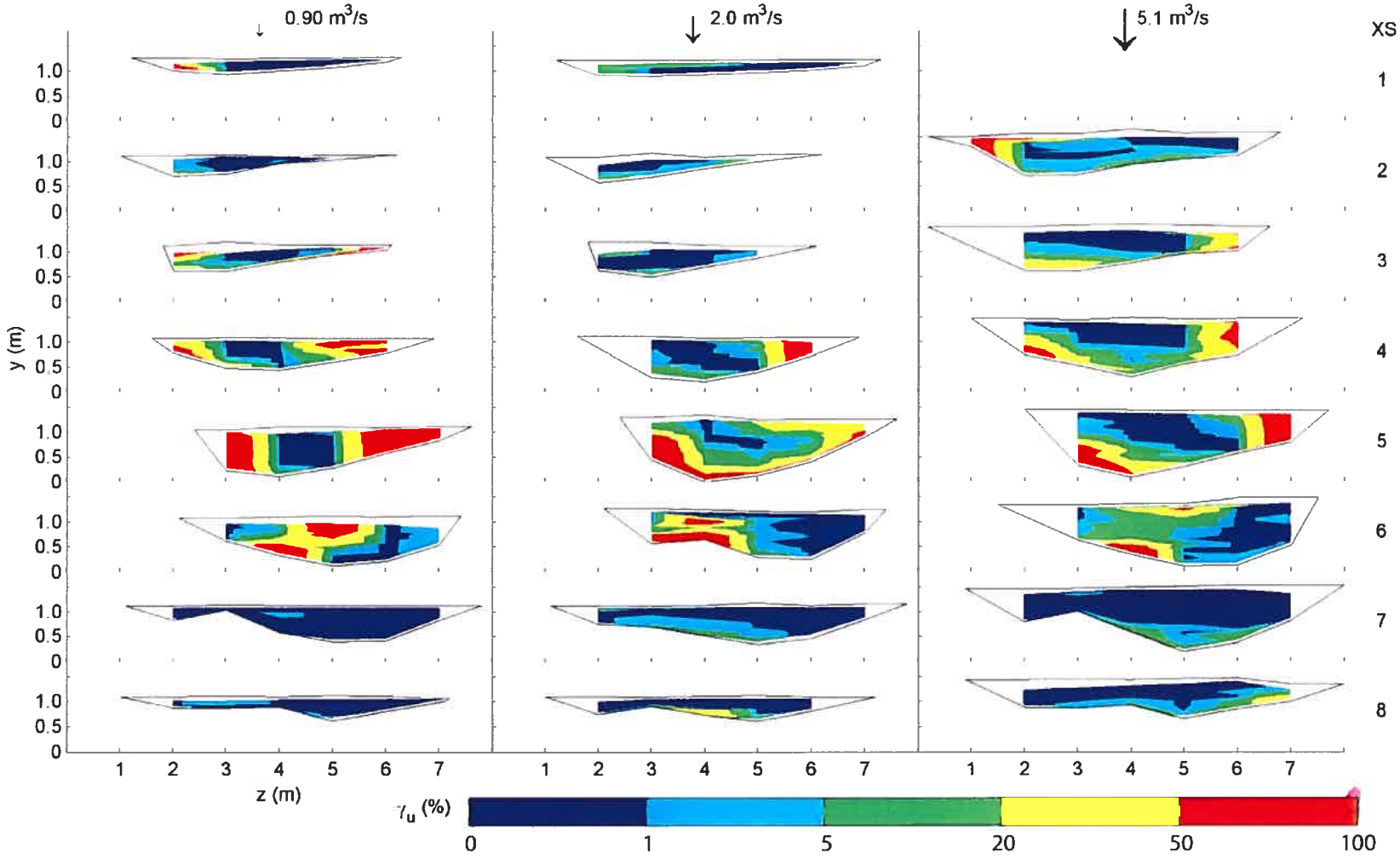

Figure 6.2 - Contours of the intermittency of the streamwise velocity (γ_u) at three discharges. Flow direction is from top to bottom. The tree that forces the pool is located between sections 5 and 6 on the left bank out to a distance of approximately 5m.

6.3.2 *Spectral analysis*

Although it is not possible to present spectra at all locations and at all flow stages, we present a sample of streamwise (S_{fu}) and the vertical (S_{fv}) spectra that show how spectral densities in the thalweg change with position in the riffle-pool and over the range of sampled discharges (Figure 6.3). Before discussing the details of the plots it is important to examine the overall patterns in spectral density. At the lowest discharge, the spectral density increases between sections 1 and 2, decreases from sections 2 to 5 in the riffle and pool-head, and then stays low through section 8. At $Q = 2$ m^3/s, there is an increase between sections 1 and 2, a decrease between sections 2 and 3, and another decrease between sections 5 and 6. It is useful to note that, unlike what was observed at lower discharges, the spectral density through sections 3 to 7 at $Q = 2$ m^3/s are equal to or greater than the spectral densities in section 1. It was not possible to measure the upstream section during the bankfull flood, but the highest spectral densities of the measured sections clearly occur in sections 3 to 5 at this discharge. This shows that the pool environment switches from one in which the turbulent energy decays through the pool during low flow to one in which the turbulent energy peaks in the pool and especially in the pool-head during high flow. This also confirms the large increases in turbulence intensity that were observed near the bed at high flows in the companion article.

Spectral plots do not always follow the model of four subranges that has been applied to uniform flows in gravel-bed rivers [*Nikora*, 2005]. Instead, the extent of the subranges varies with the position in the riffle-pool and discharge. In all cases, a steep fall-off is observed above a frequency of 4 Hz. This fall-off is a result of spatial averaging within the sampling volume [*Soulsby*, 1980] and, above a frequency of ≈ 7 Hz, the 3rd order Butterworth filter that is applied to remove all variance above the Nyquist frequency. For frequencies immediately below a frequency of 4 Hz, $S_f \propto f^{-5/3}$ is a reasonable approximation of the slope in most locations and at most flow rates. This inertial subrange covers a variable frequency range in the plots. In some areas, such as S_{fu} in section 2 for all flow rates, the range is small ($f \approx 2$ - 4 Hz), while in other areas, such as S_{fu} in section 5 at moderate flow rates, the range is much larger ($f \approx 0.4$ - 4 Hz). In general, it appears that wide inertial subranges are associated with locations where energy is decreasing in a downstream direction.

At frequencies higher than the inertial subrange, behavior falls into three categories. For low and moderate discharges in sections 3 to 8, spectral densities follow a negative slope that is less than that in the inertial subrange. Some areas, particularly in sections 6 to 8 during the three lowest discharges, appear to follow $S_f \propto f^{-1}$ as suggested by *Nikora* [1999]. Other areas, such as for $Q = 0.1$ m^3/s in sections 5 to 7, slopes are flatter than the suggested value. The reason for this behavior is not clear but the inertial subrange is very short to non-existent in these areas, and instrument noise may be affecting signal quality due to the low turbulent intensity in the essentially still water of the pool at the lowest flow rates. A second category corresponds to S_{fu} plots where slopes are essentially flat for frequencies lower than the inertial subrange. This is characteristic of sections 1 and 2 at all discharges and for all the other sections at moderate to high discharges. It indicates that turbulence changes from a four range to a three range model (the dissipative range is expected to occur in all cases but at higher frequencies than what is shown in Figure 6.2) as discharge increases. The third category of spectra displays positive slopes for frequencies lower than the inertial subrange. This is shown for S_{fv} in the pool sections 3 to 5, and again at section 8. Positive slopes indicate turbulence generation. They are useful for the identification of broad peaks and have been used to identify eddy shedding frequencies downstream of dunes, isolated boulders, and pebble clusters [*Venditti and Bennett*, 2000]. For the results presented here, the peak frequency is between 0.8-2 Hz, which, at the depth-averaged velocities of 1.05-1.22 m/s (see Table 5.3) and assuming the D_{84} as the length scale in Equation 6.1, yields $N_s = 0.22$ - 0.25. This value is larger than the theoretical value of $1/2\pi$ adopted by *Levi* [1991], but close to the value of 0.2 suggested by *Clifford et al.* [1992] and within the range of 0.10 - 0.25 observed over dunes by *Venditti and Bauer* [2005]. Using other available length scales in the river such as the depth ($Y = 0.9$ - 1.34) or the width ($Z_{bf} = 6$ m) yields estimates of N_s that range upwards from 0.6, a value that is much greater than those in the other studies. Another length scale that is relevant is the height of the zone of intermittent flow detachment in the pool-head (Figure 6.2). Though precise determination of the dimensions of this area is not possible with the measurements obtained in this study, it appears that the zone is on the same order of magnitude as D_{84}. This suggests that eddy shedding frequencies are determined by the near-bed conditions and controlled by particle sizes or the zone of intermittent separation in the pool-head.

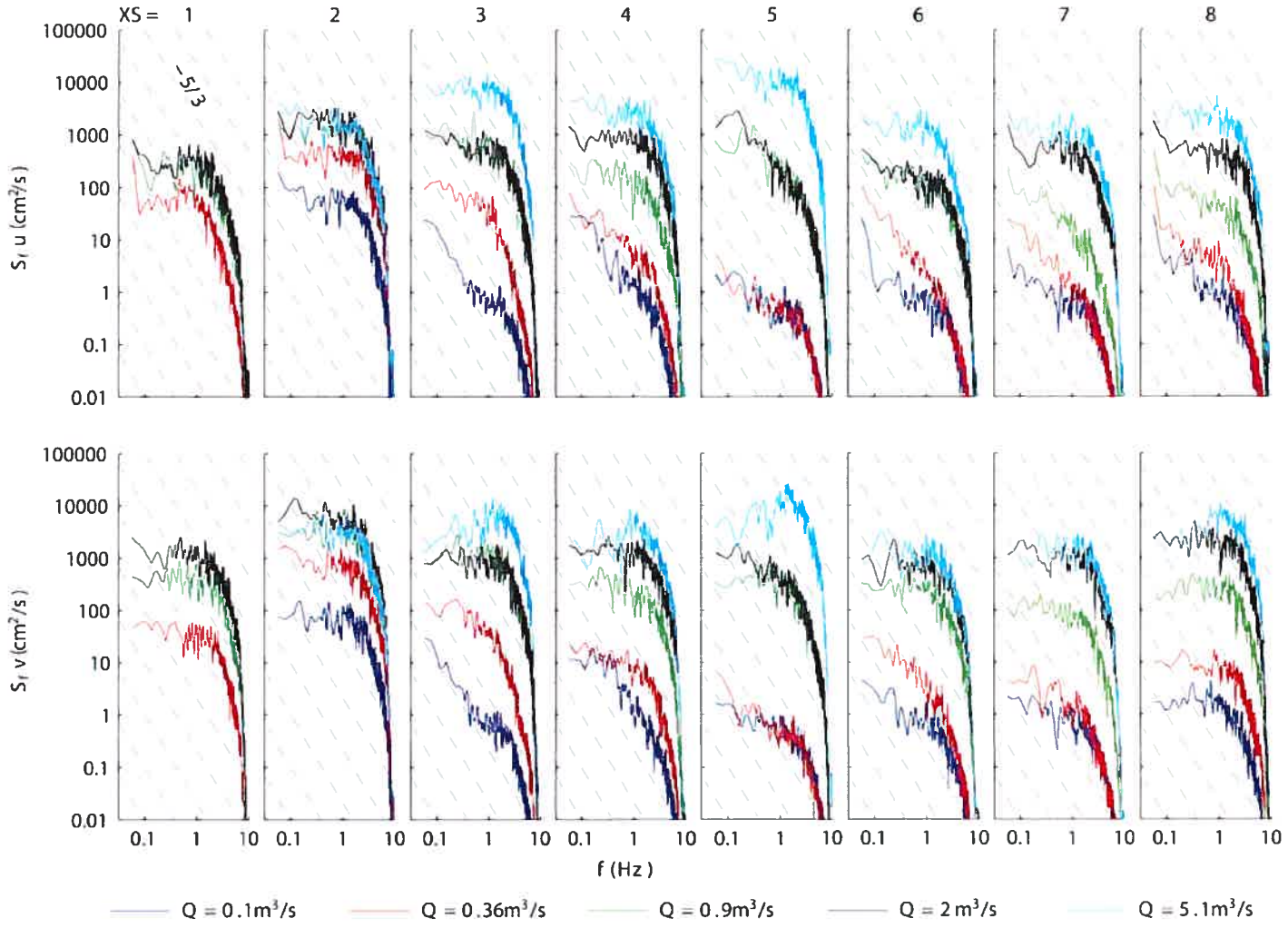

Figure 6.3 - Spectral density plots of probes at y = 15 cm in thalweg at five discharges.

6.3.3 *Space-time correlation and auto-correlation*

Figure 6.4 shows the maximum space-time correlation (r_{max}) between probe pairs at 5 and 15 cm above the bed and at 15 and 25 cm above the bed, as well as the time lag at which the maximum correlation occurs (l_{max}). Looking first at the r_{max}, represented by the radius of the circle where the correlation is statistically significant ($\alpha = 0.05$) and by a square where it is not, some broad patterns are evident. The highest values correspond with the recirculation eddy on the right side of the channel. Values of $r_{max} > 0.5$ occur in this area. Other areas with above average r_{max} values occur immediately downstream of the tree and on the left side of the channel upstream of the tree. In the thalweg, a swath of values that are not significantly different from 0 occurs downstream from the tree and a smaller cluster of such values also occurs of sections 2 and 3. These areas correspond with those in which boils were commonly observed. In contrast, significant but moderate values of r_{max} were found in the pool-head. Values are typically less than 0.2, which is lower than all values reported in *Roy et al.* [1996a], *Buffin-Bélanger et al.* [2000], and *Roy et al.* [2004] for probes with similar spacing in uniform flow conditions. It is interesting to compare Figure 6.4 with the diagram of flow separation (Figure 6.2). r_{max} appears to correspond with γ_u as they are both high in the recirculation zone and moderate in the pool-head close to the bed.

Contrary to *Buffin-Bélanger and Roy* [2000] and *Roy et al.* [2004], who observed predominantly negative time lags in the maximum correlation between adjacent probes (l_{max}), Figure 6.4 shows a mixed population of positive and negative values. In this mixture of values, two general observations can be made. First, sections 2 to 4 have predominantly negative time lags. Exceptions occur but are primarily located in the channel margins. This indicates that flow entering the pool generally follows the model of forward leaning high and low-speed flow wedges advanced by *Buffin-Bélanger and Roy* [2000]. In this model, events first occur in the outer layer, which would indicate that near-bed events are controlled by the passage of large-scale structures in the flow. In contrast, l_{max} is predominantly positive in sections 5 to 7. Exceptions to this rule also occur and the frequency of values that are not significantly different from 0 reduces the confidence in this observation, but it does suggest that new turbulence is being generated at or close to the bed in the pool-head and around the tree because the turbulent events primarily occur close to the bed first and can then be followed out into the outer regions of the flow. Although data

is limited, it indicates that turbulence production often occurs near the bed in areas associated with intermittent flow separation in the pool-head and with the production of vortices and boils around shear zones.

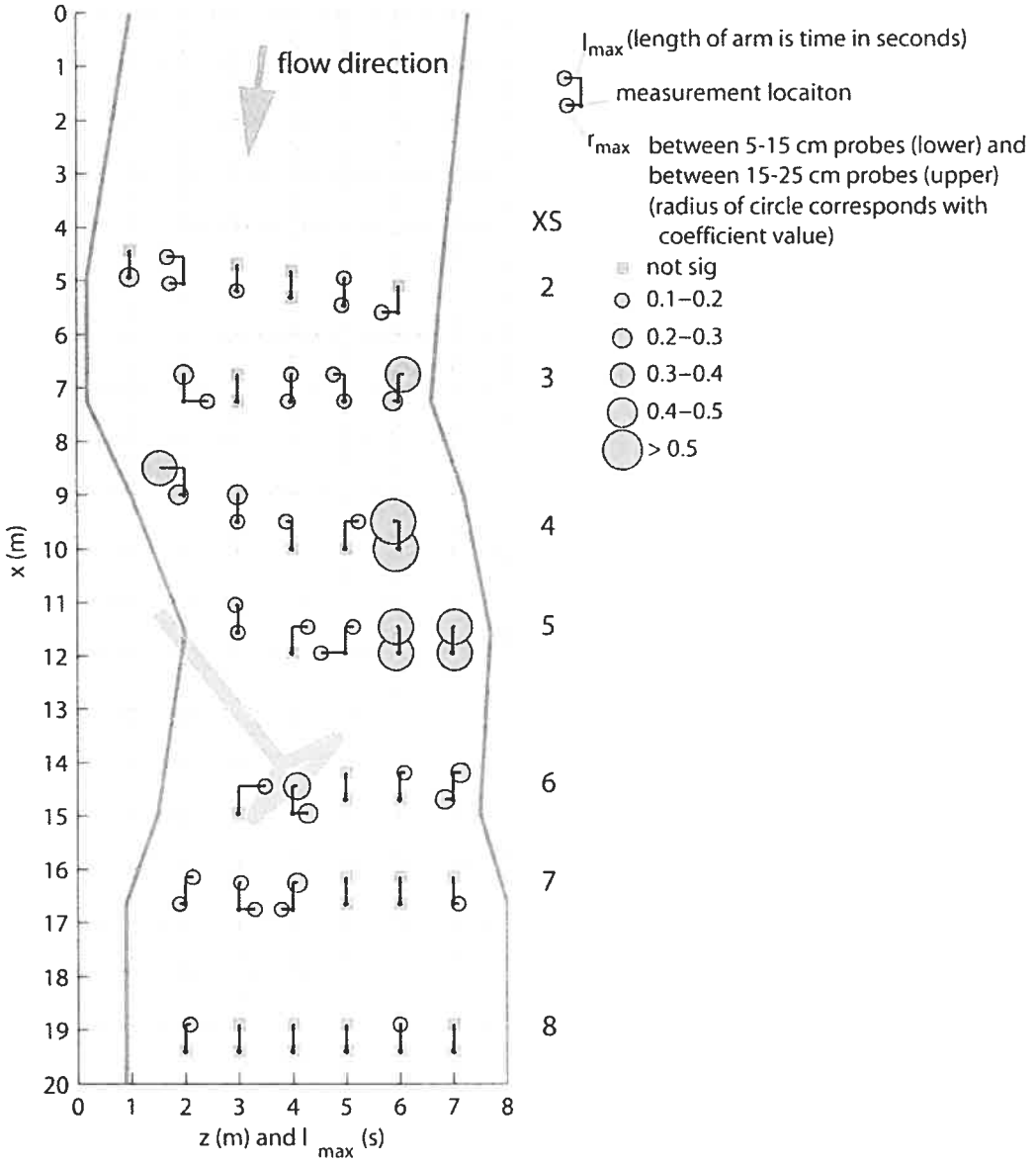

Figure 6.4 – Space-time correlations between probe-pairs at 5 and 15 cm from the bed and 15 and 25 cm from the bed. The maximum correlation coefficient (r_{max}) and the time lag at r_{max} (l_{max}) are represented as shown in the legend. l_{max} is positive to the right and negative to the left.

Contour plots of the integral time scale (*ITS*) of the streamwise and vertical velocity components at the cross-sections are shown in Figure 6.5 and Figure 6.6, respectively. For comparison, *Roy et al.* [1996] found $ITS_u \approx 0.65$ s and *Roy et al.* [2004] found a range of $ITS_u = 0.4$ - 1.2 s in gravel-bed rivers during base flow discharges. At low flow, both ITS_u

and ITS_v often exceed 1 s in the pool and channel margins (sections 4 to 7). *ITS* does not exceed 0.5 s in the thalweg through the deep part of the pool and in the shallower sections 1 to 2 and 8. As a general rule, *ITS* has a negative relation in the pool with discharge. *ITS* values are lower in the thalweg through the center of the pool at the moderate discharge. Values in the recirculation flow zone upstream of the tree and in the boil zone downstream of the tree are also reduced, although values above 1 s still occur in the channel margins. At high flow, ITS_u does not exceed 0.2 s at any position in the thalweg and through the deepest part of the pool. The values through sections 3 to 7 are generally higher than those in sections 2 and 8. Although the absolute value of ITS_u is lower at high flow, the same patterns observed at lower discharges are still visible, as ITS_u is higher downstream of the tree in section 6 and in the recirculation zone on the right side of the channel upstream of the tree. ITS_v shows similar patterns to ITS_u but is typically smaller. While ITS_u generally increases toward the banks in recirculation zones, ITS_v is generally highest away from the banks. This feature is more evident at the lowest discharge and occurs in the zone characterized by shear between the fast velocities in the thalweg and the low velocities in the recirculation zone.

It is clear from the spatial patterns in Figure 6.5 and Figure 6.6 that a relationship exists between the velocity and the integral time scale. To clarify the relation, we plotted ITS_u versus the local mean velocity (U) in Figure 6.7. All data points measured in Moras Creek during this study are shown. There is a negative relation between *ITS* and U. Due to the broad scatter, we have fit two bounding relations by eye. A few points with values of $ITS \approx 0.1$ s do not fit within the bounding relations. These points generally tend to be located in nearly still water in the pool during the lowest discharges and corresponded with points characterized by low spectral density and relatively flat S_f - f slopes (Figure 6.3). For the rest of the data, it is interesting to note that, despite the scatter observed during any one flood and the fact that flows are generally faster for higher discharges, all floods collapse into the same area of the plot. Comparison with other studies is limited, but the data from *Roy et al.* [1996a] fall close to the upper bounding relation.

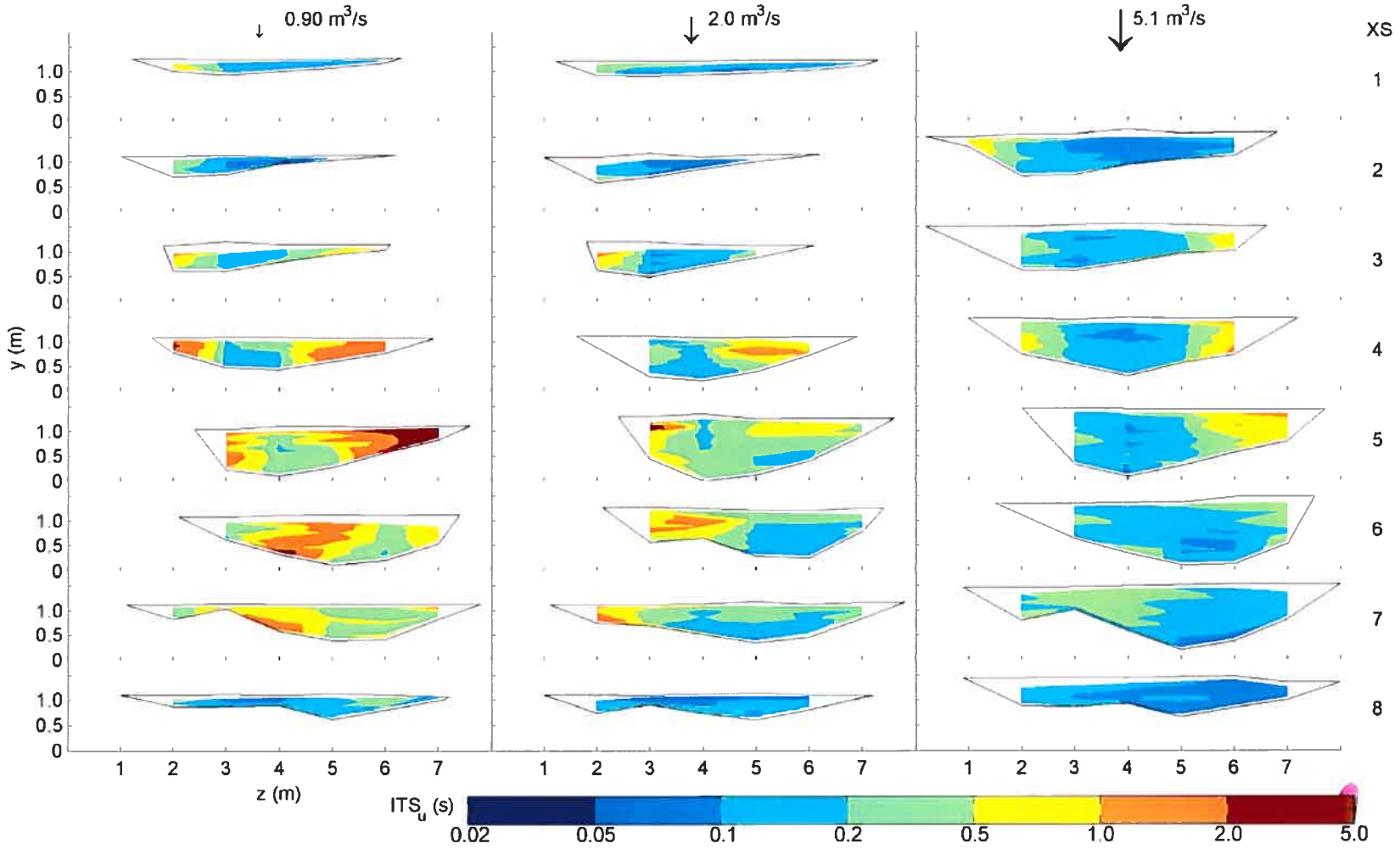

Figure 6.5 - Contours of Integral Time Scale (*ITS*) for streamwise component of velocity (*u*) at three discharges. Flow direction is from top to bottom. The tree that forces the pool is located between sections 5 and 6 on the left bank out to a distance of approximately 5m.

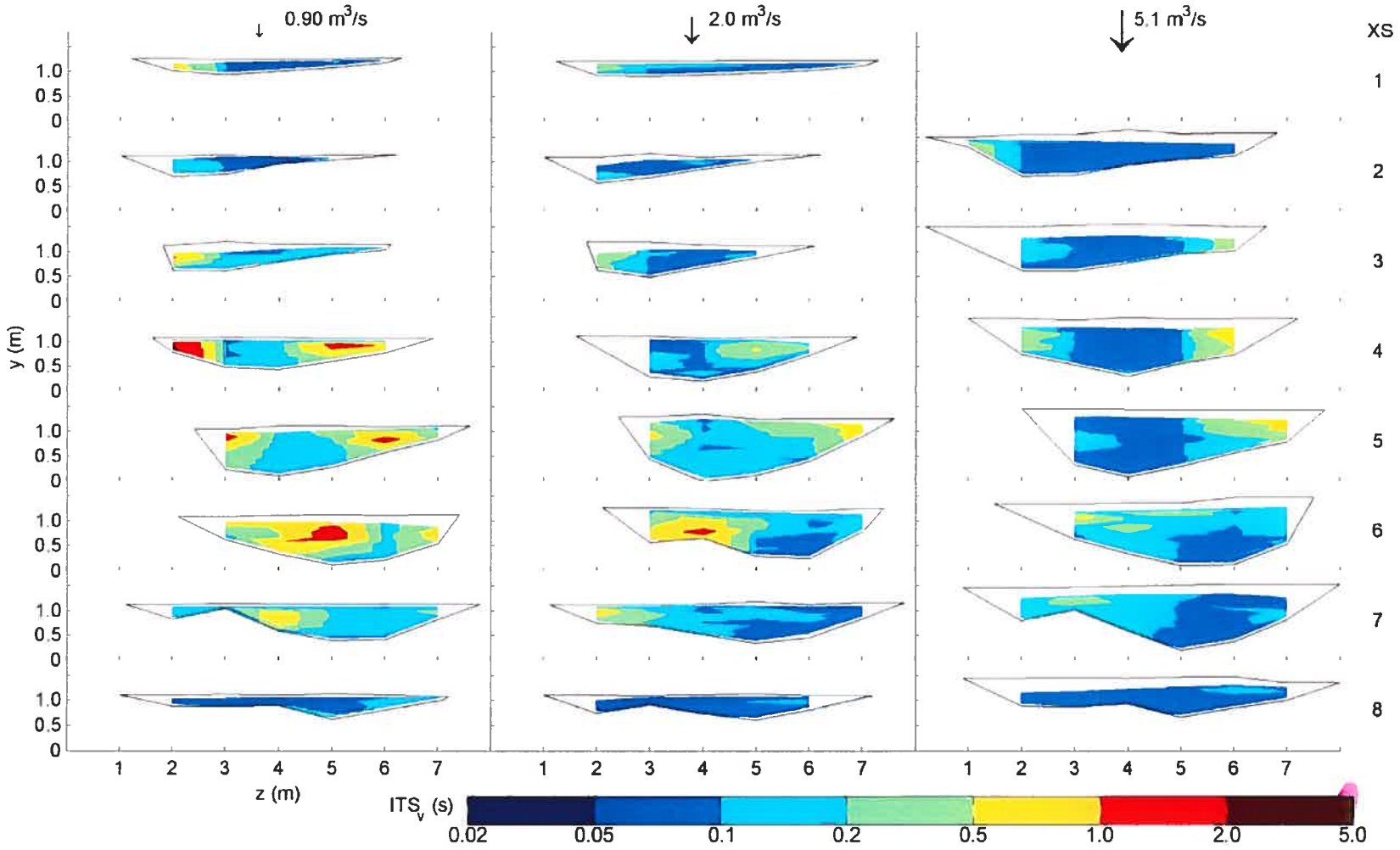

Figure 6.6 - Contours of Integral Time Scale (*ITS*) for vertical component of velocity (*v*) at three discharges. Flow direction is from top to bottom. The tree that forces the pool is located between sections 5 and 6 on the left bank out to a distance of approximately 5m.

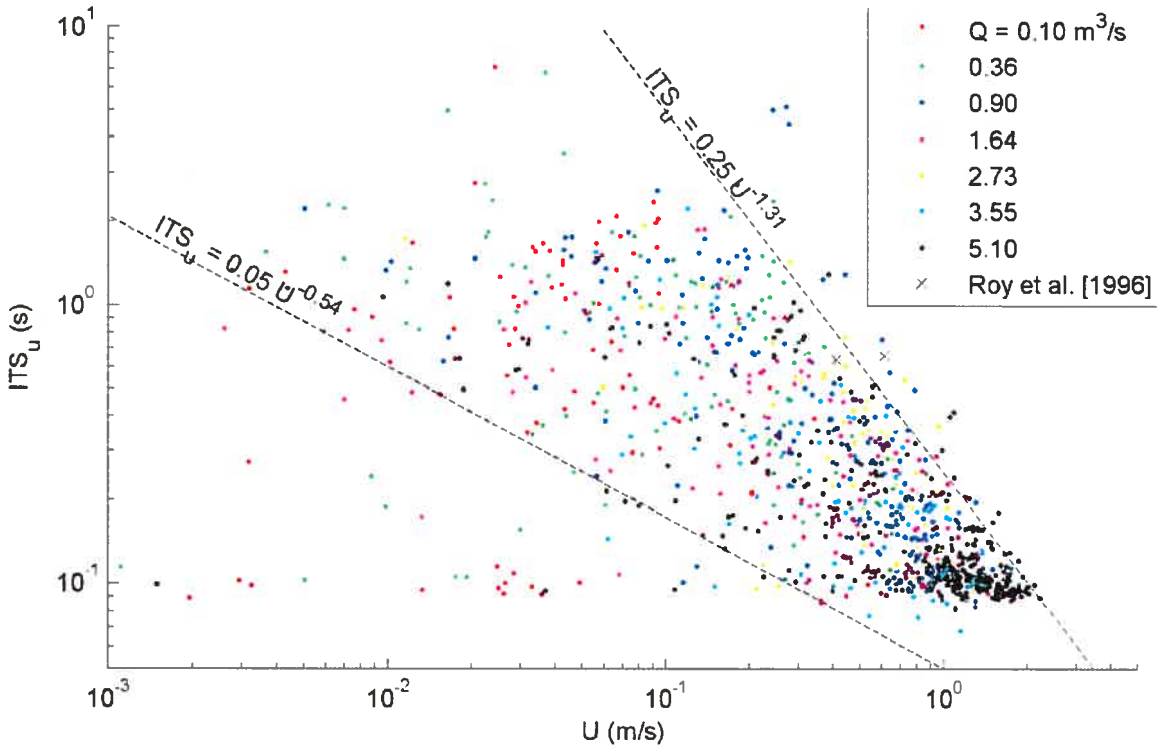

Figure 6.7 – Integral time scale of the streamwise velocity (ITS_u) versus mean streamwise velocity (U). Two relations were fit by eye to encompass the dense region of data points.

6.3.4 Event analysis

Figure 6.8 presents examples of space-time streamwise velocity matrices. This figure is intended to introduce the spatial and flood stage variability encountered in the characterization of the event structure in this highly energetic and heterogeneous flow environment. The plots represent the simultaneous quadrant fluctuations on a vertical profile during 10 seconds. This length of time allowed for a reasonable comparison of areas characterized by highly variable flow with those where the flow is more organized. Three to four probes per position are shown at three different flood levels. The positions are shown in Figure 6. . Uniform flow in gravel-bed rivers has been characterized by low and high-speed flow wedges usually visible as forward leaning (to the right) and alternating dark and light bands occupying the full depth of the flow [*Buffin-Bélanger et al.*, 2000]. These wedges may last several seconds. Although we observe some periods where the same quadrant is present at all heights above the bed simultaneously, the occurrence of these wedges is not well developed within the thalweg (Figure 6.8a-d). Variability, as identified by rapid temporal switching between quadrants, is too high to definitely observe a typical structure, although many individual structures appear to lean backwards. A larger

scale structure is visible in section 6 at moderate flow consisting of slow moving fluid convecting toward the surface. A general picture of high variability observed at most positions contrasts with the occurrence of large-scale structures in the recirculation zone (Figure 6.8e). These structures lean both forward and backward, which means that many forms, such as a zone of dark (fast) quadrants at $Q = 2.0$ m^3/s, are first expressed near the bed. The zone downstream of the tree is characterized by a smaller scale of coherent flow structures as discharge increases (Figure 6.8f). At the lowest discharge, the wavelength for the structure is longer than the isolated section of the velocity signal, but at high discharge, quadrant variability is similar to what occurs in the thalweg. Similar to (e), events are often first expressed near the bed and propagate upwards. This agrees with the spatial correlation analyses, which showed that the pool perturbs the flow wedge model and structures first expressed at the lowest probe and propagating upward become more common through the pool. These observations correspond with visual observations of boils at the water surface.

Frequency duration curves are shown for the probes at $y = 0.15$ m in the thalweg at bankfull flow (Figure 6.9). A log-linear regression was calculated to determine the slope (s_u) as shown on the figure. For comparison, 100 time series were randomly generated with a normal distributions defined by local mean velocities and standard deviations. Error bars were calculated to encompass 95% of the statistical variability. Comparison with the measured frequencies demonstrates that the occurrence of longer-duration events is not predicted with the random model. This figure also demonstrates that the frequency-duration method obtains reliable estimates of straight-line plots in log-log space. There are slight differences between positions, but no clear trends are visible and results from the full data set, described below, will better illustrate the spatial variability of this parameter. The slopes tend to be slightly steeper than the near-bed measurements of *Paiement-Paradis et al.* [2003] who found $s_u \approx -1.7$.

Figure 6.8 - Space-time velocity matrices of six positions at three discharges. Three to four probes along a vertical profile at each location are shown. Locations consist of four positions in the thalweg (a-d), one position in the recirculation zone to the right of the channel (e), and one position immediately downstream of the tree that was characterized by recirculation at low flow and boils at high flow (f). Time is reversed on the horizontal axes so that velocity structure appears as it would if, assuming 'frozen' turbulence, a photo was taken from a side view of the river.

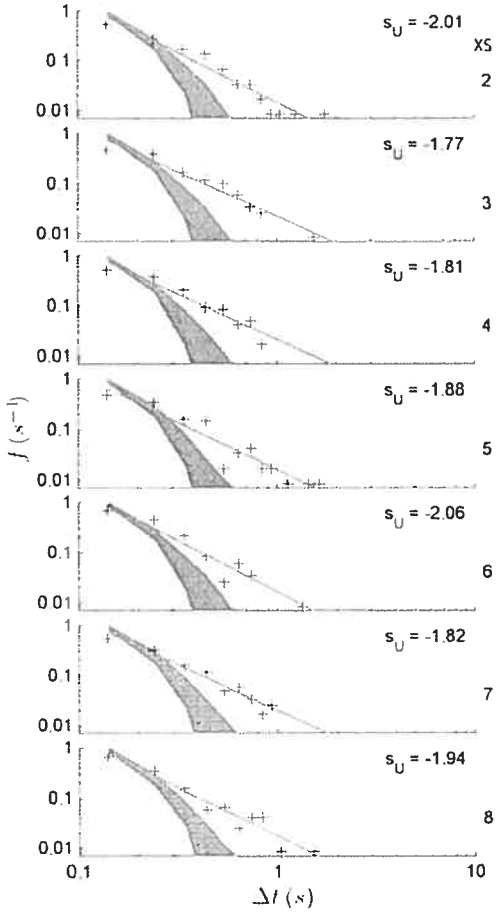

Figure 6.9 - Duration-frequency plots of high-speed events ($u' > U$) at y = 15 cm in the thalweg at bankfull discharge. The linear regression model is shown and the frequency-duration slope (s_u) is included. Event analysis of 100 permutations of normally distributed random signals was used to generate the random event envelopes defined by the shaded area.

Contour plots of s_u are shown at three flow rates in Figure 6.10. Values range from s_u = -2.5 to - 0.5. This is a much larger range than what was observed in *Paiement-Paradis et al.* [2003] where flows were uniform and velocities generally lower. Overall, the spatial patterns of s_u are similar to those of ITS_u. There is a tendency towards decreasing s_u in the thalweg and with discharge so that the lowest values occur during the bankfull flood. The major difference is that there is better separation of values in the thalweg where s_u is steep and ITS_u is low. This sensitivity is thought to be the result of sensitivity in s_u to relatively rare intermittent events. The new information in this plot shows that, within the pool-head sections 3 to 5, the lowest values of s_u occur near to the surface. In contrast, the lowest values in the center and pool-tail at sections 6 to 7 occur near to the bed. This switching of s_u profiles follows that of the mean velocity profiles as discussed in the companion article

and indicates that, similar to *ITS*, s_u is a function of mean velocity. We plotted U against s_u to clarify this relation. Figure 6.11 shows that there is a boundary that defines an upper limit on the relation between s_u and U. This boundary has a negative slope and is similar to observations from Figure 6.6 regarding ITS_u. Where U is low, there appears to be an important difference between s_u and ITS_u, however. Unlike *ITS*, where different discharges were found to be bounded by similar relations, the lower boundary of the relation between s_u and U is variable. At the lowest discharges, s_u is much less than what is observed at the highest discharge at a similar U. More research is needed to investigate the nature of the relation between ITS_u, s_u, and U. What is important for this study, however, is the fact that all measurements of scale in the riffle-pool indicate that coherent flow structures have a negative relation with velocity and discharge.

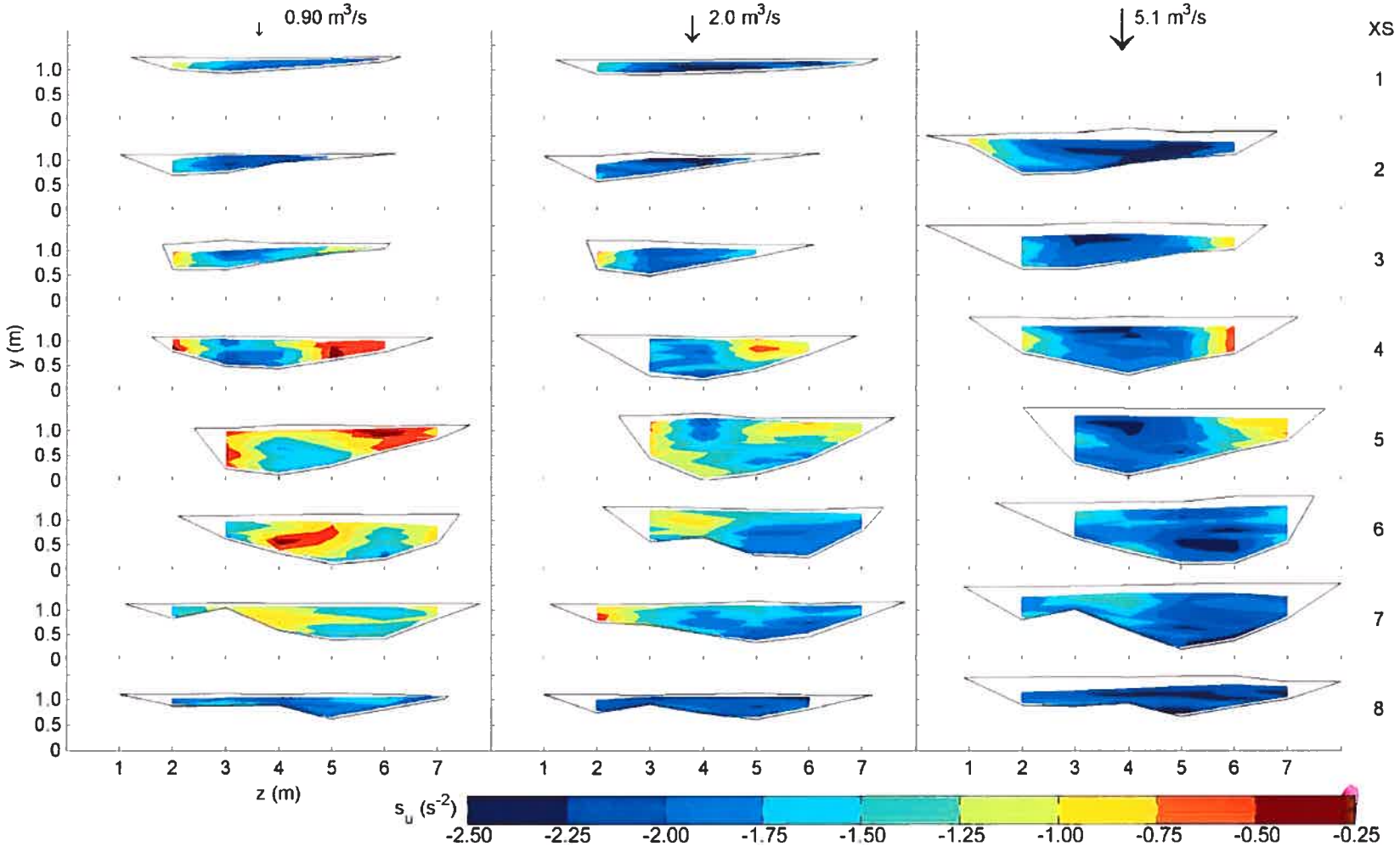

Figure 6.10 - Contour plot of the frequency-duration slope of high-speed events (s_u) at three discharges. Flow direction is from top to bottom. The tree that forces the pool is located between sections 5 and 6 on the left bank out to a distance of approximately 5m.

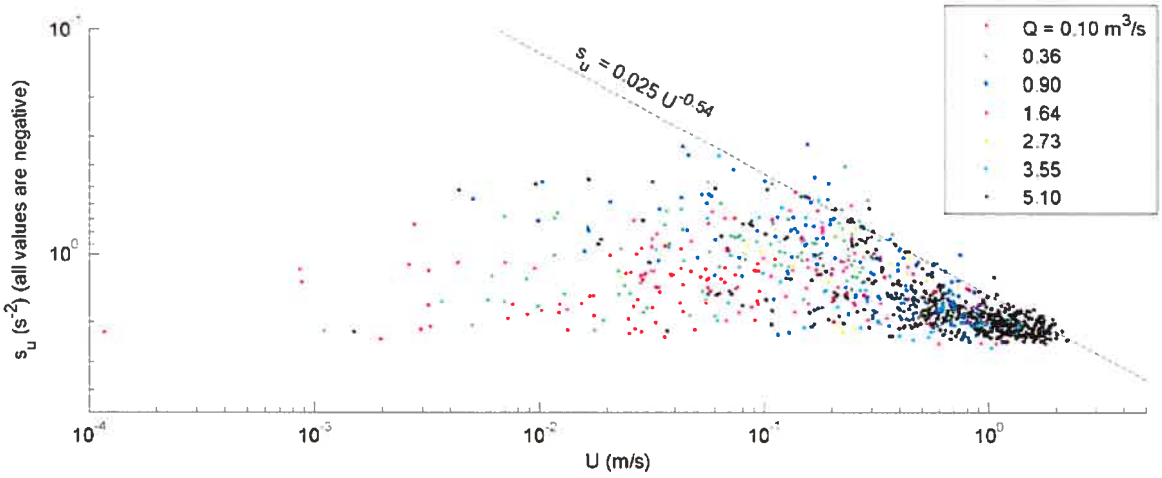

Figure 6.11 -Slope of the frequency-duration relation of high-speed events (s_u) versus mean streamwise velocity (U).

Finally, we have examined changes to the relative contributions of the different quadrants to the Reynolds shear stress. Figure 6.12 shows a hole size analysis of selected probes during the bankfull flood. As previously noted, we have normalized by the shear stress in the positive quadrants only in order to avoid normalizing by the total stress, which was close to zero or negative in some cases. The examples shown are located at the same points as those in Figure 6.8. In Figure 6.12a, the contributions of the positive quadrants ($\chi_2 + \chi_4 = \chi_{24}$) at the upstream end of the riffle-pool unit are larger than those from the negative quadrants (χ_{13}), which means that the total Reynolds shear stress is positive. This pattern is expected in the turbulent boundary layer in open-channel flows [*Nezu and Nakagawa*, 1993]. Figure 6.12b shows the results from the pool-head where it is clear that the pattern observed upstream is perturbed. $\chi_{13} > \chi_{24}$ at y = 15-25 cm, which means that the total Reynolds shear stress is negative in this area. χ_1 and χ_3 are particularly strong at y = 15 cm and at larger values of H, where $\chi_{24} \approx 0$. In Figure 6.12c, measurements obtained immediately downstream of the constriction show a return to the pattern seen in Figure 6.12a, with the exception of y = 35 cm, where the total Reynolds shear stress is negative. It is interesting to note that $\chi_4 > \chi_2$ for all measurements in Figure 6.12a-c. Measurements in rough boundary layers typically find $\chi_2 > \chi_4$, although some have found χ_4 to be greater near the bed. Figure 6.12d shows the results in the pool-tail, where total Reynolds shear stress is negative at all heights. This is a complete reversal from the flow structure observed at entrance of the pool in section 2. In addition, $\chi_2 > \chi_4$ near to the bed, and $\chi_1 > \chi_3$ at all heights, two features that were not seen at upstream locations. Measurements in the

recirculation zone show negative Reynolds shear stresses at all probe heights (Figure 6.12e). Also similar to the results in Figure 6.12d is the dominance of q_2 events over q_4 events near the bed. q_1 and q_3 alternate in terms of their importance for the four heights shown. Also, the distribution of the Reynolds shear stress contributions among the four quadrants is more uniform for the higher measurements in Figure 6.12d and Figure 6.12e. In Figure 6.12f, measured where strong boils were observed at the surface, negative Reynolds shear stresses occur at all heights. In this case, shear stress is most uniformly divided amongst the four quadrants at the lowest probe height. Away from the bed, χ_4 is much greater than the stress contributions from the other quadrants.

To visualize the overall patterns at different flow stages, contour plots of χ_4 and χ_{13} are shown in Figure 6.13 and Figure 6.14. χ_4 is larger than χ_2 ($\chi_4 > 50\%$) at most positions for the three discharges (Figure 6.13). At the lowest stage, the extreme values reach $\chi_4 = 75\%$ in the thalweg near to the surface. As discharge increases, these extreme values only occur near the channel banks, first in section 2-3 at the moderate stage and through sections 3-6 at the highest stages. q_2 events are mostly dominant (defined by $\chi_4 < 50\%$) in the recirculation zone on the right side of the channel in sections 4-5 and in the area immediately behind the tree in section 6. The importance of q_2 events also increases in sections 7 and 8, particularly at high flow where the thalweg in section 8 is entirely characterized by values of $\chi_4 < 50\%$. In Figure 6.14, sections 1 and 2 show that positive Reynolds shear stresses are dominant ($\chi_{13} < 100\%$) as flow enters the pool, as would be expected from results in uniform flows. In sections 3-5, areas with locally high values of χ_{13} occur. These areas can be close to the channel margin as found in section 3 but, similar to ITS_v, they are more often some distance from the channel banks. As discharge increases, the areas where χ_{13} is high occur closer to the banks. Additionally, at high flow, extreme peaks are a common feature near to the bed in the thalweg in sections 3-5. These peaks occur within the zone of intermittent separation near to the stream bed in the pool-head. Downstream of the tree, there is a similar association of extreme high values of χ_{13} with the recirculation zone downstream of the tree, and this zone is similarly pushed towards the channel margin at high flows, although it does not appear at $Q = 2.0$ m^3/s. A strong difference in sections 6-8, however, is that $\chi_{13} > 100\%$ in the thalweg at all flow stages. The only exceptions to this pattern are near the bed in section 6 at high flow and in section 8 at lower flow rates.

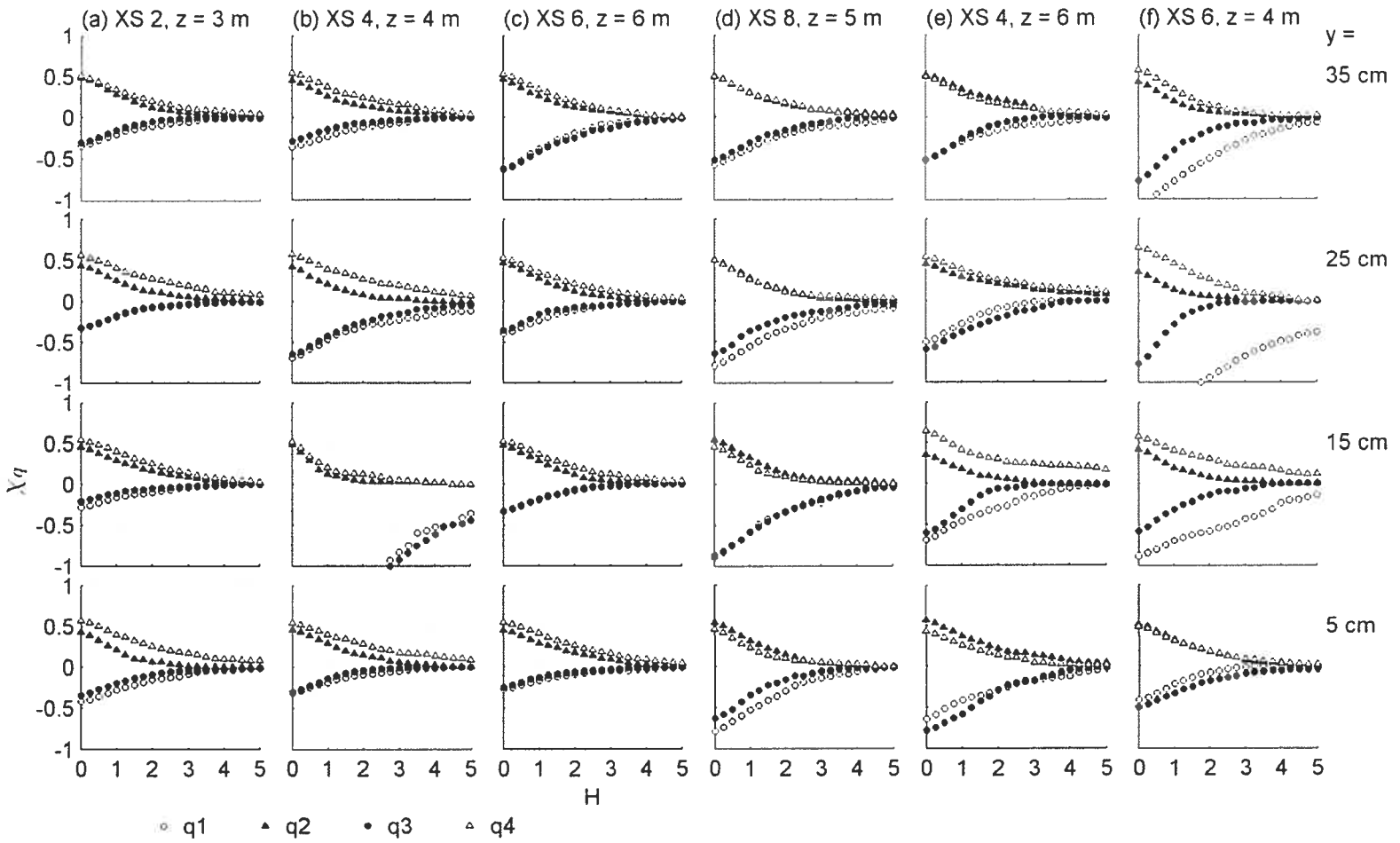

Figure 6.12 - Hole size analysis of six positions at bankfull discharge. Positions are the same as those shown in Figure 6.8.

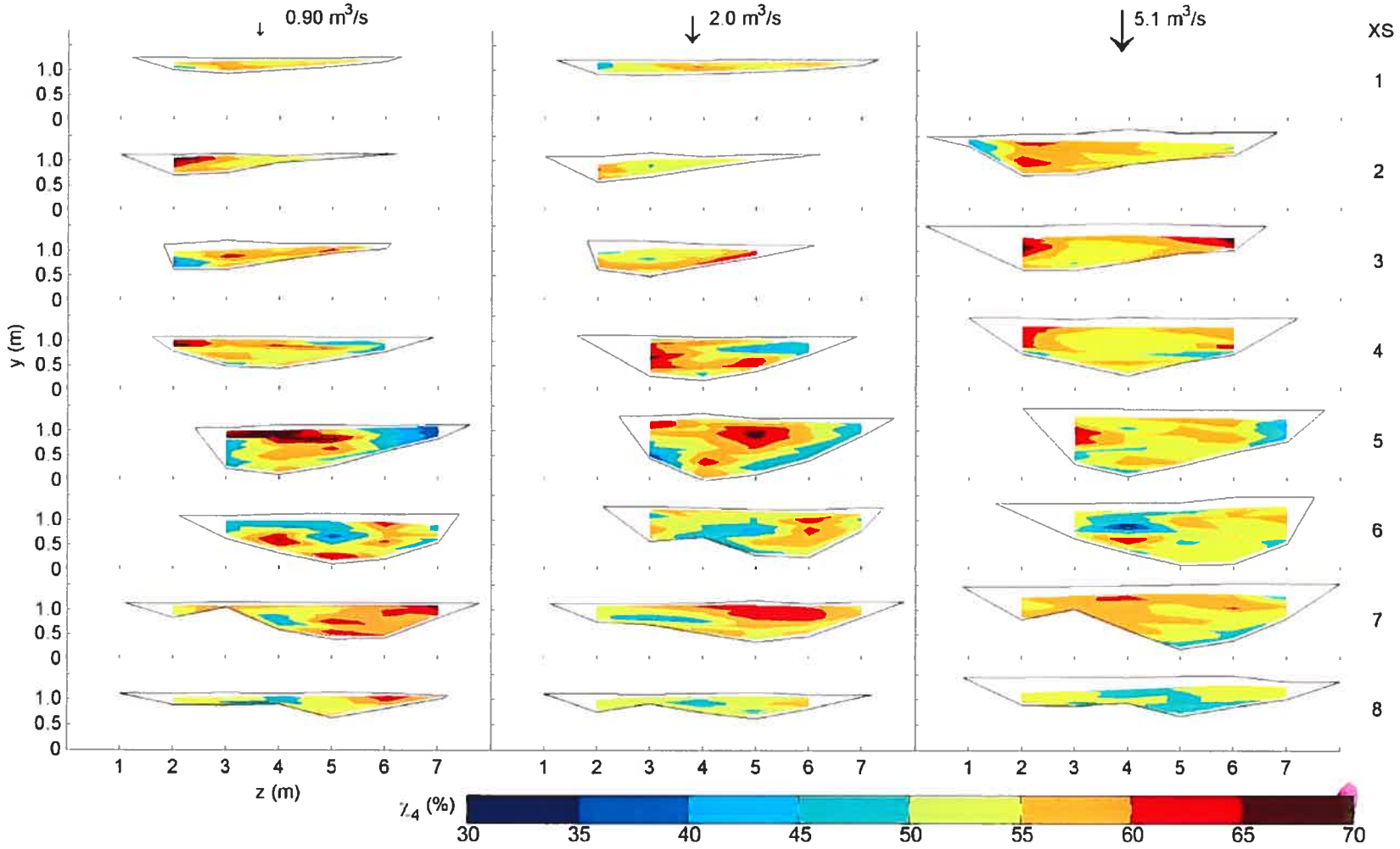

Figure 6.13 - Contours of the normalized contributions of *q4* to the Reynolds shear stress (χ_4) at three discharges. Flow direction is from top to bottom. The tree that forces the pool is located between sections 5 and 6 on the left bank out to a distance of approximately 5m.

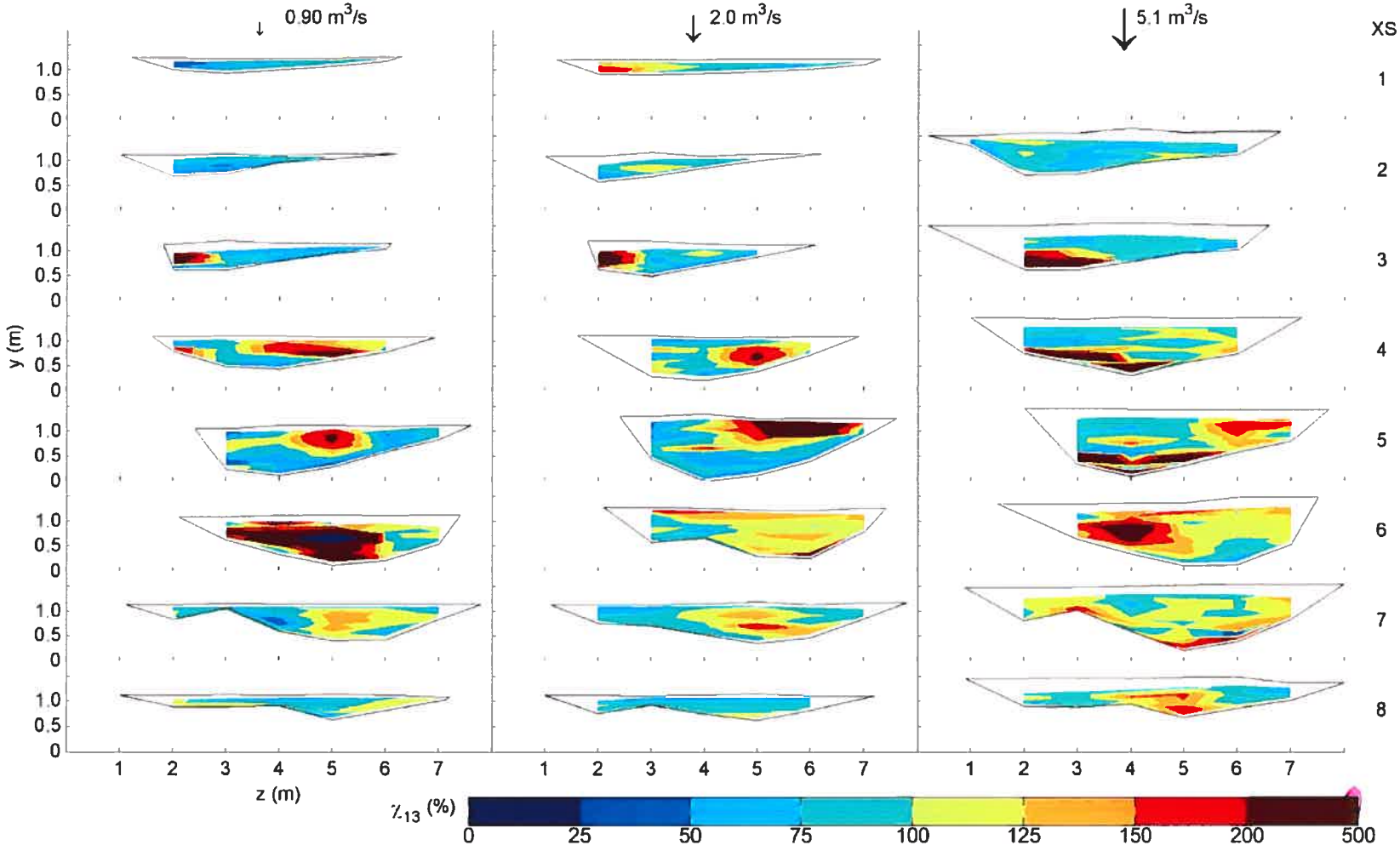

Figure 6.14 - Contours of the normalized contributions of the negative quadrants (*q1* and *q3*) to the Reynolds shear stress (χ_{13}) at three discharges. Flow direction is from top to bottom. The tree that forces the pool is located between sections 5 and 6 on the left bank out to a distance of approximately 5m.

6.3.5 *Effect of discharge*

To further examine the effects of discharge on turbulence scales, γ_u, ITS_u, s_u, and χ_{13} are plotted versus discharge (Q) in Figure 6.15. Values from all the inner zone measurement locations ($y < 0.2Y$) were averaged to give a general view of the near-bed character in the flow. Thalweg values are shown along with the positions adjacent to the thalweg. With the exception of the pool-head sections 3 to 5, γ_u is relatively insensitive and remains close to zero at all discharges. In the pool-head, γ_u is close to 1 at the lowest discharge but decreases quickly as discharge increases to moderate flow levels. As discharge continues to increase, however, there is a change in this relation, and a secondary peak in γ_u occurs at high flow. Near-bed ITS_u generally decreases with discharge, and all values at the highest flow rates are low. Higher values occur at low discharges in sections 2-7 and at moderate discharges in sections 4-5. There is also a general negative relation between Q and s_u. This trend is most evident for sections 3 and 6-8. In the pool section 4-5 there appears to be a peak at moderate flow rates, which is similar to observations from ITS_u. Some positions in the pool-head, including section 2, appear to be increasing slightly at the highest flows. In terms of the contributions of different event types to the overall Reynolds shear stress, the relations of χ_{13} with Q appear to be fairly noisy. One clear trend is with respect to the neutral value of $\chi_{13} = 1.0$. At low discharge, $\chi_{13} < 1$ at all sections upstream of the tree. At $Q \geq 3.0$ m^3/s, this tends to reverse as $\chi_{13} > 1$ in the pool-head sections 3 to 5. There are also some complex patterns downstream of the tree. χ_{13} peaks at moderate flow rates close to the tree and appears to be flat or decreasing with Q at high discharges. In sections 7 and 8, χ_{13} seems to follow a positive trend with Q. The significance of these patterns is not known, but it appears that negative quadrant events become relatively important for the transfer of Reynolds shear stress near the bed at high flows.

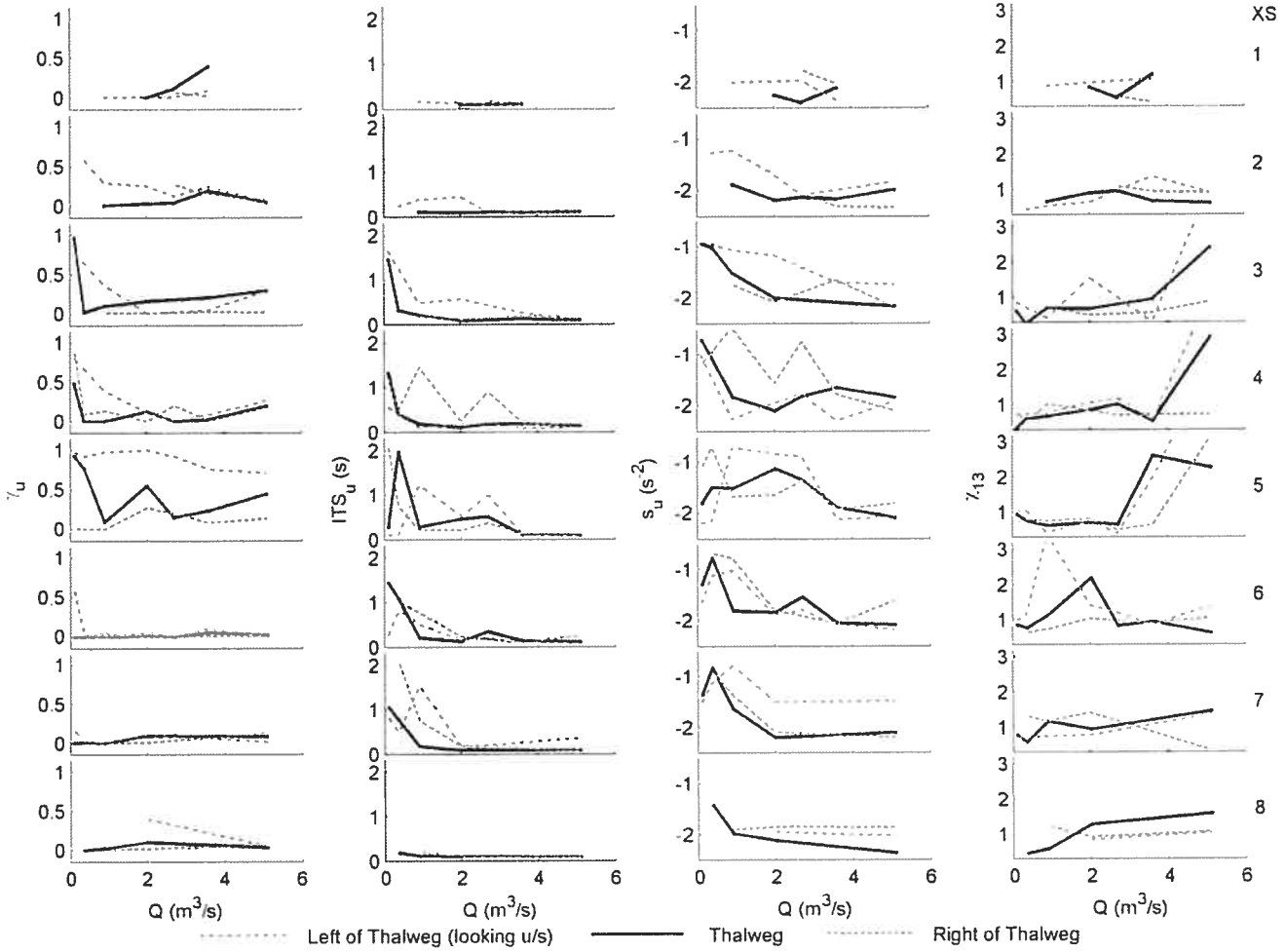

Figure 6.15 – Effect of the discharge (Q) on intermittency (γ_u) the integral time scale (ITS_u) and frequency-duration slope (s_u) of the streamwise velocity and on the contribution of quadrants *q1* and *q3* to the Reynolds shear stress (χ_{13}). Points represent an average of the near-bed probes (y/Y < 0.2).

6.4 Discussion

The main objective of this study was to examine the spatial and temporal variability of the size, scales and types of turbulent events in a forced riffle-pool. We were particularly interested in identifying the sources of increased turbulence production in the pool at high flow and clarifying how the scale of coherent turbulent events changes with discharge. In this discussion we synthesize the results and compare with other studies. We also discuss the role of the forcing element, examine possible interactions between coherent turbulence and morphological scales, and suggest directions for new research.

Spectral plots of the streamwise velocity signals reveal that signal variance increases in the pool-head during the bankfull discharge. This contrasts sharply with what occurs during low discharge, where spectral densities decay through the pool. Potential sources of energy generation are bed roughness, the perturbation of mean velocity profiles, including the development of a zone of intermittent separation near the bed, and high lateral velocity gradients in the pool, including zones of mean velocity separation upstream of the tree in the pool-head and immediately downstream of the tree through the center of the pool. Bed roughness is not likely to account for the increases in spectral densities observed at high flow in the pool-head for the simple reason that relative roughness decreases with stage. Because of this, we consider the generation of turbulence in the pool to be a function of pool morphology and non-uniform flow. Non-uniform flow occurs in a lateral direction as a result of the constriction of the flow by the tree and in a vertical direction due to the expansion and contraction of the flow in the pool-head and pool-tail, respectively.

Near-bed conditions in the pool-head are characterized by intermittent separation. These dynamics have been observed over low angle expansions in flumes [*Simpson*, 1981; *Simpson*, 1989; *Sano and Shirakashi*, 1994; *Azad*, 1996; *Aubertine and Eaton*, 2005] and dunes [*Carling et al.*, 2000; *Best and Kostaschuk*, 2002]. *Simpson* [1989] provides a useful description of flow dynamics of zones of intermittent separation. He found that momentum exchange in zones of intermittent separation is driven by large eddies that are generated away from the boundary and convected towards the bed. Vortices near to the bed grow quickly in scale before being ejected into the outer region. The Simpson model appears to describe momentum exchanges near the bed in the pool-head during low to moderate discharges. Though not consistent for all locations, ITS_u and s_u are higher in the pool-head during moderate flow. This indicates that longer duration events are more common during

these intermediate stages. The structure of the Reynolds shear stress shows that q_4 events generally contribute more than the q_2 events, and that the contributions from quadrants q_1 and q_3 are relatively minor. These observations are consistent with larger coherent turbulent events at moderate discharges. At a high discharge, however, there are many observations that do not fit with such a model. Based on the Strouhal number and the frequency of peaks observed in the spectra of the vertical velocity component, it appears there are structures related to the zone of intermittent separation that are generated near the bed. However, the overall Reynolds shear stress near the bed in the pool-head is often negative and a small zone of intense turbulence with very high contributions to the Reynolds stress from quadrants q_1 and q_3 was found.

Other studies allow some comparison, although no studies have been completed in a zone of flow expansion over a rough bed at high Reynolds numbers. *Aubertine and Eaton* [2005] found that over a smooth-wall low-angle expansion at relatively low Reynolds numbers, the contributions of quadrants q_1 and q_3 increased in terms of their contribution to the Reynolds stress, especially near to the bed, although they remained less than those from q_2 and q_4. This does not agree with some previous studies in areas of flow expansion. *Best and Kostaschuk* [2002] measured low contributions from q_1 and q_3 in the trough of a low-angled dune, as did *Sano and Shirakashi* [1994] in the diverging flow over a wavy boundary. An additional observation we made was that Reynolds stress in q_4 was larger than that in q_2 at all flow levels. Again in contrast, *Aubertine and Eaton* [2005] found that while q_4 had the largest contributions near to the bed, the contributions from q_2 were larger than those from q_4 farther away from the boundary. To explain the disagreement between our results and previous studies, it may be necessary to consider the effects of Reynolds number. *Priyadarshana and Klewicki* [2004] show that, in uniform flows, the contributions of q_1 and q_3 to the Reynolds shear stress increase at high Reynolds numbers. More data are needed before firm conclusions can be drawn, but it appears that coherent turbulent events in the intermittent separation zone of the pool-head do not follow the model of sweeps and ejections developed for uniform flows. It is also clear that the scale of these highly energetic events is small, especially during high discharges.

Observation of coherent vortices downstream of width constrictions is common in forced riffle-pools [*Buffington et al.*, 2002; *Hassan and Woodbridge*, 2004]. Such events were also observed at the water surface during high discharges at the study site in Moras

Creek. These vortices occurred in an area of strong shear between the high velocity flow in the thalweg and the low flow velocity immediately downstream of the tree. Boils in the zone downstream of the tree were also present particularly at high flow. We specifically measured in this zone in order to quantify these turbulent structures and their relation with channel morphology. From the spatial patterns of mean velocity we have shown that strong downwelling occurs in the thalweg and strong upwelling occurs behind the tree. Mean velocities are negative in a few locations immediately downstream of the tree (*see Chapter 5*). The coherence in this area is largely restricted to the flow near the surface in the thalweg in section 6, where ITS_u and ITS_v are larger than either near the bed or elsewhere in the thalweg. Near the bed, there are many indicators of high variability and very few that would support the occurrence of large-scale coherent structures. *ITS* and s_u are low at high discharge when boils are most evident. In addition, spatial correlations are negligible in the thalweg. Future experiments could be designed to simultaneously sample along streamlines in order to more thoroughly investigate spatial correlations using methods from *Buffin-Bélanger et al.* [2000]. Also, it may be worth sampling longer time series. The length of the time series in this study was selected to give reliable estimates of common statistics [*Buffin-Bélanger and Roy*, 2005] and needed to be short enough to allow characterization of the entire pool within a flood. It is possible that very long time series would reveal coherent flow structures at lower frequencies than what was possible to establish from our measurements. Nevertheless, the results in this article indicate that short duration, high frequency coherent structures dominate the zone close to the bed at high discharge. This result agrees with *Clifford* [1993] and does not tend to support the application of the *Yalin* [1971] coherent flow-bed form development model to riffle-pools.

It is clear that a more general understanding of the interrelations between morphology, discharge, turbulence intensity and the coherence of turbulence is needed. At low flow, high velocity flow enters the pool. The coherence of the flow, as measured with *ITS* and s_u, increases through the pool-head as kinetic energy decays and the high velocity core of the flow is dissipated. At more moderate flow levels ($\approx 0.5\ Q_{bf}$), the overall energy levels do not decrease in the pool-head, but do decrease downstream of the tree. Under these conditions the coherence of the flow is sometimes higher in the pool-head near the bed, but is generally less than the same values at high flow. At high flow, energy levels increase in the pool, which means that turbulence is being generated in this area.

Turbulence intensity is high and all measures of coherence are low. In an attempt to clarify the interaction amongst the variables, we have plotted ITS_u and s_u against velocity and found negative relations. There is a great deal of scatter within the trend. One source of the variability seems to be related to the decay or generation of turbulence energy. Coherence increases where turbulent energy is decaying, such as the pool at low discharge, and decreases when turbulence is being generated, such as the pool-head at high discharge. There is some relevant literature from engineering fluid mechanics that may assist us with this problem. A series of experiments and numerical simulations have been run to investigate the self-organization of decaying turbulent vortices [*McWilliams*, 1984; *Rutgers*, 1998; *Maassen et al.*, 2002; *Maassen et al.* 2003]. Large structures are shown to organize into slow rotational vortices with low energy levels. The key mechanism appears to be the decay of vorticity at a much slower rate than energy. From this, it appears that coherence is low in the pool at high flow because new turbulence is generated at smaller scales and with high energy levels near the bed. More comparable data is needed from other systems to confirm the interrelations between morphology, mean velocity, turbulence intensity and turbulence coherence.

In the absence of large scale coherent flow structures at high discharge when sediment transport is active, an alternate hypothesis is needed for riffle-pool scaling. The results in this article suggest that the formation of the pools is related to the perturbation of the boundary layer. It therefore seems reasonable to infer that the scale of riffle-pools would be related to the distance it takes for the boundary layer to recover. The Reynolds shear stress may provide an indicator of the perturbation to the boundary layer through the pool. The contribution of quadrants q_1 and q_3 to the Reynolds shear stress is typically greater than those from quadrants q_2 and q_4 downstream of the tree. At lower discharges, this perturbation only remains through the middle of the pool and the boundary layer has largely recovered so that the net Reynolds shear stress is positive in the last cross section. At high discharge, however, this recovery is not evident and the net Reynolds shear stress will be negative as the flow leaves the pool, particularly near the bed. The generality and the significance of this phenomenon are not known, but future research is warranted.

6.5 Conclusion

This study has documented the spatial distribution of coherent turbulent flow structures in a forced riffle-pool. This has rarely been attempted and there are no

comparable data sets from riffle-pools, especially for flows near the bankfull stage. The results allow us to describe a number of key mechanisms that underlie the flow dynamics of the bed form. Intermittent separation occurs near the bed in the pool-head. Mean velocity separation occurs near the bank and downstream of the obstruction that forces the pool. Power spectra of the flow velocity signals reveal that signal variance decreases in the pool during low discharges, but increases in the pool-head at high discharges. This energy influx is the result of turbulence generation and appears to occur at scales related to the zone of intermittent separation. Turbulence generation as a result of the intermittent separation perturbs the structure of the flow from what would occur in uniform flow. Specifically, forward-leaning flow wedges appear to be broken up in the pool and the dominant structures originate near the bed. Additionally, dominant quadrants are reversed at high flows so that the Reynolds shear stress near the bed is often negative. The constriction induces downwelling of the flow in the channel thalweg and upwelling in the form of strong boils downstream of the forcing element. These boils are characterized by increased coherence near the water surface, but the near-bed region through the center and pool-tail is characterized by relatively negligible levels of spatial coherence. Alternate sampling designs should be tested to confirm this conclusion. We found a negative relation observed between measurements of flow coherence, such as the integral time scale, and streamwise velocity. The source of scaling in riffle-pools remains uncertain.

Linking Paragraph E

In the previous two chapters, we detailed the flow dynamics in a forced riffle-pool. In the pool-head, flow deceleration results in relatively low mean velocities near the bed, but enhanced turbulence generation in the outer zone and the generation of high amplitude short duration turbulent fluctuations in a zone of intermittent flow separation. In the mid-pool, the constriction forces flow acceleration, which pushes high velocity flow close to the bed, and boils and vortices are generated in the shear zone caused by mean flow separation. In the pool-tail, flow acceleration results in fast mean velocities near the bed and a velocity reversal occurs at about 3/5 of the bankfull discharge. In this final article we present results that document the effect of these different hydraulic environments on sediment transport and pool morphology. Riffle-pools are characterized by two phases of sediment transport and sediment sorting by size. More field data is needed to characterize the spatially distributed entrainment and deposition of different sediment size fractions. This final article[5] details the morphology and sediment transport in a forced riffle-pool measured over an 18 month period. A series of large floods during this period turned the forcing element and allowed us to study a period of active pool formation. Sediment transport data was obtained with a new sediment tracking technique [*Lamarre et al.*, 2005]. Key results show the initiation of the pool upstream of the tree in a zone of flow deceleration, the size-dependant nature of sediment transport in the pool-head that leads to the development of the riffle, and the extension of the pool downstream of the tree. The central conclusion is that these processes can be explained with the model of deceleration, enhanced turbulence generation, and acceleration that was developed in the previous two chapters. The results also substantially agree with what was hypothesized in the development of a simulation model in Chapter 3. Refinements of the model are possible and will be discussed in the final chapter of this thesis.

---

[5] MacVicar, B. J. and A. G. Roy (*in preparation*), Sediment dynamics of a forced pool in a gravel-bed river. *Geomorphology*.

7 SEDIMENT DYNAMICS OF A FORCED POOL IN A GRAVEL-BED RIVER

7.1 Introduction

Riffle-pools are a characteristic bed form of many gravel-bed rivers [*Richards*, 1976; *Grant et al.*, 1990; *Montgomery and Buffington*, 1997] and thus increase the stability of the rivers [*Madej*, 1999; *Eaton and Lapointe*, 2001]. In spite of considerable effort, the dynamics that lead to their formation are still incompletely understood [*Milan et al.*, 2001; *Wilkinson et al.*, 2004]. There is, however, an apparent requirement of sediment size heterogeneity for this class of bed forms to develop. For instance, *Brush* [1961] found that a population of coarser sediments tends to gather in riffles and remain immobile except during rare floods. *Leopold and Wolman* [1957] also argued that sediment heterogeneity was particularly important for the formation of pools and riffles in streams with a straight planform. *Church and Jones* [1982] observed that the larger material imparts structural or 'framework' stability to the lee face of sediment bars, without which all material is moved relatively easily and the riffle does not develop. In spite of this requirement, there are only a few studies that document the variability of sediment transport in riffle-pools [*Sear*, 1996, *Booker et al.*, 2001]. More field data is needed to characterize the spatially distributed entrainment and deposition of different sediment size fractions at a range of flood stages in order to clarify the links between sediment size heterogeneity, bed form stability, and the development of riffle-pool bed forms.

The dominant sediment sorting pattern in riffle-pools is the association of coarser sediment with topographic highs - the riffles - and finer sediment with topographic lows - the pools [*Keller*, 1971; *Church*, 1972; *Hirsch and Abrahams*, 1981; *Lisle and Hilton*, 1992; *Lisle et al.*, 1993; *Sear*, 1996; *Pyrce and Ashmore*, 2005]. This pattern is not universal, and a number of studies have reported inconsistencies [*Milne*, 1982] or larger sediments in the pool [*Thompson et al.*, 1999; *Milan et al.*, 2001]. Variability between field sites is thought to be related to spatial heterogeneity, especially in pools where lateral variability is strong due to the formation of bars [*Milne*, 1982], the collection of lag material in the pool-center [*Richards*, 1976; *Heritage and Milan.*, 2004], and deposition in the pool-tail, where size distributions are sensitive to antecedent flood history and sediment

supply [*Lisle and Hilton*, 1992; *Madej*, 2001; *Thompson and Hoffman*, 2001].
The most general two dimensional model appears to be that of *Sear* [1996], where the coarser sediments are located on the riffle with a fining trend through the pool. In three dimensions, lateral bars are ubiquitous features of riffle- pool systems, with the bars and riffles forming a continuous sedimentological unit [*Church and Jones*, 1982; *Lisle*, 1991; *Pyrce and Ashmore*, 2005]. Sediment routing around the deepest part of the pool may also play a role in pool maintenance [*Booker et al.*, 2001].

Sediment transport in riffle-pools is commonly characterized as having two or three phases [*Jackson and Beschta*, 1982; *Sidle*, 1988; *Warburton*, 1992; *Ryan et al.*, 2002]. In the two-phase model, phase I transport refers to the size-selective transport of fine material over a relatively static bed. This phase has been well documented by the studies of *Meade* [1985], *Sidle* [1988], and *Lisle and Hilton* [1992, 1999] and can be characterized by the winnowing of fines to pools. Phase I transport is characterized by a relatively flat relation between discharge and transport rate [*Ryan et al.*, 2002], path length distributions that follow positively skewed distributions such as exponential or gamma functions [*Pyrce and Ashmore*, 2003], and partial mobility of median sediment sizes [*Hassan and Woodsmith*, 2004]. Phase II transport occurs at shear stresses sufficiently high to cause the break-up and transport of the gravel bed. *Meade* [1985] and *Sidle* [1988] found that riffles aggrade during this phase of transport. Phase II transport is characterized by a steep relation between discharge and transport rate [*Ryan et al.*, 2002], bimodal or symmetrical path length distributions [*Pyrce and Ashmore*, 2003], and equal mobility of median sediment size fractions [*Hassan and Woodsmith*, 2004].

A third phase of sediment transport in riffle-pool streams remains poorly documented. Phase III transport has been found to occur in steep channels associated with the breakup of steps [*Warburton*, 1992]. A similar phase is possible in riffle-pools when the transport of clasts composing the riffle framework occurs. *Sidle* [1988] observed net scour at a riffle section during a 5-year event, but this event was complicated by the release of sediment associated with wood debris and the variable effects of antecedent floods. *Madej* [1999] found that riffle-pool patterns were disrupted during a 12-year flood, but the movement of large clasts was not measured. Riffle-pools whose locations were forced by bedrock or woody debris were more stable than other types of pools. *Ryan et al.* [2002] were not able to document Phase III transport from transport-discharge relations. They

hypothesized Phase III transport to be hidden within the large variability that was observed, but this hypothesis was not supported by the observations of *Hassan and Woodsmith* [2004] in a forced pool, where full mobility of the largest sizes was not documented in spite of discharge greater than three times the bankfull discharge. These observations show that it is possible that riffle-pool violate the condition of equal mobility [*Parker et al.*, 1982], which states that the grain size distribution of the bed load should be similar to that of the substrate [*Parker and Toro-Escobar*, 2002]. In a review of sediment transport in a range of system types, *Lisle* [1995] found a systematic deviation from the condition of equal mobility, also referred to as downstream fining [*Hoey and Ferguson*, 1997; *Ferguson and Wathen*, 1998], associated with narrow streams characterized by a wide range of particle sizes. Riffle-pools are likely to be common in streams with these characteristics and may be relevant to the sediment budget.

This study will examine the links between sediment size heterogeneity, the stability of riffle-pools during large floods, and downstream fining in a forced riffle-pool. The study benefited from an intensive examination of flow hydraulics at the site during floods up to and including the bankfull flow (*see Chapters 5 and 6*). There was also a need for spatially distributed sediment tracking at the site, and we applied a relatively new sediment tracking technique using Passive Integrated Transponder (PIT) tags [*Lamarre et al.*, 2005] that is particularly advantageous for this purpose. This study had begun when the tree that forces the pool moved, an event that initiated a period of active pool formation that we were able to characterize. The objectives of the study were to (a) characterize the morphological changes associated with floods of different stages, (b) describe relations between particle size and transport distance, and (c) describe the spatial patterns of sediment entrainment and deposition in relation to the spatial distribution of mean and instantaneous shear stresses.

7.2 Methodology

Moras Creek is located in eastern Quebec, Canada. We used a Trimble 5700 GPS system to map the channel and floodplain (Figure 7.1). The channel is sinuous but does not exhibit a regular meandering pattern. Impingement on the valley wall is common and a heterogeneous glacial till contributes a wide range of particle sizes to the stream. The study site is in the bend at the downstream end of a relatively long straight reach. A longitudinal profile of the channel thalweg is plotted in Figure 7.2. The bed is composed of long runs

with occasional steps. Shallow pools, such as the one located at approximately 240 m along the thalweg, are typically `free` or autogenetic pools. Deeper pools, such as the study site, also occur and are invariably associated with forcing mechanisms such as boulders, sharp bends, or wood debris. Average bankfull width (Z_{bf}) is 6 m, bankfull depth in the riffle (Y_{bf}) is 0.7 m, and the average bed slope (S) is 1.2%. The studied pool is forced by a large dead tree with an intact root bole that slid into the creek as the result of a previous bank failure. The pool spans the width of the channel, is 10 m long, and has a residual depth of 0.8 m. As a note, x, y, and z refer to the streamwise, vertical, and lateral dimensions. Flow is from top to bottom in all of the spatial plots and the left and right sides of the channel are defined looking upstream.

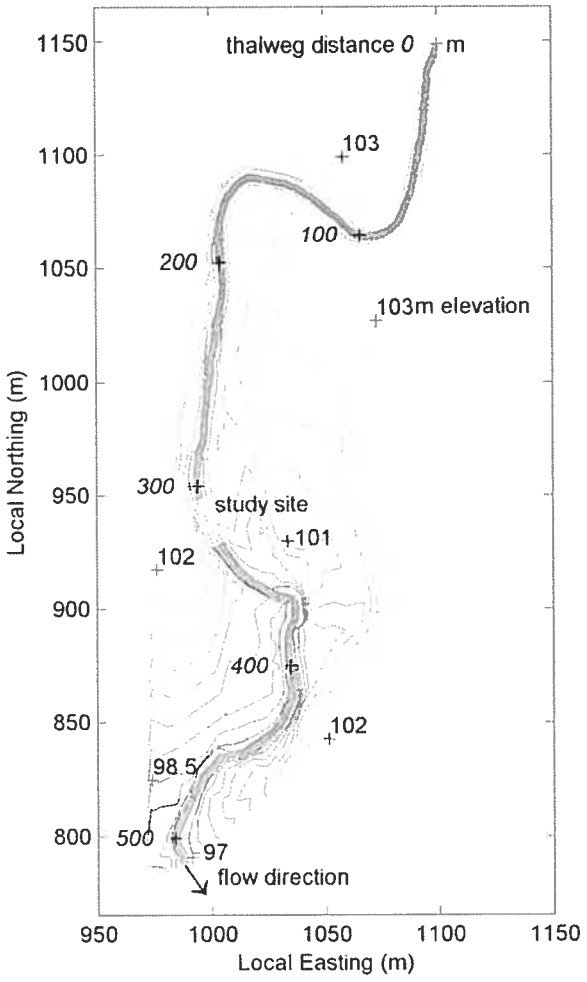

Figure 7.1 - Topography of area surrounding Moras Creek field site.

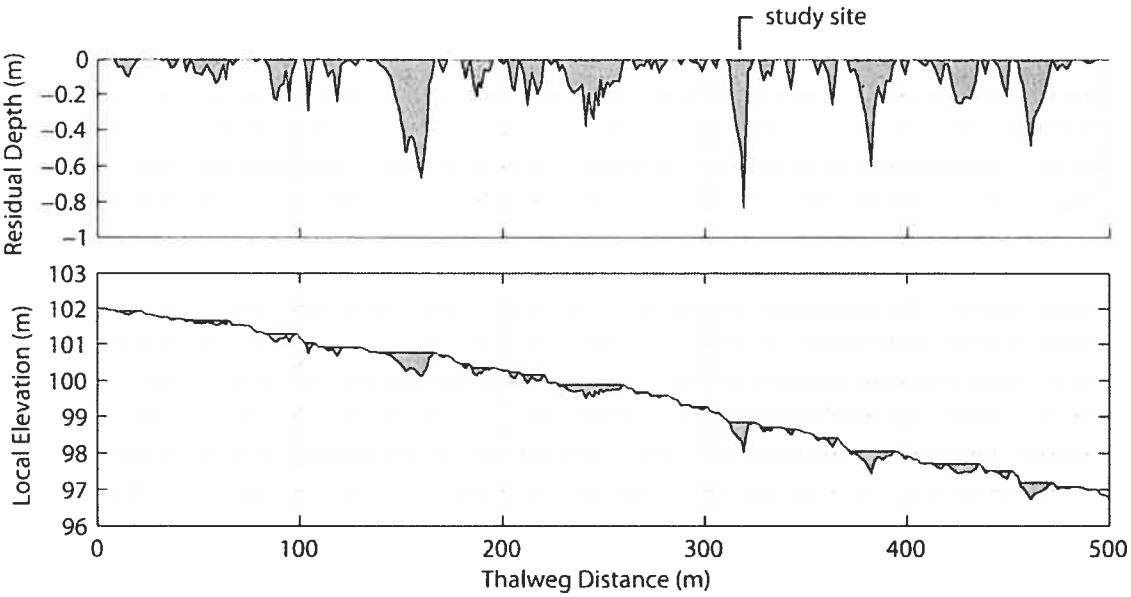

Figure 7.2 - Moras Creek thalweg profile and residual pools.

The site was monitored from May 2003 until November 2004. We installed a pressure transducer, located approximately 100 m downstream of the reach shown in Figure 7.1, at the beginning of the study period. Data is shown in Figure 7.3. $Y_{bf} = 0.70$ m was established based on observed flooding in overbank areas on August 13, 2004. Flow stage was recorded at 10 minute intervals, although the gauge needed to be removed in the winter and could not be reinstalled until after the large spring floods in 2004. Stream gauge data from the nearby Bulstrode River (Station number 030106 in the Centre d'expertise hydrique du Québec database) were used to fit with the available data from Moras Creek in order to give an estimate of flood peaks during the missing period. The accuracy of the estimates from the Bulstrode record was not confirmed and there is a large difference in drainage area between the Moras Creek (drainage area $\approx$ 14 km^2) and the Bulstrode (drainage area = 338 km^2). An example of the possible disagreement is shown in July 2003 where an above bankfull event in Moras Creek was not exceptional in the Bulstrode data, while a subsequent event in August of 2003 resulted in extensive flooding and damage in the larger basin but did not produce overbank flows in the Moras basin. Nevertheless, the Bulstrode data confirm the occurrence of a number of extreme events in the winter of 2003-2004. Overall, there were 15 events that were within 10 cm of the bankfull depth and of these, 9 exceeded the bankfull depth. The four largest overbank events were confirmed by visual observation at Moras Creek and occurred on July 21/03, December 24/03, April

15/04, and July 31/04. The first of these events turned the fallen tree and initiated a period of riffle-pool development.

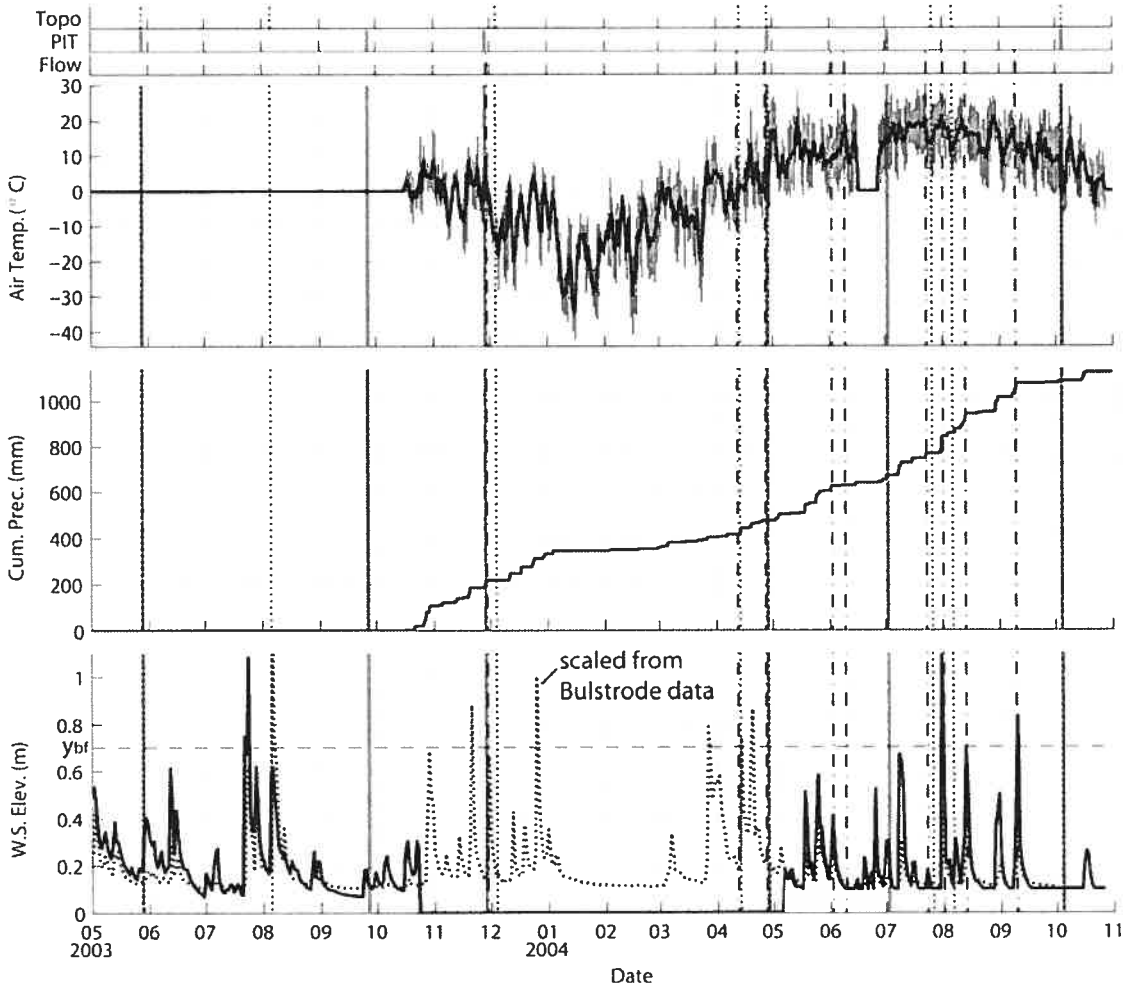

Figure 7.3 - Precipitation and temperature data from on site meteorological station and water stage data from pressure transducer installed approximately 100 m downstream of the river reach shown in Figure 7.1. Dates on which topographical surveys (Topo) tagged particle surveys (PIT) and flow measurements (Flow) were made are also shown. Scaled data from a nearby government gauging station was used to fill in the period where the pressure transducer was removed for winter.

A meteorological station was installed in October 2003 to record temperature and precipitation, also at 10 minute intervals (Figure 7.3). We compared those data with data from the closest government maintained meteorological station in Sherbrooke (Quebec) approximately 80 km to the south of the site. The total rainfall for the one-year period during which the precipitation gauge was active was 1120 mm. The total precipitation for the same period in Sherbrooke was 1074 mm. Based on over 40 years of data from the same station, mean annual rainfall is 873 mm and total precipitation is 1144 mm. The

study period seems to have been a period with intense precipitation compared to the normal. On average there are only 5.5 days/year with more than 25 mm of rainfall. The rain gauge at the site measured 11 such days over 12 months, with the largest daily rainfall of 69.6 mm occurring on July 31, 2004. This has only been exceeded twice in 42 years of data, which indicates that it was approximately a 15 year storm. The Sherbrooke data shows a total of 14 days with more than 25 mm of rainfall from May 2003 to November 2004, with the largest daily precipitation of 94.5 mm occurring on August 5, 2003. This is the second highest one day total over the recorded period and is very close to the largest ever one day total of 98 mm.

Stream bed topography was surveyed using a Trimble 5600 total station. The strategy was to measure in the period between flood events that were significant for sediment transport (Figure 7.3), preferably at the same time as the mapping of the locations of tagged particles. The dates at which this information was collected are also indicated in Figure 7.3. Flow conditions for each of the periods between topographical surveys are summarized in Table 7.1. Erosion and deposition were estimated from the difference between successive topographic surveys to quantify changes in bed height. A threshold of 10 cm difference between successive surveys was used to ensure that changes were morphological adjustments and not the result of variability in topographical sampling due to the rough bed.

Period	Start Date	End Date	Number of floods $y > Y_{bf}$	y_{max} (m)	yYS (Pa)
1	May 28/03	Aug 05/03	1	+ 0.4	130
2	Aug 05/03	Dec 12/03	1	+ 0.2[a]	106
3	Dec 12/03	Apr 13/04	2	+ 0.3[a]	118
4	Apr 13/04	Apr 28/04	2	+ 0.4[b]	130
5	Apr 28/04	July 28/04	0	- 0.05	75.5
6	July 28/04	Aug 06/04	1	+ 0.4	130
7	Aug 06/04	Oct 04/04	2	+ 0.1	94

Note a - flood level estimated from Bulstrode data

b - estimated from high water marks, Bulstrode data indicated a maximum flood of + 0.2 m.

Table 7.1 - Summary of flood sequences between topographical surveys. y_{max} is calculated relative to the bankfull depth.

Bed particles were marked with Passive Integrated Transponder (PIT) tags. The PIT tag used is a cylindrical 4 by 23 mm glass-encapsulated passive transponder manufactured by TIRIS Technology and distributed by Texas Instruments. When activated

by an antenna that uses a RFID (radio frequency identification) technology, the tags return coded signals to a handheld computer. A unique identification code was associated with each tag to allow us to associate sediment movement with clast characteristics such as size, weight, and shape. Long-term studies are possible because the tags do not have internal batteries. Also, because the location of a marked particle is done using a remote antenna, the bed is not disturbed during recovery. Tagged particles can become embedded within the substrate and will move in a manner that is representative of the overall sediment population. Sources of particle loss can include signal 'shadowing' due toseveral particles in close proximity; incomplete scanning of the bed surface; transport beyond the surveyed section; broken tags due to poor installation; and particles buried deeper than 25 cm in the substrate [*Lamarre et al.*, 2005]. In controlled conditions, the range of detection by the antenna is 30 cm in any direction. The last known position of lost particles were plotted in this study to identify any patterns associated with particle loss.

The particle tagging technique consists of drilling holes (6.5 mm in diameter and 25 mm deep) in sediment clasts, inserting a PIT tag, sealing the hole and protecting the tag with masonry caulking, and then placing the tagged particle in the river. The particle size distribution for Moras Creek was determined from a Wolman pebble count (n = 800, Figure 7.4). Representative clast sizes are D_{16} = 18 mm, D_{50} = 60 mm, and D_{84} = 190 mm, and particles as large as 900 mm were measured. We tagged 299 clasts that were taken from the stream (size distribution also shown in Figure 7.4). It was not possible to match the sediment size distribution of the overall population due to the difficulty of tagging the smallest and the largest particles. Sample sizes by sediment class are listed in Table 7.2. Particles were returned to the bed surface and allowed to work their way into the active layer through subsequent events. There is a bias with this method such that entrainment probabilities during the initial flood events are higher than during subsequent events [*Ferguson and Hoey*, 2002].

Size Class	Size (mm)	Number tagged
$> D_{84}$	190 – 280	16
D_{67} - D_{84}	99 – 189	92
D_{50} - D_{67}	60 – 99	142
$< D_{50}$	25 – 59	49
	Total	299

Table 7.2 - Samples of tagged particles by size class

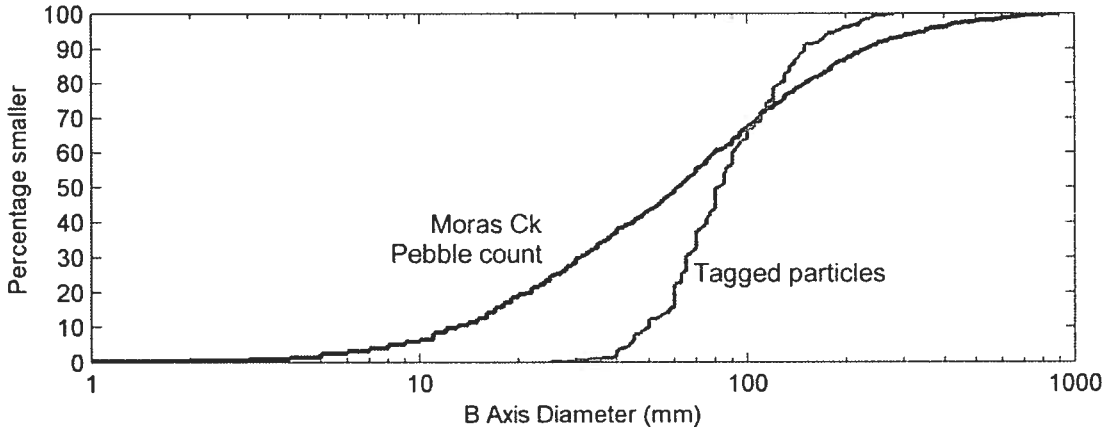

Figure 7.4 - Particle size distributions of the stream sediment, as measured by a Wolman pebble count (n = 800), and the tagged particles (n = 299).

Tagged particles were added in three waves (Figure 7.5). The first was a test of the method and the second consisted of the bulk of the particles added in the first year. Our strategy was to initially feed the particles within the study section and upstream. In the study section, an effort was made to place all sizes of sediment in all morphological subunit. This strategy allowed us to comment on the sediment routing theory [*Booker et al.*, 2001] in which pool maintenance is accomplished by sediment transport around the deepest part of the pool instead of actual sediment entrainment. In the second year of the study we added a third wave to supply fresh tagged particles in areas such as the pool-tail where most marked particles had been previously eroded. At each survey, particles locations were found by sweeping a portable antenna over the bed surface and were recorded using the total station. In the river, conditions did not always allow visual confirmation of the particle location. To avoid any false detections of movement, we considered only transport distances greater than 1 m in this study. Only 66% of the particles were found on November 28, 2003 because of icy conditions that prevented scanning in all areas of the creek. In surveys during 2004, recovery percentages were 89, 87, and 91%. The flood sequences between PIT tag surveys are shown in Table 7.3. Only 6 of 299 particles were never found after their placement in the river, which confirms the reliability of PIT tags as a technique to track particles in gravel-bed rivers. Approximately 300m of the stream was surveyed. The time required to complete a PIT tag survey was approximately 5 hours. The initial and the final positions of all particles are shown in Figure 7.6. The path length of each particle was calculated as the vector between these two

points. The curvature of the stream was accounted for by calculating particle positions and path length vectors in a two dimensional space defined by the channel centerline, measured during the GPS survey of the creek (Figure 7.1), and the cross-stream direction.

Period	Start Date	End Date	Number of floods $y > Y_{bf}$	y_{max} (m)	γYS (Pa)
1	May 28/03	Sept 26/03	1	+ 0.4	130
2	Sept 26/03	Nov 28/03	2	+ 0.2[a]	106
3	Nov 28/03	Apr 28/04	3	+ 0.4[b]	130
4	Apr 28/04	July 02/04	0	- 0.05	75
5	July 02/04	Oct 06/04	3	+ 0.4	130

Note a - flood level estimated from Bulstrode data

b - estimated from high water marks, Bulstrode data indicated a maximum flood of + 0.3 m.

Table 7.3 - Summary of flood sequences between PIT tag surveys. y_{max} is calculated relative to the bankfull depth.

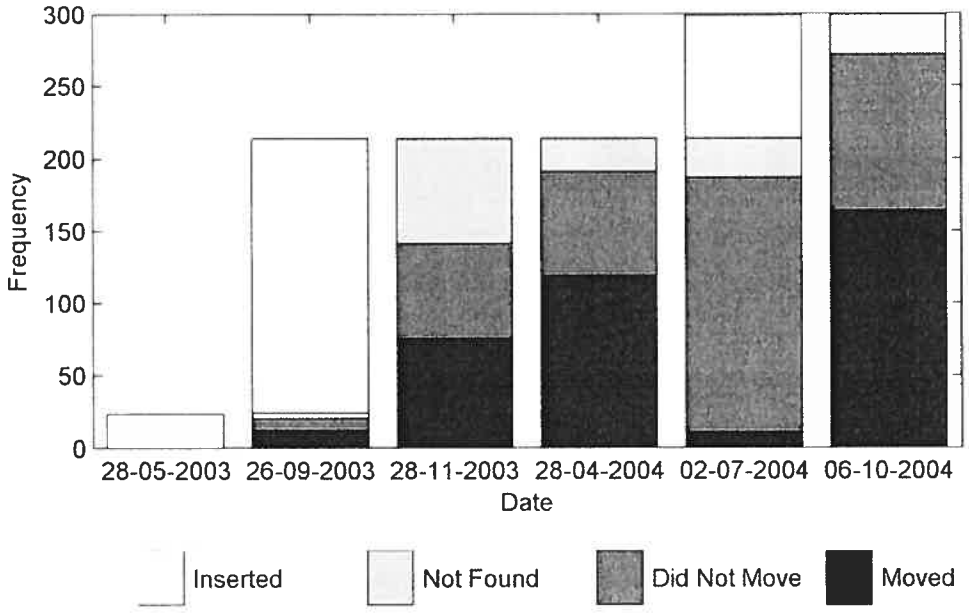

Figure 7.5 - Stacked bar charts of tagged particle surveys.

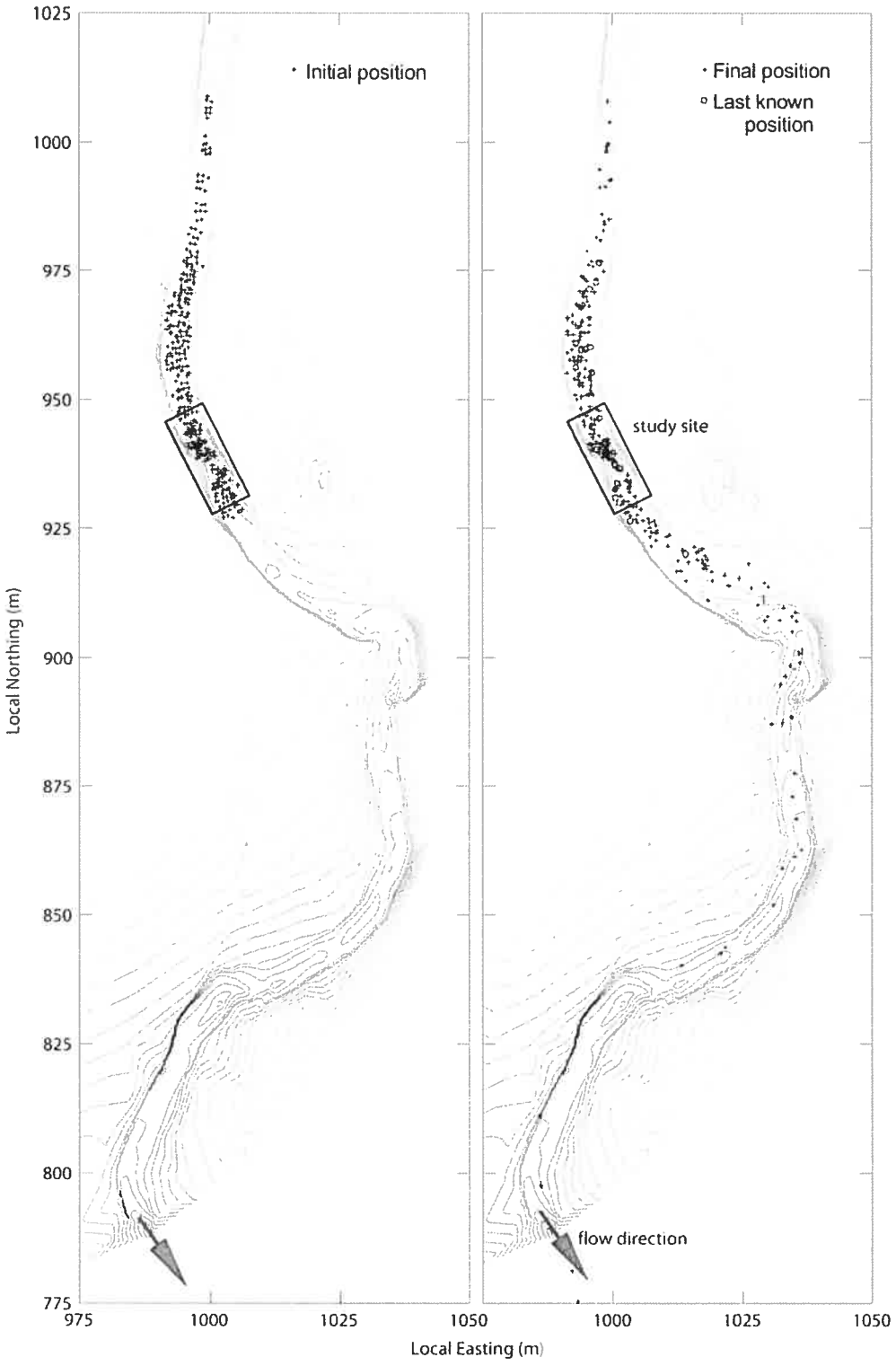

Figure 7.6 - Initial (date is variable) and end (Oct 06/04) positions of tagged particles. Last known position gives the last coordinates of particles whose locations were not found in the final survey.

Sediment entrainment is commonly related to shear stress. To estimate the spatial distribution of shear stress on the bed, we measured turbulent flow properties at seven different flow stages, including the bankfull discharge. However, a variety of methods are used to estimate shear stress [*Wilcock*, 1996; *Kim et al.*, 2000; *Biron et al.*, 2004]. A non-uniform boundary, the definitive characteristic of pools and riffles, further complicates this exercise because flow deceleration and acceleration alters mean velocity and turbulence intensity profiles [*Song and Graf*, 1994; *Kironoto and Graf*, 1995; *Song and Chiew*, 2001; *see Chapter 5*]. We therefore used two methods to estimate the shear stress. The first is a function of the mean velocity at a point near the bed surface (τ_u) and the second is a function of the turbulent kinetic energy (τ_k). In uniform flow, these methods typically give similar estimates [*Biron et al.*, 2004]. In the riffle-pool under study, however, the methods gave divergent estimates as a result of the perturbation to the relation between the mean velocity and turbulence (*see Chapter 5*). Stress calculated as a function of the turbulent kinetic energy was much larger in the pool-head. This was linked with the occurrence of intermittent detachment of the flow, as shear stress derived from the mean velocity will underestimate the stresses on the bed in this situation [*Simpson*, 1981;1989]. Using the mean velocity measurements nearest to the bed as recommended by *Wilcock* [1996], τ_u was estimated as:

$$\tau_u = \rho\left(\frac{\kappa U}{\ln(10y/D_{84})}\right)^2 \tag{7.1}$$

where κ is the Von-Karman constant (≈ 0.40), U is the mean velocity, and y is the measurement height of the probe above the bed. τ_k was estimated using the method outlined in *Kim et al.* [2000], and *Biron et al.* [2004] but modified as in Chapter 5 for measurements in two dimensions:

$$\tau_k = 0.75\rho K_1(\overline{u_i^2}+\overline{v_i^2}) \tag{7.2}$$

where ρ is water density (1000 kg/m^3), K_1 is a constant (≈ 0.19) and u_i and v_i are the instantaneous fluctuations about the mean of the streamwise and vertical components of velocity, respectively. Critical shear stress for a given size class (τ_c) was estimated based on a threshold criteria for mixed sediment [*Komar*, 1996]:

$$\tau_c = 0.045(\rho_s-\rho)gD_{50}^{0.6}D_N^{0.4} \tag{7.3}$$

where D_N is the percentile N size of sediment, D_{50} is the median size of sediment for the creek, ρ_s is the density of the sediment, and g is the gravitational constant (9.81 m/s^2). It should be noted that we use a single D_{50} value for the entire section. This method does not account for local sorting effects and implicitly assumes that the sorting is dependant on the observed hydraulic conditions. The effect of this assumption is discussed.

7.3 Results

7.3.1 Topographical changes

The bed morphology determined from the topographical surveys of the study section is shown in Figure 7.7. A summary of the hydraulic conditions for each of the periods between topographical surveys is given in Table 7.1. Figure 7.7 documents the morphological changes during the study period. The tree that forces the pool moved in July, 2003 during an extreme event that was 0.4 m above bankfull stage. This movement resulted in the infilling of the previous pool and scouring around the root bole. In the early winter of 2003, a few large rain-on-snow events occurred and the pool reformed downstream of its original location, but upstream of the tree. Flow decelerates in this area because of the partial barrier to the flow presented by the tree. The pool was slightly reworked through the winter of 2003-2004, but substantial subsequent change did not occur until the spring of 2004 when a second event approximately 0.4 m above the bankfull level resulted in the pool eroding to the right of the tree and extending downstream from the constriction. This phase of erosion was accompanied by the growth of the bar on the left side of the channel downstream of the tree. As a result, the deepest part of the channel shifted from left to right (looking upstream). This pool was enlarged and extended during subsequent floods. Fine loose sands were frequently observed at the bottom of the pool downstream of the tree.

The erosion-deposition maps show that the development of the pool downstream of the tree followed a relatively simple trajectory (Figure 7.8). Erosion occurred on the right side and deposition on the left side of the channel during all events. The development of the bed form is more complicated upstream of the tree, as shown by the sequence through the first four plots in the location of the original pool from x = 8-12 m. This area was initially filled, but subsequent events reworked the sediments and led to net erosion. The large flood in the spring of 2004 deposited more sediment in this location and marked the

end of the local morphological changes. Even the large event in the summer of 2004 resulted in no further net erosion or deposition in this area. Instead, it initiated a new sequence of changes closer to the tree. Areas of deposition during the large event in the summer of 2004 and of erosion during two subsequent bankfull floods are visible. The development of the riffle and pool-head morphology has occurred over a range of flood stages, and areas of deposition tend to be areas of erosion in subsequent floods. There is a tendency toward a stabilized morphology in the riffle and pool-head, however, demonstrated by the decreasing amounts of change in subsequent floods of similar magnitude. There is a direction to this process of stabilization, as the initial scour of the pool and the deposition-erosion sequences occur first in the upstream portion of the pool and then progress downstream. This would suggest that the process of deceleration and enhanced turbulence generation that occur in the pool-head are the critical mechanisms for pool initiation, although the ultimate length of the pool will be determined by the scour downstream of the tree that occurs in a zone of flow acceleration. Scour downstream of the tree occurred at both bankfull and above bankfull events, and pool length did not stabilize within the study period.

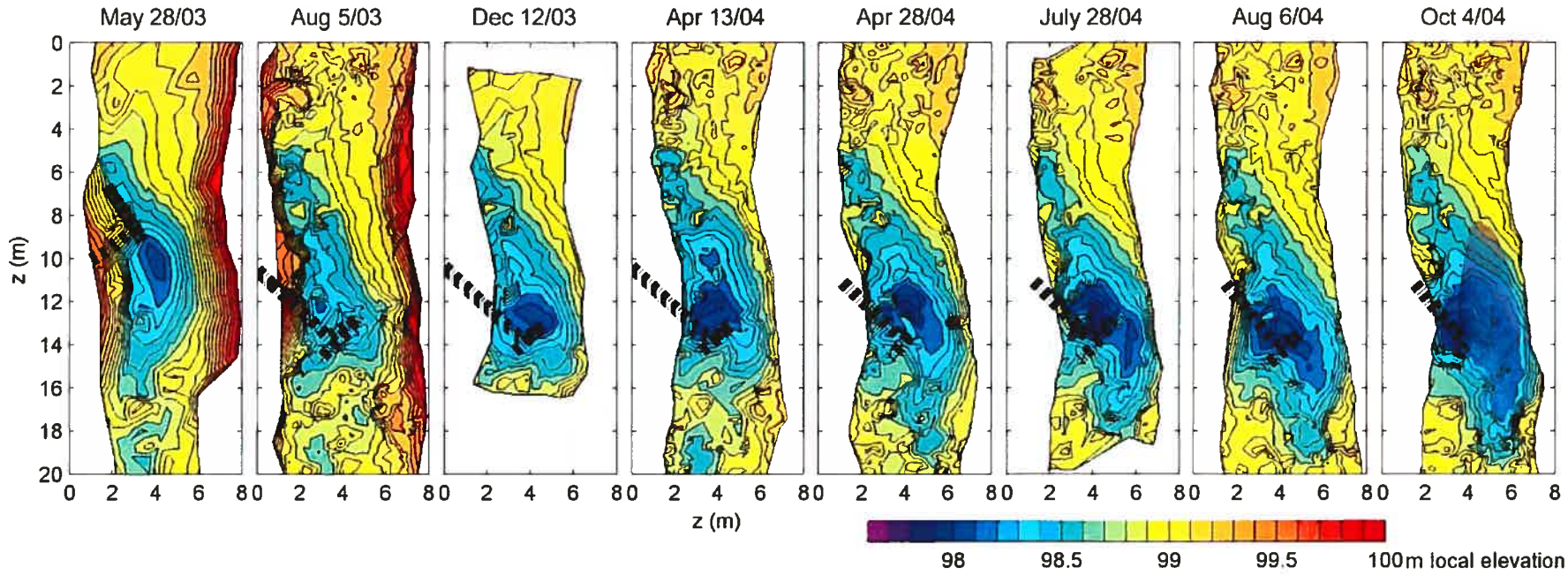

Figure 7.7 – Bed topography during the study period. The extent of the third survey was limited by icy conditions.

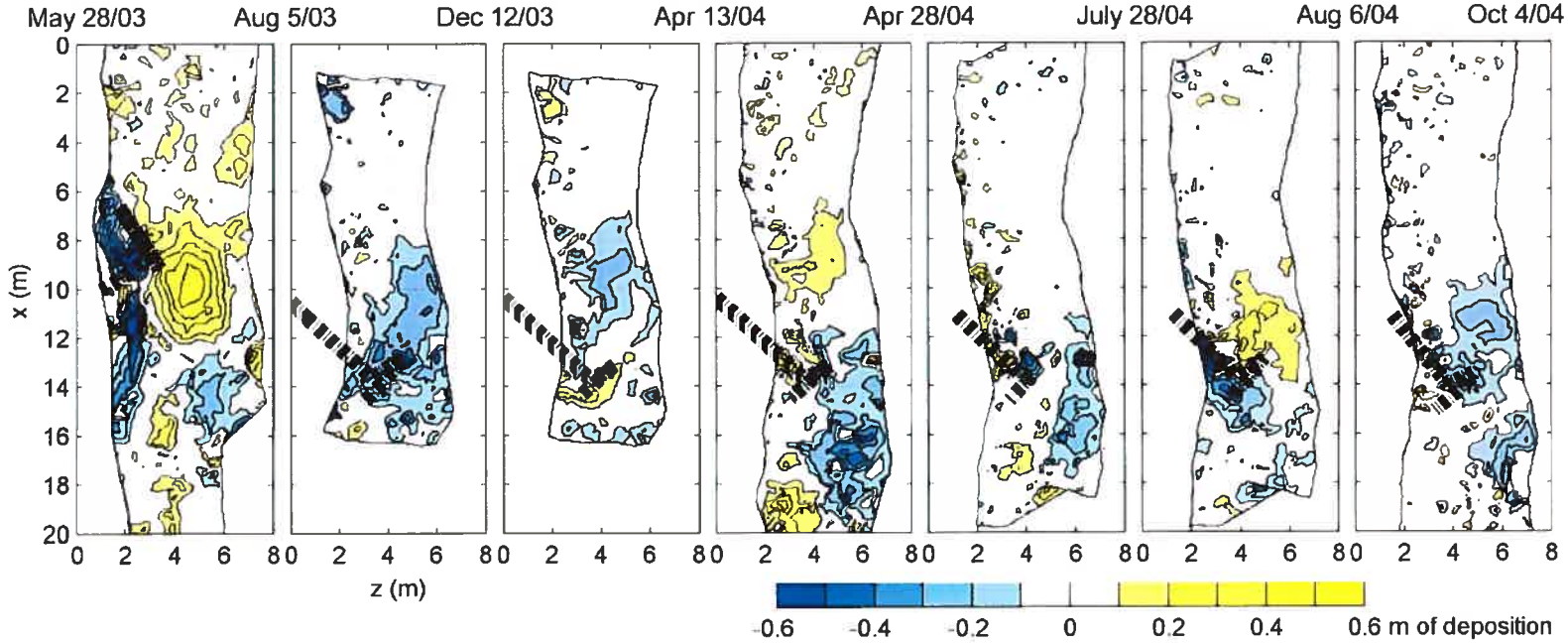

Figure 7.8 - Erosion/deposition maps over the study period. The extent of any map is the minimum of the two morphology maps that were used to calculate it.

7.3.2 *Path lengths of sediment transport*

Final positions of the tagged particles are shown in comparison to their initial positions in Figure 7.6. There is some tendency for the particles to cluster in certain areas, such as the pool-head and channel side bars, but in general they are dissipated over large distances downstream of the study site. A histogram of the cumulative transport distances over the duration of the study period is shown in Figure 7.9. Approximately 1/6 of the particles never moved from their initial positions. Slight adjustments of less than 1 m may be hidden within this group. 5/6 of the particles have moved more than 1 m. Their cumulative transport distances follow a unimodal distribution if zero values are not considered. If zero values are included in the statistics, the mode is 20-50 m, the median is 9.5 m, the mean is 22.6 m, the standard deviation is 35.7 m, and the skewness is 3.5. While there is a strong mode in the data, it is not clear whether such a model supports a model of morphological transport. To investigate the data further, we differentiated within the data set based on date of insertion and particle size.

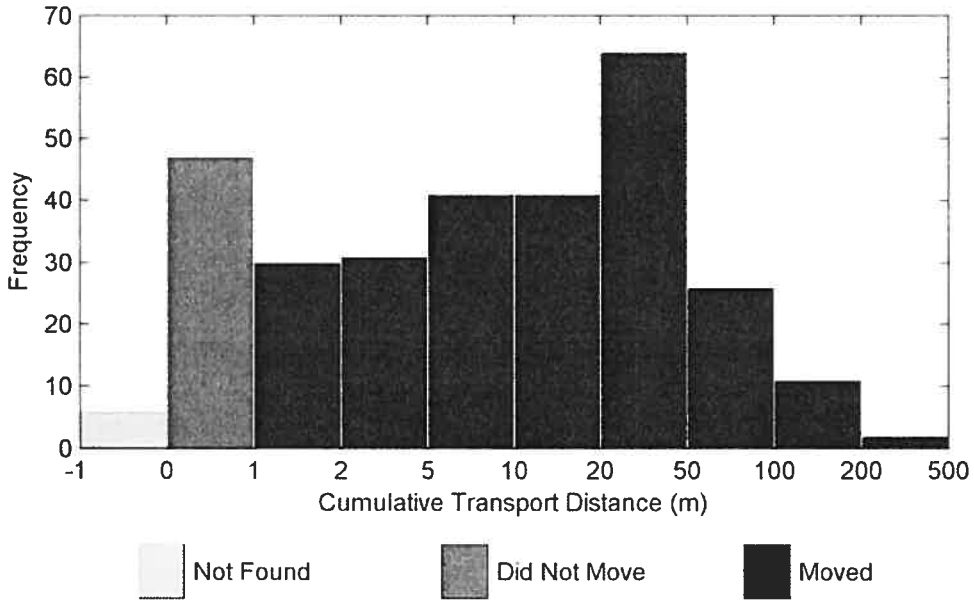

Figure 7.9 - Cumulative transport distance for all tagged particles at the end of the study period. Particles that were never found after their initial placement are also shown.

Particles placed on the surface of the bed are expected to behave differently than those which have been reworked by previous flood events [*Ferguson and Hoey*, 2002]. For this reason we divided the total sample of tagged clasts in three groups according to the initial seeding date. Transport distance between successive measurement dates is plotted as

a series of histograms in Figure 7.10. Hydraulic conditions between PIT tag surveys are summarized in Table 7.3. Path lengths in Figure 7.10 follow a bimodal distribution during initial transport events for the three samples. This is most evident for the initial small sample, which has two modes of 2-5 m and 20-50 m, and the last sample added during the summer of 2004, which also has two modes of 2-5 m and 20-50 m. Recovery of the second sample after its initial transport event was complicated by ice that prevented many particles from being found. Ice was particularly a problem downstream of the study site and a second mode between 20-50 m could not be identified. Instead, this mode shows up in the third measurement date where most of these particles were located for the first time. The relative importance of the five periods is indicated by the behavior of the first sample of 23 particles, which shows that periods 1, 3, and 5 have the highest sediment transport rates. Based on Table 7.3, this indicates that sediment transport rates increase sharply with maximum water level. Sediment transport is highest when flow stages are 0.4 m above bankfull.

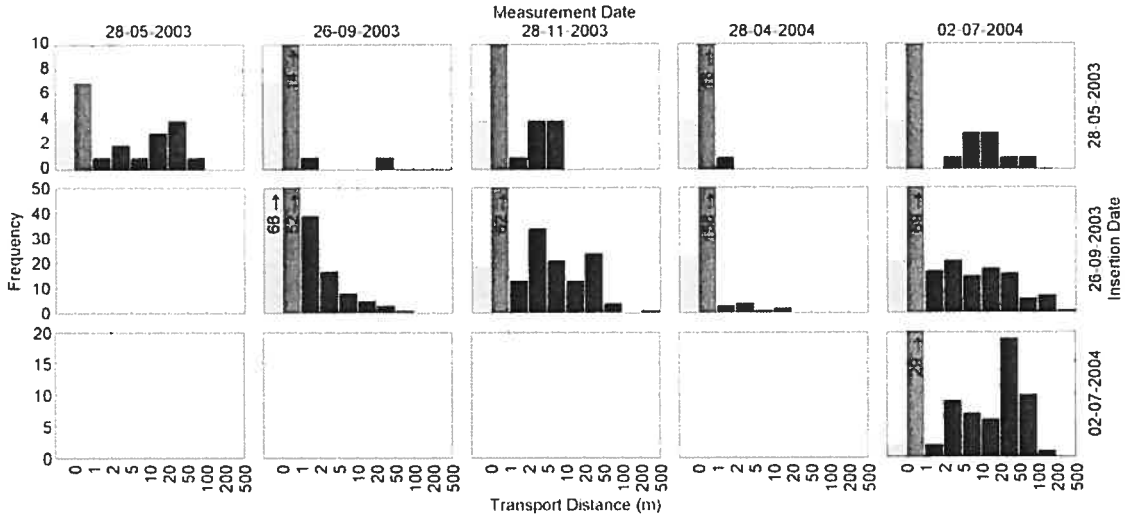

Figure 7.10 - Path lengths of tagged particles for each measurement date separated by insertion date.

The period of July 2, 2004 to October 6, 2004 provides an excellent example with which to compare the movement of particles that had been worked by previous floods to those newly inserted on the bed surface. This event has been broken down by sediment size class in Figure 7.11. As expected, the proportions of particles that were not found and particles that do not move are larger for the reworked sediment. Separated by size class, transport distributions are unimodal, with a single exception of the smallest size class (<

D_{50}) of the reworked sediment, with modes at 2-5 m and 100-200 m. The shorter mode of these two modes does not appear for newly inserted sediment, where all transported particles in the smallest size category were transported more than 10 m. The shorter of the two modes for the smaller particles is the same as the mode in the larger sediment classes ($> D_{67}$). This suggests that there is a subpopulation in the $< D_{50}$ size class whose path lengths are reduced as a result of interactions with other particles. If we consider only the second, longer mode for the smallest particles, there is a clear negative relationship between transport distance and size for both the reworked and newly inserted particles. The negative trend is most evident for the newly inserted particles where there is a larger proportion of the subsamples contained within the modes of the two smallest size classes, and the standard deviations of these distributions are reduced in comparison with those of the reworked particles. A final observation is that the differences between the transport distance distributions of reworked and newly inserted particles are less in the larger than in the smaller size classes. In the D_{67} - D_{84} size class there is little difference in mean, mode, or skewness. Observations of the largest size class ($> D_{84}$) are limited by the small samples, but they indicate that fewer reworked particles moved than newly inserted particles and that transport distances in both cases have a similar distribution as the D_{67} - D_{84} size class.

7.3.3 Spatial distribution of entrainment and deposition of tagged particles

We present a series of plots to document the spatial distribution of the entrainment and deposition of tagged particles in the riffle-pool during the five tracking periods in this study (Figure 7.12-Figure 7.16). A summary of the significant floods within these periods is shown in Table 7.3. Figure 7.12 is useful to illustrate the presentation of the results as there were only a few tagged particles in this initial test of the method. Four plots are included in each figure to present the different sediment size classes. On the plots, zones where the measured shear stress during the bankfull flood on August 13, 2004 exceeds the critical shear stress for each sediment size class are shown. Where shear stress estimated using the mean velocity is greater than the critical shear stress ($\tau_u > \tau_c$) the bed is shaded a dark gray. Where $\tau_u < \tau_c$, yet the shear stress estimated using the turbulent kinetic energy is greater than the critical shear stress ($\tau_k > \tau_c$) the bed is shaded a light gray. We used the hydraulics measured during the bankfull flood as a reference for the presentation of the sediment transport data. It was not possible to measure flow properties during floods

significantly greater than bankfull and the bankfull flood is the closest approximation of flow hydraulics for all of the periods. τ_u exceeds τ_c for all size classes upstream of x = 6 m and in the pool center and tail. Within the pool-head from x = 8-14 m, τ_k always exceeds τ_c on the left side where flow is concentrated in the thalweg. τ_u exceeds τ_c over the bar to the right side of the channel, but only for the smaller sediment sizes. Overlain on the shear stress exceedence plots are the start and end positions of each tagged particle and the interpolated transport path. Freshly inserted particles as well as those that did not move during the period are also indicated. The first period was a test of the method, as shown in Figure 7.12. One event where $Q>Q_{bf}$ occurred during the period and the flood had a peak flood level of 0.4 m above bankfull. Due to the low numbers of particles and high variability of their movements, no clear patterns are discernable from this initial test.

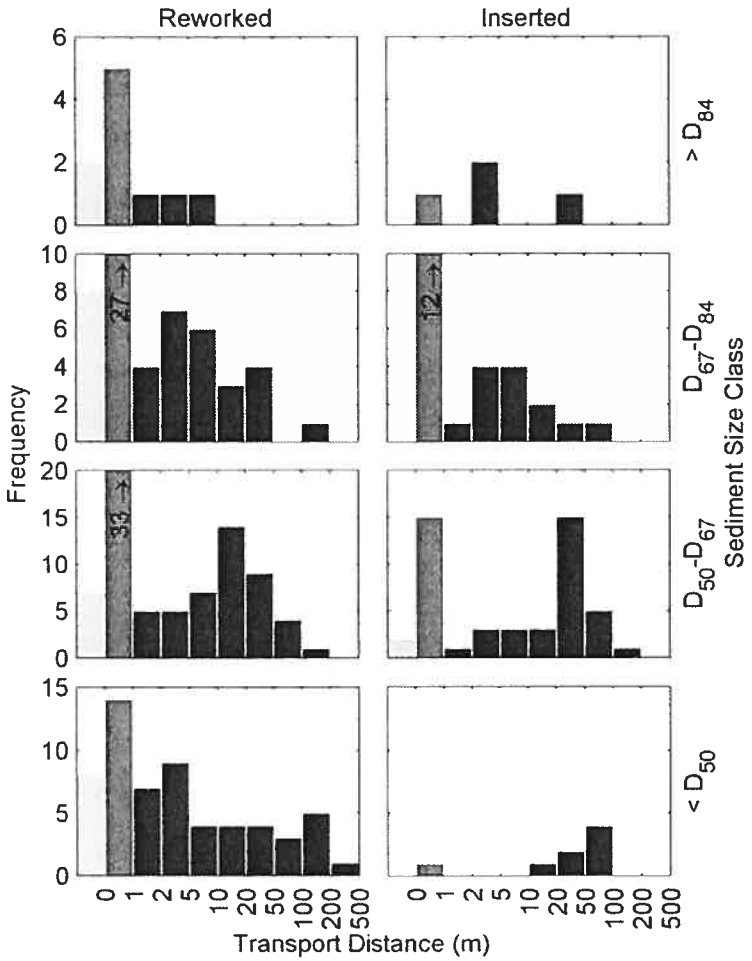

Figure 7.11 - Path lengths for sediment transport in the final survey period of the tagged particles. Sediment has been divided into 'reworked' and 'inserted' classes to distinguish particles

that had been in the river for previous floods from those that had been placed on the bed at the beginning of the period.

Figure 7.13 documents the results from the initial movement of the second wave of particles added to the stream. There were two events greater than bankfull during this period and the maximum flood level was 0.2 m above bankfull. The survey to recover the tagged particles was limited by ice and no information on particle movements downstream of the tree was obtained. Upstream of the tree, partial mobility occurred in all size classes. Larger particles moved less frequently than smaller particles. The deposition patterns differ with clast size. The smallest particles are transported from upstream and frequently move to the right of the channel where they are deposited high on the bar close to the right bank. The larger sizes are progressively deposited towards the left. Particles larger than D_{84} are transported off of the bar and into the thalweg of the pool-head. In the subsequent flooding period (Figure 7.14) it is important to note that, for the particles that were not found in the previous survey, the movements shown accumulate those in the previous period. This third period covers the winter of 2004 where at least three events greater than bankfull occurred, all of them associated with ice, and the maximum flow level was approximately 0.4 m above bankfull. Entrainment and deposition is quite patchy, which makes interpretation difficult, but there are some observations that can be made. It is clear that all the particles located downstream of the tree were entrained. Even the largest sediment sizes were transported downstream or deposited on the developing bar to the left of the channel. Also clear is that no particles larger than D_{84} were transported through the pool. This observation is limited by the small sample size, but is supported by the behavior of particles in the D_{67}-D_{84} size class because the majority of particles located in the $\tau_k > \tau_c$ zone did not move. Instead, the particles in or close to the $\tau_u > \tau_c$ zone were eroded. In contrast, almost all of the smaller particles in the pool-head were entrained. These results confirm that forces from the water are sufficient to entrain smaller particles in the pool-head, which counteracts the argument of *Booker*, 2001 who postulates that pools are primarily maintained by sediment routing. The shear stress threshold criteria estimated with τ_k does not predict entrainment of the largest particle sizes. The threshold criteria estimated with τ_u appears to suitably predict the movement of all particle sizes. The implication of this observation is that the fluctuating shear stress that occurs in the pool-head does not efficiently transport large particles.

Figure 7.15 shows particle movement during a period in which the maximum flood was just below the bankfull level, thus illustrating the low sediment transport during events less than bankfull. Some erosion did occur downstream of the pool in this period, but there were no tagged particles in this area because they had been removed during previous floods. New particles were added in the summer of 2004, and their response to a flood 0.4 m above bankfull is shown in Figure 7.16. In general, the results confirm those from Figure 7.14. All particles downstream of the tree are transported except those located on the bar to the left of the channel. No large particles upstream of the tree are transported through the pool. Most of the smaller size particles are entrained and many are transported through the pool. A number of relatively short movements of small particles are observed in the thalweg where $\tau_k > \tau_c$. These movements correspond with the mode of 2 - 5 m seen in the histograms for larger particles, which suggests that transport distances of small particles are shorter in the pool-head, perhaps due to the different hydraulic conditions, or due to entrapment by the larger particles. It is also important to note that many particles are transported out of the pool-head zone whrAlso shown on Figure 7.16 are the last known positions of particles that were not found in the final survey of the tagged clasts. 11 of 26 lost particles were last found in the pool-head and the bar downstream of the tree. Deposition of up to 60 cm occurred over the study period, which suggests that the burial of particles is a major source of error with the PIT tag method in this study.

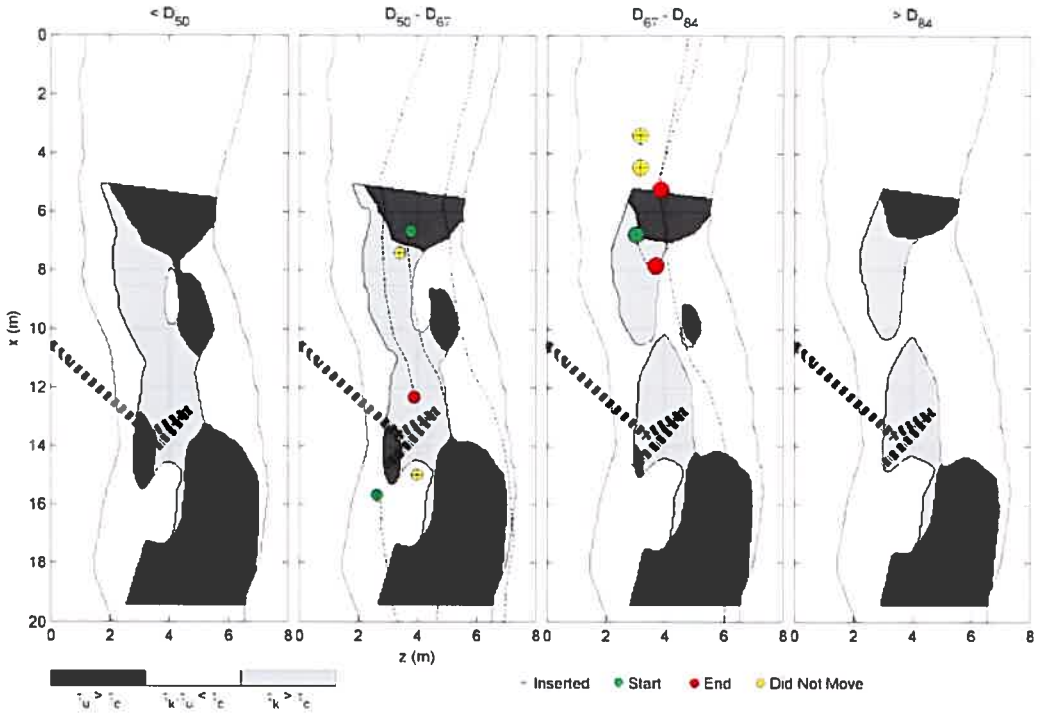

Figure 7.12 - Spatial plot of sediment movement for initial seeding of particles between May 28/03 and September 26/03. Particles are distinguished by sediment class. Particle movements are overlain on zones of excess shear stress during the bankfull event for shear stress as a result of both mean velocity (τ_u) and turbulent velocity fluctuations (τ_k).

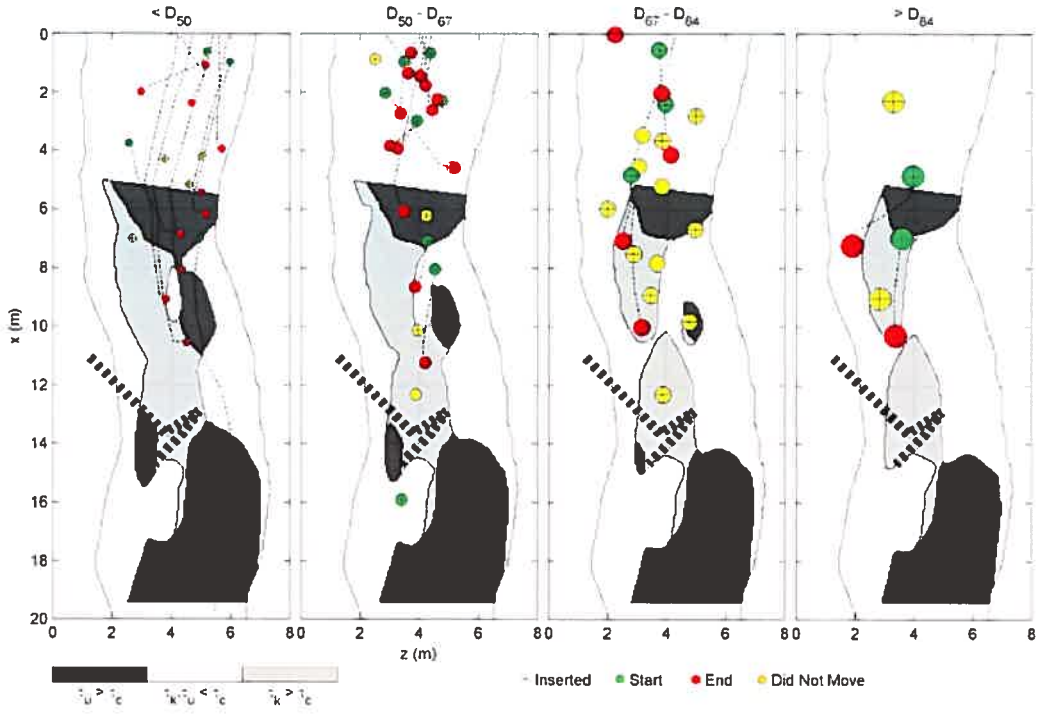

Figure 7.13 - Spatial plot of sediment movement between September 26/03 and November 28/03. It was not possible to survey downstream of the tree due to ice. See Figure 7.12 for more complete explanation.

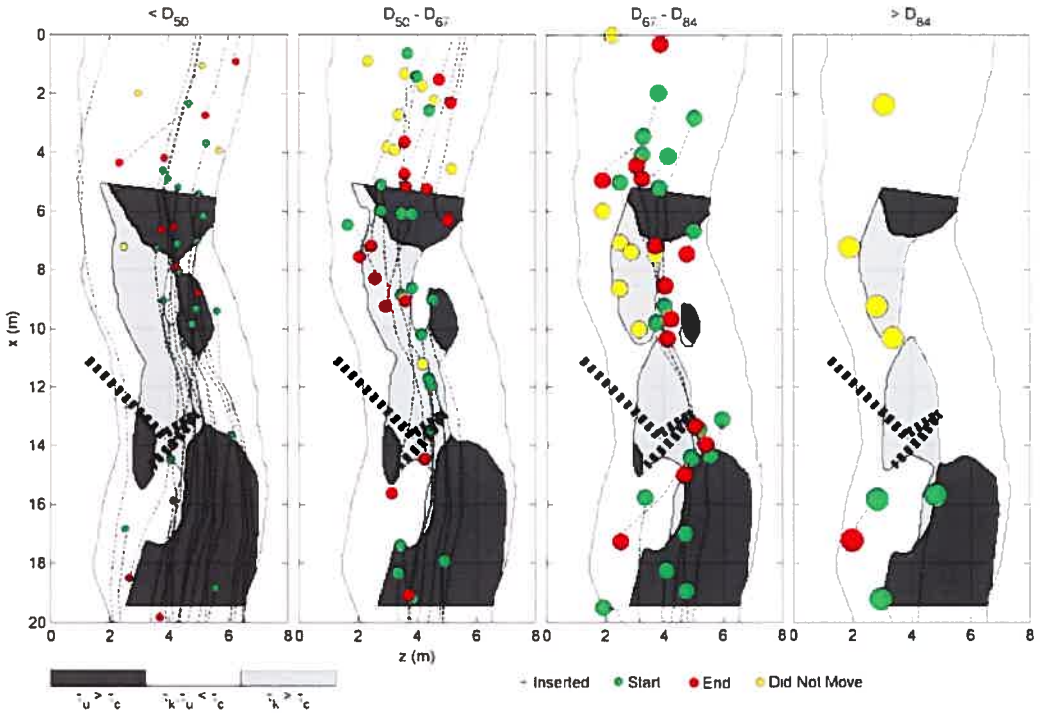

Figure 7.14 - Spatial plot of sediment movement between November 28/03 and April 28/04. Some movements downstream of the tree may have taken place during the previous period. . See Figure 7.12 for more complete explanation.

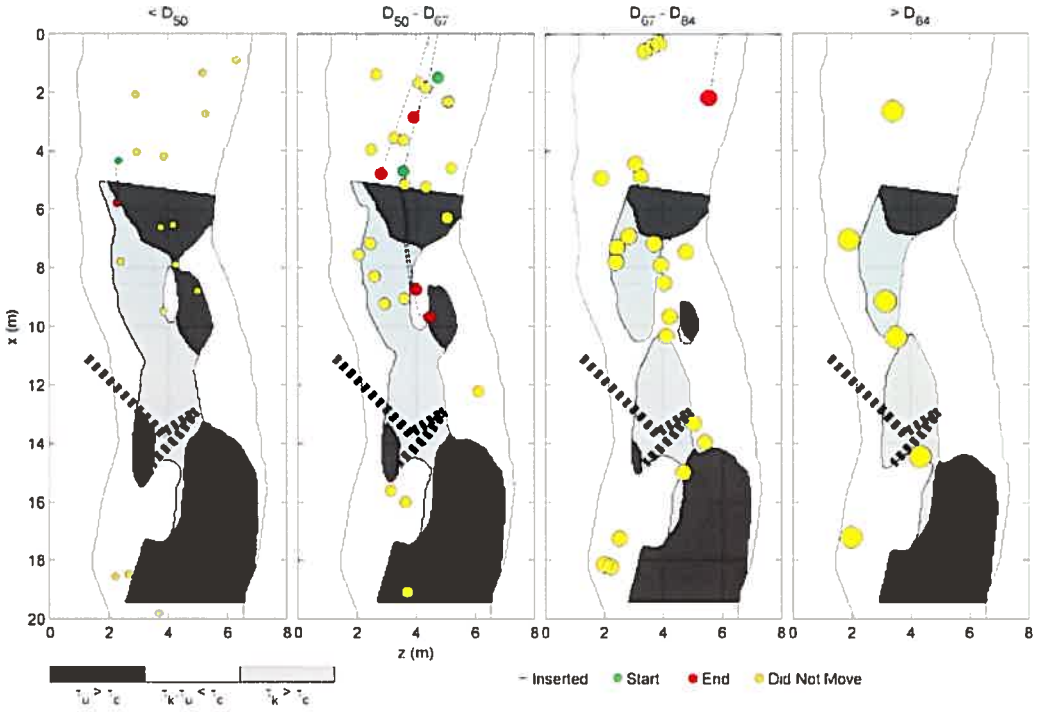

Figure 7.15 - Spatial plot of sediment movement between April 28/04 and July 2/04. See Figure 7.12 for more complete explanation.

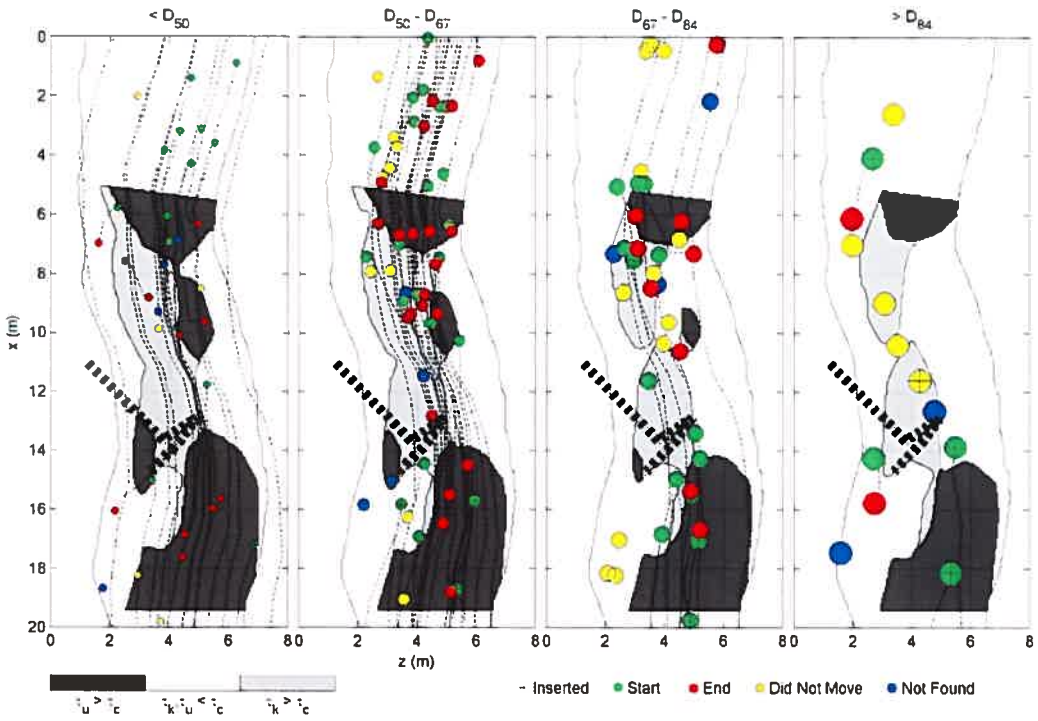

Figure 7.16 - Spatial plot of sediment movement between July 2/04 and October 6/04. The last known positions of particles that were not found on the final survey are also shown. See Figure 7.12 for more complete explanation.

7.4 Discussion

In this article we have presented morphologic change and sediment transport data that allow us to consider the development and maintenance of a forced riffle-pool in a relatively straight and narrow stream with a wide range of particle sizes. The pool was initiated as a result of large woody debris that changed location and moved downstream, thus reinitializing the scouring processes. A series of floods at and above bankfull stages resulted in patterns of deposition and erosion that varied with flood peak and sediment size. In the sections without bed forms, as we would expect, sediment transport of all sizes increased with flow stage. A similar situation also occurred in the mid-pool and pool-tail, as material of all sizes was scoured out during extreme events. The pool-head is more complicated, and its dynamics appear to hold key mechanisms for bed form initiation and maintenance. This discussion will summarize key results in a conceptual model of riffle-pool development, compare this model with other studies that have documented different phases in sediment transport, discuss the role of turbulence in sediment transport and the role of the tree in pool formation, and consider the effects of riffle-pools on larger scale properties of the system such as the sediment budget.

Figure 7.17 shows a simplified model of morphological changes and particle movements at the field site. We observed two major cycles of scour and fill during a period of active pool development. As a result of the most extreme events, the riffle and pool-head fill with the material transported from upstream. All sizes can be transported during these events, depending on the flood level. Some material is transported through the pool center and tail, but this material is sorted by size. Visual observations shows that large particles do occasionally move through from the pool-head, but sediment tracers larger than D_{84} never moved from the pool-head to the pool-tail during the study period. Downstream of the tree, flow acceleration leads to erosion of all sizes of particles in the developing pool. In more moderate events, large material is not transported in the straight sections of the stream and there is less material transported onto the riffle and pool-head. Topographical surveys indicate that erosion occurs in the pool-head during this time, but this trend was not revealed by the tagged particles, which indicates that the transported material is likely smaller than approximately 3 cm, the lower limit of the particle size for which it was possible to insert PIT tags. Critically, this transport leaves the largest material in the upstream portion of the developing pool and this material appears to have a stabilizing effect on the bed form (Figure 7.8). Subsequent large events transport new sediment into the pool, but deposition occurs downstream from the location of deposition during the previous event. Subsequent bankfull events expose more of the larger sediments so that a distinct sedimentological unit begins to appear in the riffle and pool-head. Erosion due to acceleration out of the pool occurs during all flood stages at or greater than bankfull. The larger events have the potential to move the position of the downstream riffle crest due to their capacity to transport the larger clasts.

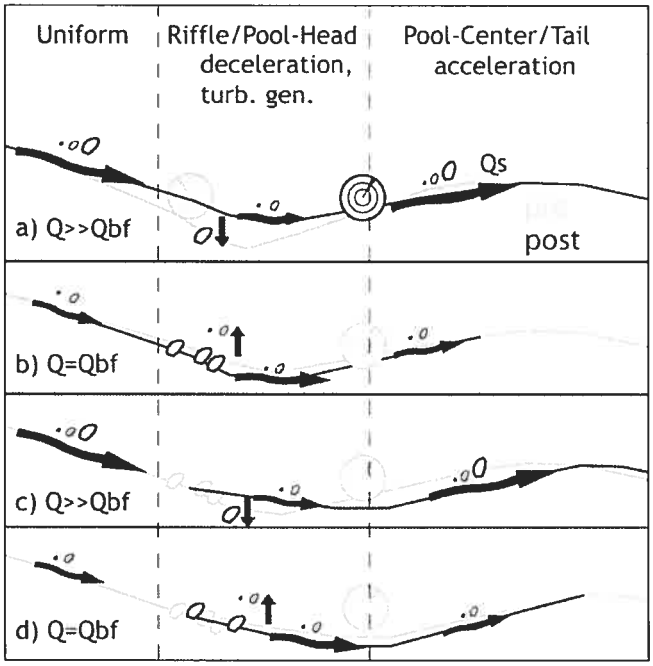

Figure 7.17 - Summary diagram of morphology changes in response to two cycles of flood events of various magnitudes. The movement of the tree is shown in (a) for a flood event greater than the bankfull discharge ($Q>>Q_{bf}$). Sediment flux is indicate by black arrows, and transported size fractions are indicated. Note alternating cycles of scour and fill that lead to development of distinct sedimentology in riffle/pool-head in zone of flow deceleration and turbulence generation, and enlargement of the pool downstream of the tree in zone of flow acceleration.

In general, Figure 7.17 supports existing studies that have documented two phases of sediment transport and identified reversals in sediment transport associated with riffle-pools. The results of this study are much more detailed, however, providing key information on sediment pathways and bed morphology changes. The parallel study of flow hydraulics also allowed us to estimate shear stress during the bankfull flood. These advantages helped to significantly refine the understanding of the morphology and dynamics of riffle-pools that has been developed by previous studies. *Meade* [1985] presented a relatively simple model in which pools scour and riffles aggrade at high flow and fill and erode, respectively, at low flow. We observed sand deposits in the pool center and tail at low flow, which supports previous observations of phase I transport in gravel-bed rivers. Large deposits of fine material are not present in Moras Creek, however, and we were not able to tag what fine sediment was present. Based on topographic surveys, scour of sediment from the riffle/pool-head occurred on three occasions. This transport is dependant on antecedent conditions, as erosion only occurred in areas with significant deposition during a previous, high flow event. The importance of antecedent conditions

mirrors the observations of *Sidle* [1988] and fits with observations of phase I transport in which sediment is supply limited. Transport only occurs where deposition of mixed or fine sizes occurred during previous events.

High flow, or phase II, transport as identified by *Jackson and Beschta* [1982] and *Sidle* [1988], is characterized by aggradation on riffles [*Meade*, 1985] and bimodal or symmetrical path length distributions [*Pyrce and Ashmore*, 2003]. These general characteristics were observed three times during the study period. Discussion is limited by the fact that the pool understudy was developing and some features may be remant from previous morphologies. Nevertheless, our study yielded some new information with which to discuss sediment transport and morphological change during large floods. First, aggradation typically occurred in the downstream portion of the riffle and the pool-head. We did not observe an increase in riffle crest elevation, though it may have occurred at some stage during the flood. Second, the largest particles were not transported through the pool. A possible explanation for this is the imbrication of larger clasts in the pool-head [*Clifford,* 1993; *Sear,* 1996]. It is doubtful, however, that imbrication is the cause of riffle-pools. Riffle-pools are commonly observed to scale with stream width, a variable that is closely related to the flow. We propose that sediment dynamics can be better explained based on flow dynamics. In the pool-tail, shear stress is dominated by high mean velocity in a zone of flow acceleration (*see Chapter 5*). The effects of mean flow velocity on sediment transport have been intensively researched over many years. Due to the deformation of the velocity profile in accelerating flows, sediment transport is likely to be higher in the pool-tail than in uniform flows. In the pool-head, however, shear stress is dominated by high-amplitude turbulent fluctuations of short duration in a zone of flow deceleration and intermittent separation (*see Chapter 6*). The effect of turbulence on transport is not completely understood. *Nelson et al.* [1995] and *Sumer et al.* [2003] have documented a positive relation between turbulence and sediment transport, but the effect on heterogeneous sediments has not been tested. The principal inference from the results shown here is that sediment transport by enhanced turbulence is highly sensitive to sediment size. This inference is supported somewhat obliquely by *Nelson et al.* [1995], who noted the duration of turbulent events to be relevant to the prediction of the number of sand grains transported. They reported that long duration events transported a disproportionate amount of the sediment. Tests on heterogeneous sediment were not done,

but this principle may also be relevant in the pool-head, with the obvious difference that it is not possible to transport a proportion of a large clast. Large clasts remain stable in spite of extremely high shear stress values because, based on considerations of momentum, they require longer duration events to move. Smaller sediments respond more quickly to the velocity fluctuations and are selectively removed from areas that present a negative bed slope to the river - i.e. the lee slope of the riffles and the pool-heads.

Conceivably, there is a level above Phase II in which riffle and pool-head sediments will be eroded. *Warburton* [1992] proposed a three phase model of sediment transport in rivers with bed forms. The break-up and transport of riffle sediments, however, have rarely been observed. *Jackson and Beschta* [1982] and *Campbell and Sidle* [1985] documented the transport of riffle-sized material at high flow, but the source of this material was not identified, and it is possible that the key riffle sediments remained stable during the floods. In this study, only short movements of large particles were observed within the riffle and pool-head. Large particles were not transported through the pool-head during the study period despite floods that were up to 0.4 m above bankfull, a flood estimated to have a return period of 15 years. This matches the results of *Hassan and Woodsmith* [2004] who observed only partial mobility of large clasts during extreme events that were up to three times the bankfull flow rate. The best data set to examine this issue may be that of *Madej* [1999], where 20 years of topographical data in seven reaches in three rivers were assessed. She found that, for rivers in which riffle-pools were mostly forced, even extreme events were insufficient to disturb bed features in a manner that would be indicative of Phase III transport. Some randomization of bed features occurred in rivers with mostly free riffle-pools after a 12 year flood. The difference in response to extreme events may be the result of differences in the flow hydraulics between forced and unforced riffle-pools. The forcing element induces deceleration and acceleration regardless of the bed condition. Our results show that the riffle and pool-head tend to infill during extreme floods. Without a forcing element, it is conceivable that the pool will tend to become shallower during this time and reduce the non-uniform flow dynamics that maintain it. If enough sediment is transported, the pool could infill entirely. This is not possible where the pool is forced. In forced pools, the pool is unlikely to infill unless the forcing element moves.

Finally, it is worth considering the effects of riffles and pools on larger scale properties of the river. When all tagged particles were considered, we obtained a median of 22.6 m for the cumulative path lengths over the entire study period a distance approximately four times the channel width, a result consistent with the datasets analysed by *Pyrce and Ashmore* [2003] and the formation of alternate bars. Also similar to these previous results, however, is that the distributions in response to individual events are strongly skewed, often with multiple modes. We obtained relatively normal and unimodal results by considering a log transform of the path lengths and separating sediment by size class. Under these transformations, the agreement between path length and bar growth breaks down as modes are typically longer for sediment smaller than the median and shorter for sediment larger than the median. Longer term studies with reworked sediment are necessary if a consistent behavior is to be identified. It is also necessary to consider the possibility that Moras Creek may not fit with established models of bar growth and path length distributions as proposed from flume studies such as that of *Lisle et al.* [1991] and *Pyrce and Ashmore* [2005]. The flumes they used both have higher width-to-depth ratios, which allows the active channels to reduce in width as bars develop and emerge. In Moras Creek, it appears that the narrow width restricts such processes from occurring and bars are poorly developed. Morphological estimates of sediment transport would drastically underestimate total transport as demonstrated by the large numbers of particles that are transported through the pool during large events. The hypothesis of equal mobility may also break down in this system. Our results show that there is a relation between size and transport distance. This follows the results of *Ferguson and Wathen* [1998], who noted a strong decrease of transport distance with size for sediment larger than D_{50}. *Hoey and Ferguson* [1997] considered that the rate of downstream fining would be controlled by the mechanics of sediment sorting. Riffle-pool sequences offer a powerful sediment sorting mechanism due to their ability to push the onset of phase III transport to extreme floods that accomplish only a small proportion of the geomorphic work in the channel. This perturbation to the flow-sediment transport interaction fits with the observations of *Lisle* [1995] and *Parker and Toro-Escobar* [2002], who concluded that the principle of equal mobility does not hold in low-order streams that are relatively straight and narrow with a wide range of particle sizes.

7.5 Conclusions

This study offers the most detailed results and spatial representation of sediment transport in a riffle-pool system yet available. We have found that patterns of erosion and deposition are sensitive to flood stage. Progressive erosion occurred in the pool-tail as the pool extended downstream from the constriction. All sizes of sediment were evacuated from the pool-tail on at least two occasions. We have found a straightforward hydraulic explanation for these observations. Flow acceleration dominates the flow hydraulics in the pool-tail. This resulted in very high mean velocities close to the bed so that shear stresses are high and available equations appear to predict entrainment thresholds reasonably well. The riffle and pool-head is more complex. Pool morphology was characterized by cycles of erosion and deposition combined with signs of stabilization. Material deposited during floods higher than bankfull was reworked by events closer to bankfull stage. Sediment transport out of the pool-head is size-dependant, and the largest material accumulated in this area in spite of flood peaks with a 15 year return period. Repeated inputs of sediments resulted in the accumulation of large particles that appeared to locally stabilize the bed during subsequent events greater than bankfull. The pool-head is also critical to theories of pool formation because the pool was initiated upstream of the tree. Flow hydraulics show that this zone is characterized by decelerating flow and high shear stresses as a result of instantaneous flow separation and turbulent fluctuations. These turbulent fluctuations offer a hydraulic explanation for the sediment transport in the pool-head. Short powerful fluctuations appear to be ineffective in transporting the largest sizes so that the smaller sizes are selectively removed. More study at the process scale is needed on the effects of turbulence on sediment transport, particularly in heterogeneous sediments. Study of free pools is also warranted to determine how flow and sediment dynamics differ from forced pools. Finally, it appears that stable riffle-pool sequences can influence the sediment budget of a stream by selectively removing the largest sediment sizes from the transported population. Larger scale study is needed to properly test the significance of this sorting mechanism.

8 GENERAL DISCUSSION AND CONCLUSIONS

8.1 Introduction

This thesis is concerned with the formation and maintenance of riffle-pools. We have utilized two approaches to investigate this problem: numerical simulations and field-based research. These approaches are complementary. The field-based research presents new data over a range of discharges, including channel forming events, that advance our understanding of the flow and sediment dynamics in riffle-pools. Specifically, we demonstrate the central role of turbulence in pool initiation and development. These data, however, were largely obtained at a single field site. It is not possible to confirm a general model of riffle-pool mechanics because of the local context of any field site. In contrast, simulation models are notoriously difficult to apply to the investigation of process scale behavior of the system. Sediment and turbulent flow dynamics are not yet understood to the point where a completely physical model of their interaction is possible. Instead, we employ a hierarchical strategy whereby the process scale dynamics are represented by simple rules. These simple rules were based on physical considerations and informed by the field-based results. Constructed in this manner, the simulation model is a useful tool for testing the significance of results from the field-based component study. This improves confidence that the mechanisms we identify in the field are both sufficient and necessary for the generation of pools and riffles. In this way we develop a general theory of riffle-pool formation that we discuss in this final chapter of the thesis. We begin by summarizing the key findings from each of the article chapters. We then present a conceptual model on pool and riffle formation and conclude this chapter and the thesis with directions for future research.

8.2 Summary of key findings

This section summarizes key findings from the modelling and field-based research that we undertook to explore the formation and maintenance of riffle-pools in gravel-bed rivers. The third chapter in the thesis presents the two dimensional model of gravel-bed river system dynamics. The model structure is fairly unique in fluvial geomorphology because it simulates the movements of discrete particles and uses simple rules to represent flow and sediment dynamics. The main result is the emergence of a range of bed form

types in response to feedback mechanisms. Larger scale bed forms develop when flow field parameters are linked to the bed configuration. A critical step was the link between bulk velocity and turbulence intensity. Without this link, scour of the bed does not occur and bed forms are small scale and of a strictly low relief nature. Flow separation was necessary to produce a downstream celerity of the bed forms that is characteristic of such features as ripples and dunes. This confirms results and observations made by several researchers (e.g. *Best* [2005]). The emergence of modelled bed forms with similar scale, sorting patterns, and stability as riffle-pools required three items: the link between acceleration and turbulence intensity, flow separation, and heterogeneous particle sizes. These three factors are central to the conclusions of chapters 5, 6, and 7, respectively.

The fourth chapter of this thesis is the first that presents results from the field campaign. It is a technical article on the reliability of instruments used to measure instantaneous water velocity in highly turbulent environments such as riffles and pools during floods. The study was necessary to ensure the accuracy of the flow data used in this thesis. We compared the two most common instruments used in field studies. The field sites chosen for the test presented a range of conditions including spatially variable flow environments in which flow was rapidly accelerated and decelerated. The key result was that the Electromagnetic Current Meter (ECM) is more reliable that the Acoustic Doppler Velocimeter (ADV) in highly turbulent flows. This is related to the sampling methods of the instruments. The ECM makes an instantaneous recording from a resistance capacitor whereas the ADV requires a correlated measurement over a small time interval. While the ECM results in a dampened signal, the small time interval needed by the ADV is still too large to allow accurate measurements in highly turbulent flows, a fact that is not reflected in a number of published methods used to estimate ADV error. For this thesis, the critical result was that it supported the choice of the ECM for further measurements of velocity while rivers are in flood and highly turbulent.

The main results of the intense field study of a forced riffle-pool are presented in chapters 5, 6, and 7 of the thesis. Chapter 5 presents the mean velocity and turbulence intensity statistics in our main study site, Moras Creek, over a range of discharges that includes the bankfull discharge. These data demonstrate the controlling influence that acceleration and deceleration have on flow dynamics. Acceleration leads to a fuller velocity profile such that mean streamwise velocities are frequently higher near the bed

than at the surface. This is important because velocity reversal can occur on the positive slope of the pool-tail. Comparing uniform and accelerating flows for a given bulk velocity, the change to the velocity profile means that near-bed velocity and shear stress are higher in accelerating flow. Deceleration produces the opposite effect such that high streamwise velocities tend to concentrate in the center of the channel near the water surface. Mean streamwise velocities near the bed can be very low and even negative, and shear stress estimates that are functions of the mean velocity are also low. However, a key argument from this article, and one that is central to the entire thesis, is that the mean shear stress underestimates the forces on bed particles in the pool-head. Turbulence intensities are high in the pool-head. Velocity gradients over the full depth of flow mean that turbulence is generated over the entire profile and not just near the bed, as is typical in uniform flows. Shear stress estimates based on turbulence intensity indicate high levels of stress on the bed and may account for sediment transport in this area. We propose a conceptual model of mean velocities and turbulence intensity for the forced riffle-pool. The forcing element appears to act as a catalyst that forces the changes to mean velocity and initiates riffle-pool development. Because acceleration and deceleration will be a general feature of all macro-scale bed forms, we also propose a simplified general model for a range of riffle-pool types.

The fourth article uses the same data set as the third article but characterizes the flow environment in a different way. Rather than using the time-independent statistics of the flow, we sought to characterize the time-dependant or coherent character of the turbulent flow in the pool. We found that instantaneous flow separation occurs near the bed in the pool-head. Spectral density indicates that the pool switches from an environment in which energy decays at low discharge to one in which energy is generated at high discharge. The size of coherent turbulent events indicates that the source of this generated energy is likely the zone of instantaneous flow separation. The constriction of the forcing elements forces a break in water surface slope and the shear zone between the main thalweg and the slower velocities produces strong boils and vortices that are visible at the water surface. Near the bed, however, the coherence of turbulent events is small in comparison to channel morphology. Overall, there is a negative relation between velocity and the coherence of turbulent events. It appears that the generation of new turbulence in the pool-head and downstream of the tree disrupts the typical organization of the flow in turbulent

boundary layers. At high discharge it is shown that recovery of this typical organization does not occur within the pool, a result that may be significant for the scaling of riffle-pools.

The final article presents the results from the study of the morphology and the sediment transport at the Moras Creek study site. Similar to the flow hydraulics, the main conclusions contrast the processes upstream and downstream of the constriction. The downstream dynamics are relatively simple to understand. A near complete evacuation of all sizes of tagged particles from the center and tail of the pool was observed on two occasions. Topographical mapping showed that there was progressive lengthening of the pool during all floods at or above the bankfull flood. These observations coincide with areas where the shear stresses derived from mean velocities exceeded a threshold value. This offers a clear hydraulic explanation of observed sediment transport and erosion. Upstream of the tree, the dynamics were more complex. Sediment transport was size-dependant so that tagged particles larger than D_{84} were never transported out of the pool-head. Full mobility did not occur, even for the smallest sizes. During the highest observed discharges, deposition occurred in the riffle and pool-head. Erosion occurred during discharges closer to the bankfull discharge, but the location and extent of this erosion was dependant on antecedent deposition. These observations coincide with areas where shear stress estimated as a function of mean velocity did not exceed a threshold value, but shear stress estimated as a function of turbulent kinetic energy did exceed a threshold value. This indicates that sediment is transported by turbulent fluctuations in the pool-head. Less is known about sediment transport in these conditions, but it appears that transport by turbulence is highly size selective. Large magnitude but short duration events do not transport the largest particle sizes, effectively trapping them in the riffle and pool-head. This hydraulic mechanism explains both the stability of riffle-pools and the requirement of heterogeneous sediments.

8.3 Originality of the Thesis

The formation of riffle-pools is a geomorphic puzzle that has resisted explanation for over 30 years. The originality of the work presented here lies in the modeling approach that we employed, in the technical innovations in our experimental design, and in the unique data set that we were able to collect, all of which contributed to some key discoveries. The numerical model ROQ-B gives us a new tool to examine the problem of

flow-particle interactions and of bed form development including the formation of riffle-pools. By designing rules to match principles of sediment transport culled from engineering as well as earth science research and combining these rules in a hierarchical model, we were able to simulate gravel-bed rivers in a more dynamic way than is possible with existing models. The model should be useful for a range of problems related to gravel-bed rivers where multiple factors interact at local scales to produce patterns that observed at global scales.

Field research on riffle-pool formation and maintenance is made difficult by the conditions during floods. Accurate and reliable measurements required a number of technical innovations. We focused on physical processes that occur on the scale of individual sediment particles and individual turbulent structures. Accurate measurements were critical and testing of the Electromagnetic Current Meter was a necessary step that will be useful for future field research. The method for tagging and tracking of sediment particles is also relatively new and our experiments demonstrate the effectiveness of this technique. In addition, the apparatus we used to measure flow properties during bankfull and larger flood events may also be useful in other studies.

A large portion of the originality of the thesis is contained in the field data we obtained. The information on flow hydraulics is one of the most extensive data sets obtained in a riffle-pool. We measured at a range of flow stages, including bankfull flow, and were able to obtain good spatial coverage. Even though we could only measure two velocity components of the flow, the data set is the most complete in terms of flow turbulence, as it is one of only a very few to measure instantaneous velocity series. The test of instrumentation gave us confidence that the series are of high quality. Morphological and sediment transport data sets are also fairly unique in the literature. Very few studies in rivers have investigated the spatial distribution of erosion and sediment entrainment, and even fewer have compared these results with detailed hydraulic characterization of the site. The data are extremely useful, not just for discussions about riffle-pools, but also for general understanding of sediment transport in non-uniform environments.

Finally, we have made a few key discoveries that, linked together, offer a coherent explanation of the formation and maintenance of riffle-pools. The first is the effect of pool morphology on hydraulic variables near the bed. Mean velocity reversal occurs in the pool-tail due to acceleration. The pool-head is dominated by turbulent fluctuations of short

duration but high amplitude so that high instantaneous shear stresses are exerted on the bed. The second key discovery is the trapping of large particles in the pool-head. These particles do not respond to rapidly fluctuating shear stresses, which provides an explanation for the stability of riffle-pools over a wide range of flood stages. Finally, large scale bed forms emerge from stream bed simulations with the inclusion of a link between flow acceleration and turbulence. It is this dynamic feedback that appears to initiate the form and determine its ultimate size.

8.4 Conceptual Model

We have shown that riffle-pools can be explained by considering the effects of acceleration on turbulence intensity and by considering the effects of short duration turbulent fluctuations on the transport of heterogeneous sediment. In this section we present a succinct picture of the key dynamics that is a modification of the classic model of the relation between turbulent flow, sediment transport, and bed forms developed by *Leeder* [1983] (see Figure 2.1). The Leeder model is central to our understanding of feedback mechanisms in river environments. However, it suffers from two limitations. First, mean velocity and turbulence are coupled in the diagram. Our results show that the interaction between the two is a critical variable with potential consequences for sediment transport. We propose to separate these two items in the same manner that bed forms are distinguished from sediment transport. Second, the diagram does not consider the driving force behind stream processes in the river, and we propose to include energy transfer in the diagram. The resulting conceptual model is shown in Figure 8.1. Energy is input to the system through the kinetic and potential energy of the flow. This assumes that additional energy inputs from the solid phase of the transport are negligible. Flow energy can be transferred either to kinetic energy downstream, sediment transport, or converted to turbulence. Sediment transport can result in the export of sediment (mass balance of sediment is not shown) or lead to the development of bed forms. Developed bed forms feed back to the distribution of energy in the system because they exert a significant control on the transfer of energy from the mean flow to turbulence. We have shown this to be particularly important in the pool-head of riffle-pool bed forms, but the same principle applies to all organizations of the bed that imply a form roughness larger than the particle roughness. Turbulence can be dissipated as heat, but it can also feedback to influence sediment transport. As shown in this thesis, sediment transport by turbulence appears to be

more size-selective than transport as a function the mean shear stress. In the studied riffle-pool system, the largest size fraction of the bed particles was not transported by these extreme levels of turbulence, even during a 15 year flood. Large particles collect on the lee face of riffles and in the pool-head. This mechanism results in positive feedback on the size of the form. In addition, because more energy is dissipated through turbulence as bed forms increase in size, less energy is available for sediment transport, which increases the stability of the form. The reduction of energy available for sediment transport eventually acts as a negative feedback on the bed form size.

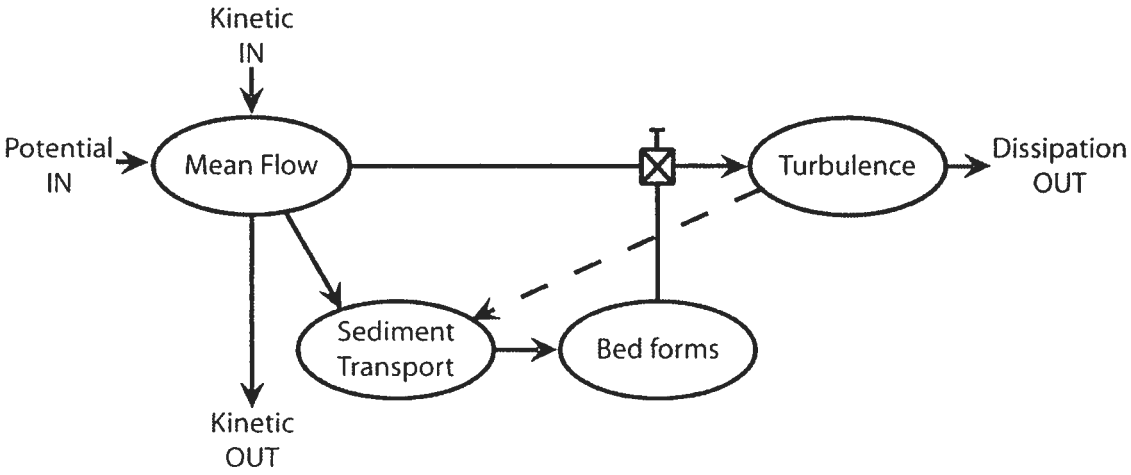

Figure 8.1 - Conceptual model of flow and sediment in dynamics in gravel-bed rivers. See text for explanation.

8.5 Future Research

There are many opportunities for future research to build on the results presented in this thesis. We have grouped these opportunities into three main areas: modelling, process-scale research, and reach or system scale research. One of the most attainable new objectives is to refine the ROQ-B model based on the conclusions from the field data. This has been done to some extent through the incorporation of a rule for flow separation, but in the design of the model, we did not anticipate the importance of the velocity profile over non-uniform boundaries. As a result, a simple, one dimensional representation of the flow field was used. Without a major reworking, it should be possible to consider the effects of the flow profile and incorporate flow separation as an extreme case of profile modification in rapidly expanding flow. A refinement of the flow model could also include some consideration of flow energetics. It appears that the key to the scaling of features lies in the transfer of energy between kinetic energy, sediment transport, and dissipation through

turbulence (Figure 8.1). We anticipate that simple rules could be designed that would allow us to explore not just how bed forms develop, but what drives them and why they emerge in certain situations. Related to this exercise, and discussed in Chapter 3, is the need to relate model control parameters to morphological variables. By incorporating energy, it should be possible to anticipate how control parameters used in the model relate to channel morphology. This should improve our understanding of the scaling of these bed forms. Finally, there are many questions for which a flexible model of stream processes may be useful. Model configuration should allow many different influences to be tested under various scenarios. It should be possible, for instance, to test the effect of riffle-pools on downstream fining, a question that was discussed in Chapter 7. Additionally, the model could be configured to look at step-pool streams, to model the effects of forcing elements, and to look at the transition between different types of systems. An interesting example in this regard was presented in Figure 3.22, where a change from a bimodal to a trimodal sediment size distribution initiated a transition from mobile dune-like forms to stable riffle-like forms. It may be possible to use the model to understand transitions in a phase space diagram of bed forms such as the one shown in Figure 2.12.

At the process scale, there are a number of interesting questions regarding flow and sediment dynamics that warrant further investigation. In Chapter 5, we observed that flow tends to concentrate in a high velocity core in decelerating flow. It is difficult to isolate the factor that was responsible for this observation, however, because there is a slight bend in the channel and the pool was formed by a lateral constriction, which necessarily leads to a core of higher velocity flow. Flume tests could be easily designed to look at the effect of a non-uniform bed on the lateral distribution of flow in the channel. A link would suggest that the lateral development of bars and meanders are products and not the determinants of non-uniform flow. This would support a universal model for the generation of riffle-pools. The thesis also examined flow coherence in the pool. Overall, we found a negative relation between velocity and the scale of coherent events. Alternate sampling designs should be tried to test the robustness of this conclusion. The streamwise sampling design utilized by *Buffin-Bélanger et al.* [2000] would allow a closer spatial sampling within a single streamline so that the duration of turbulent events could be determined. Another alternative is to sample longer time series. This would allow investigation of the relation between morphology and longer velocity pulsations such as those investigated by *Dinehart* [1999].

A third process scale question that this thesis has discussed is the effect of turbulence on transport. In spite of a few studies on the effect of turbulence over the last decade [*Nelson et al.*, 1995; *Sumer et al.*, 2003], there are very few studies that address the characteristics of shear stress in a highly turbulent environment such as was observed in the pool-head. Our results suggest that there is a strong size dependent effect such that larger sediments do not respond to high frequency fluctuations. More research is warranted.

At the reach and system scale, the final article raised some critical questions on the influence of riffle-pools on the larger scale properties of river systems. Specifically, we explored a possible link between the sorting mechanism that we identified in the pool-head and the sediment budget of the stream. The long term studies on the Alt Dubhaig [*Hoey and Ferguson*, 1997; *Ferguson and Wathen*, 1998; *Ferguson and Hoey*, 2002] have documented downstream fining in a system in which riffle-pools are common. Riffle-pools appear to represent a sediment sorting mechanism due to the trapping of large sediments in the riffle and pool-head. Sediment sorting is expected to accelerate the rate of downstream fining [*Hoey and Ferguson*, 1994]. Useful laboratory experiments and/or simulations using the ROQ-B model could be designed to test the role of riffle-pools in downstream fining.

Finally, a key remaining question is the generality of the results. Our principal field results were based on a single site where the pool location was forced by a large tree. It is important to establish how the flow and sediment dynamics differ in other systems such as freely formed pools in straight and meandering systems. Data from a second field site, the Ditton River, was gathered as part of this thesis. Due to the wealth of information obtained at Moras Creek, we have not fully investigated the second site. It is 14 m wide with a similar bed particle size distribution as Moras Creek. We sampled water velocity over a range of discharges but were not able to measure during the bankfull flow due to safety concerns. We have plotted the integral time scale of the streamwise component (ITS_u) versus the streamwise velocity (U) in Figure 8.2. For comparison, we show the dashed lines that we drew by eye to fit the range of data in Moras Creek (Figure 6.7). Data from the Ditton River do not fit within the envelope of data from Moras Creek. At a given velocity, ITS_u is generally higher in the Ditton River. This suggests a relation between coherent scales and the size of the river. In spite of the difference in magnitude between systems, the slope of the relation between ITS_u and U is similar. We could therefore

improve our understanding of the relations between velocity, coherence, and morphology by comparing results between a variety of systems.

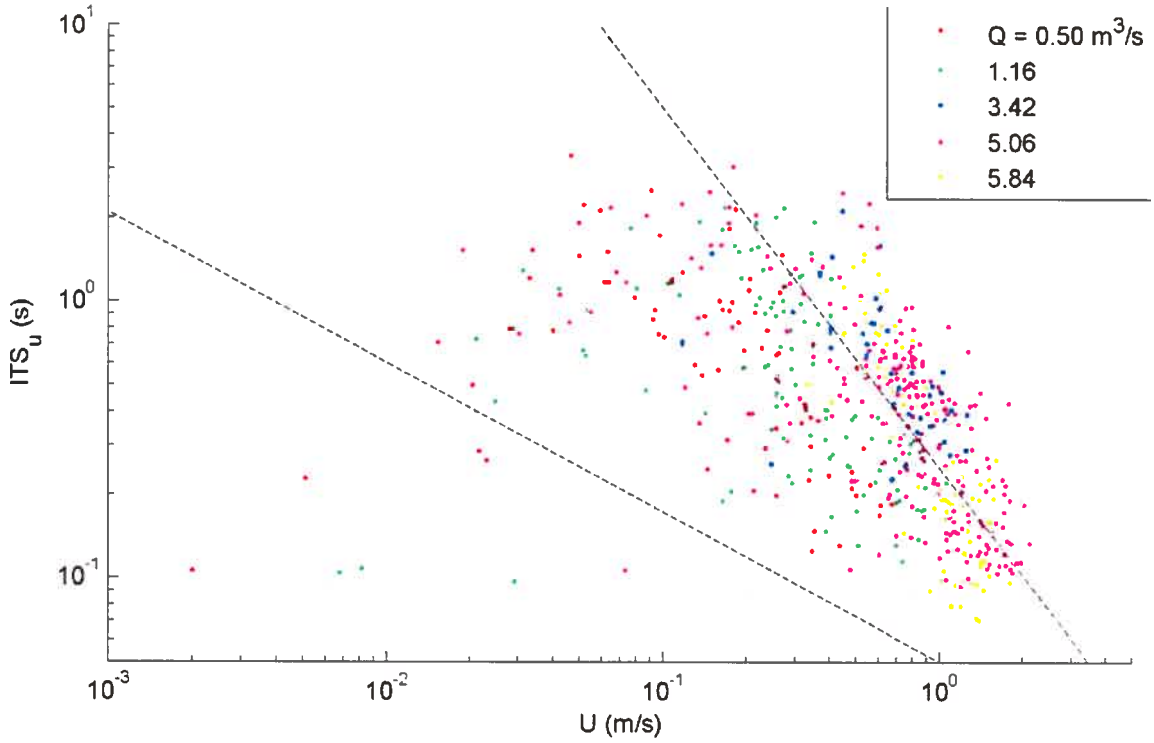

Figure 8.2 - Integral time scale of the streamwise velocity (ITSu) versus the streamwise velocity (U) at five discharges in the Ditton River. Dashed lines represent the envelope of data from Moras Creek (see Figure 6.7)

In spite of the variability between sites, the mechanisms identified in this thesis provide a framework for future study of other types of riffle-pool systems. These directions for future work are based on the insights gained through the research of this thesis. It is important to note that our results have clarified some of the controversy as to the mechanisms involved in riffle-pool formation and maintenance. For instance, it has detailed the interplay between flow velocity reversal, turbulence generation, and bed morphology. Such an insight would not have been possible without the intense observation, both in time and space, of a single site. This limited the generality but provided a fresh view of river dynamics led to the development of a model that demonstrates the implications of our observations and interpretation.

BIBLIOGRAPHY

Abbott, J. E., and J. R. D. Francis (1977), Saltating and suspension trajectories of solic grains in a water stream, *Philosophical Transactions of the Royal Society of London A*, *284A*, 225-254.

Achenbach, E. (1974), Vortex shedding from spheres, *Journal of Fluid Mechanics*, *62*, 209-221.

Afzalimehr, H., and F. Anctil (1999), Velocity distribution and shear velocity behaviour of decelerating flows over a gravel bed, *Canadian Journal of Civil Engineering*, *26*, 468-475.

Anderson, R. S. (1990), Eolian ripples as examples of self-organization in geomorphological systems, *Earth Science Reviews*, *29*, 77-96.

Anderson, R. S., and K. L. Bunas (1993), Grain-size segregation and stratigraphy in aeolian ripples modeled with a cellular-automaton, *Nature*, *365*, 740-743.

Andrews, E. D. 1979. Hydraulic adjustment of the East Fork River, Wyoming to the supply of sediment. Pages 69-94 *in* D. D. Rhodes and G. P. Williams, editors. Adjustments of the Fluvial Proceedings. Kendall Hunt Publishing Company, Binghampton, New York.

Andrews, E. D. (1994), Marginal bed load transport in a gravel-bed stream, Sagehen Creek, California, *Water Resources Research*, *30*, 2241-2250.

Anhert, F. (1994), Modelling the development of non-periglacial sorted nets, *Catena*, *23*, 43-63.

Aubertine, C. D., and J. K. Eaton (2005), Turbulence development in a non-equilibrium turbulent boundary layer with mild adverse pressure gradient, *Journal of Fluid Mechanics*, *532*, 345-364.

Aubrey, D. G., and J. H. Trowbridge (1985), Kinematic and dynamic estimates from electromagnetic current meter data, *Journal of Geophysical Research*, *90*, 9137-9146.

Azad, R. S. (1996), Turbulent flow in a conical diffuser: A review, *Experimental Thermal and Fluid Science*, *13*, 318-337.

Azad, R. S., and S. Z. Kassab (1989), Turbulent-Flow in a Conical Diffuser - Overview and Implications, *Physics of Fluids a-Fluid Dynamics*, *1*, 564-573.

Baas, A. C. W. (2002), Chaos, fractals and self-organization in coastal geomorphology: simulating dune landscapes in vegetated environments, *Geomorphology*, *48*, 309-328.

Bagnold, R. A. (1966), An approach to the sediment transport problem from general physics, *United States Geological Survey Circular*, *422-I*, 37 p.

Bagnold, R. A. (1980), An empirical correlation of bedload transprt rates in flumes and natural rivers, *Proceedings of the Royal Society of London*, *372*, 453-473.

Bathurst, J. C. (1979), Distribution of boundary shear stress in rivers, in *Adjustments of the Fluvial System,* edited by D. D. Rhodes and G. P. Williams, 95-116, Kendall/Hunt Publishing Company.

Bennett, S. J., and J. L. Best (1995), Mean Flow and Turbulence Structure over Fixed, 2-Dimensional Dunes - Implications for Sediment Transport and Bedform Stability, *Sedimentology*, *42*, 491-513.

Bennett, S. J., and J. S. Bridge (1995), An Experimental-Study of Flow, Bedload Transport and Bed Topography under Conditions of Erosion and Deposition and Comparison with Theoretical-Models, *Sedimentology*, *42*, 117-146.

Best, J. (2005), The fluid dynamics of river dunes: A review and some future research directions, *Journal of Geophysical Research-Earth Surface*, *110*, F.

Best, J., and R. A. Kostachuck (2002), An experimental study of turbulent flow over a low-angle dune, *Journal of Geophysical Research*, *107*, 3135.

Best, J. L. (1992), On the entrainment of sediment and initiation of bed defects: insights from recent developments within turbulent boundary research, *Sedimentology*, *39*, 797-811.

Best, J. L. (1996), The fluid dynamics of small-scale alluvial bedforms, in *Advances in Fluvial Dynamics and Stratigraphy,* edited by P. Carling and M. R. Dawson, 67-125, Wiley, Chicester, U.K.

Bhowmik, N. G., and M. Demissie (1982), Bed material sorting in pools and riffles, *Journal of the Hydraulic Division*, *108*, 1227-1231.

Biron, P. M., C. Robson, M. F. Lapointe, and S. J. Gaskin (2004), Comparing different methods of bed shear stress estimates in simple and complex flow fields, *Earth Surface Processes and Landforms*, *29*, 1403-1415.

Bogard, D. G., and W. G. Tiederman (1986), Burst detection with single-point velocity measurements, *Journal of Fluid Mechanics*, *162*, 339-413.

Booker, D. J., D. A. Sear, and A. J. Payne (2001), Modelling three-dimensional flow structures and patterns of boundary shear stress in a natural pool-riffle sequence, *Earth Surface Processes and Landforms*, *26*, 553-576.

Brush, L. M. (1961), Drainage basins, channels, and flow characteristics, *United States Geological Survey Circular*, *282-F*, 175 p.

Bryan, K. R., K. P. Black, and R. M. Gorman (2003), Spectral estimates of dissipation rate within and near the surf zone, *Journal of Physical Oceanography*, *33*, 979-993.

Buffin-Bélanger, T., and A. G. Roy (1998), Effects of a pebble cluster on the turbulent structure of a depth-limited flow in a gravel-bed river, *Geomorphology*, *25*, 249-267.

Buffin-Bélanger, T., and A. G. Roy (2005), 1 min in the life of a river: selecting the optimal record length for the measurement of turbulence in fluvial boundary layers, *Geomorphology*, *68*, 77-94.

Buffin-Bélanger, T., A. G. Roy, and A. D. Kirkbride (2000), On large-scale flow structures in a gravel-bed river, *Geomorphology*, *32*, 417-435.

Buffington, J. M., T. E. Lisle, R. D. Woodsmith, and S. Hilton (2002), Controls on the size and occurrence of pools in coarse-grained forest rivers, *River Research and Applications*, *18*, 507-531.

Cabrera, R., K. Deines, B. Brumley, and E. Terray. 1987. Development of a practical coherent Acoustic Doppler Current Profiler. Pages 93-97 *in* Oceans. IEEE Oceanic Engineering Society, Halifax, N.S., Canada.

Campbell, A. J., and R. C. Sidle (1985), Bedload transport in a pool-riffle sequence of a coastal Alaska stream, *Water Resources Bulletin*, *21*, 579-590.

Cao, Z. X., P. Carling, and R. Oakey (2003), Flow reversal over a natural pool-riffle sequence: A computational study, *Earth Surface Processes and Landforms*, *28*, 689-705.

Carling, P. (1991), An appraisal of the velocity-reversal hypothersis for stable pool-riffle sequences in the River Severn, England, *Earth Surface Processes and Landforms*, *16*, 19-31.

Carling, P. A. (1999), Subaqueous gravel dunes, *Journal of Sedimentary Research*, *69*, 534-545.

Carling, P. A., Z. X. Cao, M. J. Holland, D. A. Ervine, and K. Babaeyan-Koopaei (2002), Turbulent flow across a natural compound channel, *Water Resources Research*, *38*,

Carling, P. A., A. Kesley, and M. S. Glaister (1992), Effect of bed roughness, particle shape and orientation on initial motion criteria, in *Dynamics of Gravel Bed Rivers,* edited by P. Billi, R. D. Hey, C. R. Thorne, and P. Tacconi, 23-39, John Wiley & Sons Ltd., Wallingford, U.K.

Carling, P. A., J. J. Williams, E. Golz, and A. D. Kelsey (2000), The morphodynamics of fluvial sand dunes in the River Rhine, near Mainz, Germany. II. Hydrodynamics and sediment transport, *Sedimentology*, *47*, 253-278.

Carling, P. A., and N. Wood (1994), Simulation of flow over pool-riffle topography: a consideration of the velocity reversal hypothesis, *Earth Surface Processes and Landforms*, *19*, 319-332.

Chang, H. H. (1979), Minimum stream power and river channel patterns, *Journal of Hydrology*, *41*, 303-327.

Chartrand, S. M., and P. J. Whiting (2000), Alluvial architecture in headwater streams with special emphasis on step-pool topography, *Earth Surface Processes and Landforms*, *25*, 583-600.

Church, M. (1972), Baffin Island sandurs: a study in Arctic fluvial processes, *Geological Survey of Canada Bulletin*, *216*, 208 pp.

Church, M., and M. A. Hassan (2002), Mobility of bed material in Harris Creek, *Water Resources Research*, *38*, 1237.

Church, M., M. A. Hassan, and J. Wolcott (1998), Stabilizing self-organized structures in gravel-bed stream channels: Field and experimental observations, *Water Resources Research*, *34*, 3169-3179.

Church, M., and D. Jones (1982), Channel bars in gravel-bed rivers, in *Gravel-bed Rivers,* edited by R. D. Hey, J. C. Bathurst, and C. R. Thorne, 291-338, Wiley, Chicester, UK.

Clifford, N. J. (1993), Differential bed sedimentology and the maintenance of riffle-pool sequences, *Catena*, *20*, 447-468.

Clifford, N. J. (1993), Formation of riffle-pool sequences: field evidence for an autogenetic process, *Sedimentary Geology*, *85*, 39-51.

Clifford, N. J. (1996), Morphology and stage-dependent flow structure in a gravel-bed river, in *Coherent Flow Structures in Open Channels,* edited by P. J. Ashworth, S. J. Bennett, J. L. Best, and S. J. McLelland, 545-566, Wiley, Wallingford, U.K.

Clifford, N. J., and J. R. French (1993), Monitoring and analysis of turbulence in geophysical boundaries: some analytical and conceptual issues, in *Turbulence: Perspectives on Flow and Sediment Transport,* edited by N. J. Clifford, J. R. French, and J. Hardistry, 93-119, Wiley, Chicester, UK.

Clifford, N. J., and K. S. Richards (1992), The reversal hypothesis and the maintenance of riffle-pool sequences: a review and field appraisal, in *Lowland Floodplain Rivers: Geomorphological Perspectives,* edited by P. Carling and G. E. Petts, 43-70, Wiley, Chichester, UK.

Clifford, N. J., A. Robert, and K. S. Richards (1992), Estimation of flow resistance in gravel-bedded rivers: a physical explanation of the multiplier of roughness length, *Earth Surface Processes and Landforms*, *17*, 111-126.

Coles, D. (1956), The law of the wake in the turbulent boundary layer, *Journal of Fluid Mechanics*, *1*, 191-226.

Colombini, M., G. Seminara, and M. Tubino (1987), Finite-Amplitude Alternate Bars, *Journal of Fluid Mechanics*, *181*, 213-232.

Corino, E. R., and R. S. Brodkey (1969), A visual investigation of the wall region in turbulent flow, *Journal of Fluid Mechanics*, *37*, 1-30.

Davies, T. R. H., and A. J. Sutherland (1983), Extremal hypotheses for river behaviour, *Water Resources Research*, *19*, 141-148.

de Jong, C., and P. Ergenzinger (1995), The interrelations between mountain valley form and river-bed arrangement, in *River Geomorphology,* edited by E. J. Hickin, 55-91, Wiley, Chicester, U.K.

Dietrich, W. E., J. W. Kirchner, H. Ikeda, and F. Iseya (1989), Sediment Supply and the Development of the Coarse Surface-Layer in Gravel-Bedded Rivers, *Nature*, *340*, 215-217.

Dietrich, W. E., J. D. Smith, and T. Dunne (1979), Flow and sediment transport in a sand bedded meander, *Journal of Geology*, *87*, 305-315.

Dinehart, R. L. (1992), Evolution of Coarse Gravel Bed Forms - Field-Measurements at Flood Stage, *Water Resources Research*, *28*, 2667-2689.

Drake, T. G., and J. Calantoni (2001), Discrete particle model for sheet flow sediment transport in the nearshore, *Journal of Geophysical Research-Oceans*, *106*, 19859-19868.

Drake, T. G., R. L. Shreve, W. E. Dietrich, P.J.Whiting, and L. Leopold (1988), Bedload transport of fine gravel observed by motion picture photography, *Journal of Fluid Mechanics*, *19*, 2193-2217.

Eaton, B. C., and M. Lapointe (2001), Effects of large floods on sediment transport and reach morphology in the cobble-bed Sainte Marguerite River, *Geomorphology*, *40*, 291-309.

Edo, K., and K. Suzuki (2003), Preferable summering habitat of returning adult masu salmon in the natal stream, *Ecological Research*, *18*, 783-791.

Einstein, H. A. (1937), Die eichung des im Rhein verwendeten geschiebefangers, *Schweiz. Bauztg.*, *110*, 29-32.

Elgar, S., B. Raubenheimer, and R. T. Guza (2001), Current meter performance in the surf zone, *Journal of Atmospheric and Oceanic Technology*, *18*, 1735-1746.

Elgar, S., B. Raubenheimer, and R. T. Guza (2005), Quality control of Acoustic Doppler Velocimeter data in the surfzone, *Measurement Science & Technology*, *16*, 1889-1893.

Emery, J. C., A. M. Gurnell, N. J. Clifford, G. E. Petts, I. P. Morrissey, and P. J. Soar (2003), Classifying the hydraulic performance of riffle-pool bedforms for habitat assessment and river rehabilitation design, *River Research and Applications*, *19*, 533-549.

Falco, R. E. (1977), Coherent motions in the outer region of turbulent boundary layers, *Physics of Fluids*, *20*, S124-S132.

Ferguson, R. I., and T. B. Hoey (2002), Long-term slowdown of river tracer pebbles: Generic models and implications for interpreting short-term tracer studies, *Water Resources Research*, *38*, 1142, 1110.1029/2001WR000637.

Ferguson, R. I., and S. J. Wathen (1998), Tracer-pebble movement along a concave river profile: Virtual velocity in relation to grain size and shear stress, *Water Resources Research*, *34*, 2031-2038.

Finelli, C. M., D. D. Hart, and D. M. Fonseca (1999), Evaluating the spatial resolution of an Acoustic Doppler Velocimeter and the consequences for measuring near-bed flows, *Limnology and Oceanography*, *44*, 1793-1801.

Frisch, U. (1995), *Turbulence: The Legacy of A.N. Kolmogorov*, 296 pp., Cambridge University Press, Cambridge, U.K.

Furbish, D. J. (1991), Spatial autoregressive structure in meander evolution, *Geological Society of America Bulletin*, *103*, 1576-1589.

Garcia, C., J. B. Laronne, and M. Sala (1999), Variable source areas of bedload in a gravel-bed stream, *Journal of Sedimentary Research*, *69*, 27-31.

Garcia, C. M., M. I. Cantero, Y. Nino, and M. H. Garcia (2005), Turbulence measurements with Acoustic Doppler Velocimeters, *Journal of Hydraulic Engineering*, *131*, 1062-1073.

Gomez, B., and M. Church (1989), An assessment of bed load sediment transport formulae for gravel bed rivers, *Water Resources Research*, *25*, 1161-1186.

Goring, D. G., and V. I. Nikora (2002), Despiking Acoustic Doppler Velocimeter data, *Journal of Hydraulic Engineering*, *128*, 117-126.

Grant, G. E., S. Swanson, and M. G. Wolman (1990), Pattern and origin of stepped-bed morphology in high-gradient stream, Western Cascades, Oregon, *Geologic Society of America Bulletin*, *102*, 340-352.

Grass, A. J. (1971), Structural features of turbulent flow over smooth and rough boundaries, *Journal of Fluid Mechanics*, *50*, 233-255.

Grass, A. J. 1982. The influence of boundary layer turbulence on the mechanics of sediment transport. Pages 3-18 *in* B. M. Sumer and A. Müller, editors. Euromech 156: Mechanics of Sediment Transport. Balkema, Rotterdam.

Grass, A. J., and M. Mansour-Tehrani (1996), Generalized scaling of coherent bursting structures in the near-wall region of turbulent flow over smooth and rough boundaries, in *Coherent Flow Structures in Open Channels,* edited by P. J. Ashworth, S. J. Bennett, J. L. Best, and S. J. McLelland, 41-61, Wiley, Chicester, U.K.

Gregory, K. J., A. M. Gurnell, C. T. Hill, and S. Tooth (1994), Stability of the Pool Riffle Sequence in Changing River Channels, *Regulated Rivers-Research & Management*, *9*, 35-43.

Grinstein, F. F., and C. R. DeVore (1996), Dynamics of coherent structures and transition to turbulence in free square jets, *Physics of Fluids*, *8*, 1237-1251.

Guha, R. K., and J. Z. Wang (2002), Improving web access efficiency using P2P proxies, in *Distributed Computing, Proceedings,*24-34.

Guza, R. T., M. C. Clifton, and F. Rezvani (1988), Field intercomparisons of Electromagnetic Current Meters, *Journal of Geophysical Research*, *93*, 9302-9314.

Ha, H. K., and S. K. Chough (2003), Intermittent turbulent events over sandy current ripples: a motion-picture analysis of flume experiments, *Sedimentary Geology*, *161*, 295-308.

Habersack, H. M. (2001), Radio-tracking gravel particles in a large braided river in New Zealand: a field test of the stochastic theory of bed load transport proposed by Einstein, *Hydrological Processes*, *15*, 377-391.

Harper, D., M. Ebrahimnezhad, and F. C. I. Cot (1998), Artificial riffles in river rehabilitation: setting the goals and measuring the successes, *Aquatic Conservation-Marine and Freshwater Ecosystems*, *8*, 5-16.

Hassan, M., and R. D. Woodsmith (2004), Bedload transport in an obstruction-formed pool in a forest gravelbed stream, *Geomorphology*, *58*, 203-221.

Hassan, M. A., and M. Church (1992), Virtual rate and mean distance of travel of individual clasts in gravel bed channels, *Earth Surface Processes and Landforms*, *17*, 617-627.

Hassan, M. A., and M. Church (2000), Experiments on surface structure and partial sediment transport on a gravel bed, *Water Resources Research*, *36*, 1885-1895.

Hassan, M. A., and I. Reid (1990), The influence of microform bed roughness elements on flow and sediment transport in gravel bed rivers, *Earth Surface Processes and Landforms*, *15*, 739-750.

Henderson (1966), *Open Channel Flow*, 522 pp., Macmillan Publishing Co. Ltd., New York.

Heritage, G. L., and D. J. Milan (2004), A conceptual model of the role of excess energy in the maintenance of a riffle-pool sequence, *Catena*, *58*, 235-257.

Hirsch, P. J., and A. D. Abrahams (1981), The properties of bed sediments in pools and riffles, *Journal of Sedimentary Petrology*, *51*, 757-760.

Hoey, T. B., and R. I. Ferguson (1997), Controls of strength and rate of downstream fining above a river base level, *Water Resources Research*, *33*, 2601-2608.

Horton, R. E. (1945), Erosional development of streams, *Bulletin Geological Socity of America*, *56*, 286-307.

Inoue, M., and M. Nunokawa (2002), Effects of longitudinal variations in stream habitat structure on fish abundance: an analysis based on subunit-scale habitat classification, *Freshwater Biology*, *47*, 1594-1607.

Jackson, R. G. (1976), Sedimentological and fluid-dynamic implications of the turbulent bursting phenomenon in geophysical flows, *Journal of Fluid Mechanics*, *77*, 531-560.

Jackson, W. L., and R. L. Beschta (1982), A model of two-phase bedload transport in an Oregon coast range stream, *Earth Surface Processes and Landforms*, *7*, 517-527.

Jiang, Z., and P. K. Haff (1993), Multiparticle simulation methods applied to the micromechanics of bed load transport, *Water Resources Research*, *29*, 399-412.

Judson, O. P. (1994), The Rise of the Individual-Based Model in Ecology, *Trends in Ecology & Evolution*, *9*, 9-14.

Keller, E. A. (1971), Areal sorting of bed material: the hypothesis of velocity reversal, *Geological Society of America Bulletin*, *83*, 915-918.

Keller, E. A. (1972), Development of alluvial stream channels: A five stage model, *Geological Society of America Bulletin*, *83*, 1531-1536.

Keller, E. A., and J. L. Florsheim (1993), Velocity-reversal hypothesis: a model approach, *Earth Surface Processes and Landforms*, *18*, 733-740.

Keller, E. A., and W. N. Melhorn (1978), Rhythmic spacing and origin of pools and riffles, *Geological Society of America Bulletin*, *89*, 723-730.

Kellerhals, R., and M. Church (1989), The morphology of large rivers: characterization and mangement, in *Proceedings of the International Large River Symposium*, edited by D. P. Dodge, 31-48, Canadian Special Publications of Fisheries and Aquatic Science 106.

Kessler, M. A., and B. T. Werner (2003), Self-organization of sorted patterned ground, *Science*, *299*, 380-383.

Kim, S. C., C. T. Friedrichs, J. P. Y. Maa, and L. D. Wright (2000), Estimating bottom stress in tidal boundary layer from Acoustic Doppler Velocimeter data, *Journal of Hydraulic Engineering*, *126*, 399-406.

Kirkbride, A. D. (1993), Observations of the influence of bed roughness on turbulence structure in depth limited flows over gravel beds, in *Turbulence, Perspectives on Flow and Sediment Transport*, edited by N. J. Clifford, J. R. French, and J. Hardistry, 185-196, John Wiley & Sons, Chicester.

Kirkbride, A. D., and R. Ferguson (1995), Turbulent flow structure in a gravel-bed river: Markov chain analysis of the fluctuating velocity profile, *Earth Surface Processes and Landforms*, *20*, 721-733.

Kironoto, B. A., and W. H. Graf (1995), Turbulence characteristics in rough non-uniform open-channel flow, *Proceedings of the Institution of Civil Engineers-Water Maritime and Energy*, *112*, 336-348.

Kline, S. J., W. C. Reynolds, F. A. Schraub, and P. W. Runstadler (1967), The structure of turbulent boundary layers, *Journal of Fluid Mechanics*, *95*, 741-773.

Kolmogorov, A. N. (1941), Dissipation of energy in locally isotropic turbulence in an incompressible viscous liquid, *Dokl. Akad. Nauk SSSR*, *30*, 299-303.

Komar, P. D. (1996), Entrainment of sediments from deposits of mixed grain sizes and densities, in *Advances in Fluvial Dynamics and Stratigraphy*, edited by P. A. Carling and M. R. Dawson, 127-181, Wiley, Chicester, U.K.

Kostachuck, R. A., and M. Church (1993), Macroturbulence generated by dunes: Fraser River, Canada, *Sedimentary Geology*, *85*, 25-37.

Kostaschuk, R. (2000), A field study of turbulence and sediment dynamics over subaqueous dunes with flow separation, *Sedimentology*, *47*, 519-531.

Kostaschuk, R., and P. Villard (1996), Flow and sediment transport over large subaqueous dunes: Fraser River, Canada, *Sedimentology*, *43*, 849-863.

Lamarre, H., B. J. MacVicar, and A. G. Roy (2005), Using Passive Integrated Transponder (PIT) tags to investigate sediment transport in gravel-bed rivers, *Journal of Sedimentary Research*, *75*, 720-725.

Landry, W., and B. T. Werner (1994), Computer-Simulations of Self-Organized Wind Ripple Patterns, *Physica D*, *77*, 238-260.

Lane, S. N., P. M. Biron, K. F. Bradbrook, J. B. Butler, J. H. Chandler, M. D. Crowell, S. J. McLelland, K. S. Richards, and A. G. Roy (1998), Three-dimensional measurement of river channel flow processes using Acoustic Doppler Velocimetry, *Earth Surface Processes and Landforms*, *23*, 1247-1267.

Lane, S. N., and K. S. Richards (1997), Linking river channel form and process: time, space and causality revisited, *Earth Surface Processes and Landforms*, *22*, 249-260.

Lane, S. N., K. S. Richards, and J. Warburton (1993), Comparison between high frequency velocity records obtained with spherical nad discoidal Electromagnetic Current Meters, in *Turbulence: Perspectives on Flow and Sediment Transport*, edited by N. J. Clifford, J. R. French, and J. Hardistry, 121-163, Wiley, Chicester, U.K.

Langbein, W. B., and L. B. Leopold (1968), River channel bars and dunes - theory of kinematic waves, *United States Geological Society Professional Paper*, *422-L*, 20.

Lapointe, M. F., B. deSerres, P. Biron, and A. G. Roy (1996), Using spectral analysis to detect sensor noise and correct turbulence intensity and shear stress estimates from EMCM flow records, *Earth Surface Processes and Landforms*, *21*, 195-203.

Laronne, J. B., and M. A. Carson (1976), Interrelationships between bed morphology and bed material tranpsort for a small gravel bed channel, *Sedimentology*, *23*, 67-85.

Lawless, M., and A. Robert (2001), Three-dimensional flow structure around small-scale bedforms in a simulated gravel-bed environment, *Earth Surface Processes and Landforms*, *26*, 507-522.

Leeder, M. R. (1983), On the interactions between turbulent flow, sediment transport and bedform mechanics in channelized flows, *International Association of Sedimentologists Special Publication*, *6*, 5-18.

Lemmin, U., and R. Lhermitte (1999), ADV measurements of turbulence: Can we improve their interpretation? Discussion, *Journal of Hydraulic Engineering*, *125*, 987-988.

Leopold, L. B. (1982), Water surface topography in river channels and implications for meander development, in *Gravel-bed Rivers*, edited by R. D. Hey, J. C. Bathurst, and C. R. Thorne, 359-383, Wiley, Wallingford, U.K.

Leopold, L. B., and M. G. Wolman (1957), River channel patterns: braided, meandering, and straight, *Geological Survey Professional Paper*, *282-B*, 85 p.

Leopold, L. B., and M. G. Wolman (1960), River meanders, *Bulletin Geological Society of America*, *71*, 769-794.

Lhermitte, R., and U. Lemmin (1994), Open-channel flow and turbulence measurement by high-resolution Doppler sonar, *Journal of Atmospheric and Oceanic Technology*, *11*, 1295-1308.

Lisle, T. E. (1979), A sorting mechanism for a riffle-pool sequence, *Geologic Society of America Bulletin*, *90*, 1142-1157.

Lisle, T. E. (1982), Effects of aggradation and degradation on riffle-pool morphology in natural gravel channels, northwestern California, *Water Resources Research*, *18*, 1643-1651.

Lisle, T. E. (1986), Stabilization of a gravel channel by large streamside obstructions and bedrock bends, Jacoby Creek, northwest California, *Geological Society of America Bulletin*, *97*, 999-1011.

Lisle, T. E. (1995), Particle size variations between bedload and bed material in natural gravel-bed channels, *Water Resources Research*, *31*, 1107-1118.

Lisle, T. E., and M. Church (2002), Sediment transport-storage relations for degrading, gravel bed channels, *Water Resources Research*, *38*,

Lisle, T. E., and S. Hilton (1992), The volume of fine sediment in pools: an index of sediment supply in gravel bed streams, *Water Resources Bulletin*, *28*, 371-383.

Lisle, T. E., and S. Hilton (1999), Fine bed material in pools of natural gravel bed channels, *Water Resources Research*, *35*, 1291-1304.

Lisle, T. E., H. Ikeda, and F. Iseya (1991), Formation of stationary alternate bars in a steep channel with mixed-size sediment: A flume experiment, *Earth Surface Processes and Landforms*, *16*, 463-469.

Lisle, T. E., F. Iseya, and H. Ikeda (1993), Response of a Channel with Alternate Bars to a Decrease in Supply of Mixed-Size Bed-Load - a Flume Experiment, *Water Resources Research*, *29*, 3623-3629.

Lisle, T. E., J. M. Nelson, J. Pitlick, M. A. Madej, and B. L. Barkett (2000), Variability of bed mobility in natural, gravel-bed channels and adjustments to sediment load at local and reach scales, *Water Resources Research*, *36*, 3743-3755.

Lu, S. S., and W. W. Willmarth (1973), Measurements of the structure of the Reynolds stress in a turbulent boundary layer, *Journal of Fluid Mechanics*, *60*, 481-511.

Luchick, T. S., and W. G. Tiederman (1987), Timescale and structure of ejections and bursts in turbulent channel flows, *Journal of Fluid Mechanics*, *174*, 529-552.

Maassen, S. R., H. J. H. Clercx, and G. J. F. van Heijst (2002), Self-organization of quasi-two-dimensional turbulence in stratified fluids in square and circular containers, *Physics of Fluids*, *14*, 2150-2169.

Maassen, S. R., H. J. H. Clercx, and G. J. F. Van Heijst (2003), Self-organization of decaying quasi-two-dimensional turbulence in stratified fluid in rectangular containers, *Journal of Fluid Mechanics*, *495*, 19-33.

Madej, M. A. (1999), Temporal and spatial variability in thalweg profiles of a gravel-bed river, *Earth Surface Processes and Landforms*, *24*, 1153-1169.

Madej, M. A. (2001), Development of channel organization and roughness following sediment pulses in single-thread, gravel bed rivers, *Water Resources Research*, *37*, 2259-2272.

Malanson, G. P. (1999), Considering Complexity, *Annals of the Association of American Geographers*, *89*, 746-753.

Malmaeus, J. M., and M. A. Hassan (2002), Simulation of individual particle movement in a gravel streambed, *Earth Surface Processes and Landforms*, *27*, 81-97.

Markham, A. J., and C. R. Thorne (1992), Geomorphology of gravel-bed river bends, in *Dynamics of Gravel-Bed Rivers,* edited by P. Billi, R. D. Hey, C. R. Thorne, and P. Taconi, 433-450, Wiley, Chicester, UK.

Marsh-McBirney (1994), *Instruction Manual 500 series Special Products 4-in-1 Current Meter*, 42 pp., Frederick, MD.

Matthes, G. H. (1947), Macroturbulence in natural stream flow, *Transactions, American Geophysical Union*, *28*, 255-262.

McEwan, I. K., H. M. Habersack, and J. G. C. Heald (2000), Discrete particle modelling and active tracers: New techniques for studying sediment transport as a lagrangian phenomenon, in *Gravel-Bed Rivers V*, edited by M. P. Mosley, 339-367, New Zealand Hydrological Society, Wellington, N.Z.

McLelland, S. J., and A. P. Nicholas (2000), A new method for evaluating errors in high-frequency ADV measurements, *Hydrological Processes*, *14*, 351-366.

McQuivey, R. S. (1973), Summary of turbulence data from rivers, conveyance channels and laboratory flumes, *United States Geological Survey Circular*, *802B*,

McWilliams, J. C. (1984), The emergence of isolated coherent vortices in turbulent-flow, *Journal of Fluid Mechanics*, *146*, 21-43.

Meade, R. H. (1985), Wavelike movement of bedload sediment in the East Fork River, Wyoming, *Annals of the Association of American Geographers*, *78*, 520-533.

Milan, D. J., G. L. Heritage, A. R. G. Large, and M. E. Charlton (2001), Stage dependent variability in tractive force distribution through a riffle-pool sequence, *Catena*, *44*, 85-109.

Milne, J. A. (1982), Bed-material size and the riffle-pool sequence, *Sedimentology*, *29*, 267-278.

Moir, H. J., C. N. Gibbins, C. Soulsby, and J. Webb (2004), Linking channel geomorphic characteristics to spatial patterns of spawning activity and discharge use by Atlantic salmon (Salmo salar L.), *Geomorphology*, *60*, 21-35.

Momiji, H., R. Carretero-Gonzalez, S. R. Bishop, and A. Warren (2000), Simulation of the effect of wind speedup in the formation of transverse dune fields, *Earth Surface Processes and Landforms*, *25*, 905-918.

Monin, A. S., and A. M. Yaglom (1981), *Statistical Fluid Mechanics: Mechanics of Turbulence*, 900 pp., MIT Press, Cambridge, Massachusetts.

Montgomery, D. R., and J. M. Buffington (1997), Channel reach morphology in mountain drainage basins, *Geological Society of America Bulletin*, *109*, 596-611.

Montgomery, D. R., J. M. Buffington, R. D. Smith, K. M. Schmidt, and G. Pess (1995), Pool spacing in forest channels, *Water Resources Research*, *31*, 1097-1105.

Murray, A. B. (2003), Contrasting the goals, strategies, and predictions associated with simplified numerical models and detailed simulations, in *Prediction in Geomorphology,* edited by P. R. Wilcock and R. M. Iverson, 151-165, AGU, Washington, D.C.

Murray, A. B., and C. Paola (1994), A Cellular-Model of Braided Rivers, *Nature*, *371*, 54-57.

Myers, T., and S. Swanson (1997), Variability of pool characteristics with pool type and formative feature on small Great Basin rangeland streams, *Journal of Hydrology*, *201*, 62-81.

Naden, P. (1987), Modelling gravel-bed topography from sediment transport, *Earth Surface Processes and Landforms*, *12*, 353-367.

Naden, P. S., and A. C. Brayshaw (1987), Small and medium scale bedforms in gravel-bed rivers, in *River Channels: Environment and Process,* edited by K. S. Richards, 249-271, Blackwell, Oxford, U.K.

Nelson, J. M., S. R. McClean, and S. R. Wolfe (1993), Mean flow and turbulence fields over two-dimensional bed forms, *Water Resources Research*, *29*, 3935-3953.

Nelson, J. M., R. L. Shreve, S. R. McClean, and T. G. Drake (1995), Role of near-bed turbulence structure in bed load transport and bed form mechanics, *Water Resources Research*, *31*, 2071-2086.

Newbury, R., and M. Gaboury (1993), Exploration and rehabilitation of hydraulic habitats in streams using principles of fluvial behaviour, *Freshwater Biology*, *29*, 195-210.

Nezu, I., and H. Nakagawa (1993), *Turbulence in Open-channel Flows*, 281 pp., A.A. Balkema, Rotterdam.

Nicholas, A. P. (2001), Computational fluid dynamics modelling of boundary roughness in gravel-bed rivers: An investigation of the effects of random variability in bed elevation, *Earth Surface Processes and Landforms*, *26*, 345-362.

Nikora, V. (1999), Origin of the "-1" spectral law in wall-bounded turbulence, *Physical Review Letters*, *83*, 734-736.

Nikora, V. 2005. Hydrodynamic effects in gravel-bed rivers: from micro- to macro- turbulence. Pages 1-42 *in* Gravel Bed Rivers VI, St. Jakob, Austria.

Nikora, V. I., and D. G. Goring (1998), ADV measurements of turbulence: Can we improve their interpretation?, *Journal of Hydraulic Engineering*, *124*, 630-634.

Nino, Y., A. Atala, M. Barahona, and D. Aracena (2002), Discrete particle model for analyzing bedform development, *Journal of Hydraulic Engineering*, *128*, 381-389.

Nino, Y., M. Garcia, and L. Ayala (1994), Gravel saltation 1: Experiments, *Water Resources Research*, *30*, 1907-1914.

O'Neill, M. P., and A. D. Abrahams (1984), Objective identification of pools and riffles, *Water Resources Research*, *20*, 921-926.

Paiement-Paradis, G., T. Buffin-Bélanger, and A. G. Roy (2003), Scalings for large turbulent flow structures in gravel-bed rivers, *Geophysical Research Letters*, *30*, 1773.

Paola, C., G. Parker, R. Seal, S. K. Sinha, J. B. Southard, and P. R. Wilcock (1992), Downstream Fining by Selective Deposition in a Laboratory Flume, *Science*, *258*, 1757-1760.

Parker, G., P. C. Klingeman, and D. G. MacLean (1982), Bedload and size distribution in paved gravel-bed streams, *Journal of the Hydraulics Division*, *108*, 544-571.

Parker, G., and C. M. Toro-Escobar (2002), Equal mobility of gravel in streams: The remains of the day, *Water Resources Research*, *38*, 1264, 1210.1029/2001WR000669.

Parrott, L., and R. Kok (2001), A generic primary producer model for use in ecosystem simulation, *Ecological Modelling*, *139*, 75-99.

Pender, G., T. B. Hoey, C. Fuller, and I. K. McEwan (2001), Selective bedload transport during the degradation of a well sorted graded sediment bed, *Journal of Hydraulic Research*, *39*, 269-277.

Petit, F. (1987), The relationship between shear stress and the shaping of the bed of a pebble-loaded river La Rulles - Ardenne, *Catena*, *14*, 453-468.

Priyadarshana, P. J. A., and J. C. Klewicki (2004), Study of the motions contributing to the Reynolds stress in high and low Reynolds number turbulent boundary layers, *Physics of Fluids*, *16*, 4586-4600.

Pyrce, R. S., and P. E. Ashmore (2003), The relation between particle path length distributions and channel morphology in gravel-bed streams: a synthesis, *Geomorphology*, *56*, 167-187.

Pyrce, R. S., and P. E. Ashmore (2005), Bedload path length and point bar development in gravel-bed river models, *Sedimentology*, *52*, 839-857, 810.1111/j.1365-3091.2005.00714.x.

Rathburn, S. L., and E. E. Wohl (2001), One-dimensional sediment transport modeling of pool recovery along a mountain channel after a reservoir sediment release, *Regulated Rivers-Research & Management*, *17*, 251-273.

Raudkivi, A. J. (1963), Study of sediment ripple formation, *Proceedings of the American Society of Civil Engineering*, *89*,

Rice, S., and M. Church (1998), Grain size along two gravel-bed rivers: Statistical variation, spatial pattern and sedimentary links, *Earth Surface Processes and Landforms*, *23*, 345-363.

Richards, K. S. (1976), The morphology of riffle-pool sequences, *Earth Surface Processes and Landforms*, *1*, 71-88.

Richards, K. S. (1978), Simulation of flow geometry in a riffle-pool stream, *Earth Surface Processes and Landforms*, *3*, 345-354.

Robert, A. (1990), Boundary roughness in coarse-grained channels, *Progress in Physical Geography*, *14*, 42-70.

Robert, A. (1997), Characteristics of velocity profiles along riffle-pool sequences and estimates of bed shear stress, *Geomorphology*, *19*, 89-98.

Robert, A., A. G. Roy, and B. deSerres (1996), Turbulence at a roughness transition in a depth limited flow over a gravel bed, *Geomorphology*, *16*, 175-187.

Rodriguez, A., A. Sanchez-Arcilla, J. M. Redondo, and C. Mosso (1999), Macroturbulence measurements with electromagnetic and ultrasonic sensors: a comparison under high-turbulent flows, *Experiments in Fluids*, *27*, 31-42.

Roy, A. G., and A. D. Abrahams (1980), Rhythmic spacing and origin of pools and rifflies: Discussion, *Geological Society of America Bulletin*, *91*, 248-250.

Roy, A. G., P. Biron, and B. DeSerres (1996), On the necessity of applying a rotation to instantaneous velocity measurements in river flows, *Earth Surface Processes and Landforms*, *21*, 817-827.

Roy, A. G., P. M. Biron, and M. F. Lapointe (1997), Implications of low-pass filtering on power spectra and autocorrelation functions of turbulent velocity signals, *Mathematical Geology*, *29*, 653-668.

Roy, A. G., T. Buffin-Bélanger, and S. Deland (1996), Scales of turbulent coherent flow structures in a gravel bed river, in *Coherent Flow Structures in Open Channels,* edited by P. J. Ashworth, S. J. Bennett, J. L. Best, and S. J. McLelland, 147-164, Wiley, Chicester, U.K.

Roy, A. G., T. Buffin-Belanger, H. Lamarre, and A. D. Kirkbride (2004), Size, shape and dynamics of large-scale turbulent flow structures in a gravel-bed river, *Journal of Fluid Mechanics*, *500*, 1-27.

Rutgers, M. A. (1998), Forced 2D turbulence: Experimental evidence of simultaneous inverse energy and forward enstrophy cascades, *Physical Review Letters*, *81*, 2244-2247.

Ryan, S. E., L. S. Porth, and C. A. Troendle (2002), Defining phases of bedload transport using piecewise regression, *Earth Surface Processes and Landforms*, *27*, 971-990, 910.1002/esp.1387.

Sano, M., and M. Shirakashi (1994), Turbulence Structure in a Periodically Diverging Converging Channel Flow, *Flow Measurement and Instrumentation*, *5*, 164-169.

Schindler, R. J., and A. Robert (2005), Flow and turbulence structure across the ripple-dune transition: an experiment under mobile bed conditions, *Sedimentology*, *52*, 627-649.

Schmeeckle, M. W., and J. M. Nelson (2003), Direct numerical simulation of bedload transport using a local, dynamic boundary condition, *Sedimentology*, *50*, 279-301.

Sear, D. A. (1996), Sediment transport processes in pool-riffle sequences, *Earth Surface Processes and Landforms*, *21*, 241-262.

Sekine, M., and H. Kikkawa (1992), Mechanics of saltating grains, *Journal of Hydraulic Engineering*, *118*, 536-558.

Seminara, G., M. Colombini, and G. Parker (1996), Nearly pure sorting waves and formation of bedload sheets, *Journal of Fluid Mechanics*, *312*, 253-278.

Shields, A. (1936), Anwendung der Aehnlichkeitsmechanik und der Turbulenzforschung auf die Geschiebebewegung (Application of similarity principles and turbulence research to bed-load movement), *Mitteilungen der Preuss Versuchsanst fur Wasserbau und Schiffbau*, *26*,

Shinbrot, T. (1997), Competition between randomizing impacts and inelastic collisions in granular pattern formation, *Nature*, *389*, 574-576.

Sidle, R. C. (1988), Bed load transport regime of a small forest stream, *Water Resources Research*, *24*, 207-218.

Simons, D. B., E. V. Richardson, and C. F. N. Jr. (1965), Bedload equation for ripples and dunes, *United States Geological Survey Circular*, *462H*, 9:00 PM.

Simpson, R. L. (1981), REVIEW - A review of some phenomena in turbulent flow separation, *Journal of Fluids Engineering*, *103*, 520-533.

Simpson, R. L. (1989), Turbulent boundary-layer separation, *Annual Review of Fluid Mechanics*, *21*, 205-234.

Smith, J. D. (1970), Stability of a sand bed subjected to a shear flow of low Froude number, *Journal of Geophysical Research*, *75*, 5928-5940.

Smyth, C., and A. E. Hay (2003), Near-bed turbulence and bottom friction during SandyDuck97, *Journal of Geophysical Research-Oceans*, *108*, 3197.

Song, T., and Y. M. Chiew (2001), Turbulence measurement in nonuniform open-channel flow using acoustic doppler velocimeter (ADV), *Journal of Engineering Mechanics*, *127*, 219-231.

Song, T., and W. H. Graf (1994), Non-uniform open channel flow over a rough bed, *Journal of Hydroscience and Hydraulic Engineering*, *12*, 1-25.

Sontek/YSI (2001), *SonTek ADVField Acoustic Doppler Velocimiter: Technical Documentation*, 165 pp., San Diego, CA.

Soucek, B. (2001), Universal brain theory: The self organization of understanding, consciousness, emotions and knowledge, *Periodicum Biologorum*, *103*, 219-228.

Soulsby, R. L. (1980), Selecting record length and digitization rate for near-bed turbulence measurements, *Journal of Physical Oceanography*, *10*, 208-219.

Strahler, A. N. (1952), The dynamic basis of geomorphology, *Geological Society of America Bulletin*, *63*, 923-938.

Strom, K., A. N. Papanicolaou, N. Evangelopoulos, and M. Odeh (2004), Microforms in gravel bed rivers: Formation, disintegration, and effects on bedload transport, *Journal of Hydraulic Engineering-Asce*, *130*, 554-567.

Stuart, T. A. (1953), Spawning migration, reproduction and young stages of loch trout, *Freshwater Salmon Fish. Res.*, *5*, 39 pp.

Sukhodolov, A., M. Thiele, and H. Bungartz (1998), Turbulence structure in a river reach with sand bed, *Water Resources Research*, *34*, 1317-1334.

Sukhodolov, A. N., and B. L. Rhoads (2001), Field investigation of three-dimensional flow structure at stream confluences, *Water Resources Research*, *37*, 2411-2424.

Sumer, B. M., L. H. C. Chua, N. S. Cheng, and J. Fredsoe (2003), Influence of turbulence on bed load sediment transport, *Journal of Hydraulic Engineering*, *129*, 585-596.

Teleki, P. G. (1972), Areal sorting of bedload material: the hypothesis of velocity reversal, Discussion, *Geologic Society of America Bulletin*, *83*, 911-914.

Theodorsen, T. 1952. Mechanism of Turbulence. Pages 1-18 *in* 2nd Midwestern Conference on Fluid Mechanics. Ohio State University, Columbus.

Theraulaz, G., J. Gautrais, S. Camazine, and J. L. Deneubourg (2003), The formation of spatial patterns in social insects: from simple behaviours to complex structures, *Philosophical Transactions of the Royal Society of London Series a-Mathematical Physical and Engineering Sciences*, *361*, 1263-1282.

Thompson, D. M. (2001), Random controls on semi-rhythmic spacing of pools and riffles in constriction-dominated rivers, *Earth Surface Processes and Landforms*, *26*, 1195-1212.

Thompson, D. M. (2002), Geometric adjustment of pools to changes in slope and discharge: a flume experiment, *Geomorphology*, *46*, 257-265.

Thompson, D. M. (2004), The influence of pool length on local turbulence production and energy slope: a flume experiment, *Earth Surface Processes and Landforms*, *29*, 1341-1358.

Thompson, D. M. (2006), The role of vortex shedding in the scour of pools, *Advances in Water Resources*, *29*, 121-129.

Thompson, D. M. (in press), The characteristics of turbulence in a shear zone downstream of a channel constriction in a coarse-grained forced pool, *Geomorphology*.

Thompson, D. M., and K. S. Hoffman (2001), Equilibrium pool dimensions and sediment-sorting patterns in coarse-grained, New England channels, *Geomorphology*, *38*, 301-316.

Thompson, D. M., J. M. Nelson, and E. E. Wohl (1998), Interactions between pool geometry and hydraulics, *Water Resources Research*, *34*, 3763-3681.

Thompson, D. M., E. E. Wohl, and R. D. Jarrett (1999), Velocity reversals and sediment sorting in pools and riffles controlled by channel constrictions, *Geomorphology*, *27*, 229-241.

Tribe, S., and M. Church (1999), Simulations of cobble structure on a gravel streambed, *Water Resources Research*, *35*, 311-318.

Tufillaro, N. B. (1993), Discrete dynamical models showing pattern formation in subaqueous bedforms, *International Journal of Bifurcation and Chaos*, *3*, 779-784.

Venditti, J. G., and B. O. Bauer (2005), Turbulent flow over a dune: Green River, Colorado, *Earth Surface Processes and Landforms*, *30*, 289-304.

Venditti, J. G., and S. J. Bennett (2000), Spectral analysis of turbulent flow and suspended sediment transport over fixed dunes, *Journal of Geophysical Research-Oceans*, *105*, 22035-22047.

Venditti, J. G., M. A. Church, and S. J. Bennett (2005), Bed form initiation from a flat sand bed, *Journal of Geophysical Research-Earth Surface*, *110*,

Voulgaris, G., and J. H. Trowbridge (1998), Evaluation of the Acoustic Doppler Velocimeter (ADV) for turbulence measurements, *Journal of Atmospheric and Oceanic Technology*, *15*, 272-289.

Walker, D. R., R. G. Millar, and R. W. Newbury (2004), Energy profiles across constructed riffles, *Journal of Hydraulic Engineering*, *130*, 199-207.

Warburton, J. (1992), Observations of bed-load transport and channel bed changes in a proglacial mountain stream, *Arctic and Alpine Research*, *24*, 195-203.

Welch, P. D. (1967), The use of fast fourier transform for the estimation of power spectra: a method based on time averaging over short modified periodograms., *IEEE Trans. Audio Electroacoust.*, *AU-15*, 70-73.

Werner, B. T. (1995), Eolian dunes: computer simulations and attractor interpretation, *Geology*, *23*, 1107-1110.

Werner, B. T. (1999), Complexity in natural landform patterns, *Science*, *284*, 102-104.

Whiting, P. J. (1997), The effect of stage on flow and components of the local force balance, *Earth Surface Processes and Landforms*, *22*, 517-530.

Whiting, P. J., and W. E. Dietrich (1991), Convective accelerations and boundary shear-stress over a channel bar, *Water Resources Research*, *27*, 783-796.

Whiting, P. J., W. E. Dietrich, L. B. Leopold, T. G. Drake, and R. L. Shreve (1988), Bedload sheets in heterogeneous sediment, *Geology*, *16*, 105-108.

Wilcock, P. R. (1996), Estimating local bed shear stress from velocity observations, *Water Resources Research*, *32*, 3361-3366.

Wilcock, P. R., and B. W. McArdell (1993), Surface-based fractional transport rates: mobilization thresholds and partial transport of a sand-gravel sediment, *Water Resources Research*, *29*, 1297-1312.

Wilcock, P. R., and B. W. McArdell (1997), Partial transport of a sand/gravel mixture, *Water Resources Research*, *33*, 235-245.

Wilkinson, S. N., R. J. Keller, and I. D. Rutherfurd (2004), Phase-shifts in shear stress as an explanation for the maintenance of pool-riffle sequences, *Earth Surface Processes and Landforms*, *29*, 737-753.

Willmarth, W. W., and S. S. Lu (1972), Structure of the Reynolds stress near the wall, *Journal of Fluid Mechanics*, *55*, 65-92.

Wohl, E. E., and D. M. Thompson (2000), Velocity characteristics along a small step-pool channel, *Earth Surface Processes and Landforms*, *25*, 353-367.

Wohl, E. E., J. R. Vincent, and D. J. Merritts (1993), Pool and riffle characteristics in relation to channel gradient, *Geomorphology*, *16*, 99-110.

Wolfram, S. (1984), Cellular automata as models of complexity, *Nature*, *311*, 419-426.

Yakhot, V. (1998), Probability density and scaling exponents of the moments of longitudinal velocity difference in strong turbulence, *Physical Review E*, *57*, 1737-1751.

Yalin, M. S. (1971), On the formation of dunes and meanders, *Proceedings of the 14th International Conference of the Hydraulic Research Association*, *C13*, 1-8.

Yalin, M. S., and A. M. F. da Silva (2001), *Fluvial Processes*, 197 pp., International Association of Hydraulic Engineering and Research (IAHR), Delft, The Netherlands.

Yang, C. T. (1971), Formation of riffles and pools, *Water Resources Research*, *7*, 1567-1574.

Yang, C. T. (1976), Minimum unit stream power and fluvial hydraulics, *Journal of the Hydraulics Division*, *102*, 919-934.

Zedel, L., A. E. Hay, R. Cabrera, and A. Lohrmann (1996), Performance of a single-beam pulse-to-pulse coherent Doppler profiler, *Ieee Journal of Oceanic Engineering*, *21*, 290-297.

Zimmerman, A., and M. Church (2001), Channel morphology, gradient profiles and bed stresses during flood in a step-pool channel, *Geomorphology*, *40*, 311-327.

APPENDIX A – ACCORD DES COAUTEURS ET PERMISSION DE L'ÉDITEUR

Bruce MacVicar, Ph.D. Géographie

Article 1

MacVicar, B., L. Parrott, A. Roy (*accepted*), A 2-D discrete particle model of gravel-bed river systems, *Journal of Geophysical Research - Earth Surface.*

À titre de coauteur de l'article identifié ci-dessus, je suis d'accord pour que Bruce MacVicar inclue cet article dans sa thèse de doctorat qui a pour titre *On Turbulence and the Formation of Riffle-Pools in Gravel-Bed Rivers.*

Coauteur	Signature	Date
Coauteur	Signature	Date

Article 2

MacVicar, B., E. Beaulieu, V. Champagne and A. Roy (*submitted*), Measuring water velocity in highly turbulent flows: Field tests of an Electromagnetic Current Meter (ECM) and an Acoustic Doppler Velocimeter (ADV), *Earth Surface Processes and Landforms.*

À titre de coauteur de l'article identifié ci-dessus, je suis d'accord pour que Bruce MacVicar inclue cet article dans sa thèse de doctorat qui a pour titre *On Turbulence and the Formation of Riffle-Pools in Gravel-Bed Rivers.*

Coauteur	Signature	Date
Coauteur	Signature	Date
Coauteur	Signature	Date

Article 3

MacVicar, B., and A. Roy (*in preparation*), Flow dynamics of a forced pool in a gravel-bed river Part A: Mean velocity and turbulence intensity, *Water Resources Research.*

À titre de coauteur de l'article identifié ci-dessus, je suis d'accord pour que Bruce MacVicar inclue cet article dans sa thèse de doctorat qui a pour titre *On Turbulence and the Formation of Riffle-Pools in Gravel-Bed Rivers.*

Coauteur	Signature	Date

Article 4

MacVicar, B., and A. Roy (*in preparation*), Flow dynamics of a forced pool in a gravel-bed river Part B: The structure and scale of turbulent events, *Water Resources Research.*

À titre de coauteur de l'article identifié ci-dessus, je suis d'accord pour que Bruce MacVicar inclue cet article dans sa thèse de doctorat qui a pour titre *On Turbulence and the Formation of Riffle-Pools in Gravel-Bed Rivers.*

Coauteur	Signature	Date

Article 5

MacVicar, B., and A. Roy (*in preparation*), Sediment dynamics of a forced pool in a gravel-bed river, *Geomorphology*.

À titre de coauteur de l'article identifié ci-dessus, je suis d'accord pour que Bruce MacVicar inclue cet article dans sa thèse de doctorat qui a pour titre *On Turbulence and the Formation of Riffle-Pools in Gravel-Bed Rivers.*

Coauteur	Signature	Date

APPENDIX B – AUTORISATION DE RÉDIGER LA THÈSE EN ANGLAIS

Université de Montréal

Registrariat

DATE 04 mai 2001

Admission

BRUCE MACVICAR
[redacted]

CODE PERMANENT [redacted]

(non résident du Québec)

J'ai le plaisir de vous informer que vous êtes admis(e) à:

3-155-1-0 PH.D. GEOGRAPHIE

pour l'automne 2001 comme étudiant(e) régulier(ière) à plein temps.

Je vous souhaite la bienvenue et du succès dans vos études.

. durée minimale de la scolarité (en trimestres équivalent plein temps): 6.0 trimestre(s)

N.B. Vous êtes autorisé(e) à soumettre une thèse rédigée en langue anglaise

N.B. Avant la fin de votre premier trimestre d'études, vous devrez, sous peine d'annulation de votre inscription, subir un test de français auquel vous serez convoqué(e) à votre arrivée à Montréal.

. c.c.: Rock Faulkner

[redacted]

Responsable : KATHLEEN LENNON tél : 514 343-6426

Pour LOUIS MAHEU, DOYEN
ETUDES SUPERIEURES

[redacted]

FERNAND BOUCHER
REGISTRAIRE

0181

À CONSERVER

AO (03-1999) sca225

APPENDIX C – AUTORISATION DE RÉDIGER LA THÈSE SOUS FORME D'ARTICLES

Université de Montréal

Faculté des études supérieures
Vice-décanat

Le 7 mars 2005

Monsieur Bruce MacVicar
Étudiant Ph.D.
Département de géographie
Université de Montréal

Objet : Autorisation de déposer votre thèse de doctorat sous forme d'articles

Monsieur,

Suite à votre demande, j'ai le plaisir de vous autoriser à présenter votre thèse de doctorat sous forme d'articles. Il est entendu que vous devrez vous soumettre aux conditions minimales de dépôt décrites dans le « Guide de présentation des mémoires de maîtrise et des thèses de doctorat », édition de mars 2001. Ce document est disponible sur le site de la FES. Vous pouvez également vous le procurer à la Librairie de l'Université de Montréal.

Cependant, afin de respecter la loi canadienne sur les droits d'auteurs, vous devrez, au moment du dépôt de votre thèse, remettre avec les formulaires de reproduction et de diffusion dûment complétés et signés, les déclarations écrites de tous les coauteurs des articles inclus dans votre thèse autorisant la reproduction et la diffusion de votre thèse de doctorat.

Veuillez agréer, Monsieur, l'expression de mes sentiments les meilleurs.

Le vice-doyen,

[redacted]

Jacques Bélair

/rbo.

cc. : Monsieur André Roy
Monsieur François Cavayas
Département de géographie

C.P. 6128, succursale Centre-ville
Montréal QC H3C 3J7

Téléphone : (514) 343-5891
(514) 343-6957
(514) 343-6922

Télécopieur : (514) 343-2252